Dissertation

submitted to the

Combined Faculty of Natural Sciences and Mathematics

of Heidelberg University, Germany

for the degree of

Doctor of Natural Sciences

Put forward by

Michael Rudolf Ciupek

born in Landstuhl, Germany

Oral examination : 05.02.2024

Using spectator neutrons to determine the fluctuating shapes of the QGP droplets created in heavy-ion collisions at the LHC

Referees:

Prof. Dr. Silvia Masciocchi

Prof. Dr. Norbert Herrmann

Scientific Advisor:

Dr. Ilya Selyuzhenkov

Abstract

The strong force is one of the four fundamental forces that describes the interaction of quarks and gluons. Its theory is called quantum chromodynamics (QCD), and one of its features is the running of the coupling constant, which depends on the momentum transfer between quarks and gluons. This gives rise to the notion that nuclear matter can be heated up to the temperatures when a new state of matter, governed by deconfined quarks and gluons, will be created. This state is called the quark-gluon plasma (QGP). The different phases and transitions of the QCD matter can be studied via relativistic heavy-ion collisions, in which extreme temperature and baryon density can be achieved. Under conditions of small baryon chemical potential, $\mu_b \approx 0$ MeV, the lattice QCD predicts a crossover transition at temperature about 156 MeV. These conditions can be achieved in relativistic heavy-ion collisions at LHC energies.

The initial energy density in the overlap region of two colliding nuclei is asymmetric, and its shape fluctuates due to the inner structure of the nuclei. This spatial anisotropy is converted during the hydrodynamic expansion of the QGP into momentum anisotropies in the distribution of produced particles, known as anisotropic flow. The anisotropic flow develops a particle-type dependence due to the hydrodynamic expansion since the particles of different masses are affected differently by the radial fluid velocities.

A detailed understanding of the initial state of a heavy-ion collision is important in order to extract the transport properties of the QGP, e.g., the shear and bulk viscosities, from the comparison with the hydrodynamic model calculations. A unique role in this context is played by the spectator nucleons, which are the remnants of the collision. Due to the strong Lorentz contraction of the nuclei, their passing time is much shorter than the expansion time of the QGP. Consequently, spectator nucleons are sensitive to the early times of the collision evolution and using them in flow measurements has a unique potential to improve understanding of the initial conditions.

The results presented in this thesis provide new insights for the understanding of the initial state and the hydrodynamic evolution of the QGP. The thesis presents novel measurements of the anisotropic flow relative to the neutron spectator plane, $v_2\{\Psi_{\mathrm{SP}}\}$, in Pb–Pb collisions at $\sqrt{s_{\mathrm{NN}}} = 2.76\,\mathrm{TeV}$ recorded by the ALICE experiment at the LHC. The measurements are performed for charged pions, kaons, and (anti)protons at mid-rapidity as a function of transverse momentum, p_{T} = 0.2-6 GeV/c, and collision centrality. The $v_2\{\Psi_{\mathrm{SP}}\}$ is compared to anisotropic flow relative to the participant plane, estimated by the two- and four-particle cumulants. A significant difference between charged pions and (anti)protons (kaons) of 3.6% (1.6%) was found, suggesting a coupling of the effects of the hydrodynamic expansion of the QGP and the subsequent hadronization with the initial state fluctuations. These novel measurements open new opportunities to control contributions from initial state fluctuations in flow measurements, which is crucial for precise determination of the QGP transport properties from the systematic comparison of the experimental data to the hydrodynamic model calculations.

Zusammenfassung

Die starke Kraft ist eine der vier Grundkräfte, die die Wechselwirkung von Quarks und Gluonen beschreibt. Ihre Theorie wird Quantenchromodynamik (QCD) genannt, und eines ihrer Merkmale ist der Verlauf der Kopplungskonstante, die von der Impulsübertragung zwischen Quarks und Gluonen abhängt. Daraus ergibt sich die Vorstellung, dass die Kernmaterie bis zu den Temperaturen aufgeheizt werden kann, bei denen ein neuer Materiezustand entsteht, der durch entkoppelte Quarks und Gluonen bestimmt wird. Dieser Zustand wird als Quark-Gluon-Plasma (QGP) bezeichnet. Die verschiedenen Phasen und Übergänge der QCD-Materie können durch relativistische Schwerionenkollisionen untersucht werden, bei denen extreme Temperaturen und Baryonendichten erreicht werden können. Unter den Bedingungen eines kleinen chemischen Baryonenpotentials $\mu_b \approx 0$ MeV sagt die Gitter-QCD einen Übergang bei Temperaturen um 156 MeV voraus. Diese Bedingungen können in relativistischen Schwerionenkollisionen bei LHC-Energien erreicht werden.

Die anfängliche Energiedichte im Überlappungsbereich zweier kollidierender Kerne ist asymmetrisch, und ihre Form schwankt aufgrund der inneren Struktur der Kerne. Diese räumliche Anisotropie wird während der hydrodynamischen Expansion des QGP in Impulsanisotropien der erzeugten Teilchen umgewandelt, die als anisotroper Fluss bezeichnet werden. Der anisotrope Fluss entwickelt aufgrund der hydrodynamischen Expansion eine Abhängigkeit vom Teilchentyp, da die Teilchen unterschiedlicher Masse unterschiedlich von den radialen Flussgeschwindigkeiten des QGP beeinflusst werden.

Ein detailliertes Verständnis des Anfangszustandes einer Schwerionen-Kollision ist wichtig, um die Transporteigenschaften des QGP, z.B. die Scher- und Volumenviskosität, aus dem Vergleich mit den hydrodynamischen Modellrechnungen zu extrahieren. Eine besondere Rolle spielen in diesem Zusammenhang die Zuschauernukleonen, die die Überbleibsel der Kollision sind. Aufgrund der starken Lorentz-Kontraktion der Kerne ist ihre Verweilzeit viel kürzer als die Expansionszeit des QGP. Folglich sind Zuschauernukleonen empfindlich für die frühen Zeiten der Kollisionsentwicklung, und ihre Verwendung in Strömungsmessungen hat ein einzigartiges Potenzial, um das Verständnis der Anfangsbedingungen zu verbessern.

Die in dieser Arbeit vorgestellten Ergebnisse liefern neue Erkenntnisse für das Verständnis des Anfangszustands und der hydrodynamischen Entwicklung des QGP. Die Arbeit stellt neue Messungen des anisotropen Flusses relativ zur Zuschauernukleonenebene $v_2\{\Psi_{\mathrm{SP}}\}$ in Pb-Pb-Kollisionen bei $\sqrt{s_{\mathrm{NN}}} = 2.76\,\mathrm{TeV}$ vor, die vom ALICE-Experiment am LHC aufgezeichnet wurden. Die Messungen werden für geladene Pionen, Kaonen und (Anti-)Protonen bei mittlerer Geschwindigkeit als Funktion des transversalen Impulses, p_{T} = 0.2-6 GeV/c, und der Kollisionszentralität durchgeführt. Der $v_2\{\Psi_{\mathrm{SP}}\}$ wird mit dem anisotropen Fluss relativ zur Teilnehmerebene verglichen, der durch die Zwei- und Vier-Teilchen-Kumulanten geschätzt wird. Es wurde ein signifikanter Unterschied zwischen geladenen Pionen und (Anti-)Protonen (Kaonen) von 3,6% (1,6%) festgestellt, was auf eine Kopplung der Effekte der hydrodynamischen Expansion des QGP und der anschließenden Hadronisierung mit den Fluktuationen des Anfangszustands schließen lässt. Diese neuartigen Messungen eröffnen neue Möglichkeiten zur Kontrolle der Beiträge von Anfangszustandsfluktuationen bei Strömungsmessungen, was für die genaue Bestimmung der QGP-Transporteigenschaften durch den systematischen Vergleich der experimentellen Daten mit den hydrodynamischen Modellrechnungen entscheidend ist.

Contents

1 Introduction

The work presented in this thesis focuses on improving our understanding of one of the fundamental forces included in the Standard Model of particle physics. This force is called strong interaction, which is described in the context of quantum chromodynamics (QCD). The particles described by the strong interactions are quarks and gluons, typically bound in our everyday experience within composite particles known as hadrons. Under extreme conditions, this hadronic matter undergoes a phase transition into a state where quarks and gluons exist as free entities. This state of strongly interacting, deconfined matter is known as quark-gluon plasma (QGP). It is of special interest since the QGP is believed to have existed in the very first microseconds after the Big Bang [1]. This makes it necessary to investigate different properties of the QGP and this work is intended to add a contribution to this endeavor. The QGP can experimentally be produced in relativistic heavy-ion collisions. This chapter shall provide an introduction to the essential theoretical background necessary for the discussion presented in this thesis.

1.1 Standard model of particle physics and QCD

The Standard Model (SM) is a relativistic quantum field theory that successfully describes all known elementary particles and three out of four fundamental forces, namely the electromagnetic, weak, and strong interactions. An overview of the particles described by the Standard Model is shown in Figure 1.1.

The particles within the Standard Model can be broadly categorized into two groups: gauge bosons and fermions. Gauge bosons are characterized by their spin of 1 and serve as the mediators of the electromagnetic, weak, and strong forces acting on their respective charges. For instance, the photon (γ) mediates the electromagnetic force, acting on particles with an electric charge, while the $W^{\pm}$ and Z^0 bosons interact with the flavor charges. In contrast, gluons (g) facilitate strong interactions between particles with color charges.

The second group are fermions, which have a half-integer spin. Fermions can be further divided into two subgroups: quarks, which carry charges associated with all three interactions, and leptons, which only interact through electromagnetic and/or weak interaction.

The Higgs boson completes the Standard Model and is the only scalar spin-zero particle in the theory. Through the mechanism of spontaneous symmetry breaking [3], the Higgs boson provides masses to the $W^{\pm}$ and Z^0 bosons, as well as the masses of quarks and leptons via Yukawa interactions. A comprehensive overview of the entire Standard Model

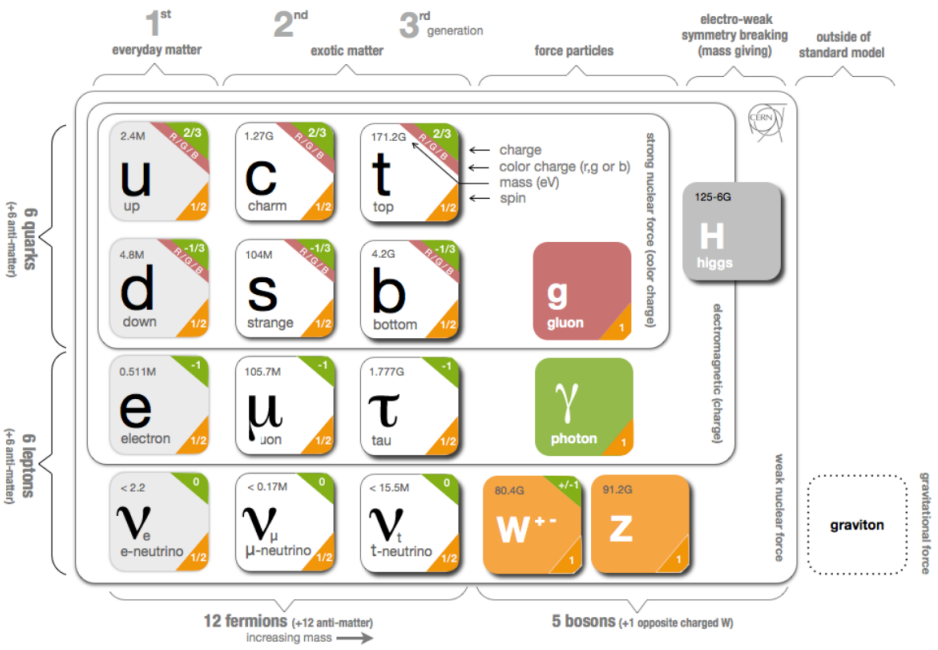

Figure 1.1: Elementary particles in the standard model. The figure is taken from [2].

is beyond the scope of this thesis. Interested readers are encouraged to refer to [4] for more in-depth information. This thesis will primarily focus on the strong interaction and behavior of the strongly-interacting matter under extreme conditions.

The strong force is described by quantum chromodynamics (QCD), which is based on the local gauge symmetry SU(3). The conserved charge in QCD is called color charge, and due to the underlying SU(3) symmetry, it can take one of three different values: blue, green, or red. Gluons carry unbalanced color charges because the SU(3) group is non-commutative. This unique feature allows gluons to change the color charge of particles they interact with. These characteristics distinguish QCD from quantum electrodynamics (QED), which describes the electromagnetic force. In QED, there is only one charge, the electric charge, and the photon does not carry any charge. The fact that gluons carry color charges allows for self-interactions, which leads to anti-screening.

To understand the concept of anti-screening and its consequences, it is beneficial to first understand the screening effect in QED. In the vacuum, virtual electron-positron pairs are continuously created and annihilated. In the presence of an electric charge, the vacuum becomes polarized, resulting in virtual particles of the opposite charge being attracted to the charge. In contrast, particles of the same charge are repelled. This polarization leads to a partial cancellation of the electric field at varying distances from the charge. As one moves closer to the charge, the effect of vacuum polarization diminishes, consequently increasing the effective electric charge observed.

In the context of QCD, a similar phenomenon occurs with the creation of quark-antiquark pairs, leading to a screening effect. Since gluons carry color charges, they can engage in self-interactions, producing gluon pairs within the vacuum. The net effect of these virtual gluon interactions is not to screen the charge at large distances but to enhance it and change its color. This behavior is known as anti-screening.

The screening and anti-screening have opposing effects, and which one dominates depends on the number of different quark flavors involved. It has been demonstrated that for QCD with three colors, the screening effect becomes dominant when there are more than 16 quark flavors, exceeding the six quark flavors observed in nature.

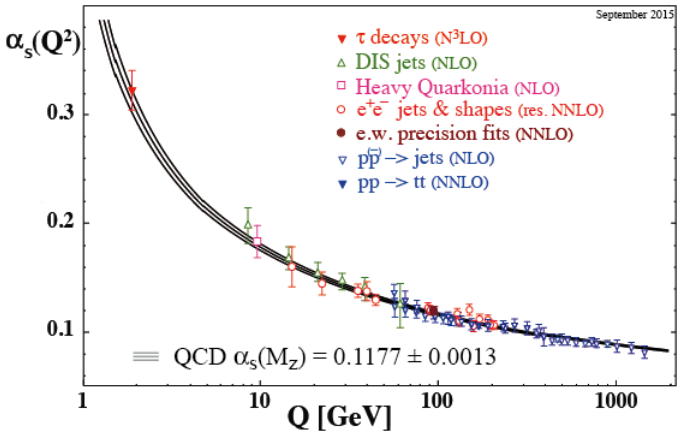

Figure 1.2: The running coupling constant of QCD α_s as a function of the momentum transfer Q^2. The figure taken from [5].

The dominance of anti-screening relative to screening causes the strong coupling constant α_s to decrease as the distance between the two quarks decreases or as the momentum transfer (Q^2) between the two quarks increases. This running of α_s is proven by numerous experiments, as illustrated in Figure 1.2, and gives rise to two fundamental phenomena observed in QCD: color confinement and asymptotic freedom.

As Q^2 decreases, the strong coupling constant diverges, meaning that quarks cannot be separated from each other and are bound into hadrons, known as color confinement. Currently, there is no analytical proof for color confinement, but experimentally, quarks and gluons have never been observed as free particles. On the other hand, as the momentum transfer increases, the strong coupling constant becomes very small, and the quarks can be treated as quasi-free particles.

At higher momentum transfers the coupling constant α_s is small and perturbative QCD (pQCD) becomes a reliable approach to calculating physics processes. In the pQCD, the calculations of physics processes are performed in an expansion in powers of α_s, where higher orders of α_s can be neglected. However, for small energy transfers and

correspondingly large α_s, higher order terms in α_s cannot be neglected. Lattice QCD, calculations on a discretized spacetime, allows to perform non-perturbative caclulations for large values of the strong coupling constant [6]. Lattice QCD has proven to be successful in predicting the properties of hadrons and determining the fundamental properties of the QCD matter.

1.2 QCD matter under extreme conditions

The observation of QCD as an asymptotically free gauge theory, characterized by the running strong coupling constant, leads to the existence of different states of nuclear matter. As described in the previous section, quarks and gluons are confined into hadrons under normal conditions. This changes when hadronic matter is put under extreme conditions, such as high temperature or density. According to the lattice QCD calculations, a phase transition exists between the confined hadronic matter and a phase where quarks and gluons act as free constituents. To grasp this concept intuitively, consider that hadrons have a size of around 1 fm. As the density of hadronic matter increases, the hadron's wave functions start to overlap. This results in a new state of matter where partons behave as free particles in a volume larger than the typical hadron size, known as the quark-gluon plasma [7].

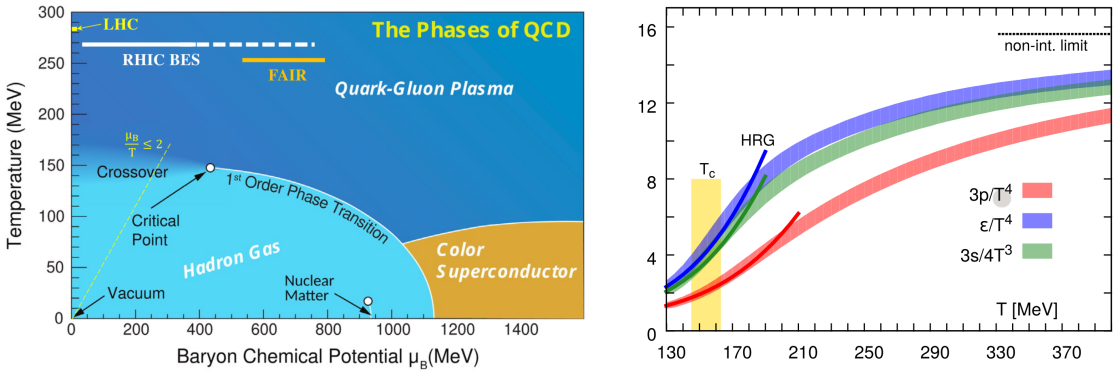

Figure 1.3: [Left Panel] Sketch of the QCD phase diagram as a function of temperature T and baryochemical potential μ_B. [Right Panel] Predictions of lattice QCD (colored band) for pressure p, energy density ε and entropy density s of nuclear matter as a function of temperature T. The crossover region around $T_c \approx 156$ MeV (yellow band) is shown. Figures was taken from [8, 9].

A illustration of the QCD phase diagram is shown in the left panel of Figure 1.3 where it is depicted as a function of the temperature T and the baryochemical potential μ_B, which is a measure of the net baryon density. At temperatures below $T \approx 150$ MeV and $\mu_B \approx 1100$ MeV, the QCD matter exists as a hadron gas, where quarks and gluons are confined. At higher baryochemical potential and low temperatures, the QCD matter is predicted to form a color superconductor, where quarks and gluons form color Cooper pairs. This color superconductor is hypothesized to be a state of matter within the cores of neutron stars,

where μ_B is extremely high due to the intense gravitational compression of nuclear matter [10].

For high-energy densities reached at large temperatures and/or large baryochemical potentials, QCD matter undergoes a phase transition from a hadron gas to the QGP. The type of the phase transition differs depending on the temperature and μ_B of the matter. At sufficiently high μ_B, the hadron gas is predicted to undergo a sharp first-order transition, effectively separating it from the deconfined QGP phase [11]. At vanishing μ_B, the transition is predicted to be of the crossover type [12]. The possible existence of the switch from a crossover to a first-order phase transition with increasing μ_B, suggests the existence of a critical point [13]. The region of large μ_B is poorly understood. Theoretically, first principle calculations by lattice QCD in this region of the phase diagram are impossible due to the fermion sign problem [14].

The region of vanishing baryochemical potential can be accessed using lattice QCD methods [8], which allows the computation of thermodynamic properties of the QCD matter. Predictions for fundamental parameters such as pressure p, energy density ε, and entropy density s, as a function of the temperature T are presented in the right panel of Figure 1.3. Calculations are performed for a system of light quarks (2+1 flavor) and gluons [8]. Colored bands represent the results obtained from the Lattice QCD model, whereas colored lines show predictions from hadron gas models. The hadron gas models align well with the lattice calculations below the crossover temperature, where nuclear matter exists in a hadronic state. Above the crossover temperature, the hadron gas model deviates from the lattice QCD predictions, indicating the change in the degrees of freedom in the QGP phase. According to lattice QCD, the crossover phase transition at zero baryochemical potential occurs at around $T(\mu_B = 0) = (156.5 \pm 1.5)$ MeV [13].

1.3 Heavy-ion collisions

The QCD phase diagram can be experimentally studied in the laboratory via relativistic heavy-ion collisions, where conditions of high energy density can be reached. Heavy-ion collisions have been intensely studied over the last five decades, starting with fixed target experiments at SIS18, AGS, and SPS covering the region of collision energies $\sqrt{s_{NN}} = 10\,\text{GeV}$ and progressing to collider experiments at RHIC and the LHC with top energies of 200 GeV and 5.36 TeV, respectively. These experiments play a crucial role in exploring the QCD phase diagram as they probe different regions.
Collider experiments at the LHC and RHIC explore the phase diagram at the $\mu_B \approx 0$ MeV. Experiments at lower center-of-mass energies probe the region of large baryochemical potentials. Among the future experiments at high μ_B is the Compressed Baryonic Matter (CBM) [16] experiment, which is under construction at FAIR. The space-time evolution of a heavy-ion collision at TeV energies is illustrated in Figure 1.4. The region of interaction of a heavy-ion collision is governed by the shape of the colliding nuclei and the internal spatial arrangement of nucleons within them. At $\tau = 0$ fm/c, the extreme energy and en-

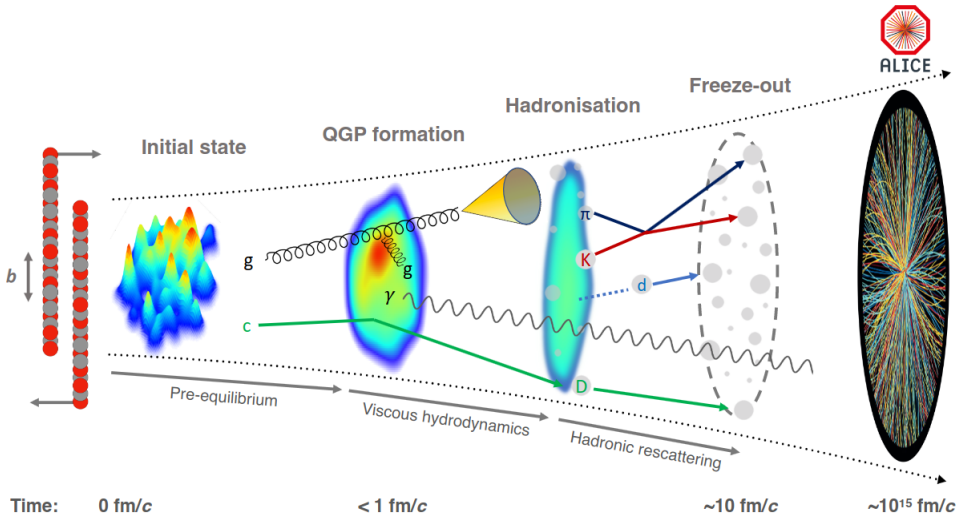

Figure 1.4: Sketch of the evolution of a heavy-ion collision at LHC energies. Figure was taken from [15].

tropy densities are reached in the overlap region of the two nuclei. During Pb–Pb collisions at $\sqrt{s_{\mathrm{NN}}} = 2.76\,\mathrm{TeV}$, the average energy density achieved at $\tau = 1$ fm/c is approximately 12 GeV/fm^3, which is roughly twenty times greater than the energy density of a single hadron [17].

The nucleons that do not undergo inelastic collisions in the overlap region are referred to as spectator nucleons, and their role in the collision depends on the center-of-mass energy. At lower energies, the Lorentz contraction of the nuclei is relatively small, resulting in a noticeable longitudinal size. The passing time of the spectator nucleons compared to the interaction time of the matter in the overlap region is comparable. This means that the spectator nucleons are essential for the description of the matter created in the overlap region of the nuclei at small center-of-mass energies. As the collision energies increase, the passing time of the spectators is getting smaller and smaller compared to the thermalization time. Consequently, the interaction between the overlap region and spectator nucleons is confined to earlier stages of the collision evolution. The spectators are becoming sensitive to the initial state of the heavy-ion collision at the TeV energies, making them a unique probe to study the initial state.

The phase following the initial moment of the collision is the ”pre-equilibrium phase”. Many quarks and gluons are produced during this phase, involving various QCD processes spanning a broad spectrum of momentum transfers Q^2. Each range of Q^2 contributes to the overall evolution of the collision. Most of the quarks and gluons undergo interaction of small-Q^2, which defines the overall energy density and entropy deposition in the initial state of the collision. Due to fluctuations in the distribution of nuclear matter within the

colliding nuclei, these soft interactions lead to 'lumpiness' in the initial energy density, as shown on the left-hand side of Figure 1.4.

The small-Q^2 interactions dominate the pre-equilibrium phase, giving rise to quarks and gluons, thus forming the strongly coupled QGP phase. During this pre-equilibrium phase, some quarks and gluons engage in large-Q^2 interactions, creating high-momentum partons and heavy charm and beauty quarks, as illustrated Figure 1.4. Since they are generated early in the collision, these high-momentum particles interact within the QGP, losing energy that is transferred to the medium during these interactions.

Approximately at $\tau < 1$ fm/c, due to the small-Q^2 interactions, the created matter reaches a thermal equilibrium, and the QGP is formed. At this point in time, the temperature of the system is $T > 300$ MeV, as estimated by the measured yields of thermal photons emitted by the QGP [18]. The QGP expansion can be described by relativistic fluid dynamics, as detailed in [19].

As the system expands, the energy density of the QGP progressively reduces until it falls below the crossover temperature of $T \approx 156$ MeV. At this moment, hadronization (see Section 1.6) occurs, in which quarks and gluons form color-neutral hadrons. At a certain temperature, inelastic scattering processes among these hadrons cease, known as the chemical freeze-out. The hadron gas remains at high density and temperature, allowing for elastic scattering within the gas. At $\tau \approx 10$ fm/c the kinetic freeze-out temperature, at which elastic scatterings also cease, is reached and distributions of the particles become fixed. The produced hadrons free-stream and at this moment, they can be registered with the detector.

1.4 Initial state of a heavy-ion collision

Understanding the initial state of the heavy-ion collision is crucial for gaining insights into the rapid thermalization of the hot and dense QCD matter created in such collisions. It is vital for understanding the mechanism entropy production, as most entropy is generated in the initial stages of the collisions and determines the particle multiplicity in the final state [17].

The shape and inner structure of the colliding nuclei define the shape of the initial energy density. The nuclear density distribution of many nuclei is described by a Woods-Saxon distribution, with parameters determined from electron-ion scattering experiments [20]. The shape of the initial energy distribution can be broadly categorized by a geometrical and fluctuating component. This is illustrated in Figure 1.5, where the left panel is representing the geometrical and the right panel the fluctuating component.
The geometrical component can be understood by imagining the two colliding nuclei as particles having a smooth density distribution. Depending on the impact parameter b

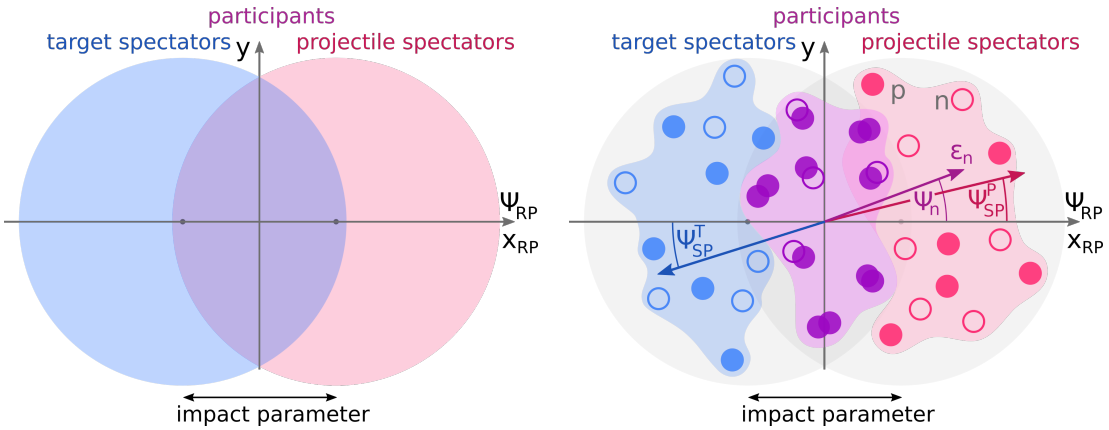

Figure 1.5: [Left panel] Transverse view of the initial state assuming a smooth density of both nuclei. The impact parameter b is indicated by the black horizontal arrow. [Right panel] Transverse view of the initial distribution of protons and neutrons composing the nuclei.

and the underlying geometry of the colliding nuclei, a different shape (close to elliptical) and size of the overlap region is formed, as shown in the left panel of Figure 1.5. The internal structures of the nuclei results in the ”lumpiness” in the initial energy density as shown at the left-hand side of Figure 1.4. In the right panel of Figure 1.5 the shape of the energy density in the overlap region becomes deformed and is subject to fluctuations on a collision-by-collision basis. These fluctuations are not unique to the overlap region. The distribution of spectator nucleons is also subject to these fluctuations.

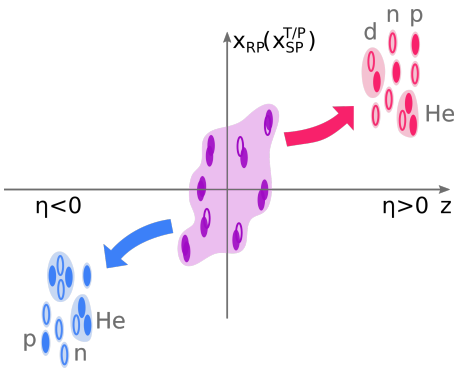

Figure 1.6: Longitudinal view of the initial state of a heavy-ion collision, treating the nuclei as a composed object of protons and neutrons.

As described in the previous section, the spectators in collisions at TeV energy only interact with nuclear matter at the early times of its evolution. These lead to a deflection of the spectators, which is illustrated in the in Figure 1.6. The magnitude of the deflection

depends on the properties of the nuclear QCD matter formed in the overlap region and the momentum transfers between the overlap region and the spectators. Consequently, the fluctuation of the overlap region results in fluctuations in the deflection of the spectators.

Modelling the initial stage in QCD is challenging and nonperturbative real-time dynamics cannot be calculated with lattice QCD. Therefore, one needs to use effective theories to describe the initial state of the heavy-ion collision. At the LHC energies, models of the initial stage of heavy-ion collisions can be categorized into two groups. The first category are the dynamical models of the pre-equilibrium phase using effective field theories [21]. The second category includes static theories, which are based on a snapshot of the collision at thermalization point, such as the MC Glauber [22] and the T$_\mathrm{R}$ENTo [23] models. Such description of the initial stages is applicable for collision energies, where, due to the high Lorentz contraction, the interaction time between spectators and overlap region is very short. Current initial state models, used to describe the heavy-ion collisions at the TeV energies, do not incorporate the dynamics between the spectator nucleons and the overlap region.

1.5 Hydrodynamic evolution of QGP

As described in Section 1.3, the matter produced in relativistic heavy-ion collision is initially out-of-equilibrium and undergoes rapid thermalization, after which it can be described as QGP. To study its properties the framework of hydrodynamics, which gives a macroscopic description of liquids in motion, is used. Hydrodynamics allows encoding the microscopic interactions of many particles to a few thermodynamic properties encoded in the equation of state and transport properties of the QCD matter. For hydrodynamics to work the local thermal equilibrium has to be achived. This means that pressure and temperature vary slowly over time for each point in the fluid. In addition, the mean free path between collisions in the medium should be significantly shorter than the characteristic scale of the system, which is acheived in the case for QGP due to the high-energy densities produced in the heavy-ion collision.

Due to the large pressure gradients the QGP expands and cools down. The symmetric expansion in all directions in the plane transverse to the collision, so-called radial flow, creates a common outward velocity field. The rate of this hydrodynamic expansion is influenced by the QGP bulk viscosity, which measures its resistance to volume changes. Additionally, the system exhibits anisotropic flow due to initial state asymmetries (Figure 1.5), resulting in directional-dependent pressure gradients. These spatial asymmetries transform into momentum anisotropies during the hydrodynamic evolution of the QGP. The specific relation between these anisotropies is influenced by the QGP shear viscosity, quantifying the fluid resistance to deformation.

1.6 Hadronization of the QGP

Hadronization is the process of transition from the partonic phase (QGP consisting of quarks and gluons) to the hadronic phase (hadron gas). In heavy-ion collisions, this transition occurs when the quark-gluon plasma expands and cools down below the crossover temperature. The hadronization of quarks and gluons occures at small momentum transfers and perturbative approaches for the description of hadronization are not applicable.
To describe this process, phenomenological models such as the Statistical Hadronization Model (SHM) [24] are used. The SHM is based on the assumption that the strong QCD interactions lead to the formation of colorless objects, which statistically decay into hadrons when reaching the crossover temperature [25].

The description itself is based on the work of Fermi in the year 1950, who postulated that particles evenly occupy all available phase space states [26]. The core assumption of the SHM is that: All multihadronic states within the cluster volume and compatible with its quantum numbers are equally likely[27].

In heavy-ion collisions, the hadronization is modeled using the grand canonical ensemble with a partition function Z that includes all known meson and baryon states. The QGP can be described using a grand canonical ensemble since the fireball created in such a collision is expected to be large, and particles are created and destroyed constantly in the medium. The SHM model involves three parameters: temperature T, baryo-chemical potential μ_B, and the volume of the medium.

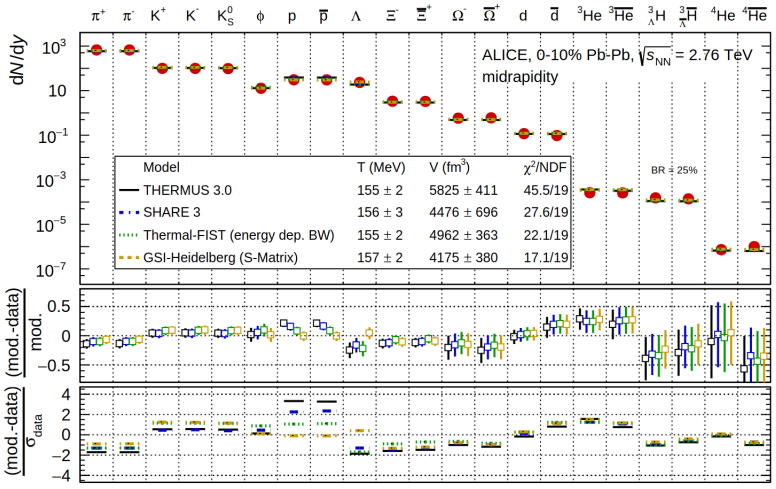

Figure 1.7: Measured multiplicity per unit of rapidity of different hadron species and light nuclei compared to different calculations of the Statistical Hadronization Model. Figure is taken from [15].

In Figure 1.7, a comparison of four distinct implementations of the Statistical Hadronization Model against the observed multiplicity of hadrons in central Pb–Pb collisions is

presented. The parameter ,μ_B, was fixed constant at $\mu_B = 0$ MeV for most models, except for the GSI-Heidelberg variant, where it was found to be compatible with zero within the associated uncertainties. This choice reflects the nearly equal abundances of particles and antiparticles at LHC energies. The volume of the QGP, consistently measures at 4500 fm^3 for nearly all models. The exception is the THERMUS model, which reported a significantly larger value.

The SHM model capture the abundance of various particle species, spanning over nine orders of magnitude [15]. The model also provides a quantitative description of light nuclei despite their binding energy being considerably lower than the temperature of the QGP.

The temperature at which the QGP hadronize, as determined from the fit of SHM models to hadron yields, is $T = 156$ MeV, with uncertainties ranging from 2 to 3 MeV and minimal differences of 1 MeV among the various models. This temperature closely aligns with the values derived from lattice QCD at $\mu_B = 0$ MeV, representing the transition from the Quark-Gluon Plasma (QGP) to the hadron gas. As highlighted in [28], this correspondence can be attributed to the rapid decline in particle density and, consequently, multi-particle scattering rates as the temperature decreases.

1.7 Extracting QCD matter properties with experimental data

The sections above provided an overview of the theory of strong interaction and behaviour of the QCD matter under extreme conditions. The QCD matter exhibits different states depending on temperature and net-baryon density. A great interest to the research conducted in this thesis, is the QGP, a state of matter where quarks and gluons are deconfined. The QGP properties can be experimentally investigated with heavy-ion collisions. The space-time evolution of a heavy-ion collision is a complicated process and understanding its different stages determines the precision of the extraction of the QGP properties. The remaining part of this section is dedicated to the motivation for the work presented in this thesis, which is dedicated to the topic of using spectator nucleon for determination of the QGP properties.

The role of spectators changes depending on the center-of-mass energies. At lower energies, they affect the whole evolution of the strongly interacting matter created in the overlap region of the two nuclei. At high energies, their influence is limited to the initial stages of the collision since they decouple very early from the interaction region. Understanding the initial state is important for several resasons as discussed in Section 1.4. The measurement of spectator nucleons allows us to investigate the dynamics between the spectators and the overlap region, which in current state-of-the-art initial state models are not considered.

Details of the initial state fluctuations are important for modelling the transformation of the spatial anisotropies into momentum anisotropies which happens during the hydrodynamic expansion of the QGP. The efficiency of converting spatial anisotropy into momentum space is strong sensitive to transport coefficients of the QGP, e.g., shear and bulk viscosities. The measurement of how momentum anisotropies depends on particle mass also probes the QGP's transport coefficients. The estimation of the shear and bulk viscosity of the QGP can be achieved by comparing the measured momentum correlations of particles with hydrodynamic model calculations. Precise extraction of the QGP transport properties is possible with the Bayesian estimation method [29]. An Example of such Bayesian analysis based on T$_R$ENTo initial state model with a boost-invariant hydrodynamic model is shown in Figure 1.8. These studies revealed a minimum shear viscosity of $\left(\frac{\eta}{s}\right)_{min} = 0.085^{+0.026}_{-0.025}$ for the Bayesian approach [29] and $\frac{\eta}{s} = 0.165^{+0.070}_{-0.079} \pm 0.007$ for the Fluid$u$M approach [30] The extraction of the QCD transport coefficients is still affected by large uncertainties. One source of these uncertainties is initial state modelling, which consequently biases the extraction of the QCD transport coefficients from the hydrodynamic model calculations.

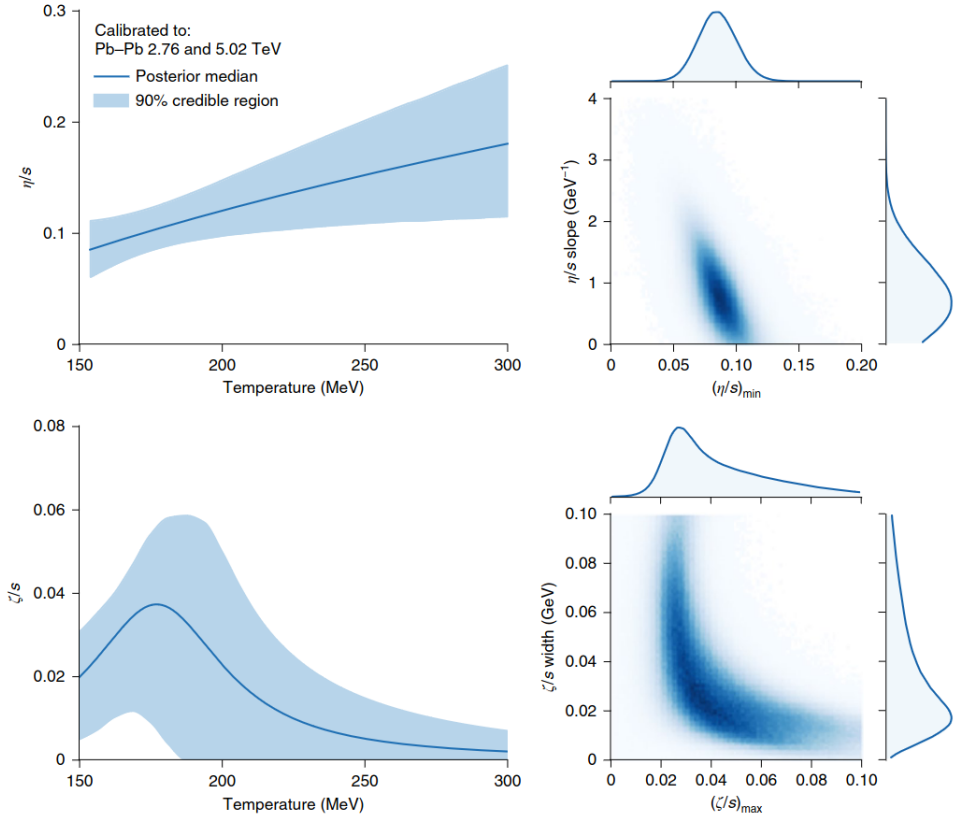

Figure 1.8: Shear and bulk viscosity extracted from fits to of hydrodynamic model simulation to experimental data for Pb–Pb collisions at $\sqrt{s_{\mathrm{NN}}} = 2.76\,\mathrm{TeV}$ and $\sqrt{s_{\mathrm{NN}}} = 5.02\,\mathrm{TeV}$. Figure was taken from [29].

The primary focus of this thesis revolves around the measurement and analysis of spectator

nucleons. The studies of the momentum anisotropies of the produced particles relative to the spectator plane and its particle-type dependence will help to improve the extraction of the QGP transport coefficients from the hydrodynamic model calculation. The measurements of the particle-type dependence of the momentum anisotropies relative to the spectator plane, will help to add new constrains on the parameters of the initial state models, the transport properties of the QGP and its mechanism.

2 Collective flow in heavy-ion collisions

Collisions of relativistic heavy ions create a hot and dense QCD matter in the nuclei overlap region. Large temperature and pressure gradients within the QCD matter transform the initial spatial asymmetries in the overlap region of the colliding nuclei into anisotropies in the momentum space. This collective expansion of the QCD matter is referred to as collective flow. Collective flow can be divided into the isotropic expansion, known as radial flow, and the anisotropic expansion resulting from the asymmetries in the initial state, referred to as anisotropic flow.

This chapter introduces the main flow observable and connected to them parameters of the initial state anisotropies, as well as provides an overview of the measurements concerning collective flow. First, the radial and anisotropic flow are introduced. Afterward, the anisotropic flow fluctuations and their connection to the fluctuations of the initial energy density are discussed. Then, the anisotropic flow relative to the spectator plane and connection to flow fluctuations is presented. Next, the sensitivity of the p_{T} and particle-type dependence of anisotropic flow to the hydrodynamic phase of the QGP and the hadronization is explained. The chapter concludes with a summary positioning the work of this thesis within the broader context of collective flow studies.

2.1 Radial flow

The radial expansion of the QGP is imprinted in the distribution of the final-state hadrons, leading to modifications of the invariant yield as a function of the transverse momentum. In Figure 2.1, the invariant yields of pions, kaons, and (anti)protons in central collisions for Pb–Pb collisions at $\sqrt{s_{\mathrm{NN}}} = 2.76\,\mathrm{TeV}$ and Au–Au collisions at $\sqrt{s_{\mathrm{NN}}} = 200\,\mathrm{GeV}$ are shown.
Radial flow leads to a flattening of the yields as a function of transverse momentum, with a more pronounced effect on heavier particles, as seen from the comparison between pion and proton yields. This can be understood as stronger push from the radial flow on heavier particles. This modification is proportional to the mass multiplied by the radial flow velocity, pushing low transverse momentum particles toward higher values. The degree of flattening in the transverse momentum yield is stronger at higher center-of-mass energies.

The average radial flow velocity can be determined by comparing the experimentally measured yields with hydrodynamical model predictions. The Blast-Wave parametrization

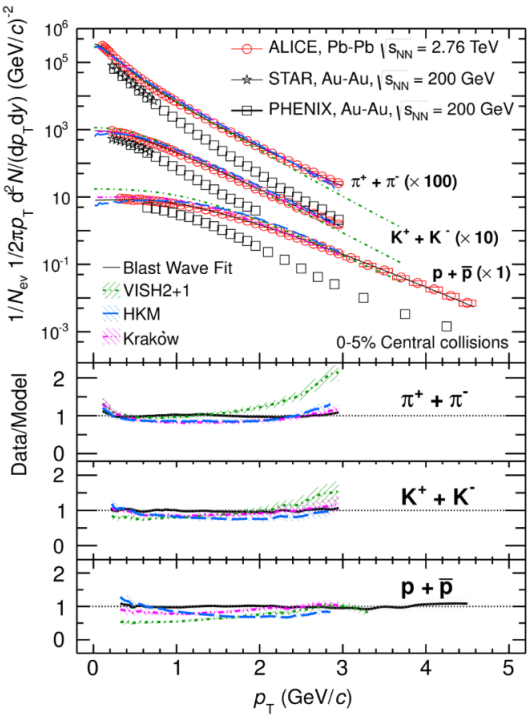

Figure 2.1: Transverse momentum distriubtion of pion, kaons and protons in Au-Au collsions at $\sqrt{s_{NN}} = 200$ GeV at RHIC and Pb-Pb collisions at $\sqrt{s_{NN}} = 2.76$ TeV at the LHC. The data is compared to different hydrodynamic models and the blast-wave model. Figure taken from [31].

[32], is typically used to extract the velocities from the measured spectra of identified hadrons. In this model, all particles are produced from a thermal source with transverse velocity profile:

$$\beta_T(r) = \beta_s \left(\frac{r}{R}\right)^n \tag{2.1}$$

where r is the radial distance from the center of the medium with radius R, β_s the surface velocity of the medium, and n is a free parameter. The particle spectra from the velocity profile is given by superposition of all thermal fluid cells within the medium.

The Blast-Wave fit to experimental data, along with hydrodynamical model calculations, is shown in Figure 2.1. It provides a good description of the data, as indicated in the lower panels by the ratio between data and model prediction. The average transverse velocity for Pb–Pb collisions at $\sqrt{s_{\mathrm{NN}}} = 2.76\,\mathrm{TeV}$ is $\langle\beta\rangle = 0.65 \pm 0.02$, which is approximately 10% larger than in Au–Au collisions at $\sqrt{s_{\mathrm{NN}}} = 200\,\mathrm{GeV}$ ($\langle\beta\rangle = 0.59 \pm 0.05$) [31]. It has been demonstrated that the average radial flow velocity decreases as a function of the centrality, with larger radial flow in central collisions compared to peripheral ones [33]. This is because in peripheral collisions the overlap region of two nuclei is smaller than in central collisions. Consequently, the QGP expansion time is shorter in peripheral collisions compared to central collisions, reducing the time to build up radial flow.

2.2 Anisotropic flow

The asymmetry in the expansion of the QGP arises from the anisotropies present in the initial stage (Figure 1.5) of the heavy-ion collision, which are converted into the momentum anisotropies during the evolution of the QCD matter. The momentum anisotropy can be quantified using a Fourier expansion [34], with which the azimuthal differential particle yield is given as:

$$\frac{\mathrm{d}N}{\mathrm{d}\phi} \approx 1 + 2\sum_{n=1}^{\infty} v_n \cos(n(\phi - \Psi_{\mathrm{RP}})) \tag{2.2}$$

Here, ϕ represents the azimuthal angle of the detected particle in the laboratory frame and Ψ_{RP} is the angle of the reaction plane, defined by the impact parameter b and the beam axis, as shown in Figure 1.5. The coefficients, v_n, are called flow coefficients. The first three anisotropic flow coefficients are called directed flow v_1, elliptic flow v_2, and triangular flow v_3. They can be determined using the following formula:

$$\langle v_n \rangle = \langle\langle \cos(n(\phi - \Psi_{\mathrm{RP}}))\rangle\rangle \textbf{??} \tag{2.3}$$

The innermost angular bracket denotes the average over all particles within a single collision, while the outermost bracket corresponds to the average taken over events. In the ideal case of collisions of the same type of nuclei and continuous density distribution (as shown in the left panel of Figure 1.5), all odd-harmonics flow coefficients should vanish at pseudorapidity $\eta = 0$ due to the collision symmetry.

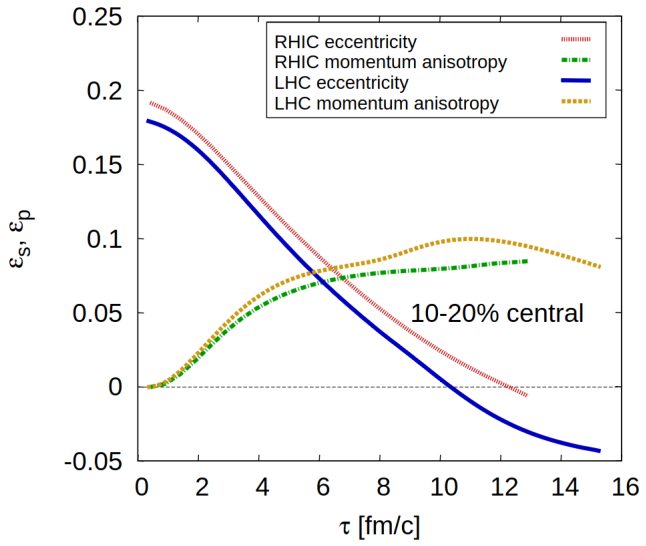

Figure 2.2: Time evolution of the eccentricity ($n = 2$) and momentum anisotropy in Au–Au collisions and Pb–Pb collisions at the LHC. Figure was taken from [35].

The time-evolution of the spatial anisotropies quantified by the ellipticity $\varepsilon_s = \frac{\langle y^2 - x^2\rangle}{\langle y^2 + x^2\rangle}$ and

the momentum anisotropies ($\varepsilon_p \approx v_2$) is illustrated in Figure 2.2 for collisions at different center-of-mass energies. At the beginning of the collision, the spatial anisotropies in the initial energy state are large, whereas no momentum anisotropies are present. During the evolution, the spatial anisotropies reduce with time. In contrast, the momentum anisotropies are building up due to interactions between the constituents of the QCD matter created in the overlap region. Most of the momentum anisotropies are built up in the first 5-6 fm/c after the heavy-ion collision. The hadronization of the medium ($\tau \approx 10$ fm/c) preserves these anisotropies and allows to measure it via the azimuthal asymmetry in the emission of the final-state hadrons.

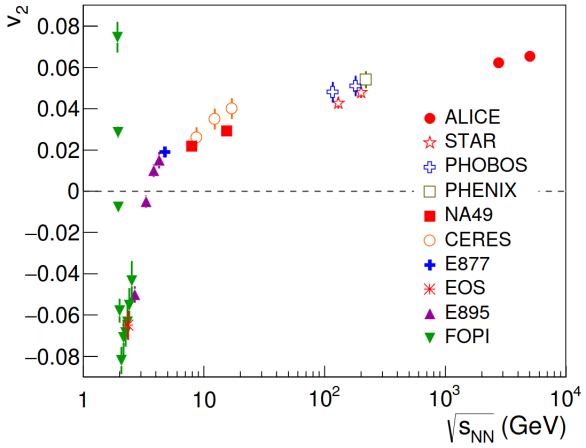

Figure 2.3: Energy dependence of the integrated elliptic flow. Figure is taken from [36].

The elliptic flow v_2 was measured by many heavy-ion experiments at different center-of-mass energies and shows a non-monotonic dependence as a function of the center-of-mass energy. This is connected to the changing role of the spectator nucleons at different energy scales. The evolution of v_2 with collision energy is shown in Figure 2.3. At very low center-of-mass energies, a positive v_2 is measured, indicating enhanced particle production aligned with the reaction plane (in-plane) compared to the perpendicular direction (out-of-plane). The positive v_2 in this region is associated with the dominance of the deflection of spectator matter, a phenomenon known as "bounce-off." At larger center-of-mass energies the sign of v_2 changes. In this region, the spectator nucleons still interact relatively long with the matter produced in the overlap region of the nuclei. This interaction between spectators and the overlap region affects the particle production in the in-plane direction and is interpreted as shadowing by the spectators. This phenomenon is known as "squeeze-out" and leads to a negative elliptic flow. At approximately $\sqrt{s_{\mathrm{NN}}} = 3$ GeV, v_2 changes sign for a second time. At this and higher energies up to a few TeV energies, the passing time of the spectators is small compared to the evolution of the matter created in the overlap region, consequently reducing their impact on the overlap region. The elliptic flow is mainly driven by the elliptic shape of the initial energy density created in the overlap region (Figure 1.5 [left panel]). The following discussion is focused on anisotropic flow in

relativistic heavy-ion collisions at the TeV energies.

2.3 Flow fluctuations

In reality, the distribution of matter inside the colliding nuclei is not uniform and this leads to event-by-event anisotropic flow fluctuations. This is closely linked to the initial state eccentricity fluctuations.

2.3.1 Eccentricity fluctuations

Similar to the anisotropic flow coefficients v_n, one can define corresponding parameters describing the shape of the initial energy density created in the overlap region of the heavy-ion collision. The shape of the transverse energy density, referred to as participant zone, is usually parametrized with the eccentricities [37] ε_n for the harmonic number n:

$$\varepsilon_n = -\frac{\int r^n e^{in\phi} \rho(r,\phi) r \mathrm{d}r \mathrm{d}\phi}{\int r^n \rho(r,\phi) r \mathrm{d}r \mathrm{d}\phi} = \varepsilon_{n,x} + i\varepsilon_{n,y} \tag{2.4}$$

Here, r and ϕ are the polar coordinates with respect to the center of gravity of the overlap region, $\rho(r,\phi)$ is the transverse energy density in the overlap region. The ε_n are connected with the reaction plane Ψ_{RP}, which is defined by the beam axis z and the impact parameter b. The eccentricity of the reaction plane $\varepsilon_{n,\mathrm{RP}}$ is defined as the eccentricity along the x-axis: $\varepsilon_{n,\mathrm{RP}} \equiv \varepsilon_{n,x}$.

In the absence of fluctuations the orientation of the initial energy density is defined by the reaction plane Ψ_{RP}. In the presence of initial state fluctuation, a set of participant symmetry planes Ψ_n describe the symmetry of the initial energy distribution, as shown in the right panel of Figure 1.5. The symmetry plane angles Ψ_n are defined as follows:

$$\Psi_n = \mathrm{atan2}(\varepsilon_{n,y}, \varepsilon_{n,x}) \tag{2.5}$$

In addition to Ψ_n there are symmetry planes Ψ_{SP} describing the distribution of the spectator nucleons. They are spanned by the deflection of the spectators and the beam direction.

Both the participant and spectator planes are affected by event-by-event fluctuations. Fluctuations of the spectator plane can arise due to the limited number of spectator nucleons measured in the experiment. Some of the spectator nucleons form fragments as illustrated in Figure 1.6. Due to limitations of the collider experiments, only unbound spectator nucleons are measured. Spectator plane fluctuations are closely tight to the fluctuation in the participant zone, since fluctuation of one leads to the fluctuation of another. Spectators interact with the matter in the participant region only at very early times. The spectator deflection is strongly correlated with the reaction plane, which enables the study of flow fluctuations relative to the geometrical orientation of the initial energy density.

Because the nuclei are composed of protons and neutrons, the eccentricities in each collision can take different values for the same impact parameter b.Different models exist to describe the eccentricity fluctuations.

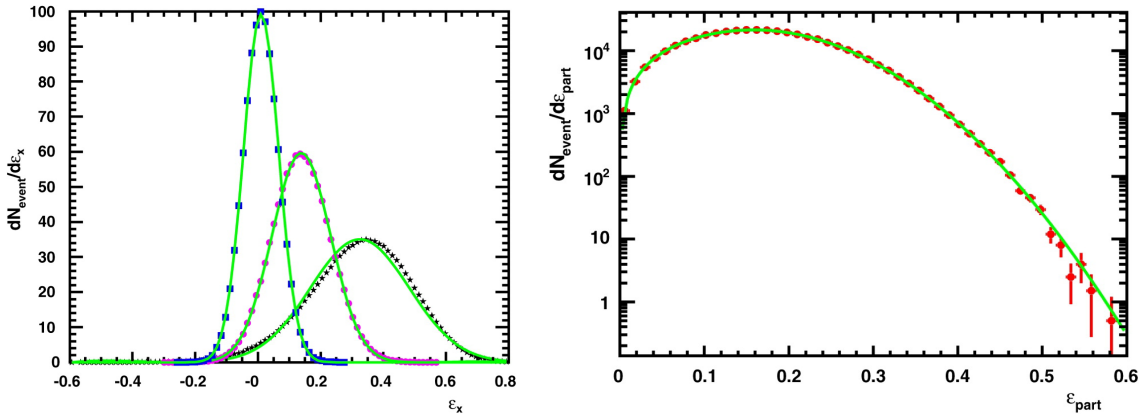

Figure 2.4: [Left panel] Distribution of ε_x together with Gaussian fits for (from left to right) for central, mid-central, and peripheral collisions. [Right] Distribution in $\varepsilon_{\text{part}}$ for mid-central collisions ($4 < \text{b} < 6$ fm) and fit with the Bessel-Gaussian function. Figure taken from [38].

One of the simplest approaches to model fluctuations is to assume Gaussian distributions of $\varepsilon_{n,x}$ and $\varepsilon_{n,y}$ with equal widths in x and y directions. This assumption works well for central and mid-central collisions but becomes less accurate for peripheral collisions. The distribution of $\varepsilon_{2,x}$ for different fixed impact parameters is shown in the left panel of Figure 2.4.

The shape of the Bessel-Gaussian distribution of the eccentricity of the participant zone, $\varepsilon_{\text{part}} = \sqrt{\varepsilon_{n,x}^2 + \varepsilon_{n,y}^2}$, is given by:

$$\frac{dn}{d\varepsilon_{\text{part}}} = \frac{\varepsilon_{\text{part}}}{\sigma_\varepsilon^2} I_0\left(\frac{\varepsilon_{\text{part}}\langle\varepsilon_{\text{RP}}\rangle}{\sigma_\varepsilon^2}\right) exp\left(-\frac{\varepsilon_{\text{part}}^2 + \langle\varepsilon_{\text{RP}}\rangle^2}{2\sigma_\varepsilon^2}\right) \tag{2.6}$$

where I_0 is the Bessel-function of the first kind, σ_ε the width of the eccentricity distribution in x and y-direction and $\langle\varepsilon_{\text{RP}}\rangle = \langle\varepsilon_{2,x}\rangle$ the reaction plane eccentricity averaged over many collisions. The distribution of $\varepsilon_{\text{part}}$ for a given impact parameter interval, together with the Bessel-Gaussian fit, is shown in the right panel of Figure 2.4.

The Bessel-Gaussian model [38] predicts a certain ordering of the cumulants of the underlying probability distribution of ε_n. Cumulants offer an alternative approach to moments for describing a given probability distribution. The first moment corresponds to the mean of the distribution, the second moment to the variance, and the third moment to the skewness of the distribution. In the realm of cumulants, the first and second-order cumulants align with their moment counterparts. However, cumulants become a linear combination of different moments from the third moment onward. The full set

of cumulants fully defines a probability distribution. Specifically, in the case of the eccentricity fluctuations under consideration here, knowing the full set of cumulants is crucial for fully characterizing the shape and form of these fluctuations. The second and fourth-order cumulants of the eccentricities $\varepsilon_n\{2\}$ and $\varepsilon_n\{4\}$ are defined as follows:

$$\varepsilon_n\{2\} = \sqrt{\langle \varepsilon_n^2 \rangle} \tag{2.7}$$

$$\varepsilon_n\{4\} = \sqrt[4]{2\langle \varepsilon_n^2 \rangle^2 - \langle \varepsilon_n^4 \rangle} \tag{2.8}$$

The interpretation of cumulants in the context of anisotropic flow will be thoroughly discussed in Section 3.1.1.

A specific hierarchy of the eccentricities extracted via the cumulant method is expected in the Bessel-Gaussian picture of fluctuations. The second order cumulant $\varepsilon_n\{2\}$ should be larger than the reaction plane eccentricity $\varepsilon_{\mathrm{RP}}$ and all higher-order cumulants $\varepsilon_n\{2m; m > 2\}$ should be identical to the average reaction plane eccentricity. The eccentricity fluctuations can also be investigated relative to the spectator nucleons. In the assumption that the spectator symmetry plane is a good proxy of the reaction plane, both eccentricities would be approximately equal ($\varepsilon_{SP} \approx \varepsilon_{RP}$). For the Bessel-Gaussian model, the following ordering is expected:

$$\varepsilon_n\{2\} > \varepsilon_n\{4\} = \varepsilon_n\{6\} = \varepsilon_n\{2m; m > 3\} = \varepsilon_{\mathrm{SP}} \approx \varepsilon_{\mathrm{RP}} \tag{2.9}$$

The Elliptic-Power model (EPM) [39] provides a more generalized description of the distribution of $\varepsilon_{n,x}$ and $\varepsilon_{n,y}$. This model overcomes the shortcomings of the Bessel-Gaussian model and provides a more accurate representation of eccentricity fluctuations, especially in peripheral collisions and smaller collision systems [39]. The EPM cumulants follow a distinct ordering compared to the reaction plane eccentricity:

$$\varepsilon_n\{2\} > \varepsilon_n\{4\} > \varepsilon_n\{6\} > \varepsilon_n\{2m; m > 3\} > \varepsilon_{\mathrm{SP}} \approx \varepsilon_{\mathrm{RP}} \tag{2.10}$$

In the EPM, the reaction plane eccentricity $\varepsilon_{\mathrm{RP}}$ is smallest of all eccentricities.

Applicability of these models can be tested in the experiment by measurements of anisotropic flow fluctuations as discussed in the next section.

2.3.2 Flow fluctuations relative to the participant plane

The eccentricity fluctuations described in the previous section results in fluctuations of the anisotropic flow coefficients. For the ideal fluid a linear scaling between eccentricities and flow coefficients is expected:

$$v_n \approx \kappa \varepsilon_n \tag{2.11}$$

where κ describes the hydrodynamic response of the medium.

This linear mapping between initial state fluctuations and anisotropic flow fluctuations allows directly to compare calculations from the models of eccentricity fluctuations (Bessel-Gaussian and EPM models) with the measured anisotropic flow coefficients.

In the presence of fluctuations Equation (2.2) need to be generalized to:

$$\frac{\mathrm{d}N}{\mathrm{d}\phi} \approx 1 + 2\sum_{i=1}^{\infty} v_n \cos(n(\phi - \Psi_m)) \tag{2.12}$$

where Ψ_m is given as defined in Equation (2.5) and the anisotropic flow given as:

$$v_n = \langle \cos(n(\phi - \Psi_m)) \rangle \tag{2.13}$$

Given Equation (2.11), the shape of eccentricity fluctuations can be studied by the measurement of anisotropic flow with respect to the produced particles in the participant zone. In the context of the Bessel-Gaussian and the Elliptic Power model, a similar hierarchy of the elliptic flow extracted via the cumulant method is expected [40] as for the eccentricities ε_2.
For the anisotropic flow, the second and fourth-order cumulants are defined as follows:

$$v_n\{2\} = \sqrt{\langle\langle \cos(n(\phi_1 - \phi_2)) \rangle\rangle} \tag{2.14}$$

$$v_n\{4\} = \sqrt[4]{2\langle\langle \cos(n(\phi_1 - \phi_2)) \rangle\rangle^2 - \langle\langle \cos(n(\phi_1 - \phi_2 + \phi_3 - \phi_4)) \rangle\rangle} \tag{2.15}$$

where ϕ_i stands for the azimuthal angle of particle i. A physical interpretation of the anisotropic flow with the cumulant method is given in Section 3.1.1.

In case of Bessel Gaussian fluctuations the following hierarchy of elliptic flow extracted via the cumulant method is expected [40]:

$$v_2\{2\} > v_2\{4\} = v_2\{6\} = v_2\{8\} = v_2\{\Psi_{\mathrm{RP}}\} \tag{2.16}$$

whereas within the EPM model:

$$v_2\{2\} > v_2\{4\} > v_2\{6\} > v_2\{8\} = v_2\{\Psi_{\mathrm{RP}}\} \tag{2.17}$$

Where $v_2\{m\}$ is the m-order cumulant and $v_2\{\Psi_{\mathrm{RP}}\}$ the elliptic flow with respect to the reaction plane, as defined in **??**. The inequality between higher-order anisotropic flow cumulants in the EPM model can be understood in the context of higher-order moments (e.g., skewness).

The anisotropic flow, measured as a function of centrality in Pb–Pb collisions at both $\sqrt{s_{\mathrm{NN}}} = 2.76\,\mathrm{TeV}$ TeV and $\sqrt{s_{\mathrm{NN}}} = 5.02\,\mathrm{TeV}$ in ALICE, is illustrated in Figure 2.5 for harmonic numbers n = 2 - 4. The elliptic flow v_2 is shown for different orders of cumulants. The elliptic flow is the largest and shows a clear centrality dependence. It first

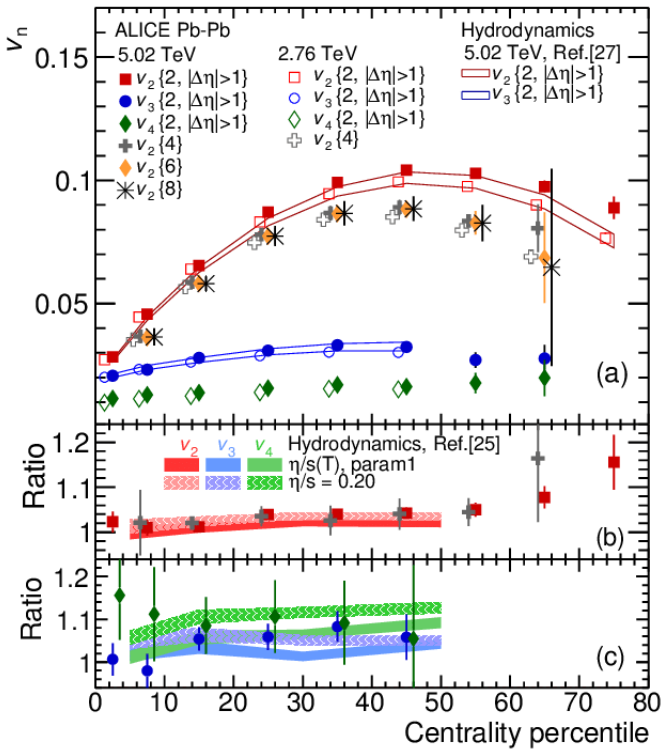

Figure 2.5: The p_{T}-integrated anisotropic flow coefficients v_n, n= 2-4, as a function of the collision centrality for Pb-Pb collisions at $\sqrt{s_{\mathrm{NN}}} = 2.76\,\mathrm{TeV}$ and $\sqrt{s_{\mathrm{NN}}} = 5.02\,\mathrm{TeV}$. The bottom two panels show the ratio of v_n between different energies, together with hydrodynamical model predictions. The figure is taken from [36].

increases with centrality, reaching a maximum, and then decreases again. The dominance of elliptic flow v_2 can be attributed to the elliptic shape of the initial energy density, as shown in the left panel of Figure 1.5. The centrality dependence can also be explained by referring to Figure 1.5. In central collisions with small impact parameters (b), the overlap region is nearly isotropic and exhibits only small elliptic modulation. An increase in the impact parameter (corresponding to higher centrality) results in a more elliptical shape for the overlap region of the two nuclei, leading to a higher elliptic flow in the final state. The v_2 reduction towards peripheral events is linked to the smaller overlap region between the two nuclei and the smaller particle produced in such events. This consequently increases the relative contribution from flow fluctuations, which reduces the elliptic flow v_2.

The emergence of triangular flow v_3 reflects triangular modulation ε_3 in the initial energy density, which has a weak centraltiy dependence.
Figure 2.6 illustrates the measurements by ALICE and ATLAS of the elliptic flow with the cumulant method up to the eighth order as a function of centrality in Pb–Pb collisions at $\sqrt{s_{\mathrm{NN}}} = 2.76\,\mathrm{TeV}$. A fine splitting is observed between the different flow coefficients

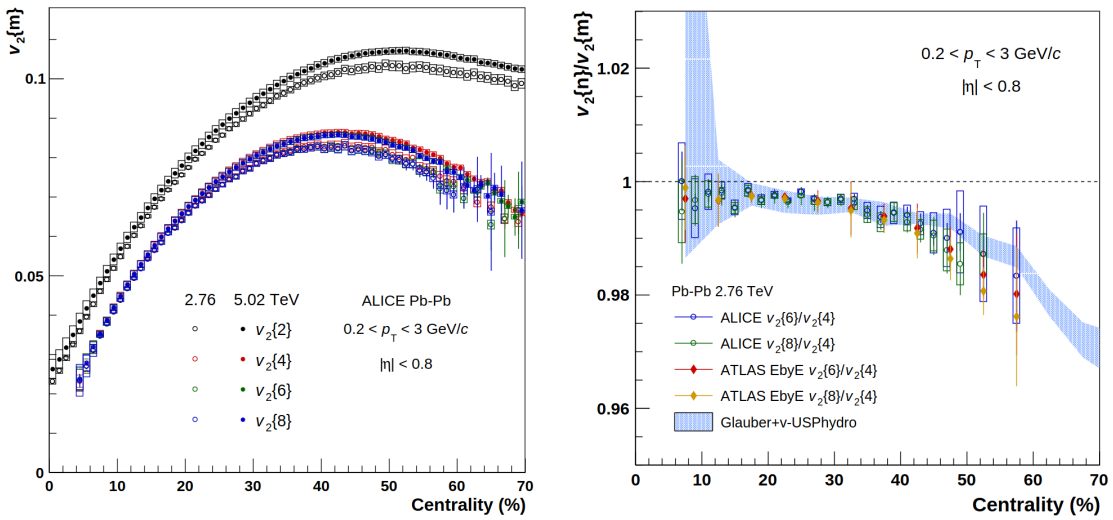

Figure 2.6: [Left panel] Elliptic flow v_2 of unidentified charged hadrons as a function of centrality, measured using the two-and multi-particle cumulant methods. Measurements for Pb–Pb collisions at $\sqrt{s_{\mathrm{NN}}} = 2.76\,\mathrm{TeV}$ ($\sqrt{s_{\mathrm{NN}}} = 5.02\,\mathrm{TeV}$) are shown by open (solid) markers. [Right panel] Ratios of elliptic flow of unidentified charged hadrons between measurements with different multiparticle cumulant methods, as a function of centrality, at $\sqrt{s_{\mathrm{NN}}} = 2.76\,\mathrm{TeV}$ measured by ALICE and ATLAS. The measured data is compared to hydrodynamic model calculation. Figure is taken from [40]

calculated from various cumulants, and this splitting increases with centrality. In central collisions, the fine splitting is approximately 0.2%, while for centralities above 50%, it can be as high as 2%. This observation of fine splitting shows deviation from Bessel Gaussian fluctuations and can be attributed to the skewness in the underlying flow probability distribution [41].

Comparisons of model calculations incorporating MC Glauber initial conditions and viscous hydrodynamics (v-USPhydro) are found to agree with the measurements of $v_2\{6\}/v_2\{4\}$ and $v_2\{8\}/v_2\{4\}$, which themselves are compatible the Elliptic-Power model.

2.4 Anisotropic flow with respect to the spectator plane

The spectators allow for the extraction of additional symmetry planes and complements anisotropic flow and flow fluctuations measurements relative to the participant plane. The anisotropic flow coefficient relative to the spectator plane can be defined as:

$$v_n = \langle \cos(n(\phi - \Psi_{\mathrm{SP}})) \rangle \tag{2.18}$$

Before discussing the elliptic flow relative to the spectator plane $v_2\{\Psi_{\mathrm{SP}}\}$ it is worth summarizing observations of the direct flow relative to the spectator plane.

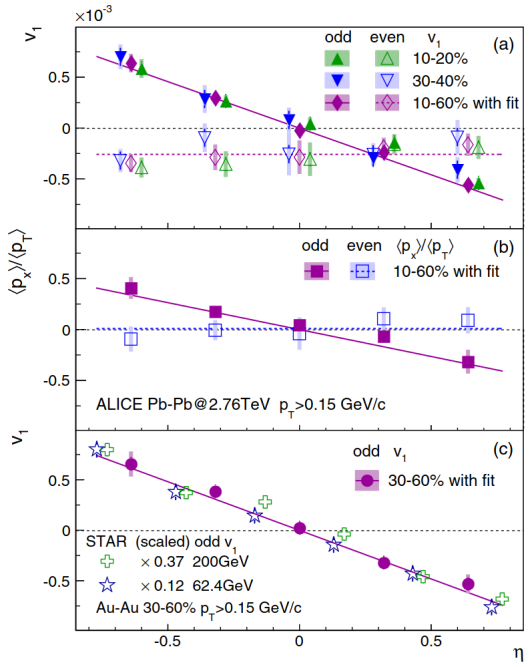

Figure 2.7: Directed flow and relative momentum shift as a function of pseudorapidity for 3 different centrality intervals measured in Pb-Pb collisions at $\sqrt{s_{\mathrm{NN}}} = 2.76\,\mathrm{TeV}$. Results are compared to measurements at lower center-of-mass energies. The data labelled even and odd correspond to the symmetric and anti-symmetric components of the directed flow. Figure is taken from [42].

The directed flow relative to the spectator plane is sensitive to the early times of the collision and the three-dimensional orientation of the initial state. As illustrated in Figure 1.6, the deflection of the spectators is positive towards positive pseudorapidity and negative towards negative pseudorapidity. The magnitude of this deflection depends on the QCD matter properties in the overlap region, its tilt along the beam axis, and the momentum transfers between the participant zone and the spectators. Consequently, measuring directed flow relative to the spectator plane probe for understanding the three-dimentional orientation of the participant region with respect to the spectator plane [42].

The measurement of directed flow relative to the spectator plane and the relative momentum shift as a function of pseudorapidity is shown in Figure 2.7. Two components are observed for directed flow: an asymmetric and a symmetric one. The asymmetric component arises from the deflection of spectators by the dense nuclear matter formed in the overlap region.

The symmetric component emerges due to initial state fluctuations. These fluctuations introduce differences between the reaction plane Ψ_{RP} and the spectator Ψ_{SP} planes. This is important for elliptic flow measurements relative to the spectator plane, which will be discussed later in this section.

comparisons of the symmetric directed flow component relative to the spectator plane with that extracted relative to the participant plane revealed 40 times smaller magnitude [42, 43]. This implies a weak correlation between the orientation and fluctuations of the participant and spectator symmetry planes. This means that the impact of the fluctuations in the participant zone on the spectators is small. In return, this makes the spectator symmetry plane an excellent proxy for the reaction plane.

The test of the hierarchy of anisotropic flow measurements with the cumulant method, as shown in Equation 2.17, can be complemented by measuring anisotropic flow with respect to the spectator plane. In the assumption that the spectator plane approximately corresponds to the reaction plane ($\Psi_{\mathrm{SP}} \approx \Psi_{\mathrm{RP}}$), the hierarchy in Equation 2.17 is modified as follows:

$$v_2\{2\} > v_2\{4\} > v_2\{6\} > v_2\{\Psi_{\mathrm{SP}}\} \approx v_2\{\Psi_{\mathrm{RP}}\} \tag{2.19}$$

Measurements of elliptic flow with respect to the neutron spectator plane ($v_2\{\Psi_{\mathrm{SP}}\}$) were performed by ALICE as a function of centrality for unidentfied hadrons in Pb–Pb and Xe–Xe collisions. The data compared with flow measurements relative to the participant plane estimated by the two- and four-particle cumulant ($v_2\{2, |\Delta\eta| > 1\}$ and $v_2\{4\}$). These measurments together with the corresponding eccentricity ratios from initial state models such as T$_{\mathrm{R}}$ENTo (shaded bands) and EPM (solid + dashed lines), are shown in Figure 2.8. Across all centrality classes $v_2\{2, |\Delta\eta| > 1\} > v_2\{4\} \approx v_2\{\Psi_{\mathrm{SP}}\}$, as predicted from the models, while differences between $v_2\{4\}$ and $v_2\{\Psi_{\mathrm{SP}}\}$ are observed. This is illustrated by the ratio $v_2\{\Psi_{\mathrm{SP}}\}/v_2\{4\}$, which is expected to be unity without or for Bessel-Gaussian shape fluctuations. $v_2\{\Psi_{\mathrm{SP}}\}/v_2\{4\}$ is found to be larger than unity for centralities smaller than 50%, with a maximum in most central collisions. In peripheral collisions a decrease of the ratio to values below unity are observed. The maximum in most central collisions is associated with large fluctuations of a small number of neutron spectators used to estimate the neutron spectator symmetry plane, which increases $v_2\{\Psi_{\mathrm{SP}}\}$. The decrease in peripheral collisions is due to the small numbers produced in the participant zone and a decrease in the number of unbound neutron spectators due to fragmentation processes. These effects induce correlations between the participants and spectators.

The ratio $v_2\{\Psi_{\mathrm{SP}}\}/v_2\{4\}$ was compared with the corresponding eccentricities from different initial state models as shown in fig. 2.8. Such comparisons are sensitive to deviations from a linear scaling between anisotropic flow and eccentricities. $v_2\{\Psi_{\mathrm{SP}}\}/v_2\{4\}$ below centralities of 50%, was significantly larger than the expectations from the Bessel-Gaussian model or $\varepsilon_2\{\Psi_{\mathrm{RP}}\}/\varepsilon_2\{4\}$ from T$_{\mathrm{R}}$ENTo and EPM. This observed difference can be due to a decorrelation between the spectator Ψ_{SP} and reaction plane Ψ_{RP}. This was already

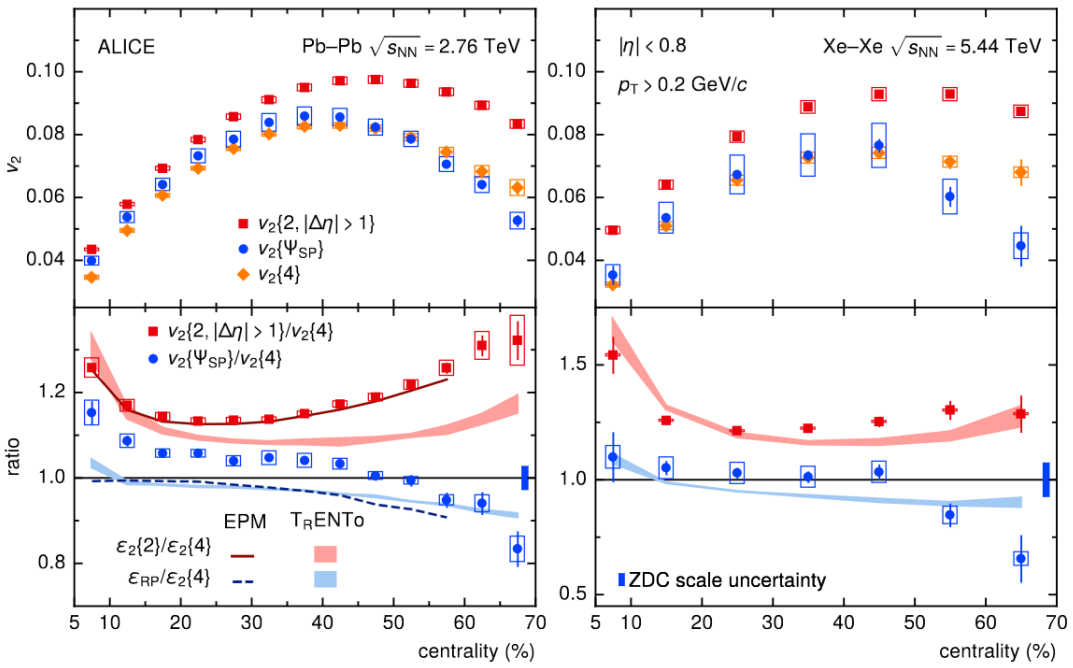

Figure 2.8: [Upper panels] Elliptic flow relative to the spectator plane, $v_2\{\Psi_{SP}\}$, and to the participant plane, $v_2\{2, |\eta| > 1\}$ and $v_2\{4\}$ as a function of centrality in Pb-Pb (left) and Xe-Xe (right) collisions. [Bottom panel] Ratios of $v_2\{\Psi_{SP}\}$ and $v_2\{2, |\eta| > 1\}$ to $v_2\{4\}$. The dashed (solid) lines show the eccentricty ratios of ε_{RP} ($\varepsilon_2\{2\}$) to $\varepsilon_2\{4\}$ from the elliptic power model. The corresponding eccentricty ratios for Trento are shown as solid bands. The error bars (open boxes) indicate statistical (systematic) uncertainties. The bin-to-bin uncorrelated uncertainties and the correlated ones are combined for $v_2\{\Psi_{SP}\}$ results. For the ratio $v_2\{\Psi_{SP}\}/v_2\{4\}$, the ZDC scale uncertainties are shown separately as solid boxes centered at unity on the right side of the lower panels. Figure is taken from [44].

suggested by the findings of a symmetric component of the directed flow (Figure 2.7). Clarifying this requires to incoprate the dynamics between spectators and participants in initial state models.

Another reason for the observed deviations could be due to viscous effects from the ydrodynamic evolution of the quark-gluon plasma and its hadronization. The importance of these effects is also suggested by the observed scaling violation between Pb–Pb and Xe–Xe collisions.

In the case of ideal hydrodynamics, the scaling between the elliptic flow and the eccentricity ε_2 is expected to be proportional to the final-state multiplicity dN_{ch}/dy per unit overlap area S, where the former is extracted from experimental measurements and the latter from initial state models such as MC Glauber and T$_R$ENTo. This means that for an ideal

fluid, different configurations of heavy-ion collisions, e.g., different impact parameters, center-of-mass energy, and size of the system, can be described by a change of the final hadron multiplicity and making the hydrodynamic evolution in different systems universal. Due to non-zero shear viscosity this scaling is violated, the scaling can also be violated due to freeze-out of the dense matter and its hadronization, which does not depend on the size of the system.

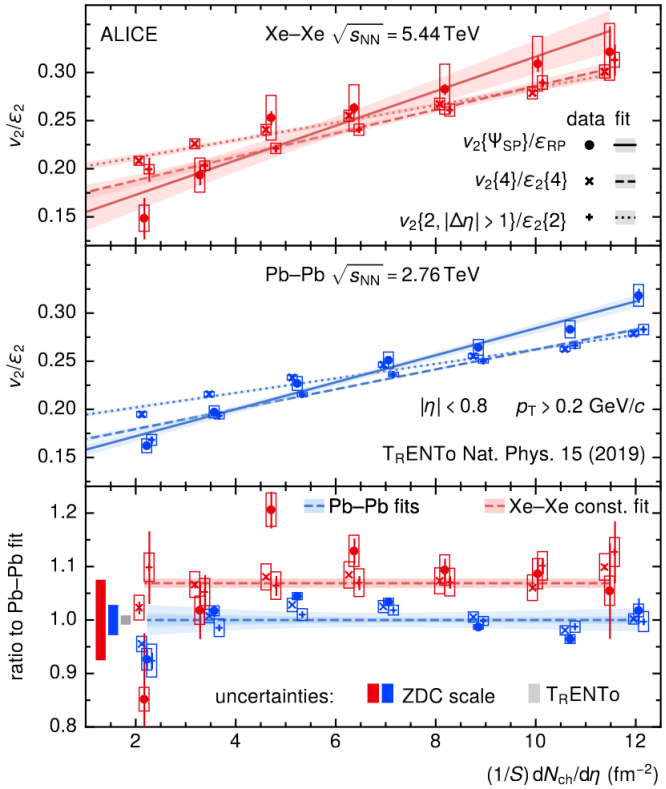

Figure 2.9: Ratios of v_2/ε_2 as a function of $(1/S)\mathrm{d}N_{ch}/\mathrm{d}\eta$ in Xe–Xe (top panel) and Pb–Pb (middle panel) collisions. The bottom panel shows the ratio of the v_2/ε_2 to the linear fit of these ratios to the Pb–Pb data [44].

The multiplicity scaling of the elliptic flow for Pb–Pb and Xe–Xe is shown in Figure 2.9 for different flow observable and their corresponding eccentricities. The bottom panel of Figure 2.9 shows the difference of this scaling between Pb–Pb and Xe–Xe collisions. A scaling violation (7±0.9%) is observed, hinting at the contribution of the hydrodynamic stage and the hadronization to the $v_2\{\Psi_{SP}\}/v_2\{4\}$ results obtained for unidentified charged hadrons.

2.5 Particle-type and p_{T}-dependence of flow and flow fluctuations

The later stages of the heavy-ion evolution, e.g., hydrodynamic expansion and hadronization, can modulate the observed anisotropic flow. One way to investigate these later stages is by measuring the p_{T} and particle-type dependence of the anisotropic flow. This was already discussed in the context of radial flow (Figure 2.1), where the expansion of the QGP medium leads to a flattening of the p_{T} spectra of particles, which depends on the mass of the particle species.

2.5.1 p_{T} and particle-type dependence of anisotropic flow

Effects of the hydrodynamic expansion and hadronization can be probed by the particle-type dependence of elliptic flow v_2, as it only originates during these stages of the collision. The elliptic flow v_2 as a function of transverse momentum is sensitive to different particle production mechanism, which relative importance depends on the particles momentum. Studying the particle-type dependence of anisotropic flow is sensitive to the properties of this relativistic fluid, such as its shear and bulk viscosity [45].

Figure 2.10, shows the p_{T}-differential elliptic flow for various particle species in Pb–Pb collisions at $\sqrt{s_{\mathrm{NN}}} = 5.02\,\mathrm{TeV}$ in various centrality classes, together with hydrodynamic model predictions. In the low-p_{T} regime ($<$3 GeV/c), a characteristic mass ordering of elliptic flow is present, which arises from the interplay between the radial and anisotropic flow. As discussed in Section 2.1, radial flow depletes the yield of particles at low p_{T} and shifts them toward higher p_{T}, with the effect becoming more pronounced for heavier particles. Due to the initial azimuthal anisotropy in the energy distribution, the radial fluid velocity has larger values in-plane (parallel to Ψ_{RP}) compared to out-of-plane (perpendicular to Ψ_{RP}). This results in a stronger in-plane push of particles counteracting the initial energy anisotropy and reducing v_2 at low p_{T} [46]. This effect is more prominent for heavier particles, meaning that, for a given p_{T}, the elliptic flow v_2 is larger for particles with smaller mass, as illustrated in Figure 2.10. The low-p_{T} region is primarily governed by the hydrodynamic evolution of the QGP, which is well described by many hydrodynamic model predictions, as illustrated in Figure 2.10.

At intermediate momenta ($3 < p_{\mathrm{T}} < 10\,\mathrm{GeV}/c$), a distinct grouping of baryons and mesons becomes visible, as shown in the left panel of Figure 2.10. This can be interpreted as a consequence of quark coalescence. Quarks coalesce when they are closely positioned in phase-space and combine into mesons and baryons [51, 52]. These physical mechanisms is particularly evident in the behavior of the ϕ-meson, which shares a mass similar to that of the proton. At low p_{T}, the proton and ϕ-meson exhibit similar elliptic flow v_2. However, at intermediate p_{T}, the ϕ-meson's elliptic flow aligns more closely with that of mesons. This suggests that in this momentum range, the elliptic flow is primarily influenced by the quark content rather than the particle's mass [47].

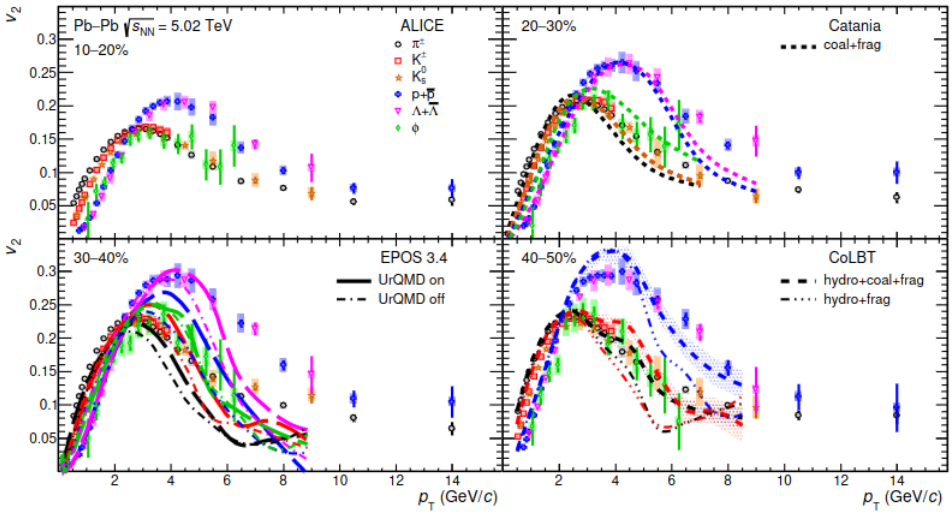

Figure 2.10: p_{T}-differential v_2 for several particle species in Pb–Pb collisions at $\sqrt{s_{\mathrm{NN}}} = 5.02\,\mathrm{TeV}$ for different centrality classes [47] compared to the Catania [48], EPOS 3.4 [49] and CoLBT [50] models. Figure is taken from [15].

For momenta exceeding 10 GeV/c, hadron production is primarily driven by parton fragmentation and is influenced by the elliptic flow of these fragmenting partons. In this scenario, the elliptic flow results from the path-length dependence of the in-medium energy loss experienced by the partons generated in hard-scattering processes and fragmentation. Consequently, the elliptic flow of mesons and baryons should exhibit no significant differences as supported by the most recent measurements of particle-type-dependent elliptic flow in ALICE [15].

2.5.2 p_{T} and partilce-type dependence of anisotropic flow flucutations

The elliptic flow in various p_{T} regions is influenced by different physical mechanisms associated with different stages of a heavy-ion collision. Examining flow fluctuations as a function of p_{T} can help to understand their origin and determine whether they share a common source.

The ratio $v_2\{\Psi_{\mathrm{SP}}\}/v_2\{4\}$ as a function of transverse momentum p_{T} in different centrality classes is supposed to be unity in the assumption of no or Bessel-Gaussian fluctuations. As can be seen from Figure 2.11, a deviation from unity is observed. This is suggesting a common origin of flow fluctuations, typically associated with eccentricity fluctuations during the initial stage of the collision. The slope as a fucntion of p_{T} can be associated with effects from the QGP evolution and the hadronization. These findings also align with previous observation of a small p_{T} dependence of the elliptic flow relative to the participant plane [53].

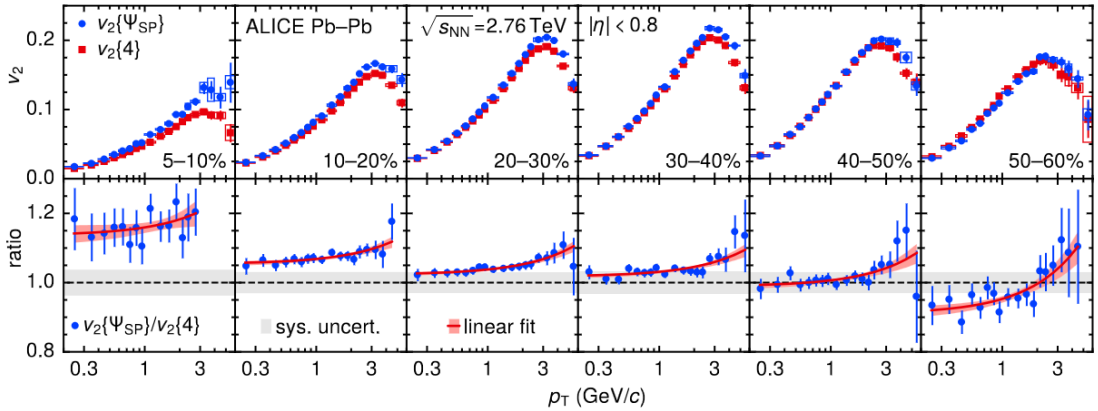

Figure 2.11: (upper panels) Elliptic flow relative to the spectator plane, $v_2\{\Psi_{SP}\}$, and to the participant plane, $v_2\{4\}$, as a function of transverse momentum in different centrality classes for Pb–Pb collisions. The linear fits to the ratio $v_2\{\Psi_{SP}\}/\ v_2\{4\}$ are shown as red lines for the individual centrality classes. The error bars (open boxes) indicate statistical (systematic) uncertainties. The correlated uncertainties, related to the ZDC, and bin-to-bin uncorrelated ones are combined for $v_2\{\Psi_{SP}\}$ (upper panels). For the ratio $v_2\{\Psi_{SP}\}/v_2\{4\}$ (lower panels), the correlated uncertainty is shown by the grey band at unity. Figure is taken from [44].

The impact of the hydrodynamic evolution and the hadronization phase on the shape of flow fluctuations can be investigated through the particle-type dependent measurement of the two- and four-particle cumulants, $v_2\{2\}$ and $v_2\{4\}$. As mentioned in Section 2.3, the difference between these two observable is sensitive to fluctuations within the picture of initial state fluctuations [54].

Figure 2.12 displays the ratio $v_2\{2\}/v_2\{4\}$ as a function of p_T for different centrality bins and particle types in Pb–Pb collisions at $\sqrt{s_{NN}} = 5.02\,\text{TeV}$. No significant p_T or particle-type dependence is observed in central collisions, but this changes for more peripheral collisions. For collisions in the 20-30% centrality range, a monotonic decrease of the ratio is observed in the p_T region between 1-5 GeV/c, and this trend becomes more pronounced in more peripheral events. For more peripheral events, a particle-type grouping emerges, with baryons exhibiting a larger value of the ratio than mesons.

The importance of final-state effects can be understood by comparing the data with hydrodynamic model predictions that incorporate these effects. One such model is the CoLBT hydrodynamical model [50], which allows for a simultaneous description of the evolution of parton showers and the bulk medium. The bulk medium is characterized by a (3+1)-D viscous hydrodynamic model initiated at 0.6 fm/c, with a specific shear viscosity η/s

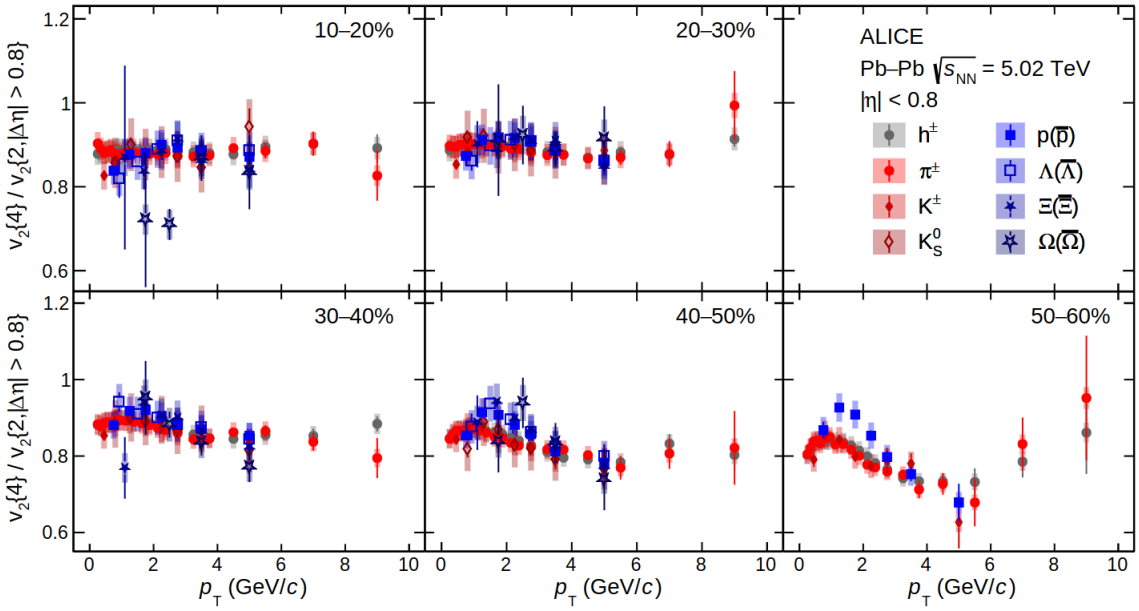

Figure 2.12: Ratio $v_2\{4\}/v_2\{2,|\eta| > 0.8\}$ as a function of the transverse momentum p_{T} for several particle species and centrality classes in Pb-Pb collisions at $\sqrt{s_{\mathrm{NN}}} = 5.02\,\mathrm{TeV}$. Figure taken from [54].

of 0.1. The freeze-out temperature is set to 150 MeV. Other parameters of the model were adjusted to reproduce measured yields, p_{T}-spectra, and integrated v_n of unidentified charged hadrons in Pb-Pb collisions. The model includes particle formation from the hydrodynamic fields at the freeze-out surface at low p_{T}, complemented by a quark coalescence prescription at intermediate p_{T}, and fragmentation at high p_{T}.

Figure 2.13 illustrates the ratio $v_2\{2\}/v_2\{4\}$ and the relative flow fluctuations $F(v_n) = \sigma_{v_n}/\langle v_n \rangle$ as a function of p_{T} for pions, kaons, and protons in the 40-50% centrality class, along with the CoLBT hydrodynamical model with quark coalescence in the (left panel) and without (right panel).

Despite the sizable uncertainties in the hydrodynamic model predictions, the calculations show that the contribution from quark coalescence is crucial for the description of the data. This highlights the importance of understanding the interplay between final-state effects, hadronization mechanisms, and the underlying hydrodynamic evolution in heavy-ion collisions.

2.6 Particle-type dependence of $v_2\{\Psi_{\mathrm{SP}}\}$

This chapter provided an overview of anisotropic flow, which develops due to the initial spatial anisotropies in the colliding nuclei's overlap region and is sensitive to the initial energy density state. Furthermore, it was discussed how the measurement of anisotropic

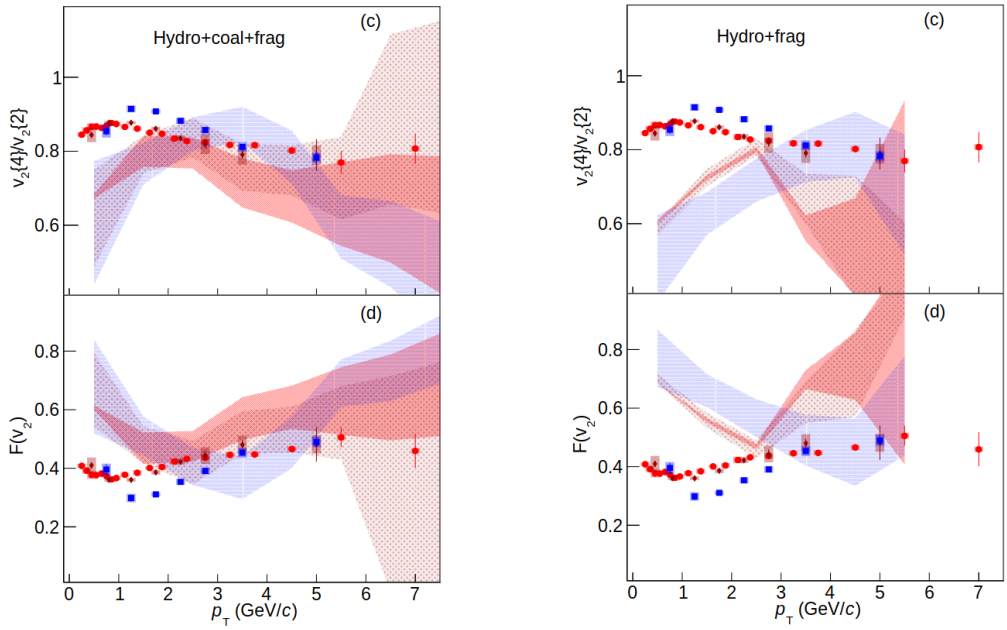

Figure 2.13: The ratio $v_2\{4\}/v_2\{2,|\eta| > 0.8\}$ and $F(v_2)$ as function of p_{T} for pions, kaons and protons in the centrality interval 40-50% in Pb-Pb collisions at $\sqrt{s_{\mathrm{NN}}} = 5.02\,\mathrm{TeV}$ compared with the CoLBT hydrodynamic model including quark coalescence [left panel] and excluding quark coalescence [right panel]. Vertical bars and shaded boxes on the data points correspond to statistical and systematic uncertainties, whereas the shaded areas correspond to the uncertainties of the hydrodynamical model. Figures are taken from [54].

flow relative to the participant and spectator plane could help to improve our understanding of the underlying event-by-event fluctuations of the initial state, suggesting non-Gaussian probability distributions with a small skewness. It was discussed how the p_{T}-dependence and particle-type dependence of anisotropic flow can help to study the later stages of the heavy-ion collision, such as the hydrodynamic expansion and the hadronization phase. Comparison with hydrodynamic models incorporating different hadronization mechanisms suggests an important role of these final state effects in observing anisotropic flow and flow fluctuations. This makes it possible to extract transport coefficients of the QGP. This section concludes this chapter, with the discussion how the measurement of the particle-type dependence of the anisotropic flow relative to the spectator plane can help to improve the understanding of the initial state fluctuations and improve the precision of the QGP properties determination.

One open question is the origin of the discrepancy between the ratios of elliptic flow relative to the spectator and participant planes ($v_2\{\Psi_{\mathrm{SP}}\}/v_2\{4\}$) and the corresponding eccentricity ratios $\varepsilon_2\{\Psi_{\mathrm{RP}}\}/\varepsilon_2\{4\}$ (Figure 2.8). The spectator and reaction planes are decorrelated, which is linked to the fluctuation of the deflection of the spectator nucleons due to the

fluctuation in the participant plane. Mesasuring only neutron spectators adds additional fluctuations. This can be investigated by comparing the measurements of $v_2\{\Psi_{\mathrm{SP}}\}/v_2\{4\}$ with the appropriate eccentricity ratios $\varepsilon_2\{\Psi_{\mathrm{SP}}\}/\varepsilon_2\{4\}$. The hydrodynamic expansion of the QGP and the hadronization results in a breaking of the linear relation between eccentricities and anisotropic flow (Equation (2.11)). The importance of these effects is suggested the observed violation of multiplicity scaling for Pb–Pb and Xe–Xe collision and the particle-type dependence of flow fluctuations relative to the participant plane (Figure 2.13). Comparisons with hydrodynamic model predictions incorporating quark coalesence and fragmentation (CoLBT model), substantiated the importance of the later stages of the heavy-ion collision.

The model calculations currently suffer from large uncertainties, which could be reduced by the measurements of the particle-type dependence of anisotropic flow relative to the spectator plane. These measurements could challenge current state-of-the-art hydrodynamic models and help to improve our understanding of the relative contributions from the initial state, hydrodynamic evolution, and the QGP hadronization.

3 Anisotropic flow measurment techniques

As outlined in Chapter 2 to measure the anisotropic flow coefficients v_n the orientation of the collision symmetry plane needs to be determined. In the absence of initial state fluctuations, the symmetry of the nuclei overlap region is given by the reaction plane Ψ_{RP}. In the presence of fluctuations, it is given by a set of symmetry planes Ψ_m. In the experiment, these symmetry planes Ψ_m and the reaction plane Ψ_{RP} are not directly accessible and need to be estimated from the measured final-state particles. This is possible since the momentum anisotropies of final-state particles are inherited from the geometrical form and orientation of the initial energy density. Using produced particles to estimate the collision symmetry planes implies that flow observables defined in Chapter 2 become two- or multi-particle correlation functions. This introduces a bias in flow measurements because not only correlations originating from the initial geometry of the collision are contributing, but also correlations from other sources (non-flow correlations), such as momentum conservation or resonance particle decays, may affect the result.

Results obtained in this thesis are produced using estimates for anisotropic flow, each influenced differently by non-flow correlations. The first set of estimates are azimuthal multi-particle correlations (cumulants). The second set is derived from the scalar product method, in which produced particles at mid-rapidity are correlated with the spectator neutrons measured in the forward direction. This method allows the extraction of anisotropic flow coefficients relative to the spectator symmetry plane Ψ_{SP}.

The fundamental element of anisotropic flow observables is the flow or Q-vector. The flow vector is evaluated separately for each harmonic n and is defined event-by-event as follows:

$$Q_{n,p} = e^{in\Psi_n} = X_{n,p} + iY_{n,p} = \sum_{j=0}^{M} w_j^p e^{in\phi_j} \tag{3.1}$$

Here, M is the multiplicity of particles in the event, ϕ and w represent the azimuthal angle and the weight assigned to each particle. The weight w is used to correct for inefficiencies in the detector. The power p associated with the weight is used in the multi-particle cumulant calculations to properly treat autocorrelations.

3.1 Multi-particle correlations and cumulant expansion

The concept of azimuthal multi-particle correlations serves as the building block for the cumulant expansion. These correlations can be used to estimate the anisotropic flow coefficients by exploiting the observation that a common symmetry plane Ψ_m give rise to correlations among all particles created in the collision. The flow harmonics v_n are investigated using the two- and four-particle correlations. The corresponding analysis is presented in Chapter 6 of this thesis. A generalization to larger number of particles is straightforward, and the interested reader is referred to the following paper for more information [55].

The single-event average two- and four-particle azimuthal correlations for the harmonic n, event multiplicity M, and weights w assigned to each particle are defined as following:

$$\begin{aligned}\langle 2\rangle &= \langle e^{in(\phi_1-\phi_2)}\rangle \\ &= \sum_{\substack{j,k=1\\ j\neq k}}^{M} w_j w_k e^{in(\phi_j-\phi_k)} \Big/ \sum_{\substack{j,k=1\\ j\neq k}}^{M} w_j w_k\end{aligned} \tag{3.2}$$

$$\begin{aligned}\langle 4\rangle &= \langle e^{in(\phi_1+\phi_2-\phi_3-\phi_4)}\rangle \\ &= \sum_{\substack{j,k,l,m=1\\ j\neq k\neq l\neq m}}^{M} w_j w_k w_l w_m e^{in(\phi_j+\phi_k-\phi_l-\phi_m)} \Big/ \sum_{\substack{j,k,l,m=1\\ j\neq k\neq l\neq m}}^{M} w_j w_k w_l w_m\end{aligned} \tag{3.3}$$

The exclusion $j \neq k$ in Equation (3.2) and $j \neq k \neq l \neq m$ in Equation (3.3) remove contributions from autocorrelations.

An average of the two- and four-particle correlations over a given number of collisions N is defined as following:

$$\langle\langle 2\rangle\rangle = \sum_{i=1}^{N} (W_{\langle 2\rangle})_i \langle 2\rangle_i \Big/ \sum_{i=1}^{N} (W_{\langle 2\rangle})_i \tag{3.4}$$

$$\langle\langle 4\rangle\rangle = \sum_{i=1}^{N} (W_{\langle 4\rangle})_i \langle 4\rangle_i \Big/ \sum_{i=1}^{N} (W_{\langle 4\rangle})_i \tag{3.5}$$

where $W_{\langle 2\rangle}$ and $W_{\langle 4\rangle}$ are weights assigned to a given event. The event weights are defined as sums over all possible products of weights w assigned to individual particles:

$$W_{\langle 2 \rangle} = \sum_{\substack{i,j=1 \\ i \neq j}}^{M} w_i w_j \tag{3.6}$$

$$W_{\langle 4 \rangle} = \sum_{\substack{i,j,k,l=1 \\ i \neq j \neq k \neq l}}^{M} w_i w_j w_k w_l \tag{3.7}$$

The meaning of the event weights can be understood by considering a detector with uniform azimuthal acceptance (w = 1 for all particles). In such a scenario the event averages in Equation (3.6) and Equation (3.7) simplify to:

$$W_{\langle 2 \rangle} = M \cdot (M-1) \tag{3.8}$$

$$W_{\langle 4 \rangle} = M \cdot (M-1) \cdot (M-2) \cdot (M-3) \tag{3.9}$$

They represent the number of possible two or four particle combinations that can be constructed for an event with multiplicity M. Events with higher particle multiplicity get a larger weight, to emphasize their statistical contribution in the calculation of the two- and four-particle correlations defined in Equation (3.2) and Equation (3.3) [56].

The two- and four-particle azimuthal correlations allow to estimate the anisotropic flow v_n without the knowledge of the symmetry plane Ψ_m, in contrast to the definition given in Equation (2.13). This can be illustrated for the two-particle correlations defined in Equation (3.2):

$$\begin{aligned}
\langle\langle 2 \rangle\rangle &= \langle\langle e^{in(\phi_1 - \phi_2)} \rangle + \delta_{2,n} \rangle \\
&= \langle\langle e^{in(\phi_1 - \Psi_m - (\phi_2 - \Psi_m))} + \delta_{2,n} \rangle\rangle \\
&= \langle\langle e^{in(\phi_1 - \Psi_m)} \rangle \langle e^{-in(\phi_2 - \Psi_m)} \rangle + \delta_{2,n} \rangle \\
&= \langle\langle v_n \rangle \langle v_n \rangle + \delta_{2,n} \rangle \\
&= \langle \langle v_n \rangle^2 + \delta_{2,n} \rangle \\
&\approx \langle v_n^2 + \delta_{2,n} \rangle \\
&\approx \langle v_n^2 \rangle
\end{aligned} \tag{3.10}$$

The term $\delta_{2,n}$ introduced in Equation (3.10) include all contributions from non-flow two-particle correlations that do not originate from the underlying initial geometry in the overlap region of the heavy-ion collision. This allows the interpretation of $\langle e^{in(\phi_1 - \phi_2)} \rangle$ as a correlation solely arising from flow anisoropies. The symmetry plane Ψ_m was introduced at the second and third lines of Equation (3.10) to reflect the flow observable of $v_n = \cos(n(\phi - \Psi_m))$. Note that in the forth line of Equation (3.10) $e^{in(\phi_1 - \Psi_m)}$ is replaced

with the v_n, which is the exponential form of the Fourier decomposition, as used in Equation (2.2).

In the last two lines of Equation (3.10) certain assumptions where made, which introduce biases into the measurements of the anisotropic flow extracted from multi-particle correlations. Firstly, it was assumed that $\langle v_n^k \rangle = \langle v_n \rangle^k$, a condition satisfied only when flow fluctuations between different events are small. Secondly the non-flow correlations $\delta_{2,n}$ are assumed to be negligible compared to the absolute magnitude of the anisotropic flow $\delta_{2,n}$, which could be not the case as demonstrated by measurements [54].

3.1.1 Cumulants method

The non-flow correlations mentioned earlier differ from the correlations arising from the collective behavior in a heavy-ion collision. These non-flow correlations are only between a small subset of all particles created in the heavy-ion collision, whereas flow induce a correlation among all particles. The cumulant expansion method provide tools to extract the genuine multi-particle correlation, while removing all contributions stemming from correlations among fewer particles.

In the following, important aspects and properties of cumulants [57] needed for the anisotropic flow extraction are presented, using the two-particle correlation function as example. The procedure can be generalized to multi-particle correlations.

Let's consider two randomly distributed observables, denoted as x_1 and x_2, along with their joint probability distribution function, denoted as $f(x_1,x_2)$. When both observables are statistically independent, the joint probability distribution $f(x_1,x_2)$ factorizes into two probability distribution function for the individual random distributed observable:

$$f(x_1,x_2) = f(x_1) \cdot f(x_2) \tag{3.11}$$

Now assume, that there exists a statistical relation between the random variables x_1 and x_2. This introduces a genuine two-particle correlation into the system, which can be quantified by introducing the genuine two-particle probability distribution function $f_c(x_1,x_2)$. The joint probability distribution function changes to:

$$f(x_1,x_2) = f(x_1) \cdot f(x_2) + f_c(x_1,x_2) \tag{3.12}$$

and can be divided into a statistically independent and dependent part.
The corresponding expectation values of Equation (3.12) can be written as:

$$E(x_1,x_2) = E(x_1) \cdot E(x_2) + E_c(x_1,x_2) \tag{3.13}$$

The term $E_c(x_1,x_2)$ is, by definition, the two-particle cumulant. It provides the contribution to the expectation value $E(x_1,x_2)$ that arises solely from the genuine two-particle correlation $f_c(x_1,x_2)$. As mentioned earlier, this procedure can be generalized to any number

of random observables, and the reader is referred to equation (2.9) in the paper [57] for a generalized formula for the multi-particle cumulant of order n. In this manner, it is possible to extract, for n random variables, the contribution to the expectation value from the n-particle cumulant $E_c(x_1, x_2, ..., x_n)$. It's important to emphasize that if one of the n random variables is statistically independent of the others, the n-particle cumulant vanishes; however, it becomes non-zero if all random variables x_i are statistically dependent [57].

3.1.2 Application of cumulants in flow analysis

The formalism of cumulants was introduced for flow analysis by Borghini et. al in [58, 59]. For the random variables x_1 and x_2 they used:

$$x_1 = e^{in\phi_1} \tag{3.14}$$

$$x_2 = e^{in\phi_2} \tag{3.15}$$

where n is the harmonic index of interest, and ϕ_1 and ϕ_2 are the azimuthal angle of two particles measured in the experiment. By substituting equations Equation (3.14) and Equation (3.15) into the equation for expectation values Equation (3.13) and solving for the genuine two-particle cumulant, we obtain:

$$E_c(e^{in(\phi_1-\phi_2)}) = E(e^{in(\phi_1-\phi_2)}) - E(e^{in\phi_1}) \cdot E(e^{in\phi_2}) \tag{3.16}$$

Together with the multi-particle correlations introduced in Section 3.1, we can use the sampled measurements of the random observable ϕ_1 and ϕ_2 from heavy-ion collisions in the experiment to extract $E(e^{in\phi_1})$, $E(e^{in\phi_2})$ and $E(e^{in(\phi_1-\phi_2)})$. One consequence in the choice of the random variables defined in Equations (3.14) and (3.15), is that for a uniform detector the expectation values $E(e^{in\phi 1})$, $E(e^{in\phi 2})$ vanish. They vanish, because azimuthal angles ϕ_1, ϕ_2 are measured with respect to the labatory coordinate system, rather than the collision's reaction plane [59]. Since the reaction plane is randomly distributed with respect to the labatory system for a set of events, the measured azimuthal angles ϕ_i of particles from these events is symmetric and the averages vanish.

The expectation value $E(e^{in(\phi_1-\phi_2)})$ on the other hand, can be extracted directly from the measured values of the azimuthal angles, using the all-event average two-particle correlation introduced in Equation (3.4). This leads to the following expression for the genuine two-particle cumulant:

$$E_c(e^{in(\phi_1-\phi_2)}) = c_n\{2\} = \langle\langle 2\rangle\rangle \tag{3.17}$$

Here, we introduced the notation $c_n\{2\}$ for the two-particle cumulant, which was defined in [59]. This notation is widely used in the analysis of anisotropic flow. The definition of the four-particle cumulant follows a similar approach to that of the two-particle cumulant. Similar to the two-particle correlation, the expectation values for the four-particle correlation can also be decomposed into its distinct contributions, as follows:

$$\begin{aligned} E(e^{\phi_1+\phi_2-\phi_3-\phi_4}) &= E(e^{\phi_1-\phi_3})E(e^{\phi_2-\phi_4}) \\ &+ E(e^{\phi_1-\phi_4})E(e^{\phi_2-\phi_3}) \\ &- E_c(e^{\phi_1+\phi_2-\phi_3-\phi_4}) \end{aligned} \tag{3.18}$$

The first two terms represent the product of two two-particle correlations, while the last term corresponds to the genuine four-particle cumulant. Additional terms involving the three-particle correlation and the single-particle distribution vanish due to similar symmetry arguments as those made for the two-particle cumulant in Equation (3.16).

Solving for the four-particle cumulant $E_c(e^{\phi_1+\phi_2-\phi_3-\phi_4})$ gives:

$$\begin{aligned} E_c(e^{\phi_1+\phi_2-\phi_3-\phi_4}) &= E(e^{\phi_1+\phi_2-\phi_3-\phi_4}) \\ &- E(e^{\phi_1-\phi_3})E(e^{\phi_2-\phi_4}) \\ &- E(e^{\phi_1-\phi_4})E(e^{\phi_2-\phi_3}) \end{aligned} \tag{3.19}$$

Using the event averages of the two- and four-particle correlations, introduced in Section 3.1, as measured estimator of the expectation values, the four-particle cumulant can be expressed as:

$$c_n\{4\} = \langle\langle 4\rangle\rangle - 2 \cdot \langle\langle 2\rangle\rangle^2 \tag{3.20}$$

Again, introducing the commonly used notation $c_n\{4\}$ for the four-particle cumulants.

With Equation (3.17) and Equation (3.20), both the two- and four- particle cumulants can be measured in the experiment.

The cumulants arise from the correlation of all particles with the common reaction plane of the collision. This gives rise to the presence of multi-particle correlations for any given number of particles created in the collision. Correlations not stemming from these flow correlations typically involve only a few particles. An illustrative example is the non-flow component, arising from particle resonance decays. Since such decays usually consist of two decay products, they introduce a bias to the true two-particle cumulant $c_n\{2\}$, whereas the four-particle cumulant $c_n\{4\}$ is not affected. Contributions from flow correlations, on the other hand, will affect both the two- and four-particle cumulant. By comparing these two cumulants, it becomes possible to extract the relative fraction of non-flow to the two-particle cumulant.

The anisotropic flow from the cumulant method is given by inserting Equation (3.10) in Equation (3.17) and Equation (3.20)

$$\sqrt{c_n\{2\}} = \sqrt{\langle\langle 2\rangle\rangle} = v_n \tag{3.21}$$

$$\sqrt[4]{c_n\{4\}} = \sqrt[4]{-\langle\langle 4\rangle\rangle + 2\langle\langle 4\rangle\rangle^2} = \sqrt[4]{-v_n^4 + 2v_n^4} = v_n \tag{3.22}$$

Equations (3.21) and (3.22) hold true in the ideal scenario where only flow correlations exist in the collision, and both flow fluctuations and non-flow contributions are neglected. In this ideal case, both the two- and four-particle cumulants will yield the same result for the anisotropic flow v_n. To specify from which particle cumulant the anisotropic flow v_n is extracted, the order of the cumulant is indicated in curly brackets, as follows:

$$v_n\{2\} = \sqrt{c_n\{2\}} \tag{3.23}$$

$$v_n\{4\} = \sqrt[4]{c_n\{4\}} \tag{3.24}$$

3.1.3 Constructing cumulants from flow vectors

The relastionship established between anisotropic flow, multi-particle cumulants and multi-particle correlations in the previous sections already provide all ingredients to estimate flow coefficients with Equations (3.23) and (3.24) in an experiment. This extraction method is computationally expensive and scales with the particle multiplicity M raised to the power of the number of particles m, i.e., $\mathcal{O}(M^m)$. This makes the calculation, particularly in central heavy-ion collisions, unfeasible. An alternative method to extract the cumulants to estimate the anisotropic flow involves flow vectors, as defined at the beginning of this chapter (Equation (3.1)), including the subtraction of autocorrelations which arise natural from this calculation method [60, 55]. The calculation time only scales linear with the number of particles $\mathcal{O}(M)$, making it perfectly well suited for the analysis of high multiplicity heavy-ion collisions.

The extraction of the two-particle cumulant $c_n\{2\}$ using flow vectors is straightforward by calculating the scalar product of the flow vector Q_n and then separating the sum into diagonal and off-diagonal elements:

$$
\begin{aligned}
|Q_n|^2 &= Q_{n,p}Q^*_{n,p} \\
&= \sum_{j,k}^{M} w_j^p w_k^p e^{in(\phi_j-\phi_k)} \\
&= \sum_{\substack{j,k=1 \\ j\neq k}}^{M} w_j^p w_k^p e^{in(\phi_j-\phi_k)} + \sum_{\substack{j,k=1 \\ j=k}}^{M} w_j^p w_k^p e^{in(\phi_j-\phi_k)} \\
&= \sum_{\substack{j,k=1 \\ j\neq k}}^{M} w_j^p w_k^p e^{in(\phi_j-\phi_k)} + Q_{0,2p}
\end{aligned}
\tag{3.25}
$$

Inserting Equation (3.25) into Equation (3.4) yields for the two-particle cumulant $c_n\{2\}$:

$$
c_n\{2\} = \langle\langle 2\rangle\rangle = \left\langle \frac{Q_{n,1}Q_{-n,1} - Q_{0,2}}{Q_{0,1}Q_{0,1} - Q_{0,2}} \right\rangle \tag{3.26}
$$

Similarly, the higher-order cumulants can be computed, although they take a more complex form. For a deeper understanding, readers are directed to [55]. The expression for the single-event average four-particle correlation $\langle 4\rangle$ in terms of flow vectors is provided as:

$$
\begin{aligned}
\langle 4\rangle = {} & Q_{n,1}Q_{n,1}Q_{-n,1}Q_{-n,1} + Q_{2n,2}Q_{-2n,2} - Q_{n,1}Q_{n,1}Q_{-2n,2} \\
& - Q_{-n,1}Q_{-n,1}Q_{2n,2} + 4Q_{n,1}Q_{-n,3} + 4Q_{-n,1}Q_{n,3} \\
& + 2Q^2_{0,2} - 4Qn,1Q_{-n,1}Q_{0,2} - 6Q_{0,4} \\
& /Q^4_{0,1} - 6Q^2_{0,1}Q_{0,2} + 3Q^2_{0,2} \\
& + 8Q_{0,1}Q_{0,3} - 6Q_{0,4}
\end{aligned}
\tag{3.27}
$$

Inserting Equation (3.26) and Equation (3.20) into Equation (3.24), we can derive the true four-particle cumulant $c_n\{4\}$ using exclusively flow vectors.

3.1.4 p_{T}-differential flow

Studying anisotropic flow differentially as a function of transverse momentum p_T and particle type is also of significant interest for understanding the evolution of the QGP and fluctuations of the initial energy density created in the overlap region of the collision. The method described in the previous section can also be used for the differential flow analysis. For this purpose the integrated flow vector Q_n needs to be replaced with the corresponding differential flow vector $Q_n(p_{\mathrm{T}}, \mathrm{PID}, ...)$. However, the differential anisotropic flow extracted in this way suffer from a reduced statistical precision due to the smaller number of particles in the specific differential region of interest.

The precision of the differential flow analyis can be greatly improved by dividing the mea-

sured particles into different group of particles. The first group, referred to as ”Particles Of Interest” (POI), contain only the particles within a specific region of interest (such as a particular kinematic region or particle type). The second group, known as ”Reference Flow Particles” (RFP), includes all particles relative to which the flow coefficients are calculated.

The differential anisotropic flow is extracted in two steps:

1. Using all particles labeled as RFP (Reference Flow Particles), referred to as the reference flow.

2. Using the particles marked as POI relative to the reference flow.

There can be an overlap between particles marked as RFP and POI. This overlap needs to be correctly accounted for to minimize bias from autocorrelations, particularly because the differential flow is extracted relative to the reference flow.
The differential aziumthal two- and four particle correlations $\langle 2' \rangle, \langle 4' \rangle$ are given as:

$$\langle 2' \rangle = \langle e^{in\phi_1 - in\phi_2} \rangle = \sum_{j}^{m_{POI}} \sum_{\substack{k \\ j \neq k}}^{m_{RFP}} w_j w_k e^{in\phi_j - in\phi_k} / \sum_{j}^{m_{POI}} \sum_{\substack{k \\ j \neq k}}^{m_{RFP}} w_j w_k \tag{3.28}$$

$$\begin{aligned} \langle 4' \rangle &= \langle e^{in\phi_1 + in\phi_2 - in\phi_3 - in\phi_4} \rangle \\ &= \sum_{j}^{m_{POI}} \sum_{\substack{k,l,m, \\ j \neq k \neq l \neq m}}^{m_{RFP}} w_j w_k w_l w_m e^{in\phi_j + in\phi_k - in\phi_l - in\phi_m} \\ &/ \sum_{j}^{m_{POI}} \sum_{\substack{k,l,m, \\ j \neq k \neq l \neq m}}^{m_{RFP}} w_j w_k w_l w_m \end{aligned} \tag{3.29}$$

Much like in Section 3.1.3, flow vectors can be used to simplfy and speed up the calculation of the differential multi-particle correlation and cumulants. For the differential case three flow vectors are needed.
The flow vector $Q_{n,p}$ is filled with all particles labeled as RFP:

$$Q_{n,p} = \sum_{j}^{m_{RFP}} w_j^p e^{in\phi_j} \tag{3.30}$$

The weighted flow vector $p_{n,p}$ is constructed using all particles labeled as POIs:

$$p_{n,p} = \sum_{j}^{m_{POI}} w_j^p e^{in\phi_j} \tag{3.31}$$

whereas the flow vector $r_{n,p}$ is filled with all particles labeled both as POI and RFPs to analytically subtract autocorrelations:

$$r_{n,p} = \sum_{j}^{m_{POI \cap RFP}} w_j^p e^{in\phi_j} \tag{3.32}$$

Together with these three flow vectors, the two- and four-particle correlations $\langle 2' \rangle$, $\langle 4' \rangle$ simplify to:

$$\langle 2' \rangle = p_{n,1} Q_{-n,1} - r_{0,2} \tag{3.33}$$

$$\begin{aligned} \langle 4' \rangle = {} & p_{n,1} Q_{n,1} Q_{-n,1} Q_{-n,1} - r_{2n,2} Q_{-n,1} Q_{-n,1} \\ & - p_{n,1} Q_{n,1} Q_{-2n,2} - 2 Q_{n,1} r_{0,2} Q_{-n,1} \\ & - 2 p_{n,1} Q_{0,2} Q_{-n,1} + 4 r_{n,3}, Q_{-n,1} \\ & + 2 Q_{0,2} r_{0,2} + 2 Q_{1,1} r_{-n,3} + 2 p_{n,1} Q_{-n,3} \\ & + r_{2n,2} Q_{-2n,2} - r_{0,4} \end{aligned} \tag{3.34}$$

The all-event averages of the differential two- and four-particle correlations are defined in a manner similar to their integrated counterparts and are presented as follows:

$$\langle \langle 2' \rangle \rangle = \sum_{i=1}^{N} (w_{\langle 2' \rangle})_i \langle 2' \rangle_i / \sum_{i=1}^{N} (w_{\langle 2' \rangle})_i \tag{3.35}$$

$$\langle \langle 4' \rangle \rangle = \sum_{i=1}^{N} (w_{\langle 4' \rangle})_i \langle 4' \rangle_i / \sum_{i=1}^{N} (w_{\langle 4' \rangle})_i \tag{3.36}$$

where the event averages $w_{\langle 2' \rangle}$, $w_{\langle 4' \rangle}$ for a non-uniform detector are given as:

$$w_{\langle 2' \rangle} = p_{0,1} Q_{0,1} - r_{0,2} \tag{3.37}$$

$$\begin{aligned} w_{\langle 4' \rangle} = {} & p_{0,1} Q_{0,1}^3 - 3 r_{0,2} Q_{0,1}^2 \\ & - 3 p_{0,1} Q_{0,1} Q_{0,2} + 3 r_{0,2} Q_{0,2} \\ & + 6 r_{0,3} Q0,1 + 2 p_{0,1} Q_{0,3} - 6 r_{0,4} \end{aligned} \tag{3.38}$$

Just like for the integrated case, assuming a uniform detector, the event weights reflect the number of possible combinations of two- and four-particle correlations that can be formed within an event.
Following the notation introduced in [58], the expressions for the differential two- and four-particle cumulants are provided as:

$$d_n\{2\} = \langle \langle 2' \rangle \rangle \tag{3.39}$$

$$d_n\{4\} = \langle \langle 4' \rangle \rangle - 2 \langle \langle 2' \rangle \rangle \langle \langle 2 \rangle \rangle \tag{3.40}$$

The two- and four-particle cumulants extracted from the integrated cases, denoted as $c_n\{2\}$

and $c_n\{4\}$ respectively. For the differential cases, they are denoted as $d_n\{2\}$ and $d_n\{4\}$ respectively and serving as basis for extracting the differential anisotropic flow.
The differential anisotropic flow is then given as:

$$v_n\{2\}' = \frac{d_n\{2\}}{\sqrt{c_n\{2\}}} \tag{3.41}$$

$$v_n\{4\}' = -\frac{d_n\{4\}}{\sqrt[4]{-c_n\{2\}^3}} \tag{3.42}$$

Both $v_n\{2\}'$, $v_n\{4\}'$ yield independent estimates for the differential anisotropic flow harmonic v_n' and are biased differently by non-flow effects and flow fluctuations. To verify the result in Equation (3.41), one can consider the ideal case, where only flow correlations are present. Consider the ideal case, which is free from non-flow and flow fluctuation. The numerator in Equation (3.41) becomes $v_n' v_n$, while the denominator results in $\sqrt{v_n v_n}$. Consequently, v_n cancels out from the equation, leaving only the differential flow v_n'.

3.2 Anisotropic flow relative to the spectator plane

The cumulant method is typically used with detectors capable of reconstructing individual particle tracks or have a fine segmentation. This ensures that the joint probability function defined in Equation (3.12) are well-sampled, allowing for reliable measurements of the anisotropic flow. This typically restricts the usage of the cumulant method to the midrapidity region.

The spectators used to measure the anisotropic flow relative to the spectator plane are measured detectors, located in forward direction. Additionally, forward detectors typically offer a limited segmentation for the measurement of the spectator plane. In such cases, the well established scalar product method [61] is used. The anisotropic flow of particles of interest (POI) is measured relative to reference flow particles (RFP), usually measured with detectors located in forward direction. Using forward detectors as RFP introduces a gap in pseudorapidty between the POI and RFP. This psuedorapidty gap reduces the contamination due to non-flow sources, as particles created in jets and resonance decays typically emitted with small relative angles [62].

3.2.1 Event plane method

The physical interpretation of the scalar product method can intuitively be understood when deriving its equation directly from the event plane method [63], which is a commonly used in anisotropic flow analysis. In the event plane method the underlying symmetry planes of the fluctuating shape of initial energy density Ψ_n are extracted directly from the measured aziumthal angles of the particles created in the collision. These symmetry planes can be derived from the events flow vector and are expressed as:

$$\begin{aligned}\Psi_n \approx \Psi'_n &= \frac{1}{n}\text{atan2}(Y_{n,p}, X_{n,p}) \\ &= \frac{1}{n}\text{atan2}(\sum_{j=0}^{M} w_j^p \sin(n\phi_j), \sum_{j=0}^{M} w_j^p \cos(n\phi_j))\end{aligned} \tag{3.43}$$

where M represents the total number of particles used for the flow vector extraction. Since only a limited number of particles is available to approximate the underlying symmetry plane Ψ_n, the anisotropic flow extracted with this approximated symmetry plane Ψ'_n is inherently biased.

This situation becomes clear when considering the following equation:

$$\begin{aligned}v_n^{obs} &= \langle \cos(n(\phi_j - \Psi'_n)) \rangle \\ &= \langle \cos(n(\phi_j - \Psi_n) - (\Psi'_n - \Psi_n)) \rangle \\ &= \langle \cos(n(\phi_j - \Psi_n)) \rangle \cdot \langle \cos(n(\Psi'_n - \Psi_n)) \rangle\end{aligned} \tag{3.44}$$

In the last line, the angle difference identity $\cos(\alpha - \beta) = \cos(\alpha)\cos(\beta) - \sin(\alpha)\sin(\beta)$ was used. The sine terms are omitted due to symmetry of particle production with respect to the reaction plane.
The first term on the right-hand side of Equation (3.44) corresponds exactly to the anisotropic flow, as introduced in Equation (2.13). On the other hand, the second term can be interpreted as a resolution term, indicating the precision of the symmetry plane determination. Because the second term is inherently smaller than unity, the measured anisotropic flow $v_{n,obs}$ is consistently lower than the true anisotropic flow v_n.

Solving for the true anisotropic flow yields:

$$v_n = \frac{v_n^{obs}}{\langle \cos(n(\Psi'_n - \Psi_n)) \rangle} = \frac{v_n^{obs}}{\mathscr{R}} \tag{3.45}$$

The resolution term $\mathscr{R}$, as stated in Equation (3.45), is not directly measurable. It can be estimated by defining different sub-events within the analyzed event and determine the symmetry planes based on each of these sub-events [64]. Given the two sub-events A and B, together with their symmetry planes Ψ_n^a and Ψ_n^b, the resolution $\mathscr{R}$ is given as:

$$\mathscr{R} = \langle \cos(n(\Psi_n^a - \Psi_n^b)) \rangle \tag{3.46}$$

Equation (3.45) can be rewritten in a form of flow vectors, where p_n is the flow vector of POI, r_n the flow vector of subevent A and s_n the flow vector of subevent B:

$$
\begin{aligned}
v_n &= \frac{v_n^{obs}}{\mathscr{R}} \\
&= \frac{\langle \cos(n(\phi_j - \Psi_n^a)) \rangle}{\langle \cos(n(\Psi_n^a - \Psi_n^b)) \rangle} \\
&= \frac{\langle p_n \frac{r_n}{|r_n|} \rangle}{\sqrt{\langle \frac{r_n}{|r_n|} \frac{s_n}{|s_n|} \rangle}}
\end{aligned}
\tag{3.47}
$$

Usually the subevents A and B are chosen with a pseudorapidty gap with respect to the flow vector r_n to reduce non-flow correlations.

3.2.2 Scalar product method

The scalar product method can be understood as a modification of the event-plane method described in Equation (3.47), with the factors $|...|$ removed from the calculation [64]. In this approach, the flow vector build of particles of interest p_n is correlated with the flow vector of the reference set r_n in order to extract the anisotropic flow:

$$
v_n = \frac{v_{n,obs}}{\mathscr{R}} = \frac{\langle p_n r_{-n} \rangle}{\mathscr{R}} \tag{3.48}
$$

The impact of non-flow contributions is suppressed by correlating the flow vectors from different detectors with a large pseudorapidity separation. The resolution correction on the observed flow $v_{n,obs}$ is not estimated using the formula presented in Equation (3.46), but instead, the three-subevent method is employed [63]. In this approach, the two flow vectors s_n and t_n are correlated with the reference flow vector r_n:

$$
R = \sqrt{\frac{\langle r_n s_{-n} \rangle \langle r_n t_{-n} \rangle}{\langle s_n t_{-n} \rangle}} \tag{3.49}
$$

3.2.3 Mixed harmonics method

The scalar product method assumes that the harmonics used in the flow vector calculation for both POI and RFP are the same. If this is not the case, the averages presented in Equation (3.48) yield zero. It is possible to extract the elliptic flow relative to the first harmonic symmetry planes, which is relevant for the measurements with spectators, by introducing a second RFP flow vector. The elliptic flow is then extracted by correlating the second harmonic POI flow vector (p_2) with two first harmonic RFP flow vectors (q_{-1}, r_{-1}):

$$
v_2 = \frac{v_{2,obs}}{\mathscr{R}} = \frac{\langle p_2 r_{-1} q_{-1} \rangle}{R} \tag{3.50}
$$

The resolution correction $\mathscr{R}$ is extracted by correlating both RFP flow vectors q_{-1} and

r_{-1}, thereby removing the assumed reference flow from the numerator in Equation (3.50). The complex product of $v_{2,obs}$ in Equation (3.50) yields four independent estimates for the elliptic flow. These components are given as:

$$\begin{aligned} v_{2,obs} &= \langle p_2 r_{-1} q_{-1} \rangle \\ &= \langle x_2 x_{-1} x_{-1} \rangle - \langle y_2 y_{-1} y_{-1} \rangle \\ &+ \langle y_2 x_{-1} y_{-1} \rangle + \langle y_2 y_{-1} x_{-1} \rangle \end{aligned} \tag{3.51}$$

where x and y are the projections of the flow vectors upon the x- and y-axis of our coordinate system.
Each of the four products provides an independent estimate of the anisotropic flow. For the first two components, the elliptic flow is given as:

$$v_2 = \frac{\langle x_2 x_{-1} x_{-1} \rangle}{2\langle x_{-1} x_{-1} \rangle} = -\frac{\langle y_2 y_{-1} y_{-1} \rangle}{2\langle y_{-1} y_{-1} \rangle} \tag{3.52}$$

In the case of the third and fourth component, the correlations $\langle x_{-1} y_{-1} \rangle$ and $\langle y_{-1} x_{-1} \rangle$ of both RFP flow vectors cannot be used for the estimation of the resolution correction, since these correlations vanish. Therefore, the resolution correction $\mathscr{R}$ for the third and fourth components is extracted by taking the geometrical mean of the non-zero components, $\langle x_{-1} x_{-1} \rangle$ and $\langle y_{-1} y_{-1} \rangle$. The elliptic flow extracted from the third and fourth components is then given by:

$$v_2 = \sqrt{\frac{\langle y_2 x_{-1} y_{-1} \rangle \langle y_2 y_{-1} x_{-1} \rangle}{4\langle y_{-1} y_{-1} \rangle \langle x_{-1} x_{-1} \rangle}} \tag{3.53}$$

In the analysis presented in this thesis the POI flow vector is extracted using reconstructed tracks from one detector at mid-rapidity (Q_2^{PP}), while the RFP flow vectors are extracted from two spectator detectors ($q_1^{\mathrm{SPa}}, q_1^{\mathrm{SPb}}$). To increase the statistical precision, the three independent elliptic flow components from Equation (3.52) and Equation (3.53) are averaged. The elliptic flow relative to the spectator plane is then expressed as:

$$\begin{aligned} v_2\{\Psi_{\mathrm{SP}}\} = \frac{1}{6}\Bigg(& \frac{\langle X_2^{\mathrm{PP}} x_1^{\mathrm{SPa}} x_1^{\mathrm{SPb}} \rangle}{\langle x_1^{\mathrm{SPa}} x_1^{\mathrm{SPb}} \rangle} \\ & - \frac{\langle X_2^{\mathrm{PP}} y_1^{\mathrm{SPa}} y_1^{\mathrm{SPb}} \rangle}{\langle y_1^{\mathrm{SPa}} y_1^{\mathrm{SPb}} \rangle} \\ & + \sqrt{\frac{\langle Y_2^{\mathrm{PP}} x_1^{\mathrm{SPa}} y_1^{\mathrm{SPb}} \rangle \cdot \langle Y_2^{\mathrm{PP}} y_1^{\mathrm{SPa}} x_1^{\mathrm{SPb}} \rangle}{\langle x_1^{\mathrm{SPa}} x_1^{\mathrm{SPb}} \rangle \cdot \langle y_1^{\mathrm{SPa}} y_1^{\mathrm{SPb}} \rangle}} \Bigg) \end{aligned} \tag{3.54}$$

The determination of the differential flow coefficients is achieved by replacing the integrated flow vector of POI $X_2^{\mathrm{PP}}, Y_2^{\mathrm{PP}}$, with its differential counterparts $X_2^{\mathrm{PP}}(p_{\mathrm{T}}, \mathrm{PID}, ...)$ and $Y_2^{\mathrm{PP}}(p_{\mathrm{T}}, \mathrm{PID}, ...)$.

4 ALICE at the LHC

4.1 The Large Hadron Collider

The Large Hadron Collider (LHC) [65] situated at CERN, the European Organization for Nuclear Research, is currently the largest hadron accelerator in the world. It is located at the borders of Switzerland and France, close to Geneva. Installed within the 26.7 km tunnel, originally constructed for the Large Electron-positron collider (LEP) and is part of a larger accelerator complex built in the last decades. This complex, illustrated in Figure 4.1, features a series of accelerator facilities that progressively increase the energy of protons and/or heavy ions before injecting them into the LHC.

The first acceleration phase consists of two components: the Linear Accelerator 2 (LINAC2) and the Proton Synchrotron Booster (BOOSTER) for protons, as well as the Linear Accelerator 3 (LINAC3) and the Low Energy Ion Ring (LEIR) for ion beams. Following this stage, protons and ions accelerate further through the Proton Synchrotron (PS) and the Super Proton Synchrotron (SPS). Afterward, they are injected into the LHC machine, accelerating the particles to the desired energy. Detailed information regarding the different acceleration steps and facilities are found in Ref. [66].

The LHC is a synchrotron accelerator composed of two rings, each hosting counter-rotating beams. To reach the intended center-of-mass energy of $\sqrt{s} = 14\,\text{TeV}$ for proton-proton collisions and $\sqrt{s_{\text{NN}}} = 5.5\,\text{TeV}$ for lead-lead collisions, the LHC consists of superconducting dipole magnets. These magnets can produce magnetic fields, with strengths that can reach up to 8.33 Tesla.
As of now, the maximum energies achieved are $\sqrt{s} = 13.6\,\text{TeV}$ for proton-proton collisions, $\sqrt{s_{\text{NN}}} = 8.16\,\text{TeV}$ for proton-lead collisions, $\sqrt{s_{\text{NN}}} = 5.44\,\text{TeV}$ for xenon-xenon collisions, and $\sqrt{s_{\text{NN}}} = 5.36\,\text{TeV}$ for lead-lead collisions.

The two beams intersect at four points, where the four major LHC experiments are located: A Toroidal LHC ApparatuS (ATLAS) [68], Compact Muon Solenoid (CMS) [69], Large-Hadron-Collider-beauty (LHCb) [70] and A Large Ion Collider Experiment (ALICE) [71]. Four more interaction points at the LHC are used to collimate, accelerate, and dump the beams.

The ATLAS and CMS experiments are general-purpose detectors designed to measure the Higgs boson, precision tests of the QCD and electroweak theory, and the search for physics beyond the standard model. LHCb is built to investigate CP violation by studying

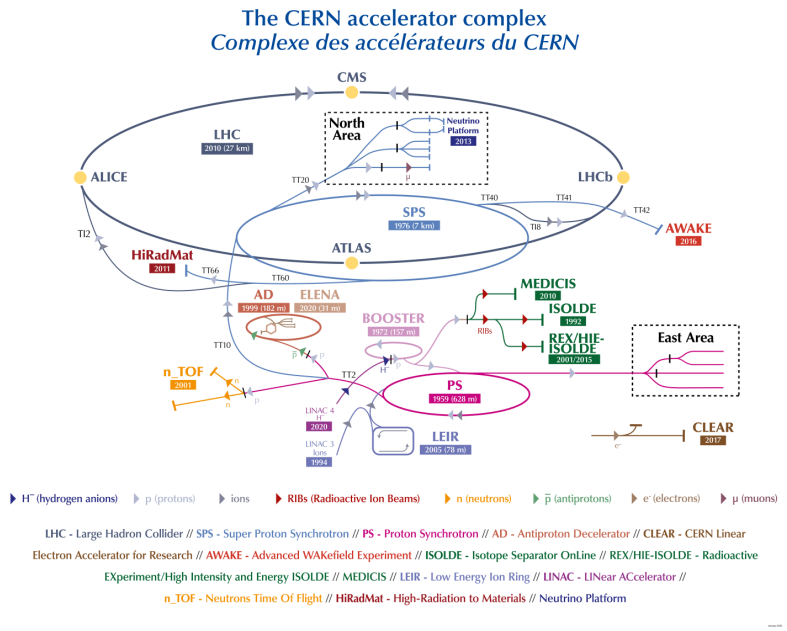

Figure 4.1: Schematic view of the CERN accelerator complex [67].

the decay of hadrons containing a beauty quark, while ALICE is specialized to investigate ultra-relativistic heavy-ion collisions. It is worth noting that all four major experiments currently have dedicated heavy-ion programs.

In addition, four smaller experiments are deployed at the LHC, sharing the interaction points with the larger experiments. The Total Elastic and Diffractive Cross Section Measurement (TOTEM) experiment [72] is dedicated to precisely measuring the cross-section for proton-proton interactions in the forward region. The Monopole and Exotics Detector At the LHC (MOEDAL) [73] focus on the search for magnetic monopols. LHC-forward (LHCf) [74] investigates the production of neutral particles in the forward direction to improve our understanding of the origin of ultra-high-energy cosmic rays. Lastly, the ForwArd Search ExpeRiment (FASER) [75] aims to search for new light, very weakly interacting particles, and explore the field of high-energy neutrino physics.

4.2 The ALICE experiment

ALICE is a general-purpose detector specially built to investigate ultra-relativistic heavy-ion collisions. It primarily focuses on the physics of strongly interacting matter and the QGP investigation under extremely high energy density and temperature conditions, as produced in heavy-ion collisions at LHC energies. To achieve this goal, particles must be measured down to low momentum within environments characterized by large charged-particle multiplicities.[1] These considerations are reflected in the detector's design,

[1] In central heavy-ion collisions, up to $\mathcal{O}(1000)$ particles are created.

deploying detectors with high granularity and a low material budget. Additionally, ALICE provides excellent particle identification (PID) capabilities over a broad range of momenta, which are needed for different physics signals.

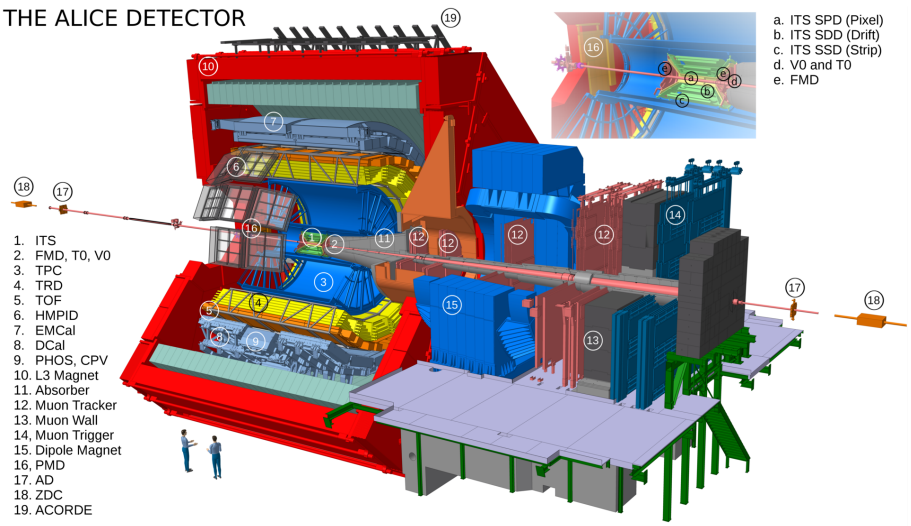

Figure 4.2: Schematic view of the ALICE detector in the configuration during Run 2 [76].

A schematic overview of the experiment is presented in Figure 4.2. The experiment is mainly divided into two main components: the central barrel, which covers the pseudorapidity region of $|\eta| < 0.9$, and the muon spectrometer, which spans the forward rapidity region (-4 $< \eta <$ -2.5). The central barrel is embedded inside the L3 magnet, providing a magnetic field of up to B = 0.5 T parallel to the beam axis. It contains detectors for tracking, primary vertex determination, PID, and multiplicity measurements.

The ALICE detector underwent a major upgrade during the LHC Long Shutdown 2 between 2019 and 2022. Most detectors were upgraded throughout this period, and the detector setup moved to a continuous readout system. This allows the recording of lead-lead collisions at rates of up to 50kHz [77].

Since the analysis described in this work relies on data collected before the major upgrade, the detectors used in the analysis are described in their pre-upgrade configuration. A detailed overview of the ALICE experiment and the performance of its sub-detectors can be found in [71, 78, 79, 80].

4.2.1 Inner Tracking System

The Inner Tracking System (ITS) [81, 82], shown in Figure 4.3, is the innermost detector and consists of six cylindrically-shaped silicon detectors. Its primary purpose is to determine the collision's primary vertex, reconstruct secondary vertices from weak decays of short-lived particles, and improve the momentum and pointing angle resolution of

particles reconstructed with the Time Projection Chamber. Three different silicon detector technologies were employed for the inner, middle, and outermost layers of the ITS.

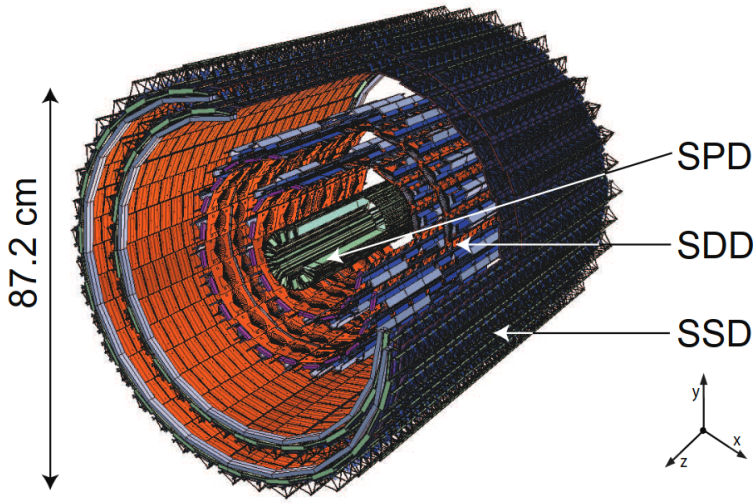

Figure 4.3: Schematic view of the ITS detector in the configuration during Run 2[82].

The two innermost layers consist of Silicon Pixel Detectors (SPD), offering a high granularity to cope with the high particle multiplicities in central heavy-ion collisions. They also provide a charged particle multiplicity estimator in the form of tracklets, defined as track segments built by associated hits in the two SPD layers. The third and fourth layers of the ITS consist of Silicon Drift Detectors (SDD), providing the possibility of particle identification via the $\langle \mathrm{d}E/\mathrm{d}x \rangle$ measurement, particularly for particles with low transverse momenta (< 1 GeV/c). Particle identification is also provided by the Silicon Strip Detectors (SDD), which are used for the two outermost layers of the ITS. They are crucial for connecting tracks from the ITS to the Time Projection Chamber. The faster readout of the SDD and SSD compared to the time projection chamber makes them essential for the treatment of pile-up events, a topic that will be discussed in greater detail in Chapter 5.

During the Long Shutdown 2 of the ALICE experiment, the ITS detector was replaced by a completely new silicon-based detector consisting of seven layers of ALPIDE [83, 84] Monolithic Active Pixel Sensors (MAPS). This upgrade aimed to improve the resolution of the reconstructed primary vertex and secondary vertex of short-lived particles. More information about the ITS detector upgrade during LHC Shutdown 2 is given in Ref. [85, 86].

4.2.2 Time Projection Chamber

The Time Projection Chamber (TPC) [87, 88], shown in Figure 4.4, is the main tracking detector within ALICE's central barrel. It can reconstruct tracks in a broad transverse

momentum range, spanning from 100 MeV/c to 100 GeV/c, while also providing excellent PID capabilities across a wide momentum range.

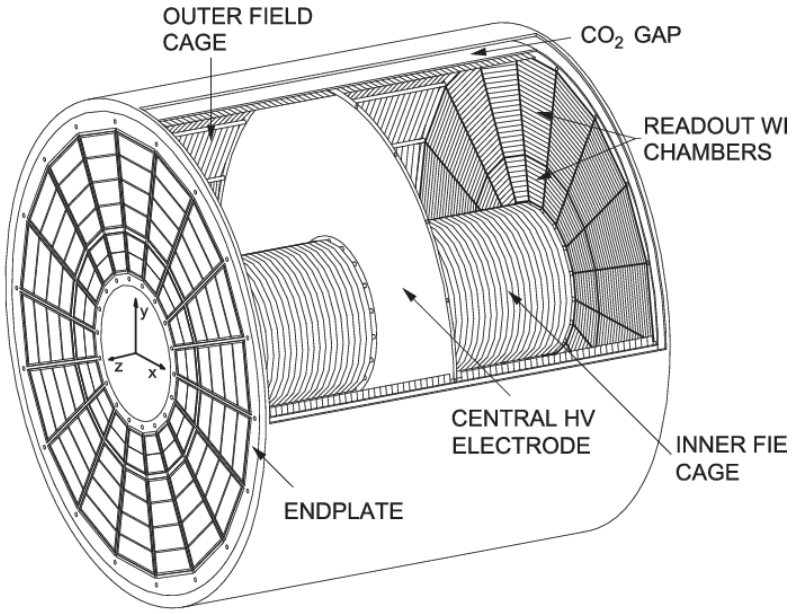

Figure 4.4: Schematic view of the TPC detector in the configuration during Run 2 [88].

The TPC is a cylindrical gas detector with an active volume that extends from an inner radius of approximately 85 cm to an outer radius of 250 cm. It has an overall length of 500 cm along the beam axis, covering a pseudorapidity range of $|\eta| < 0.9$. A central cathode divides the detector into two equally sized drift volumes. On the opposite sides of the central cathode, readout chambers are installed, consisting of Multi-Wire Proportional Chambers (MWPC) with cathode readout pads, subdivided into 18 trapezoidal sectors.

Charged particles traversing the TPC will ionize the gas. The freed electrons drift under the influence of a uniform electric field of 400 kV/m along the beam axis toward the readout chambers. In the vicinity of the anode wires, the electron signal is amplified through avalanche processes caused by the electric field near the wires. The ions produced in this avalanche process will induce a signal on the cathode readout pads, allowing a track reconstruction in the $r\phi$ plane. The location of the particle track along the beam axis is reconstructed from the drift time of electrons towards the readout chambers, providing a complete three-dimensional reconstruction of particle trajectories.
A gating grid is installed in front of the amplification zone to prevent ions created in the avalanche process from drifting back into the TPC's active volume, which could introduce space charge distortions to the drift field. A triggered event opens this gating grid for approximately 100 μs, corresponding to the time it takes for ionization electrons to drift the entire length of the TPC, thus allowing these electrons to reach the readout pad. In the closed mode, both positive and negative charges stop their drift at the gating grid.

Like the ITS, the TPC underwent an upgrade during Long Shutdown 2 of the LHC (reference: [89]). As part of this upgrade, the Multi-Wire Proportional Chambers (MWPCs) in the readout chambers were replaced by Gas Electron Multiplier (GEM) detectors [90]. The replacement with a stack of GEM detectors is a considerable improvement due to the mitigation of back-drifting ions into the active volume of the TPC. This improvement allows the removal of the gating grid from the TPC. By removing the gating grid, the TPC gains the capacity for continuous operation. This consequently allows the TPC to operate continuously and provides sensitivity to the minimum-bias interaction rates of 50 kHz in Pb–Pb collisions, as foreseen for Run 3 and beyond.

Particle identification is provided by measuring the specific energy loss $\langle \mathrm{d}E/\mathrm{d}x \rangle$ in the active volume of the TPC. The combined measurement of a particle's specific energy loss and momentum allows us to identify the particle species. Figure 4.5 shows the specific energy loss in Pb–Pb collisions at $\sqrt{s_{\mathrm{NN}}} = 5.02\,\mathrm{TeV}$ as a function of the rigidity, where p (z) corresponds to the particle momentum (charge), for different particle species. A detailed description of the particle identification via the specific energy loss $\langle \mathrm{d}E/\mathrm{d}x \rangle$ together with its parametrization in ALICE is provided in Chapter 5 of this thesis.

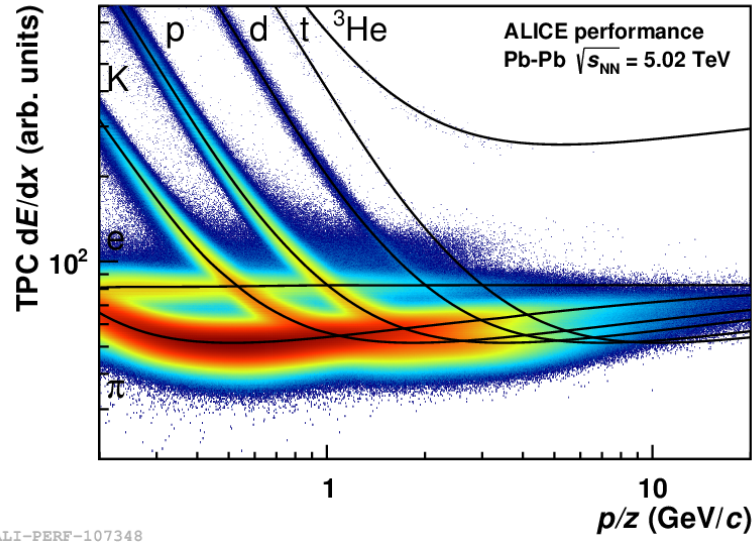

Figure 4.5: Specific energy loss $\langle \mathrm{d}E/\mathrm{d}x \rangle$ in the TPC as a function of the magnetic rigitdy for postivly charged tracks for Pb–Pb collisions at $\sqrt{s_{\mathrm{NN}}} = 5.02\,\mathrm{TeV}$. The black lines correspond to the Bethe-Bloch fit describing the expected $\langle \mathrm{d}E/\mathrm{d}x \rangle$ for a specific particle species[91].

4.2.3 Time-Of-Flight

The Time-Of-Flight detector (TOF) [92, 80] is a large area array of Multigap Resistive Plate Chambers (MRPCs), positioned 370-399 cm from the beam axis, covering the whole

azimuthal angle and the pseudorapidity $|\eta| < 0.9$. Its main purpose is to provide PID in the intermediate momentum range by measuring the arrival time of passing charged particles. Charged particles passing through the MRPCs ionize the gas. These electrons move towards the anode, start an avalanche process, and lead to a signal in the pickup electrode.

The starting time for the TOF measurement is provided by the T0 detector [93], which consists of two arrays of Cherenkov counters, T0A and T0C, positioned at opposite sides of the interaction point at -3.28 $< \eta <$ -2.97 and 4.61 $< \eta <$ -4.92, respectively. Alternatively, the start time is estimated using the particle arrival times at the TOF detector. A combinatorial algorithm based on the χ^2 minimization among all possible mass hypotheses is used in this case.

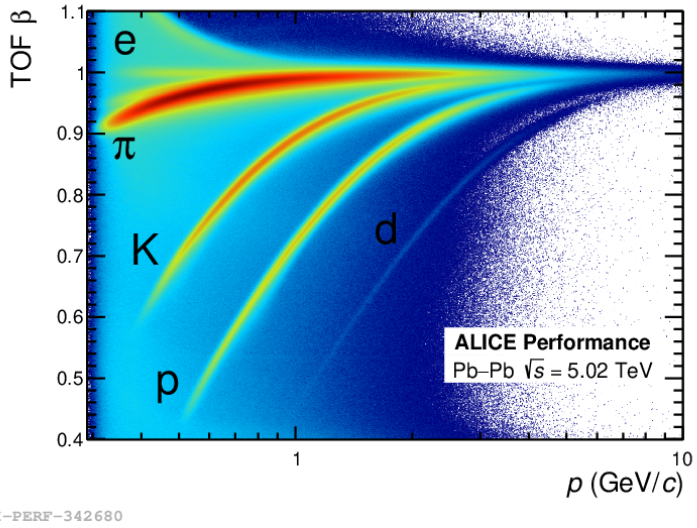

Figure 4.6: Velocity β measured by the TOF detector as a function of particle momentum in Pb–Pb collisions at $\sqrt{s_{\mathrm{NN}}} = 5.02\,\mathrm{TeV}$. Wrongly associated tracks are seen outside of the particle bands [91].

Particle identification is provided by the measured velocity β of particles in TOF and their measured momentum in the TPC. The velocity β as a function of the particle momentum p is illustrated for Pb–Pb collisions at $\sqrt{s_{\mathrm{NN}}} = 5.02\,\mathrm{TeV}$ in Figure 4.6. The background arises from tracks incorrectly matched from the ITS+TPC to TOF. The TOF detector provides effective kaon/pion separation up to momenta of 2.5 GeV/c, whereas for proton/kaon, it extends up to 4 GeV/c.

4.2.4 V0 detector

The V0 detector[94, 93] consists of two arrays of scintillator counters, V0A and V0C, respectively. The V0A (V0C) arrays provide full coverage across the azimuthal angle and

specific pseudorapidity ranges of $2.8 < \eta < 5.1$ (-3.7 $< \eta <$ -1.7). Each array is divided into four radial rings, with each ring further subdivided into eight azimuthal sections, resulting in 32 sections. The V0 detector serves many purposes that are essential for the experiment.

It provides minimum bias and high multiplicity trigger and helps to reject interactions between the beam and any residual gas within the vacuum chambers. Furthermore, it is used to measure the luminosity and the charged particle multiplicity, whereas the latter is essential for determining the centrality of a nucleus-nucleus collision. Thanks to its segmentation, the V0 detector allows the extraction of an experimental estimate of the underlying reaction plane in a heavy-ion collision. This information is important for numerous anisotropic flow analyses.

4.2.5 Zero Degree Calorimeter

The Zero Degree Calorimeter (ZDC)[95, 96] consists of two identical sets of hadronic calorimeters located on either side of the experiment. They allow the measurement of spectator nucleons, which are used for event triggering and centrality determination.
The spectators measured in ALICE consist of neutrons and protons, measured in the neutron and proton ZDC calorimeters. On the other hand, spectators bound to nuclear fragments are not measured in these detectors. This is due to their varying charge-to-mass ratio, which leads to a deflection of the fragments away from the ZDC calorimeters. The schematic view of the position of the ZDCs relative to the interaction point is shown in Figure 4.7 on the right-hand side. They are located $\approx$ 115m away from the interaction point inside the LHC tunnel and cover a pseudorapidity region of $|\eta| > 8.8$.

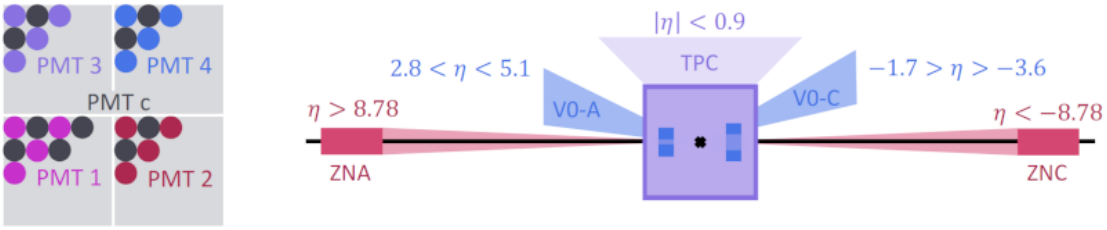

Figure 4.7: [Left panel] Schematic view of the segmenation of the neutron ZDC. The circles correspond to the individual quarz-fibers used to read out the signal. The colors correspond to the channel its associated to. [Right panel] Schematic view of the relative position of the ZDC detector to the central barrel of the ALICE experiment.

The ZDC employs a detector technology based on quartz-fiber calorimeters, often called ”spaghetti” calorimeters. When a spectator particle traverses the calorimeter, it initiates a

shower within the dense absorber material (commonly referred to as passive material).[2] Charged particles generated within the hadronic shower emit Cherenkov radiation in the quartz fibers (the active material) embedded within the absorber material. Cherenkov-based calorimeters have the advantage of providing a very fast response time thanks to the intrinsic speed of the emission process. This is utilized in the ALICE experiment to discard parasitic collisions that do not originate from the collisions of the two primary bunches at the LHC [97].

Both sets of calorimeters are divided into four segments. In each segment, only half of the quartz fibers are associated with that specific segment, while the other half is directed to a shared photomultiplier. This is illustrated for the neutron calorimeter on the left-hand side of Figure 4.7. The information on the shared channel is a complementary measurement of the shower energy and is used to calibrate the detectors.

The proton calorimeter, known as ZPA and ZPC, is positioned 19 cm away from the beam axis on the outgoing beam side and has dimensions of 20.8 x 12 x 150 cm^3. However, it is important to note that due to the influence of the quadrupole magnets in the LHC, the measured proton spot is no longer Gaussian in shape and becomes defocused in the horizontal direction. Consequently, the proton calorimeter is segmented only in the horizontal direction to effectively capture this non-Gaussian energy distribution.

The neutron ZDC, consisting of ZNA and ZNC, has a transverse size of 7x 7 cm^2 and a length of 100 cm. It is mounted on a raisable platform to account for the beam crossing angle of the two LHC beams. Unlike the proton ZDC, the neutron ZDC is segmented in the x- and y-directions perpendicular to the beam axis, employing a 2x2 scheme. This segmentation allows us to estimate the centroid position of the spectator neutrons, thereby allowing the determination of the spectator plane angle. This information is essential for the analysis of anisotropic flow within the experiment.

The composition of spectators varies depending on the centrality of the collision. In central collisions, relatively few spectators are created. As one moves towards mid-central collisions, the number of neutron spectators increases. However, in peripheral collisions, the overall number of spectators increases, but the number of neutron spectators decreases because most neutrons become bound to nuclear fragments. This ambiguity in the neutron spectator numbers between central and peripheral collisions is problematic for the centrality determination using the ZDCs and requires additional measurements. These additional measurements are provided by a third calorimeter, called ZEM, measuring the energy carried by photons. The ZEM calorimeter is located at forward rapidity with $4.8 < \eta < 5.7$ and is positioned approximately 7.35 meters away from the interaction point.

[2]The neutron calorimeter uses a tungsten absorber, whereas for the proton calorimeter brass was used as passive material.

4.2.6 Trigger system

The Central Trigger Processor (CTP) [98] makes the decision to store a collision. The trigger system evaluates inputs from the trigger detectors every 25 nanoseconds, synchronized with the LHC machine clock cycle. When the trigger requirements are met, a trigger signal is sent to the readout detectors. Due to the varying readout times of different detectors, the trigger system is divided into three levels. The Level-0 (L0) trigger is provided by fast detectors such as the SPD and V0 detectors. Its decision is made approximately 0.9 microseconds after the collision. Events accepted by the L0 trigger are further evaluated by the Level-1 (L1) trigger. The L1 trigger decision is made after $\approx 6.5\mu s$, caused by the computation time of the Transition Radiation detector (TRD) and propagation time to the ZDC.
The final trigger level, Level-2 (L2), makes its decision approximately 100 microseconds after the collision, which corresponds to the estimated maximum drift time of the TPC detector. If the L2 trigger is accepted, the event data is transmitted to the Data Acquisition System (DAQ) and the High-Level Trigger system (HLT). In the HLT, a rapid event reconstruction is performed, serving as the final decision to store the event data on tape.
The trigger used in this analysis is a minimum bias (MB) trigger. It can be subdivided into an MBand and MBor trigger. The MBore trigger requires a signal in the V0 and SPD detectors, whereas the MBand trigger requires a signal in both V0 detectors.

4.3 Track and vertex reconstruction

The track finding algorithm, schematically depicted in Figure 4.8, starts with the clusterization step. During this step, the raw detector data are converted into ”clusters” that are characterized by their positions, signal amplitudes, signal times, and associated error information. The clusterization is performed separately for each detector [80]. In the next step, a preliminary interaction vertex is determined using the SPD layers of the ITS. This vertex is identified as a space point where a maximum number of tracklets converge. In cases where no space point is found through this procedure, which particularly occurs in low-multiplicity events, a one-dimensional search along the beam axis is conducted to locate the vertex.
Once a preliminary interaction vertex is located, the track reconstruction proceeds in three stages, following an inward-outward-inward scheme [99], using the Kalman filter technique [100].

The first inward stage initiates by identifying tracks in the TPC, with the track search starting at the outer radius of the TPC, where the track density is low. Track seeds are constructed using either two TPC clusters and the preliminary interaction vertex or multiple TPC clusters without the preliminary vertex. These seeds are propagated inwards and updated with each nearest cluster until they reach the inner TPC radius. To prevent the reconstruction of the same physical track multiple times, a dedicated algorithm is used, which considers the number of shared clusters. Generally, the number of TPC clusters

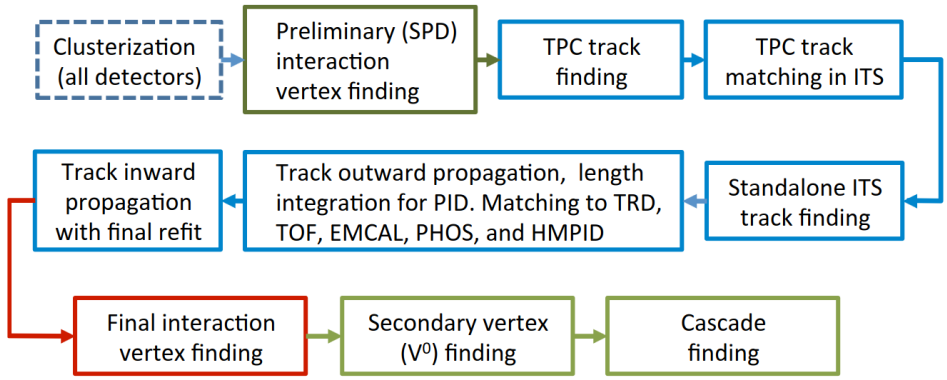

Figure 4.8: Flow chart of the central barrel event and track reconstruction in ALICE during Run 2 [80].

used for the track reconstruction is a quality indicator for the track itself. Additionally, in this step, preliminary particle identification is performed based on the specific energy loss in the TPC.
Reconstructed TPC tracks are then propagated to the SSD, serving as track seeds for the track-finding process within the ITS. These seeds are propagated inward and updated at each ITS layer, considering all clusters within predefined proximity selection criteria. This results in a ”tree” of track hypotheses in the ITS for each reconstructed track in the TPC. The highest quality candidate from each tree, determined based on the reduced χ^2 value, is then added to the reconstructed TPC track. For low-momentum tracks, a standalone ITS reconstruction is performed using clusters not used in the ITS-TPC tracking procedure. Seeds for these standalone ITS reconstructions are constructed using two clusters in the innermost layers of the ITS and the primary vertex. These seeds are propagated to the other layers and updated with clusters within a proximity selection criteria.

Following the reconstruction in the ITS, all tracks are extrapolated to their point of closest approach to the preliminary primary vertex, and the outward propagation is carried out. The tracks are refitted with the Kalman filter approach using the clusters found in the previous steps. Additionally, the tracks are matched with potential clusters in the TOF detector and tracklets in the TRD (Transition Radiation Detector). Afterward, tracks are matched with signals in the EMCal (Electromagnetic Calorimeter), PHOS (Photon Spectrometer), and HMPID (High Momentum Particle ID) detectors, concluding the outward tracking.

In the final step, the reconstructed tracks are once again propagated inwards, and the tracks are refitted using the clusters identified in the previous step. The final track position, direction, and associated covariance matrix are estimated during these steps. Tracks reconstructed in the ITS and TPC are then used to determine the final interaction vertex by extrapolating all tracks to their points of closest approach to the nominal beamline. In low-multiplicity events, the vertex-finding process is improved by constraining the fit to the nominal beam position and size.

Following track and interaction vertex reconstruction, a search is conducted for secondary vertices resulting from particle decays. After selecting potential tracks, the distance of the closest approach between pairs of such tracks is calculated and compared to the position of the primary vertex.

4.4 Centrality determination

Centrality is an experimental measure that characterizes the degree of overlap between two heavy ions during a collision. It is defined on a percentage scale, where 0% corresponds to a situation of full overlap (central collisions), and 100% corresponds to no overlap (peripheral collisions).
The centrality relative to the impact parameter b, which is defined as the distance between the centers of the two colliding nuclei, can be expressed as follows:

$$c(b) = \frac{\int_0^b \frac{\mathrm{d}\sigma}{\mathrm{d}b'}\mathrm{d}b'}{\int_0^\infty \frac{\mathrm{d}\sigma}{\mathrm{d}b'}\mathrm{d}b'} = \frac{1}{\sigma_{\mathrm{AA}}}\int_0^b \frac{\mathrm{d}\sigma}{\mathrm{d}b'}\mathrm{d}b' \tag{4.1}$$

with σ_{AA} defined as the total hadronic interaction cross-section. The impact parameter b is not directly measurable in the experiment. Therefore, the centrality is defined experimentally as the percentile of the hadronic cross-section corresponding to the number of charged particles (N_{ch}) above a certain threshold (N_{ch}^{thr}).

$$c \approx \frac{1}{\sigma_{\mathrm{AA}}}\int_{N_{\mathrm{ch}}^{thr}}^\infty \frac{\mathrm{d}\sigma}{\mathrm{d}N_{\mathrm{ch}}}\mathrm{d}N_{\mathrm{ch}} \approx \frac{1}{N_{ev}}\int_{N_{\mathrm{ch}}^{thr}}^\infty \frac{\mathrm{d}n}{\mathrm{d}N_{\mathrm{ch}}}\mathrm{d}N_{\mathrm{ch}} \tag{4.2}$$

where in the second approximation the cross section $\mathrm{d}\sigma$ is replaced by the number of observed events n, corrected for trigger efficiency and for the non-hadronic interaction background [101].

Geometric parameters of the collision, such as the number of participating nucleons (N_{part}), the number of binary collisions (N_{coll}), and the impact parameter (b), can be extracted for a given centrality class by comparing the measured multiplicity distributions with model calculations. One of the multiplicity estimators N_{ch} used in ALICE for Pb–Pb collisions is the sum of signals measured in both V0 detectors. To extract the geometric parameters for collisions in a specific centrality, the multiplicity distribution is fitted with a Monte Carlo (MC) Glauber model coupled to a simple model of particle production per source based on a negative binomial distribution (NBD) [101, 102]. The NBD describes the particle multiplicity per nucleon–nucleon collision. The number of particle-emitting sources is parameterized as $f \cdot N_{\mathrm{part}} + (1-f) \cdot N_{\mathrm{coll}}$, inspired by a two-component model that decomposes nucleus–nucleus interactions into soft and hard interactions [103]. The parameter f describes the fraction of soft interactions. The number of particles produced per source is described by the negative binomial distribution:

$$P_{\mu,k}(n) = \frac{\Gamma(n+k)}{\Gamma(n+1)\Gamma(k)} \cdot \frac{(\mu/k)^n}{(\mu/(k+1)^{n+k})}, \tag{4.3}$$

which gives the probability of measuring n particles per source, with μ the mean number of particles produced per source and k the width of the distribution.

The multiplicity computed through this method is fitted to the measured V0 multiplicity, and the free parameters f, μ, and k are determined by minimizing the χ^2 of the fit. Collisions with low V0 multiplicity are excluded from the fit since electromagnetic background events may contaminate them. The centrality definition based on the signal measured by the V0 signal may be biased compared to a selection based on the impact parameter due to the fluctuations in the V0 multiplicity. However, this bias is found to be small in the centrality range relevant for this thesis, as discussed in Ref. [102].

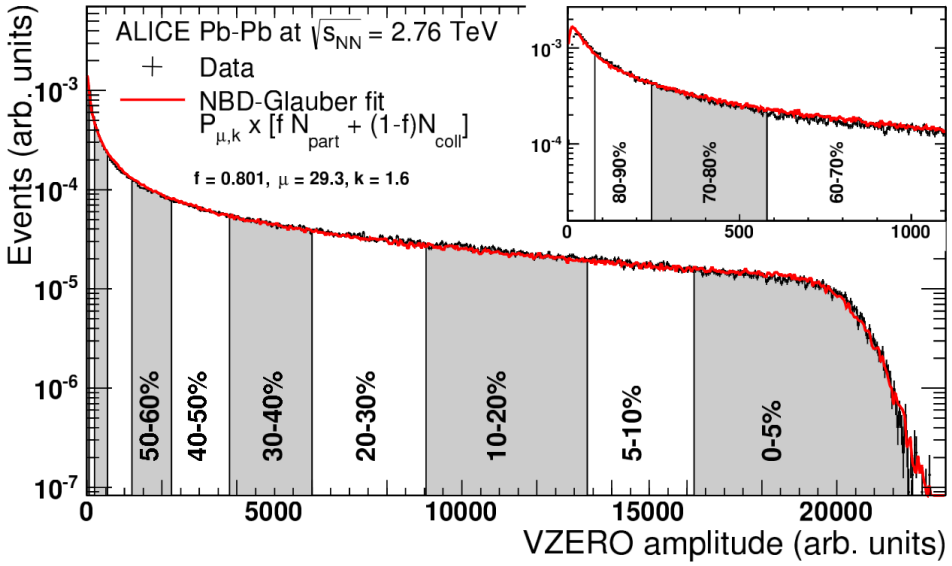

Figure 4.9: Distribution of the sum of both V0 signals in Pb–Pb collisions at $\sqrt{s_{\mathrm{NN}}} = 2.76\,\mathrm{TeV}$. The red line corresponds to the NBD-Glauber fit. Figure taken from [102].

Figure 4.9 displays the sum of signals in both V0 detectors for Pb–Pb collisions at $\sqrt{s_{\mathrm{NN}}} = 2.76\,\mathrm{TeV}$, along with the NBD-Glauber fit represented by the red line.

5 Parametrization of the specific energy loss in the ALICE TPC

Charged particles traveling through a medium will lose part of their energy by excitation or ionization of the medium's atoms. In the excitation process, an electron bound to an atom gains enough energy to transition to a higher energy state, resulting in an excited atom. In the ionization process, the electron acquires enough energy to break free from the atom. The mean energy loss of a charged particle per path length $\langle \mathrm{d}E/\mathrm{d}x \rangle$ is described by the Bethe-Bloch formula [104]. The ALICE TPC [88] measures the induced charge on the readout pads created by the drifting electrons after the amplification stage in the readout chambers. The ionization clusters are used for track reconstruction and, when combined with a momentum measurement p, allow for particle identification.

The Bethe-Bloch formula describes the energy loss in an ideal, large medium and only depends on the incident particle $\beta\gamma$. In reality, for a detector such as the ALICE TPC, additional factors influence the energy loss, introducing dependencies on variables such as the pseudorapidity η of the particle track and the detector occupancy. This became particularly important during the collection of Pb–Pb data in 2018, which were recorded at interaction rates as high as 8 kHz. To address this challenge, special treatment of the data was necessary, including a track-by-track correction to account for pileup events. The parametrization of the specific energy loss in the Pb–Pb 2018 data set, which was a part of my service work for the ALICE collaboration, will be discussed in detail in the following sections.

5.1 Specific energy loss of charged particles in matter

Charged particles, as they travel through a medium, transfer a portion of their energy through processes like ionization and excitation. The average energy loss per path length $\langle \mathrm{d}E/\mathrm{d}x \rangle$ for particles more massive than electrons (from now on referred to as "heavy" particles) is described by the Bethe-Bloch formula. A first calculation using classical methods were done already 1913 by Bohr [105]. A quantum mechanical treatment of the problem, provided by the work of Bethe [104, 106] and Bloch [107, 108] in the 1930s, remains largely valid to this day. For moderately relativistic charged heavy particles, the Bethe-Bloch formula is expressed as follows [109]:

$$-\left\langle \frac{\mathrm{d}E}{\mathrm{d}x} \right\rangle = K\frac{Z}{A}\frac{z^2}{\beta^2}\left[\frac{1}{2}\ln(\frac{2m_e c^2\beta^2\gamma^2 W_{\max}}{I^2}) - \beta^2 - \frac{\delta(\beta\gamma)}{2}\right] \tag{5.1}$$

$$K = 4\pi N_A r_e^2 m_e c^2 = 0.307075\,\mathrm{MeV\,mol^{-1}\,cm^2}$$

$$W_{\max} = \frac{2m_e c^2\beta^2\gamma^2}{1 + 2\gamma m_e/M + (m_e/M)^2}$$

This formula holds within the kinematic range of $0.1 < \beta\gamma < 1000$. In the equations, K represents a constant, Z and A denote the atomic number and mass of the absorber material, respectively, z is the charge number of the incident particle, $W_{\max}$ represents the maximum energy transfer from a heavy particle to an electron in a single collision, and I stands for the mean excitation energy of the atom. Values for I are estimated based on experimental stopping-power measurements for protons, deuterons, and alpha particles, along with oscillator-strength distributions and dielectric-response functions [109].

For a specific absorber material, the Bethe-Bloch formula only depends on the values of $\beta\gamma$ and the charge of the incident particle. As $\beta\gamma$ increases, $\langle \mathrm{d}E/\mathrm{d}x \rangle$ decreases proportional to $1/\beta^\alpha$, where α lies around 1.4-2. The exact value of α depends on the mass of the incident particle and the atomic number Z of the medium. The incident particle velocity increases with $\beta\gamma$, resulting in a shortened interaction time with the electric field of the atom or molecule, consequently reducing the energy loss to the medium. Around $\beta\gamma =$ 3-4, a broad minimum is reached, which is mostly independent of the absorber material. Particles in this region are usually referred to as minimum ionizing particles (MIP), where the $\langle \mathrm{d}E/\mathrm{d}x \rangle$ exhibits a constant value for a given medium. This characteristic can be used for an absolute calibration of the $\langle \mathrm{d}E/\mathrm{d}x \rangle$ in an experiment.

As $\beta\gamma$ continues to rise, there is a logarithmic increase in $\langle \mathrm{d}E/\mathrm{d}x \rangle$, driven by two independent mechanisms. Firstly, the maximum energy $W_{\max}$ transferred to electrons in a single collision increases proportionally with $\beta^2\gamma^2$, thereby increasing the term in the logarithm. The second effect is produced by the explicit $\beta^2\gamma^2$ dependency inside the logarithm. This is due to the increase of the transverse electric field of the relativistic particle moving in the medium due to Lorentz contraction, introducing long-range contributions to the energy loss. This region is usually referred to as the relativistic rise.
In reality, the impact of the second effect is partly reduced by the polarization of the absorber medium, effectively shielding the electric field contributions far from the path of the incident particle. The amount of shielding depends on the density of the medium and is described by the density correction $\delta(\beta\gamma)$ in Equation (5.1) introduced by Enrico Fermi [110]. A parametrization of $\delta(\beta\gamma)$ for different media can be found in [111].

The mean energy loss for muons in copper is shown in Figure 5.1 across a broad spectrum of $\beta\gamma$. The Bethe-Bloch formula, shown in Equation (5.1), holds effectively within the blue

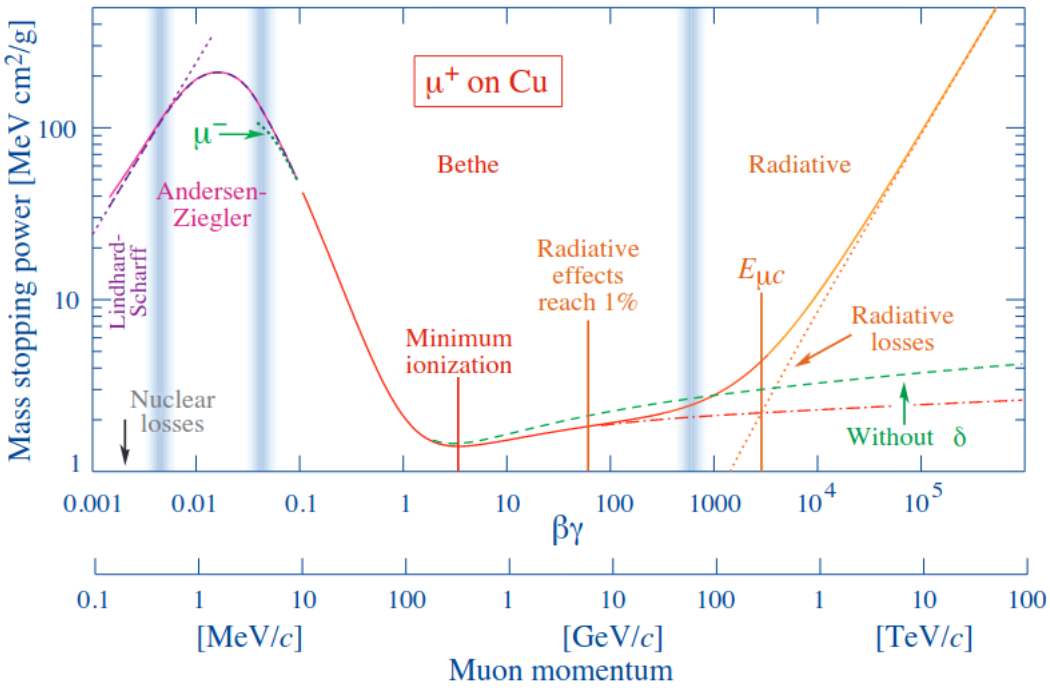

Figure 5.1: Mean energy loss for positive muons in copper as a function of $\beta\gamma$ over nine orders of magnitudes in momentum of the incoming particle. Picture taken from [109].

bands at $\beta\gamma \approx 0.1$ and $\beta\gamma \approx 1000$. For very low $\beta\gamma$ (< 0.1), the velocity of the incident particle is comparable with the orbital velocity of the electrons breaking the assumption of free electrons, assumed by the Born approximation used by Bethe to estimate the particle's energy loss. At much higher $\beta\gamma$, additional mechanisms become important, such as radiative processes like bremsstrahlung. The energy threshold at which bremsstrahlung surpasses ionization depends on the mass of the charged particle. While for electrons this regime starts already at momenta of 20-200 MeV/c, for muons and pions this occurs only at several hundreds of GeV/c. The Bethe-Bloch formula, as shown in Equation (5.1), only applies to particles more massive than the electron. This is due to the assumption made in the calculation of W_{max} that the mass of the incident particle is larger than the electron mass. Moreover, for electrons, the quantum mechanical effect of indistinguishability must be considered, while for positrons, the annihilation processes with electrons in the absorber material become important, especially at low $\beta\gamma$. The observed differences in energy loss between electrons and protons due to these effects are of the order of 10% [112].

As previously explained, the term W_{max} is directly proportional to $\beta\gamma$. This implies that for charged particles with higher energies, W_{max} increases, allowing the production of increasingly energetic electrons. These electrons, usually referred to as δ electrons, can attain energies sufficient to ionize the material on their own. In some cases, it becomes difficult to attribute their energy contribution to the original charged particle. This could

be due to δ electrons leaving the detector, especially important for very thin detectors, or their range in the material being larger compared to the size of the pick-up electrodes. The latter can result in the tracking algorithms in the experiment recognizing these electrons as independent tracks [113]. The modified Bethe-Bloch formula, including energy losses up to a maximum energy transfer per single collision W_{cut}, is expressed as follows:

$$-\left\langle \frac{dE}{dx} \right\rangle = K\frac{Z}{A}\frac{z^2}{\beta^2}\left[\frac{1}{2}ln(\frac{2m_e c^2\beta^2\gamma^2 W_{\mathrm{cut}}}{I^2}) - \frac{\beta^2}{2}\left(1+\frac{W_{\mathrm{cut}}}{W_{\mathrm{max}}}\right) - \frac{\delta(\beta\gamma)}{2}\right] \tag{5.2}$$

In this modified formula, W_{cut} replaces W_{max} in the logarithmic term, resulting in the $\beta\gamma$ contribution from W_{max} being replaced by a constant factor. It has been demonstrated (e.g., [113]) that in the limit of $\beta \to 1$, replacing W_{cut} with W_{max} completely cancels the relativistic rise, and the mean energy loss converges to a constant value, known as the Fermi-Plateau.

5.2 Fluctuations of the specific energy loss

Up to this point, the discussion has primarily centered on the average energy loss, neglecting the statistical variations around its mean value. In fact, the energy loss via ionization is of statistical nature, resulting in fluctuations. When a charged particle travels a distance Δx, its energy loss ΔE is composed of numerous individual ionization or excitation events, each characterized by an energy loss of δE_i:

$$\Delta E = \sum_{i=1}^{N} \delta E_i. \tag{5.3}$$

Statistical fluctuations can arise both in the total number of ionization/excitation processes, which follow a Poisson distribution and in the energy loss within each of these processes, characterized by a $1/E^2$ distribution. These lead to fluctuations in the energy loss of a charged particle, commonly referred to as Landau fluctuations.

The energy loss ΔE over a fixed distance Δx is governed by a probability density $f(\Delta E;\Delta x)$, normalized in an interval between the minimal and maximal energy transfer:

$$\int_{\Delta E_{min}}^{\Delta E_{max}} f(\Delta E;\Delta x)d\Delta E = 1 \tag{5.4}$$

In the case of statistically independent individual contributions δE_i to ΔE, the central limit theorem states that for $N \to \infty$, ΔE becomes normally distributed with a variance that is N times the variance of the individual processes [112]. However, this limit is never reached for relativistic particles.
Generally, fluctuations in the energy transfer of individual collisions along the particle's path lead to an asymmetric distribution of $f(\Delta E;\Delta x)$. It has a Gaussian part corresponding to several ionization processes with small energy loss and a tail toward large energy loss

values. Large energy losses correspond to rarely occurring hard collisions in which a δ electron is produced. One can distinguish between the most probable value of the energy loss (the maximum of the distribution) and the average value of $\langle \mathrm{d}E/\mathrm{d}x \rangle$ located to the right of the most probable value, depending on the asymmetry of the distribution and the number of sampled measurements.

The exact form of the distribution depends on the ratio of the mean energy loss given by the Bethe-Bloch formula and the maximum energy loss $W_{\max}$ (Equation (5.1)). An approximation of this ratio was introduced by Vavilov with the parameter κ [114]:

$$\kappa = \frac{\xi}{W_{\max}} \tag{5.5}$$

where $\xi = \frac{1}{2} K \frac{Z}{A} \rho \frac{z^2}{\beta^2} \Delta x$ is the factor in front of the Bethe-Bloch formula multiplied by the path length Δx.
Two limiting cases can now be defined: for $\kappa \geq 1$, the probability density $f(\Delta E; \Delta x)$ is of Gaussian form, whereas for small values of κ, the distribution is highly asymmetric. During the data taking period in the year 2018, the TPC was filled with a mixture of argon and CO_2. For the case of protons with a total energy of 5 GeV traversing 1 m of argon gas, κ is in the order of 0.003.

A first analytic form of the energy loss distribution was described by Landau [115] for thin layers of material (corresponding to small values of κ). This Landau distribution is defined as the definite integral:

$$f(\lambda) = \frac{1}{\pi} \int_0^\infty e^{-t \ln(t) - \lambda t} \sin(\pi t) \mathrm{d}t \tag{5.6}$$

where the parameter λ is defined as the deviation of the energy loss ΔE from the most probable value ΔE_{MP}, normalized to the width of the distribution ξ as defined above:

$$\lambda = \frac{\Delta E - \Delta E_{MP}}{\xi} \tag{5.7}$$

The Landau distribution is shown in Figure 5.2. The consequences of these fluctuations on the $\langle \mathrm{d}E/\mathrm{d}x \rangle$ measurements in the ALICE TPC are described in the next section.

5.3 Measurment of the specific energy loss in the ALICE TPC

In the ALICE TPC, a track is reconstructed from a certain number of ionization clusters formed along the particle trajectory. In the case of the ALICE TPC, up to 159 clusters could be associated with a track, and this number was reduced to 152 after the TPC readout system upgrade for Run 3 of the ALICE operation. Each cluster corresponds to one of the pad rows in the readout. As charged particles traverse the detector, they ionize the

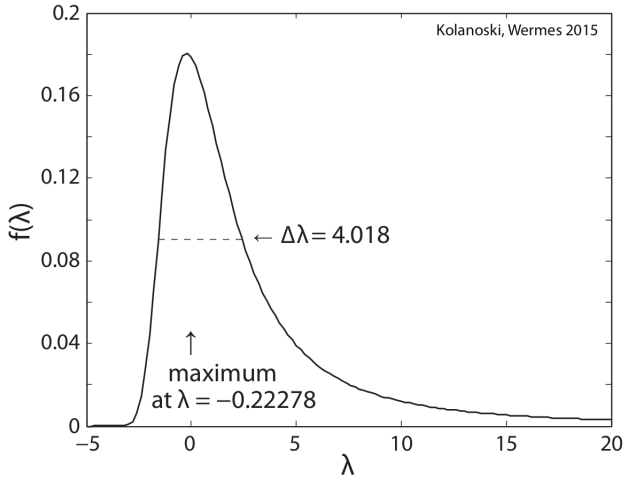

Figure 5.2: Example of a Landau distribution as defined in Equation (5.6). Also shown are the position of the maximum and the full width $\Delta\lambda$ at half maximum of the distribution. The figure was taken from [112].

gas, and the resulting ionization electrons drift towards the readout chambers under the influence of the electric field, as described in Section 4.2.2. Within the readout chambers, these electrons undergo amplification and induce a charge on the pad plane. The pad plane is organized into pads in rows, and a passing track induces a charge ΔQ in each row. This charge increment can be correlated with the deposited energy, ΔE, following a series of calibration steps. The effective track length, Δx, varies with the polar angle Θ of the particle track relative to the readout plane, as shown in Figure 5.3.

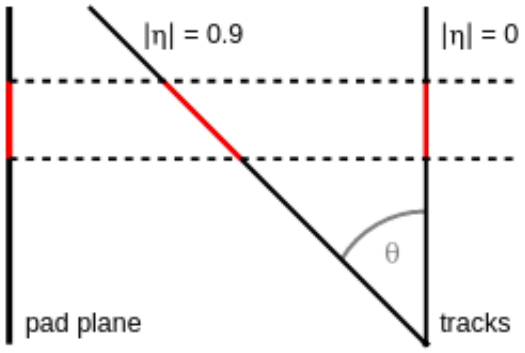

Figure 5.3: Influence of the polar angle Θ of the particle trajectory on the effective track length per pad.

On the left-hand side of the figure, the red line represents one pad row. Depending on the polar angle of the particle trajectory, this pad row observes a different length portion of the track (shown also in red for the two particle tracks). The combination of ΔE measured in a

pad row and the track length Δx allows for the calculation of a single measurement for the specific energy loss $(\frac{\Delta E}{\Delta x})_i$ for the individual cluster. The energy loss distribution of many single measurements follows a Landau distribution as described before. The individual measurements of the specific energy loss for each cluster assigned to a particle track are then combined to a global $\langle \mathrm{d}E/\mathrm{d}x \rangle$ value assigned to the corresponding particle track.

A straightforward approach to calculate the global $\langle \mathrm{d}E/\mathrm{d}x \rangle$ is to take the average overall individual measurements per pad row. However, this method may result in an unreliable estimator, as each reconstructed particle track can have a maximum of 159 specific energy loss measurements, leading to a poorly sampled Landau distribution, particularly in the tail. Consequently, this results in large fluctuations in the global $\langle \mathrm{d}E/\mathrm{d}x \rangle$ value assigned to a particle track on a track-by-track basis, negatively impacting the detector's performance. To mitigate these fluctuations, the higher end of the cluster $\langle \mathrm{d}E/\mathrm{d}x \rangle$ distribution, particularly in the poorly populated tail, is removed. This is achieved by computing the "truncated mean" S_α, which is characterized by the parameter α ranging between 0 and 1. The truncated mean is then defined as the average over the m = αn lowest values among the n single measurements $(\frac{\Delta E}{\Delta x})_i$:

$$S^\alpha = \frac{1}{m} \sum_{i=0}^{m} (\frac{\Delta E}{\Delta x})_i \tag{5.8}$$

with $(\frac{\Delta E}{\Delta x})_{i-1} < (\frac{\Delta E}{\Delta x})_i$. For the ALICE TPC, a value of α = 0.6 was selected. The $\langle \mathrm{d}E/\mathrm{d}x \rangle$ distribution for many clusters, when computed using the truncated mean method, closely approximates a Gaussian distribution, effectively suppressing the Landau tail, allowing for the extraction of a well defined global $\langle \mathrm{d}E/\mathrm{d}x \rangle$. Henceforth, when referring to $\langle \mathrm{d}E/\mathrm{d}x \rangle$, it will be in the context of the $\langle \mathrm{d}E/\mathrm{d}x \rangle$ obtained through the truncated mean method.

5.4 Parametrization of the specific energy loss for 2018 Pb–Pb

In the ALICE experiment, accurately parametrizing the expected specific energy loss $\langle \mathrm{d}E/\mathrm{d}x \rangle_{\mathrm{exp}}$ is crucial, particularly for particle identification. The nσ variable is a key tool for selecting particle species, which is defined separately for each species as:

$$n\sigma_{\mathrm{species}} = \frac{\langle \mathrm{d}E/\mathrm{d}x \rangle - \langle \mathrm{d}E/\mathrm{d}x \rangle_{\mathrm{exp}}}{\sigma^{\mathrm{res}}_{\mathrm{species}}} \tag{5.9}$$

Here, $\langle \mathrm{d}E/\mathrm{d}x \rangle$ is the measured energy loss of a charged particle in the experiment, and $\langle \mathrm{d}E/\mathrm{d}x \rangle_{\mathrm{exp}}$ is the expected energy loss for a given particle species. For correctly identified particles, the distribution in Equation (5.9) is centered around zero with a width of unity. An inaccurate parametrization of $\langle \mathrm{d}E/\mathrm{d}x \rangle_{\mathrm{exp}}$ can lead to a bias in the believed purity of the particle sample, affecting particle-type dependent analyses, especially in regions where

different particle bands intersect, as shown in Figure 4.5.

One natural choice for the parametrization of $\langle \mathrm{d}E/\mathrm{d}x \rangle_{\mathrm{exp}}$ is the Bethe-Bloch formula (Equation (5.2)). However, in reality, various factors such as pileup, detector acceptance, and signal processing introduce deviations from this ideal scenario and result in dependencies on the energy loss with respect to pseudorapidity (η) and detector occupancy.
During Run 1 and Run 2 of ALICE operations, an assumption was made that various sources contributing to the $\langle \mathrm{d}E/\mathrm{d}x \rangle$ dependency can be factorized (as shown in Equation (5.10)). This allowed the extraction of $\langle \mathrm{d}E/\mathrm{d}x \rangle$ corrections independently for each of these sources. However, it is crucial to note that in reality, the different sources contributing to the $\langle \mathrm{d}E/\mathrm{d}x \rangle$ dependency are correlated to some extent. Correctly handling these correlations would require extracting the parametrization in a multidimensional approach, typically requiring a large amount of data that was not available when the approach was developed. These sources include the $\beta\gamma$ and the pseudorapidity η of the incident particle track, and the occupancy in the TPC.

$$\left\langle \frac{dE}{dx} \right\rangle (p, \eta, N_{tr}) = \left\langle \frac{dE}{dx} \right\rangle_1 (p) \otimes \left\langle \frac{dE}{dx} \right\rangle_2 (\eta) \otimes \left\langle \frac{dE}{dx} \right\rangle_3 (N_{tr}) \tag{5.10}$$

The workflow of the $\langle \mathrm{d}E/\mathrm{d}x \rangle$ parametrization for the ALICE TPC during Run 1 and Run 2 can be divided into several steps:

1. **Data skimming**: The initial step involves reducing the size of the reconstructed data through a physics-motivated downscaling procedure while retaining the full track information for the $\langle \mathrm{d}E/\mathrm{d}x \rangle$ calibration procedure, as outlined in [116]. This "skimmed" dataset enables a quick and adaptive $\langle \mathrm{d}E/\mathrm{d}x \rangle$ calibration, which would be unpractical without such data reduction, given the substantial size of the Pb–Pb dataset recorded in 2018. At this stage, already a first basic event selection is performed.

2. **Clean samples**: From the skimmed data set, clean samples of electrons, pions, kaons, protons, and deuterons are extracted using various particle identification methods. This is achieved by using the track topology, such as neutral particle decays, and the particle identification capabilities of the TPC and TOF, as detailed in Section 4.2.

3. **$\beta\gamma$-dependent parametrization**: Within the clean samples, the Bethe-Bloch parametrization is extracted as a function of the incident $\beta\gamma$. This parametrization is obtained through measurements of the particle type and momentum p following the relation from $\beta\gamma = \frac{p}{mc}$.

4. **Low-momentum correction**: Deviations from the parametrization obtained in the previous step, especially at low momentum, require a particle-type dependent correction. This correction is derived and applied to the previously obtained parametrization to account for these deviations.

5. **η- and multiplicity-dependent correction**: A multiplicative correction, which depends on pseudorapidity and multiplicity, is extracted with respect to the calibration obtained in step 4.

6. **Parametrization of the $\langle \mathrm{d}E/\mathrm{d}x \rangle$ resolution**: The resolution parametrization of the $\langle \mathrm{d}E/\mathrm{d}x \rangle$ is extracted as function of the pseudorapidty and the number of TPC clusters used for the global $\langle \mathrm{d}E/\mathrm{d}x \rangle$ calculation.

7. **Quality assurance**: The parametrization obtained in the previous steps is validated using the $n\sigma$ variable defined in Equation (5.9). Clean samples of electrons, pions, and protons are used for this validation.

8. **Repeat**: Steps 2 to 7 are repeated using the $\langle \mathrm{d}E/\mathrm{d}x \rangle$ values corrected with the parametrization obtained from the previous steps until a satisfactory correct description of the parametrization is reached. This is quantified by comparing the $\langle \mathrm{d}E/\mathrm{d}x \rangle$ parametrization between two consecutive steps, ensuring differences are below 1%. Additionally, step 7 is employed to quantify the performance of the parametrization.

The parametrization procedure is typically stopped after one to four iterations, with the exact number varying depending on the collision system. A detailed description of the $\langle \mathrm{d}E/\mathrm{d}x \rangle$ parametrization can be found in the thesis [117].

In the Pb–Pb data recorded in 2018, the presence of pileup events due to the high interaction rate posed an additional challenge. These pileup events can significantly affect the TPC $\langle \mathrm{d}E/\mathrm{d}x \rangle$ response and thus need to be either discarded or treated. Information from the TPC and ITS is combined for the removal of problematic pileup events, as shown in Figure 5.17.

Part of my service work in the ALICE collaboration aimed at introducing improvements to the parametrization scheme. One improvement involved extracting an individual $\langle \mathrm{d}E/\mathrm{d}x \rangle$ parametrization for deuterons, a change from the previous practice of scaling the $\langle \mathrm{d}E/\mathrm{d}x \rangle$ parametrization of protons based on the mass difference between protons and deuterons. Another improvement included a correction for the bias introduced in the $\langle \mathrm{d}E/\mathrm{d}x \rangle$ measurements by pileup events. Consequently, pileup events could be considered for certain physics analyses, significantly enhancing the available data samples. A detailed understanding of the bias introduced by pileup events, an alternative treatment scheme for addressing these events, and potential adjustments to the parametrization scheme are described in more detail in Section 5.4.6.
In order to improve the clarity of the discussion ahead, the entire parametrization scheme shall be described in the case where problematic pileup events, which are removed using information from the TPC and ITS, are not considered.

5.4.1 Bethe-Bloch parametrization

At the start of the workflow, the $\langle \mathrm{d}E/\mathrm{d}x \rangle$ parametrization is initially extracted as a function of $\beta\gamma$ serving as a reference point for subsequent corrections. The $\langle \mathrm{d}E/\mathrm{d}x \rangle$ as a function of $\beta\gamma$ is modeled using the saturated Lund model. This model is an extension of the Lund model described in [118], with additional parameters p_i where $i = 0...4$, complemented by an additional saturation term $p_5 > 0$:

$$\left\langle \frac{\mathrm{d}E}{\mathrm{d}x} \right\rangle (\beta\gamma) = \exp\left(\frac{-p_5}{\mu(\beta\gamma)}\right) \cdot \mu(\beta\gamma)$$
$$\mu(\beta\gamma) = \frac{p_0}{\beta^{2p_3}} + \frac{p_1}{p_2} \ln\left(\frac{(1+\beta\gamma)^{p_2}}{1+d\cdot(1+\beta\gamma)^{p_2}}\right)$$
$$d = \exp\left(\frac{p_2(p_0-p_4)}{p_1}\right)$$

The saturation term improves the description of the low $\beta\gamma$ region and introduces an additional parameter for fine-tuning the parametrization to the data, as described in [117].

For an optimal fit, data points across a broader range of $\beta\gamma$ are necessary, covering the $1/\beta^2$, minimum ionizing particle (MIP), and relativistic rise regions. To achieve this, clean samples of electrons, pions, kaons, protons, and deuterons are selected as functions of momentum. The particle momentum can be transformed into $\beta\gamma$ using the relation $\beta\gamma = p/mc$.

The selection of different particle species relies on the PID capabilities of ALICE, specifically from the TPC and TOF detectors. At low momenta (< 0.6 GeV/c), a loose selection based on the $\mathrm{n}\sigma^{TPC}_{species}$ with respect to a preliminary $\langle \mathrm{d}E/\mathrm{d}x \rangle$ parametrization is sufficient. In this low-momentum range, the $\langle \mathrm{d}E/\mathrm{d}x \rangle$ separation between different particle species is significant. To extend the momentum range up to 3 GeV/c, the PID capabilities of TOF are used. In this case, a track is required to be within three σ_{TOF} from the expectation ($|n\sigma_{TOF}|$). The particles identified using these techniques are presented in Figure 5.4 and Figure 5.5.

To obtain clean samples of electrons, pions and protons even above 3 GeV/c, tracks are selected on the base of their topology, namely originating from decays of V^0s[1]. The following V^0s were considered and selected using the Armenteros-Podolanski variables [119]:

- $\gamma \to e^+e^-$
- $K^0_s \to \pi^+\pi^-$

[1] V^0s are neutral particles decaying into two charged particles.

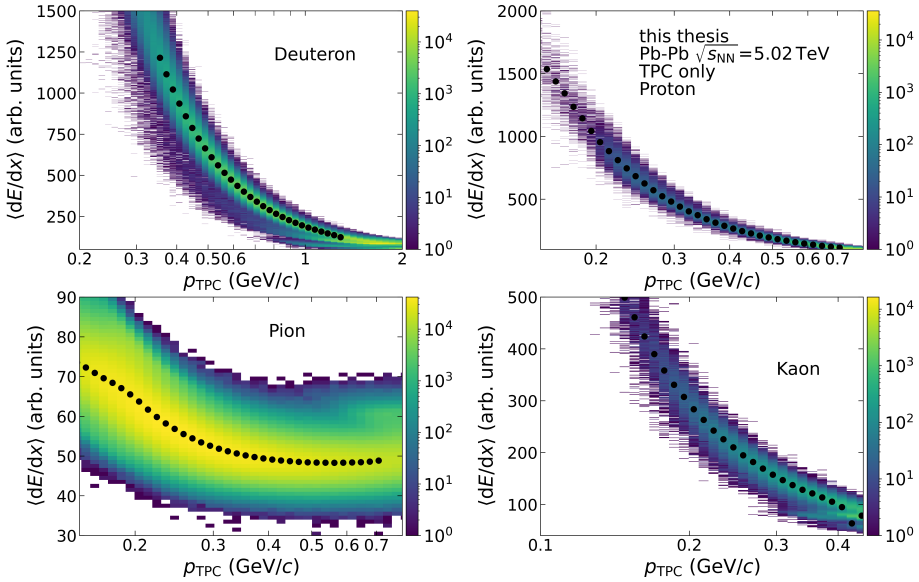

Figure 5.4: $\langle \mathrm{d}E/\mathrm{d}x \rangle$ versus particle momentum p for deuterons, protons, pions, and kaons selected via a broad inclusion cut in the TPC. Note the different particle momentum ranges for the different particle species.

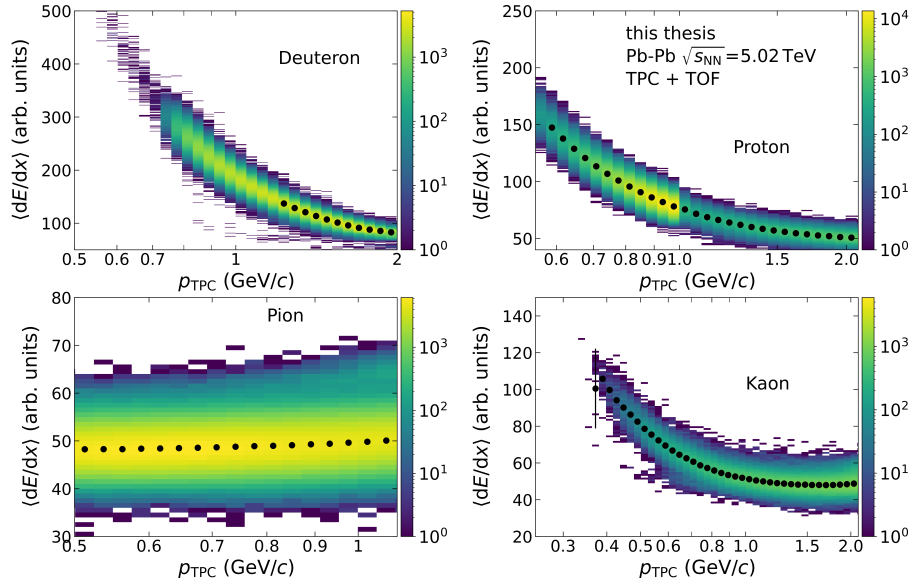

Figure 5.5: $\langle \mathrm{d}E/\mathrm{d}x \rangle$ versus particle momentum p for different particle species selected via an inclusion cut in the TPC and TOF. Note the different particle momentum ranges for the different particle species.

- $\Lambda \rightarrow p\pi^-$
- $\overline{\Lambda} \rightarrow \overline{p}\pi^+$

In addition to the selection based purely on the topology of the tracks, an additional

criterion is applied by considering the nσ_{TOF} to further refine the track sample. The track candidates selected using these two methods are shown in Figure 5.6 and Figure 5.7.

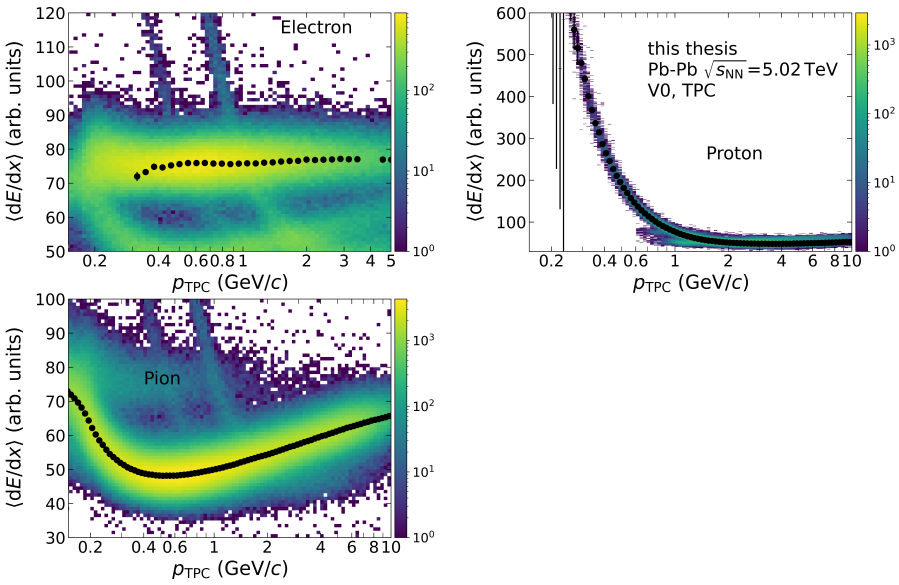

Figure 5.6: $\langle \mathrm{d}E/\mathrm{d}x \rangle$ versus momentum p for electrons, pions, and protons selected using V^0s (photoconversions, K^0_s and $\Lambda(\overline{\Lambda})$).

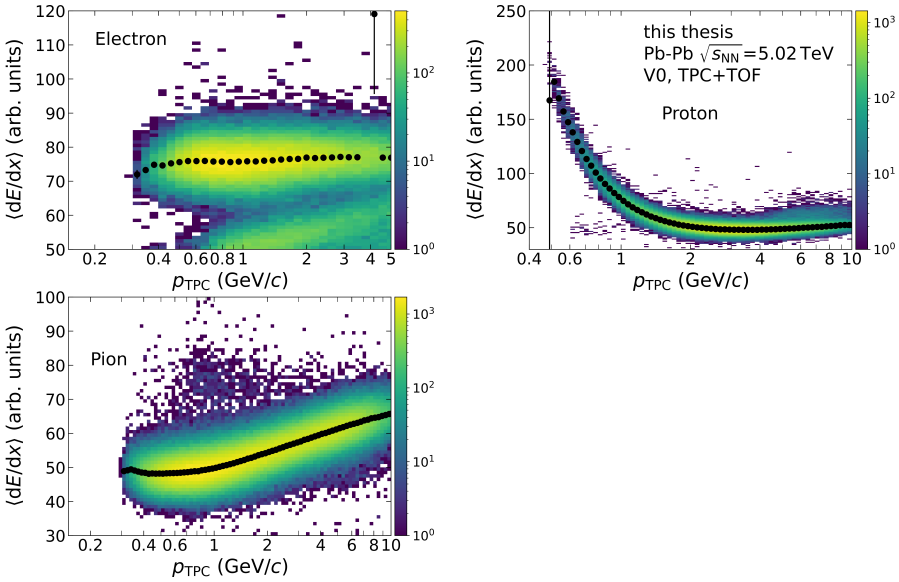

Figure 5.7: $\langle \mathrm{d}E/\mathrm{d}x \rangle$ versus momentum p for electrons, pions, and protons using V^0s (photoconversions, K^0_s and $\Lambda(\overline{\Lambda})$) and an additional inclusion cut in TOF.

With these clean selections, it becomes possible to extract the mean $\langle \mathrm{d}E/\mathrm{d}x \rangle$ as a function of momentum, which can subsequently be converted to $\beta\gamma$ since the mass of the particle

is known. The $\langle dE/dx \rangle$ distributions shown in Figure 5.4 - Figure 5.7 are sliced in fine momentum bins and fitted with a Gaussian function to extract the mean $\langle dE/dx \rangle$. An example of such a momentum slice is shown in Figure 5.8 for protons originating from decays of Λ and $\overline{\Lambda}$, in the momentum range of 1.8 GeV/c and 2.0 GeV/c.

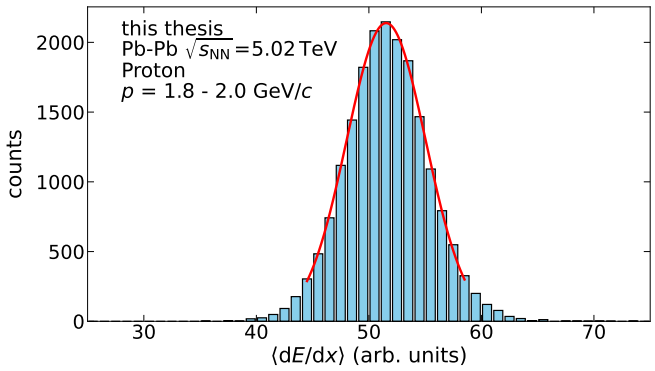

Figure 5.8: $\langle dE/dx \rangle$ distribution of protons from V^0 decays with momentum p = 1.8-2.0 GeV/c together with the Gaussian fit to extract the mean $\langle dE/dx \rangle$.

Despite the fact that the $\langle dE/dx \rangle$ associated with a track is extracted using the truncated mean method, the $\langle dE/dx \rangle$ distribution still shows small tails towards higher $\langle dE/dx \rangle$. To address this, the Gaussian fit is only performed considering $\langle dE/dx \rangle$ bins with at least 10% of the maximum value. The black markers represent the mean $\langle dE/dx \rangle$ extracted from the Gaussian fit as a function of momentum, and these values are converted to $\beta\gamma$ using the corresponding particle mass.

The average energy loss as a function of $\beta\gamma$ extracted from electron, kaon, pion, proton and deuteron samples for different selection criteria is shown together with the fit of the Bethe-Bloch parametrization in the top panel of Figure 5.9. The mean $\langle dE/dx \rangle$ values obtained through different identification techniques for the same particle type show no significant differences and are compatible with each other.

Despite the small differences in the identification techniques, only data points that yield the purest sample of the particle of interest are considered for the Bethe-Bloch fit. For electrons, pions, and protons, the purest samples are obtained from V^0 decays. In the case of deuterons, in the absence of a decay, only a loose selection using the $n\sigma^{TPC}$ was applied. The data points used for the fit are indicated as red markers in the top panel of Figure 5.9.

The data points in Figure 5.9 span over five orders of magnitude in $\beta\gamma$, effectively constraining all the crucial regions of the Bethe-Bloch curve. Deuterons are used to constrain the fit at low $\beta\gamma$ values, where the $\langle dE/dx \rangle$ rises with $1/\beta^2$. Protons and pions, on the other hand, contribute to constrain the fit near the MIP region, while electrons serve as constraints around the Fermi plateau, $\beta\gamma \approx \mathcal{O}(10^3)$.

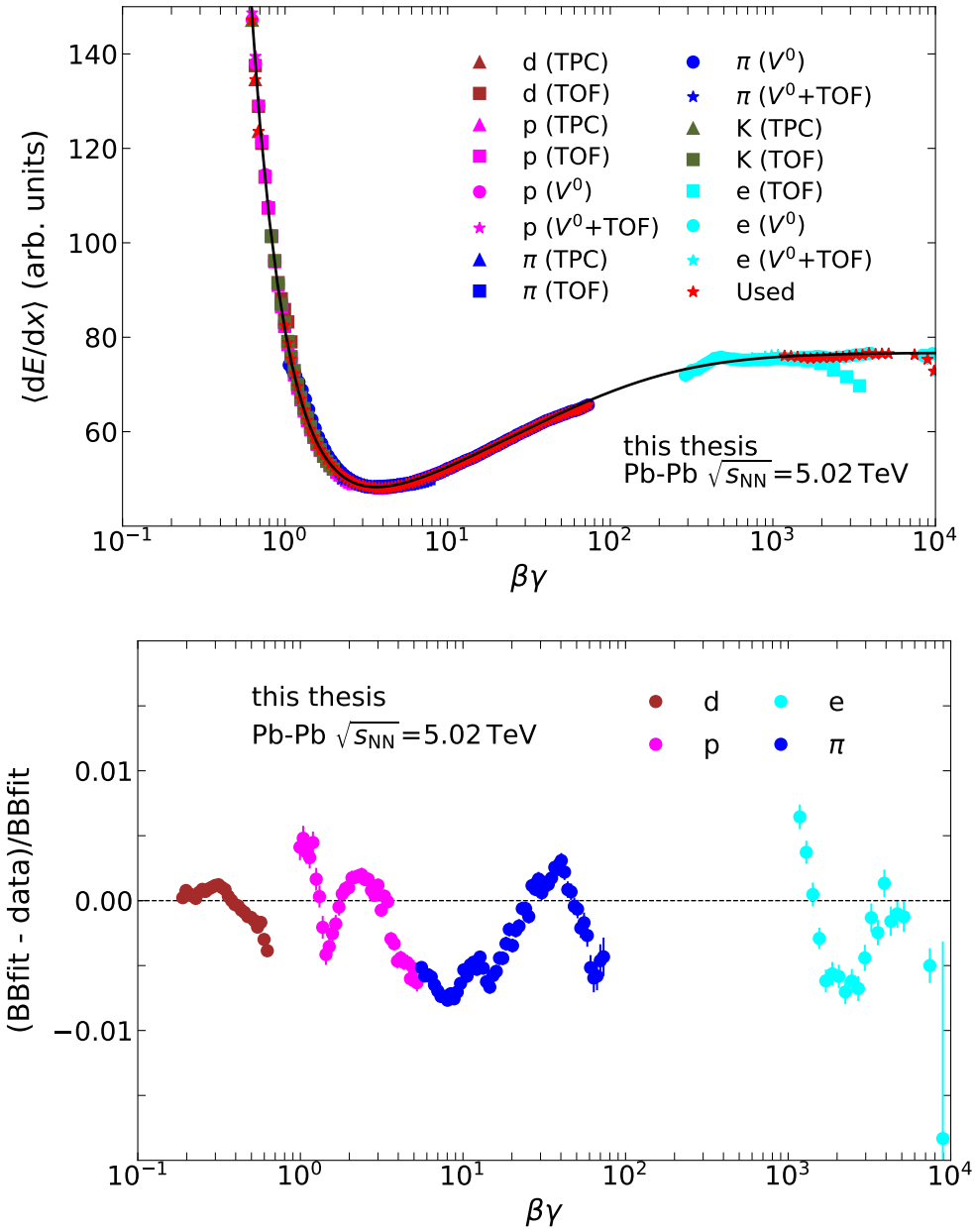

Figure 5.9: [Top panel] Bethe-Bloch parametrization fit (Saturated Lund model) together with all selected particle species from the different selection criteria (Figure 5.4 - Figure 5.7). The red data points indicated the data used for the fitting procedure. [Bottom Panel] Relative deviation of the Bethe-Bloch parametrization to the data points used for fitting. The color corresponds to the different particle species.

The bottom panel of Figure 5.9 illustrates the relative deviation of the fit from the data points used in the fitting procedure. Deviations of up to 1% are observed across the entire $\beta\gamma$ range. Some of these deviations are addressed within the low-momentum corrections

discussed in the next section.

5.4.2 Low-momentum correction

In addition to the deviations for electrons, pions, and protons observed in the bottom panel of Figure 5.9, deviations larger than 1% from the initial Bethe-Bloch fit at even lower values of $\beta\gamma$, depending on the particle species, are observed. These deviations relative to the initial Bethe-Bloch parametrization are shown in Figure 5.10 for electrons, pions, kaons, and protons and become larger than 1% for protons below $\beta\gamma = 0.6$, kaons below $\beta\gamma = 0.4$, pions below $\beta\gamma = 2$ and for electrons $\beta\gamma = 500$. Using the relation $\beta\gamma = \frac{p}{mc}$ one can see that these deviations appear at rather low momentum below approximately 0.8 GeV/c. Overall, for electrons, pions, kaons, and protons, deviations of up to 4% are observed.

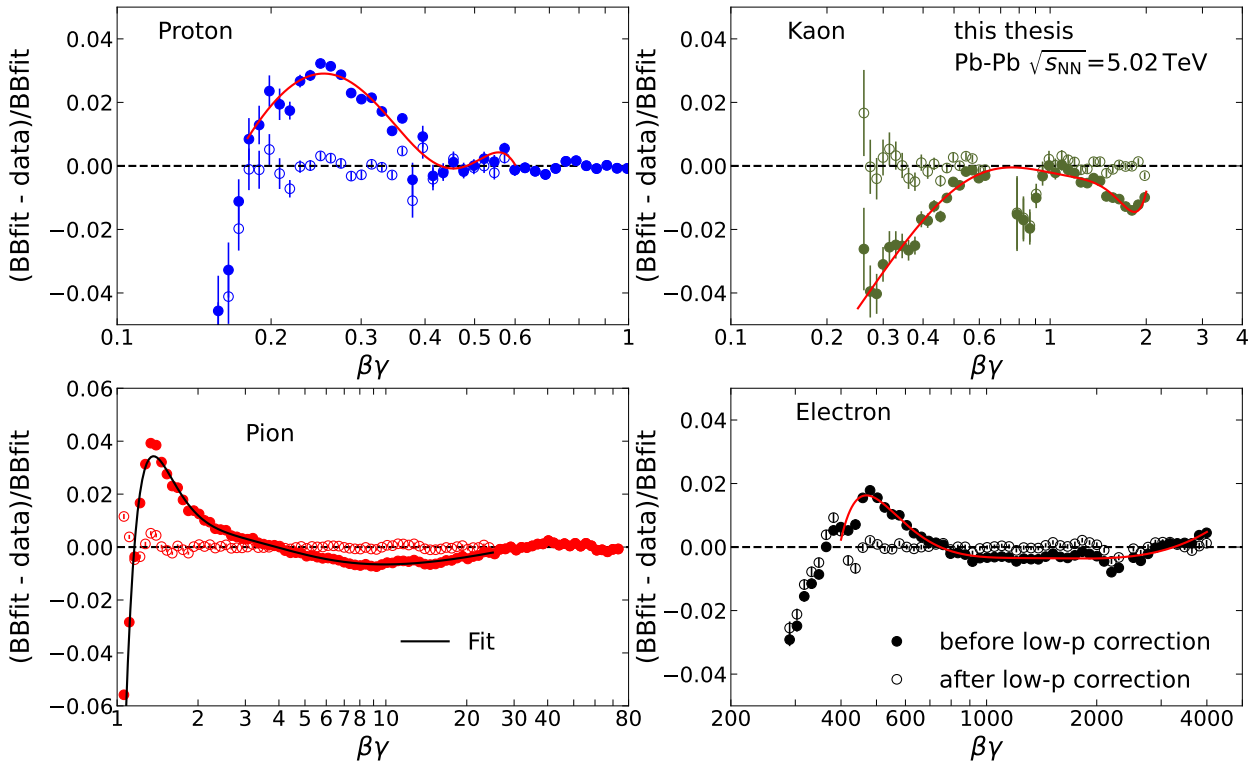

Figure 5.10: The relative deviations to the Bethe-Bloch fit (full marker) together with their parametrization as a function of $\beta\gamma$ for electrons, pions, kaons and protons. Open marker visualizes the performance of the parametrization. The low-momentum parametrization is shown as a red (black) line in the plot.

These deviations arise from the large bending of these tracks in the presence of the magnetic field, resulting in extreme inclination angles with respect to the pad row. As a consequence, this increases the effective track length on the pad row in comparison to

particles at intermediate momentum, leading to a substantial modification of the mean $\langle \mathrm{d}E/\mathrm{d}x \rangle$.
To correct these deviations, a polynomial of fifth to eighth order is fitted to the relative deviation from the Bethe-Bloch parametrization (indicated by the full markers in Figure 5.10). The order of the polynomial depends on the particle species and the specific dataset being analyzed. Additionally, it is important to state that these corrections were also extended to $\beta\gamma$ values, corresponding to momenta above 1 GeV/c, since small deviations to the initial parametrization were found. The performance of this parametrization is illustrated in Figure 5.10 using open markers, providing an estimate of the quality of the correction.

These low momentum corrections are then folded with the general Bethe-Bloch parametrization extracted in Section 5.4.1. This results in a particle-type dependent parametrization of the $\langle \mathrm{d}E/\mathrm{d}x \rangle$ as a function of $\beta\gamma$. The resulting particle-type dependent parametrization is shown together with a subsample of the analyzed data as a function of momentum p (converted via $\beta\gamma = \frac{p}{mc}$) for various particle species in Figure 5.11. At this stage of the parametrization, a quantitatively good agreement is already noticeable.

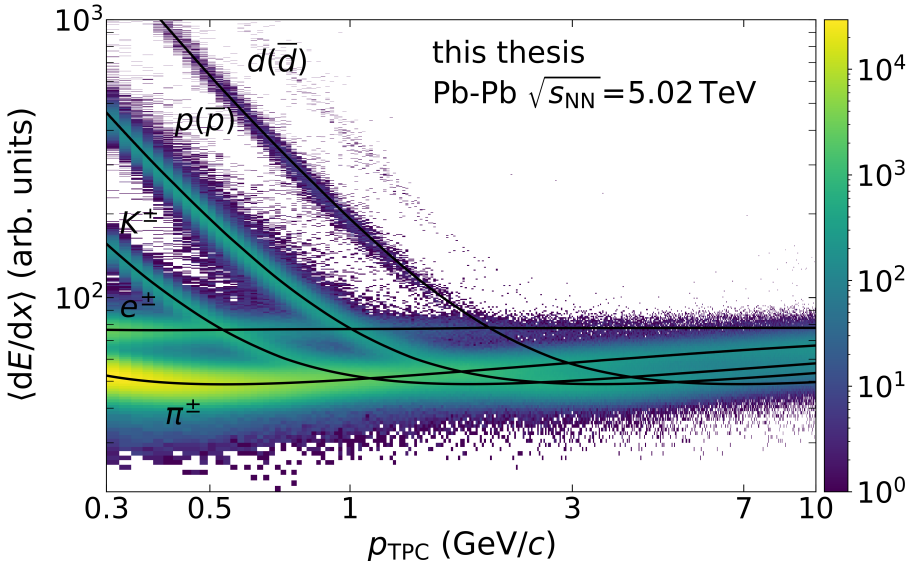

Figure 5.11: $\langle \mathrm{d}E/\mathrm{d}x \rangle$ parametrization as a function of the particle momentum for electrons, pions, kaons, protons, and deuterons (black line) together with a subsample of the data used to extract the parametrization.

5.4.3 η-dependent parametrization

As mentioned at the beginning of this section, the $\langle \mathrm{d}E/\mathrm{d}x \rangle$ of a particle depends on its pseudorapidity and thus requires a separate correction, which will be described in the following. The charge induced on the readout pads varies as a function of the particle tracks polar angle Θ, altering the mean and width of the measured $\langle \mathrm{d}E/\mathrm{d}x \rangle$. A visual

representation is shown in Figure 5.3. As the polar angle Θ increases, the effective track length projected onto a pad row also increases. As discussed in Section 5.2, this change in the effective track length will modify the shape of the Landau distribution due to the varying amount of gas traversed by the charged particle. It will introduce a dependence on both the mean and width of the $\langle \mathrm{d}E/\mathrm{d}x \rangle$ with respect to the polar angle Θ.
This, in turn, results in a dependence on the pseudorapidity due to the following relation between pseudorapidity and polar angle Θ, where $|p|$ is the absolute momentum of the particle and p_L the momentum along the beam axis:

$$\eta = \frac{1}{2}\left(\frac{|p|+p_L}{|p|-p_L}\right) = -\ln\left(\tan\left(\frac{\Theta}{2}\right)\right) \tag{5.11}$$

In addition to the previously outlined effects, variations in the $\langle \mathrm{d}E/\mathrm{d}x \rangle$ are expected as a consequence of the construction and geometry of the ALICE TPC. Near midrapidity ($|\eta| < 0.1$), a portion of the charges generated by ionization is absorbed by the central HV electrode, which divides the TPC into two volumes. This absorption results in a reduction of the charge drifting towards the readout chambers, consequently reducing the amount of charge induced on the pad plane from this charge after amplification.
In the pseudorapidity region ($|\eta| > 0.7$), the track is not fully contained in the TPC and exits the detector's acceptance. This reduces the potential number of clusters available for the calculation of the globally assigned $\langle \mathrm{d}E/\mathrm{d}x \rangle$, making it more prone to Landau fluctuations.
The parametrization as a function of pseudorapidity is derived relative to the Bethe-Bloch parametrization in the form of:

$$\Delta = \frac{\langle \mathrm{d}E/\mathrm{d}x \rangle}{\langle \mathrm{d}E/\mathrm{d}x \rangle_{\text{BB fit}}} \tag{5.12}$$

where $\langle \mathrm{d}E/\mathrm{d}x \rangle$ represents the measured energy loss in the experiment and $\langle \mathrm{d}E\mathrm{d}x \rangle_{\text{BB fit}}$ the expected energy loss obtained from the Bethe-Bloch parametrization.
Furthermore, it was observed that Δ as a function of pseudorapidity varies depending on the chosen mean $\langle \mathrm{d}E/\mathrm{d}x \rangle$, but remains consistent across different particle species, making it independent of the particle's momentum [117].
As a result, the pseudorapidity correction can be determined from a single particle species as a function of $\langle \mathrm{d}E/\mathrm{d}x \rangle$ and then applied to all other particle species. Protons are the particles of choice for this task, given that they span a large interval of $\langle \mathrm{d}E/\mathrm{d}x \rangle$ together with providing enough statistics at small and large values of $\langle \mathrm{d}E/\mathrm{d}x \rangle$ to extract a parametrization.
The Δ variable defined in Equation (5.12) is therefore extracted as a function of the pseudorapidity and the inverse of $\langle \mathrm{d}E/\mathrm{d}x \rangle$, represented in the form of a 2D lookup map. The choice of using $1/\langle \mathrm{d}E/\mathrm{d}x \rangle$ instead of $\langle \mathrm{d}E/\mathrm{d}x \rangle$ ensures a finer binning at low $\langle \mathrm{d}E/\mathrm{d}x \rangle$ values, where the separation of different particles is challenging, and a coarser binning for large $\langle \mathrm{d}E/\mathrm{d}x \rangle$ values, where a precise measurement is less needed due to the already significant separation power (see Figure 5.11).

To generate the 2D map as a function of η and the inverse of $\langle \mathrm{d}E/\mathrm{d}x \rangle$, the following procedure is employed: The pure proton sample is simultaneously partitioned into momentum p and $\tan(\Theta)$ bins, and then Δ is fitted with a Gaussian function. The binning in both variables is chosen based on available statistics to ensure sufficient data in each bin. Similarly to the $\langle \mathrm{d}E/\mathrm{d}x \rangle$ fits described in the previous section, the Gaussian fit is constrained to a region near the peak position to exclude non-Gaussian behavior away from the peak. This yields a 2D map of the mean Δ extracted from the Gaussian fit as a function of momentum and $\tan(\Theta)$. The momentum of the proton is then converted to $1/\langle \mathrm{d}E/\mathrm{d}x \rangle$ using the Bethe-Bloch parametrization obtained from Section 5.4.2.

The 2D map extracted in this manner is displayed in the top left panel of Figure 5.12. As expected, due to the symmetry of the ALICE TPC, the relative change in Δ is symmetric with respect to the pseudorapidity. The observed changes of $\langle \mathrm{d}E/\mathrm{d}x \rangle$ with respect to the Bethe-Bloch parametrization $\langle \mathrm{d}E\mathrm{d}x \rangle_{\mathrm{BB\ fit}}$ span a range of 5%.
In practice, the 2D maps should be smooth and not depend on the exact binning of $\tan(\Theta)$ and the inverse of $\langle \mathrm{d}E/\mathrm{d}x \rangle$. Therefore, refined maps are created using a bilinear interpolation approach based on the four nearest bin centers. This bilinear interpolation approach is provided by ROOT [120], and the resulting 2D map is shown in the top right panel of Figure 5.12. The refined 2D map as a function of $\tan(\Theta)$ and inverse of $\langle \mathrm{d}E/\mathrm{d}x \rangle$ serves finally as the η-dependent parametrization of $\langle \mathrm{d}E/\mathrm{d}x \rangle$ in form of a lookup table. The parametrized expected $\langle \mathrm{d}E/\mathrm{d}x \rangle_{\mathrm{exp}}$ for each track can be now extracted using the formula:

$$\langle \mathrm{d}E/\mathrm{d}x \rangle_{exp} = \langle \mathrm{d}E/\mathrm{d}x \rangle_{\mathrm{BB\ Fit}} \cdot C_{\eta} \tag{5.13}$$

where $\left\langle \frac{\mathrm{d}E}{\mathrm{d}x} \right\rangle_{\mathrm{BB\ Fit}}$ is again the Bethe-Bloch parametrization as a function of particle momentum obtained from the previous step, and C_{η} is the value extracted from the refined 2D map, as shown in the top right panel of Figure 5.12.

A first preliminary check of the performance of the parametrization and the bilinear interpolation approach to smoothing the 2D map is conducted as follows. The entire process of extracting the 2D map, as described earlier, is repeated, replacing the denominator of Equation (5.12) with the parametrized expected $\langle \mathrm{d}E/\mathrm{d}x \rangle_{\mathrm{exp}}$, incorporating the η-dependent parametrization outlined in Equation (5.13). The resulting 2D map, shown in the bottom panel of Figure 5.12, shows differences on the order of $O(‰)$. These differences are attributed to the interpolation procedure and are considered artifacts of the interpolation procedure.

5.4.4 Multiplicity-dependent parametrization

The signal induced on the readout pads of the TPC has two components, as illustrated in Figure 5.13. The fast-rising signal is attributed to the drifting electrons that enter the high electric field near the anode wires and initiate an avalanche process. The subsequent

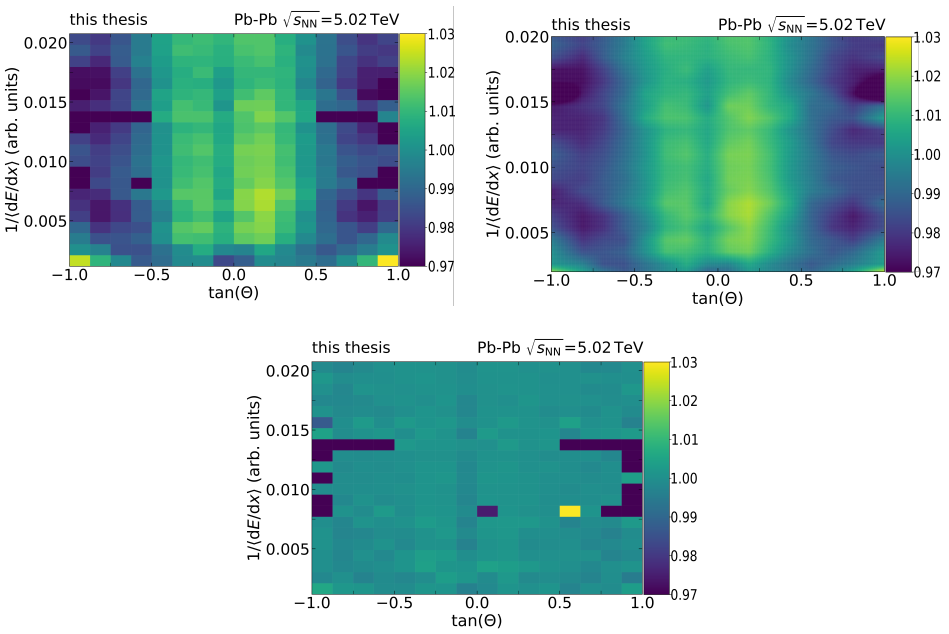

Figure 5.12: [Top left panel] η-parametrization obtained from the pure proton sample as a function of $\tan(\Theta)$ and inverse of $1/\langle \mathrm{d}E/\mathrm{d}x \rangle$. [Top right panel] η-parametrization after the bilinear interpolation approach to smoothen the 2D map. [Bottom panel] η-parametrization map obtained after applying the η-parametrization on the pure proton sample as described in the text.

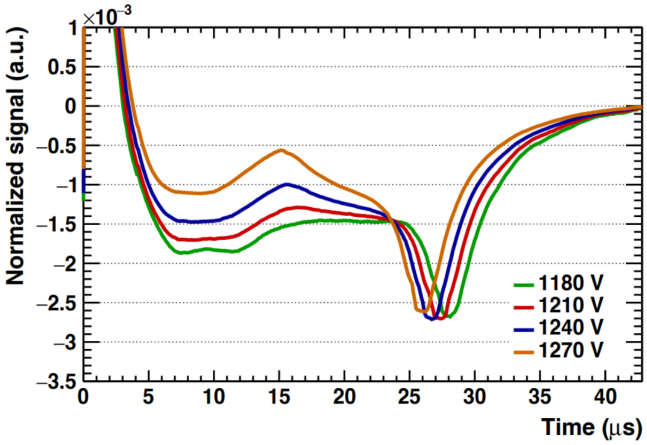

Figure 5.13: Normalized pad signal with a zoom into the y-axis showing the ion tail for different anode voltage settings [116].

plateau and negative undershoot, usually referred to as ion tail, are caused by the motion of the back-drifting positive ions into the active volume of the TPC detector [121].

The ion tail, which spans over tens of microseconds (approximately 25% of the total TPC drift time [116]), can introduce a bias for a second track, reducing the signal attributed to the second track. This issue can affect, for example, two-particle tracks produced in the same event with the same azimuthal angle but different pseudorapidities η, such that the signal from the second track comes while the ion tail of the first track is still present.

In low-multiplicity environments, like pp and p–Pb collisions, the impact of ion tails is negligible. However, in high-multiplicity environments, such as central Pb–Pb collisions, where the density of tracks present in the detector is large, the overlap of these tracks when projected onto the pad plane is high. If the ion tail is not corrected, it will introduce a bias in the measurement of the $\langle \mathrm{d}E/\mathrm{d}x \rangle$ depending on the track multiplicity in the TPC detector.

The parametrization of the $\langle \mathrm{d}E/\mathrm{d}x \rangle$ as function of the track multiplicity is extracted in a similar way to the $\beta\gamma$-dependent parametrization (see Section 5.4.1). The multiplicity-dependent parametrization is extracted using only a pure proton sample and then applied to all other particle species due to similar arguments as given in Section 5.4.3. The pure proton sample obtained in the previous step is first divided into several momentum bins. For each of these momentum bins, the resulting $\langle \mathrm{d}E/\mathrm{d}x \rangle$ distribution as a function of the charged track multiplicity is fitted with a Gaussian function. The $\langle \mathrm{d}E/\mathrm{d}x \rangle$ distribution as a function of the track multiplicity, together with the mean value extracted by Gaussian fits, is shown in Figure 5.14 for the momentum range of 0.70-0.71 GeV/c. The $\langle \mathrm{d}E/\mathrm{d}x \rangle$ as a function of multiplicity decreases slowly, due to the increasing number of signals on the TPC readout pads. The $\langle \mathrm{d}E/\mathrm{d}x \rangle$ bias is then parametrized by a polynomial of second order in each of the selected momentum slices.

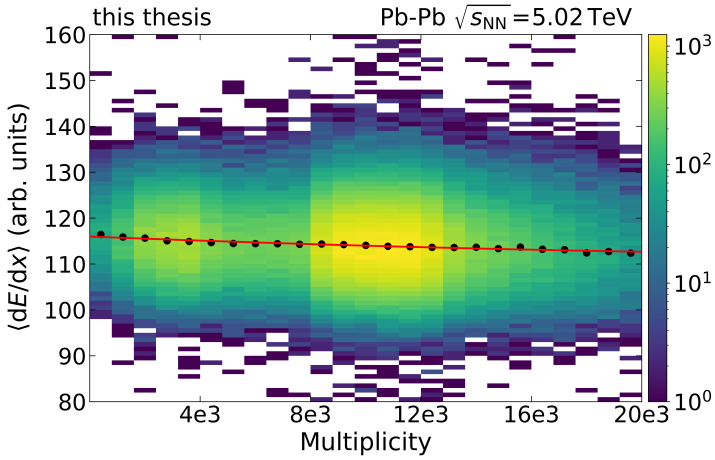

Figure 5.14: $\langle \mathrm{d}E/\mathrm{d}x \rangle$ distribution as a function of the track multiplicity for tracks with a momentum between 0.70 GeV/c and 0.71 GeV/c. The black markers indicate the mean of the Gaussian fit, which was parametrized using a polynomial of second order, shown as a red line.

The multiplicity parmetrization can then be defined as a multiplicative factor such as:

$$C_{\text{mult.}} = \frac{\text{Pol}_{2,p}}{\langle \mathrm{d}E/\mathrm{d}x \rangle_{\text{BB Fit}}} \tag{5.14}$$

where $\langle \mathrm{d}E\mathrm{d}x \rangle_{\text{BB Fit}}$ is the Bethe-Bloch parametrization as a function of particle momentum and $\text{Pol}_{2,p}$ the polynomial of second order fitted to the corresponding momentum bin p.

5.4.5 Resolution parametrization

The parametrization of the resolution of the $\langle \mathrm{d}E/\mathrm{d}x \rangle$ signal is as important as the parametrization of the $\langle \mathrm{d}E/\mathrm{d}x \rangle$. Particle identification in ALICE is typically performed using the nσ variable. If the resolution of the $\langle \mathrm{d}E/\mathrm{d}x \rangle$ signal is not correctly parametrized, it can introduce deviations in the width of the nσ distribution, leading to biases in the assumed efficiency of selected particle tracks. These biases can affect the outcome of various analyses, highlighting the significance of having a valid parametrization for the $\langle \mathrm{d}E/\mathrm{d}x \rangle$ resolution.

The parametrization of the resolution follows a similar schema as the parametrization of the pseudorapidity dependence on $\langle \mathrm{d}E/\mathrm{d}x \rangle$ (Section 5.4.3). First, the pure proton sample is divided into several bins in particle momentum p and $\tan(\Theta)$. As described in Section 5.2, the overall $\langle \mathrm{d}E/\mathrm{d}x \rangle$ associated with a track is computed by combining the individual $\langle \mathrm{d}E/\mathrm{d}x \rangle$ estimates from each cluster (pad row). The resolution of the global $\langle \mathrm{d}E/\mathrm{d}x \rangle$ improves with increasing number of TPC clusters used for the $\langle \mathrm{d}E/\mathrm{d}x \rangle$ calculation. The resolution follows Poisson statistics, and therefore improves with $1/N_{TPC}$ as denoted in

the following formula:

$$\sigma_{rel} = \sqrt{\frac{p_1^2}{N_{cls}}} \tag{5.15}$$

where p_1 characterizes the resolution of $\langle dE/dx \rangle$ per single cluster.

It is therefore important to extract the resolution parametrization not only as a function of the particle momentum p and $\tan(\Theta)$, but also the number of TPC clusters assigned to the particle track. This is accomplished by dividing the proton sample for each bin in momentum and $\tan(\Theta)$ in several bins of the number of TPC clusters. In the following the procedure for extracting the resolution parametrization is described exemplary for one such bin in momentum and $\tan(\Theta)$.

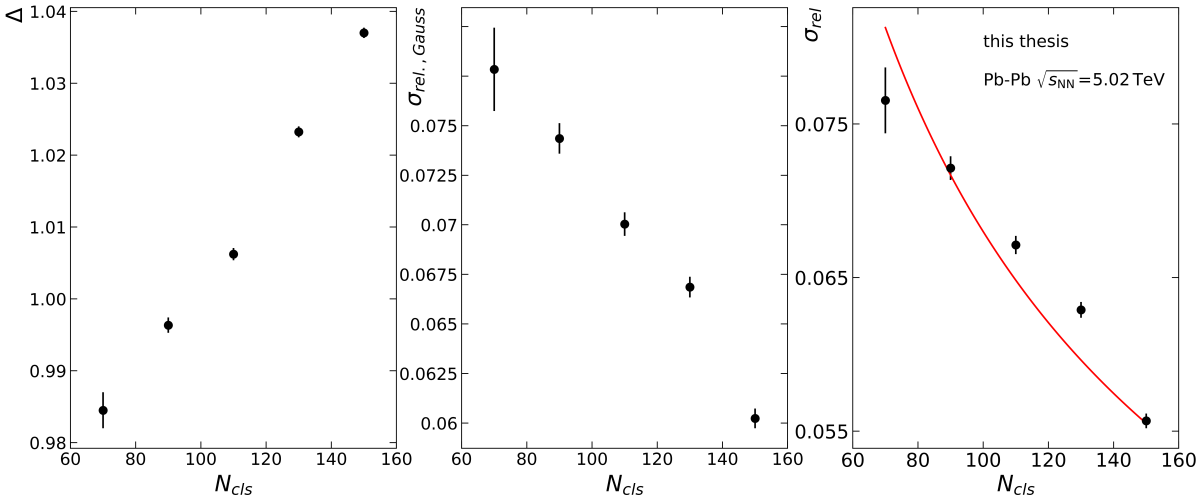

Figure 5.15: Determination of the $\langle dE/dx \rangle$ resolution as a function of the number of TPC clusters. The left panel shows the mean Δ from the fit, whereas the middle panel shows the width of Δ. In the right panel, the ratio of the middle and left panel is shown, together with the fit from Equation (5.15) as a red line.

First, the Δ-distributions (Equation (5.12)) for each bin of the number of TPC clusters are fitted with a Gaussian function and the mean and width of the Δ-distribution are extracted and shown Figure 5.15, left and middle, respectively
It is important to note that the width shown in the middle panel is not the width of the measured $\langle dE/dx \rangle$, but of Δ, which is from now on referred to as $\sigma_{rel.,Gauss}$. In order to obtain the width relative to the measured $\langle dE/dx \rangle$ the width $\sigma_{rel.,Gauss}$ is divided by Δ (middle panel divided by left panel). In such a way, the expected $\langle dE/dx \rangle_{\text{exp}}$ from the Bethe-Bloch parametrization drops out, and the width is relative to the measured $\langle dE/dx \rangle$. This width relative to the measured $\langle dE/dx \rangle$, σ_{rel}, is shown in the right panel of Figure 5.15 and is fitted by the function described in Equation (5.15), shown as a red line.

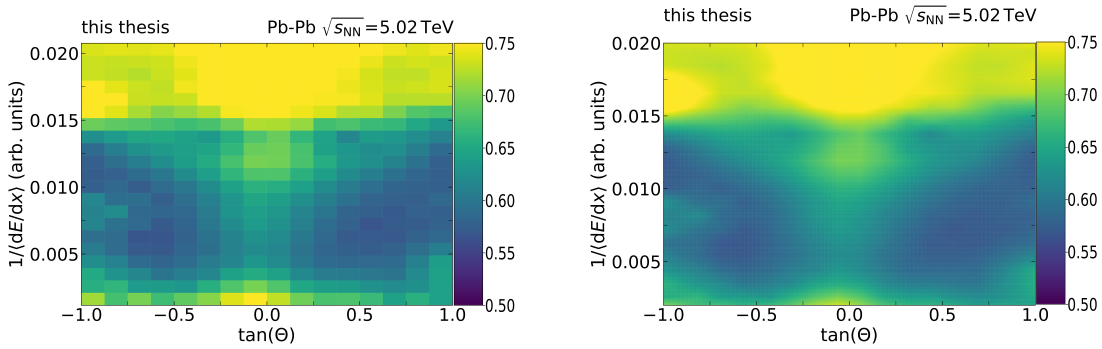

Figure 5.16: The 2D map used to parametrize the resolution of the $\langle dE/dx \rangle$ as function of $tan(\Theta)$ and inverse $\langle dE/dx \rangle$. The left panel shows the raw results from the resolution fits, whereas the right panel shows the smoothened resolution map.

In such a way, the resolution per single cluster p_1 can be obtained for each bin of momentum and tan(Θ). Similar to the η-parametrization the dimension of momentum is transferred to the inverse of $\langle dE/dx \rangle$, by using the momentum-dependent parametrization extracted in Section 5.4.2. The corresponding 2D map as function of the inverse of $\langle dE/dx \rangle$ and tan(Θ) is shown in the left panel of Figure 5.16, exhibiting similar symmetrical features as the 2D map of the pseudorapidity parametrization.

As with the pseudorapidity correction, a smoothing process is applied to the map to minimize biases resulting from the binning and to reduce fluctuations arising from an inaccurate resolution per single cluster extraction. The smoothed map is shown in the right panel of Figure 5.16. The final particle-type-dependent resolution is then extracted using the following formula:

$$\sigma_{species}(N_{cls}) = \sigma_{rel}(N_{cls}) \langle dE/dx \rangle_{\text{exp}} \tag{5.16}$$

where $\left\langle \frac{dE}{dx} \right\rangle_{exp}$ is the parametrized average energy loss obtained from the steps described in the last sections.

5.4.6 Treatment of pileup events

The procedure for obtaining a parametrization of the $\langle dE/dx \rangle_{\text{exp}}$ as described so far was consistently applied to the Run 1 and Run 2 datasets of ALICE across various collision systems.
However, following 2015, the ALICE TPC operated in Pb–Pb collisions with interaction rates of up to 8 kHz and in pp collisions at rates up to 200 MHz. These high interaction rates resulted in the occurrence of pileup events where multiple interaction vertices were present within the TPC readout time [116]. The readout time of the TPC is around 10 μs, which is given by the drift time of the electrons generated in the ionization process as they move from the central electrode to the readout pads. Consequently, tracks from other

collisions occurring within the TPC readout time contribute to the reconstructed event. These pileup collisions introduced a bias in the measured $\langle \mathrm{d}E/\mathrm{d}x \rangle$, and addressing this issue was crucial. In the following section, we will briefly discuss pileup events, explain their impact on $\langle \mathrm{d}E/\mathrm{d}x \rangle$ measurements, and describe how they were treated during the extraction of the parametrization of the $\langle \mathrm{d}E/\mathrm{d}x \rangle_{\mathrm{exp}}$.

Pileup events can be categorized into two distinct types, which are associated with the way collisions happen at the LHC. The particle beams at the LHC are organized into separate bunches, each containing a collection of particles that are brought into collisions. These bunches are spaced approximately 2.5 ns apart from each other. A bunch intended for the collision is from now on referred to as "main bunch", while bunches located adjacent to the main bunch are referred to as "satellite bunches".

The first category of pileup events is referred to as "same bunch-crossing pileup", indicating that two or more collisions occur during the same bunch-crossing. The second category is referred to as "out-of-bunch pileup," where two or more collisions happen in different bunch crossings. This typically involves collisions between main and satellite bunches.

For the first category of pileup events, the collision happens between two main bunches. This means that the different collisions within these bunches happen near in time with positions that are separated by a few cm along the beam direction. These events can be identified based on multiple reconstructed vertices from tracks reconstructed in the TPC and ITS.

For out-of-bunch pileup events, collisions occur at different times, resulting in spatial shifts of tracks reconstructed in the TPC along the drift direction due to their varying production times. This is primarily due to the long readout time of the TPC ($\approx 100\ \mu s$). Consequently, tracks from other collisions can occur within the TPC readout time and contribute to the reconstructed event. In many of these cases, the reconstructed tracks from pileup collisions do not extend to the ITS, mainly because of the ITS's fast readout and the spatial shift of these tracks within the TPC. Therefore, Out-of-bunch pileup events can be identified using a correlation between the number of TPC clusters and the sum of SSD and SDD clusters, as illustrated in Figure 5.17. This correlation between the two variables allows removing "out-of-bunch pileup" events. Around 25 % of the Pb–Pb data taken in 2018 is affected by out-of-bunch-pileup collisions, while same-bunch pileup is negligible in Pb–Pb collisions at interaction rates of about 8 kHz [116].

The exact impact of out-of-bunch-pileup events on the measured $\langle \mathrm{d}E/\mathrm{d}x \rangle$ depends on whether the pileup interactions occurred before or after the triggered interaction. This difference is connected to the ion-tail effect, as previously discussed in Section 5.4.4 and illustrated in Figure 5.13. As seen in Figure 5.13, the ion-tail influences subsequent signals in only one direction, illustrated by the fact that the normalized signal stays negative. This leads to different biases on the measured $\langle \mathrm{d}E/\mathrm{d}x \rangle$ in such events. To clarify this quantitatively, let's consider the following scenarios: Suppose we have an event that

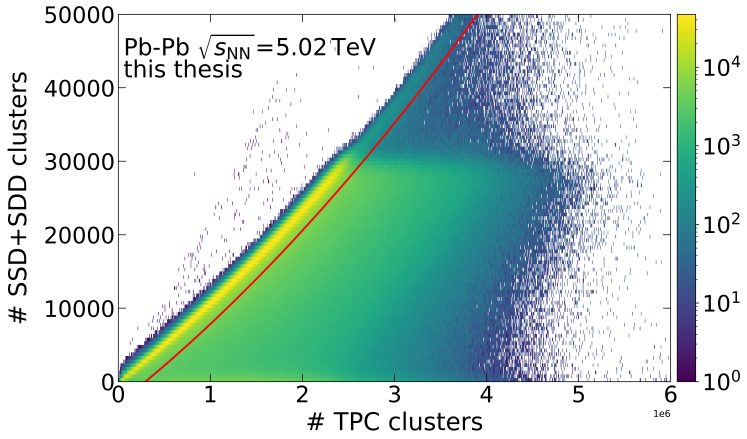

Figure 5.17: Correlation between the number of SSD+SDD clusters and the number of TPC clusters. The red line corresponds to the threshold when events are accepted or rejected as events influenced by out-of-bunch pileup.

triggers the data acquisition and pileup interactions occurring in the future and in the past relative to this event. For pileup events in the past, the tracks reconstructed from these events are spatially shifted in a way that brings them closer to the readout chambers. Therefore, the drift electrons generated by these tracks will reach the readout chambers first, get amplified, and generate ions in the process. These ions will start to drift back into the drift chamber, inducing a negative charge on the pad plane in the process according to the ion-tail effect. The charges induced on the readout pads by the drifting electrons that triggered the event will now consequently register to be smaller than they truly are, reducing the $\langle \mathrm{d}E/\mathrm{d}x \rangle$ assigned to these tracks.
On the other hand, tracks from pileup events happening after the triggered event will reach the pad plane after the tracks from the triggered one. The induced charge from these pileup tracks will now be partly associated with the induced charge of the tracks from the triggered one, consequently increasing the $\langle \mathrm{d}E/\mathrm{d}x \rangle$ assigned to these tracks.

The effect of pileup events on the $\langle \mathrm{d}E/\mathrm{d}x \rangle$ is illustrated in the left panel of 5.18, which shows the mean $\langle \mathrm{d}E/\mathrm{d}x \rangle$ of pions for the events with out-of-bunch pileup in cases the pileup event occurred before or after the triggered event and for events not affected by out-of-bunch pileup. When combining pileup events from both the past and the future, the $\langle \mathrm{d}E/\mathrm{d}x \rangle$ shift cancels out, and it exhibits similar behavior to events not affected by pileup. However, even though the $\langle \mathrm{d}E/\mathrm{d}x \rangle$ biases cancel each other out, it is not feasible to create a $\langle \mathrm{d}E/\mathrm{d}x \rangle$ parametrization using untreated pileup events. The correlated $\langle \mathrm{d}E/\mathrm{d}x \rangle$ biases won't be corrected by the $\langle \mathrm{d}E/\mathrm{d}x \rangle$ parametrization scheme, which mainly affects correlation analysis, as described in this thesis (see Chapter 6).

There are different ways to handle these biases in the measured $\langle \mathrm{d}E/\mathrm{d}x \rangle$. One approach is to simply discard the pileup interactions using the correlation between the number of TPC clusters and the sum of SSD and SDD clusters, as shown in Figure 5.17. However, this

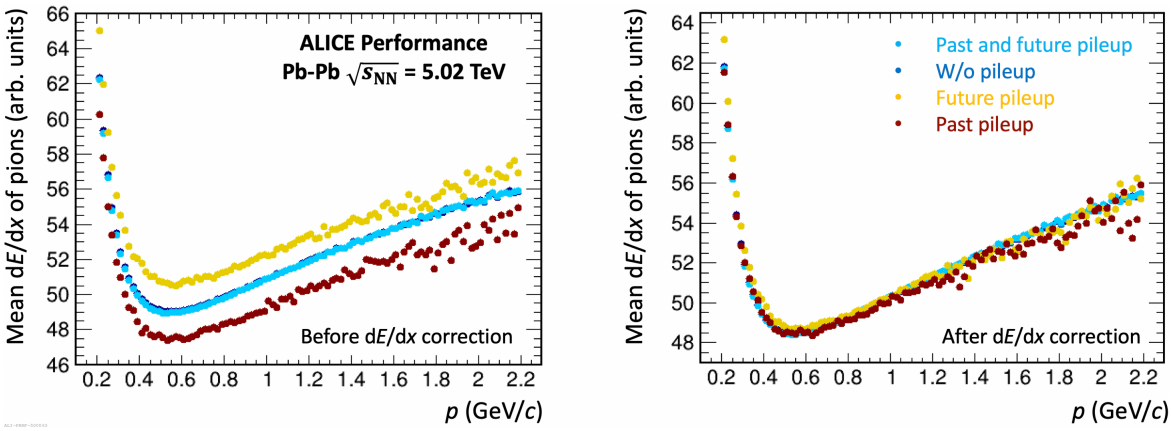

Figure 5.18: Mean $\langle \mathrm{d}E/\mathrm{d}x \rangle$ values of pions for the events with and without out-of-bunch pileup, before (left) and after (right) $\langle \mathrm{d}E/\mathrm{d}x \rangle$ correction [116].

would significantly reduce the number of events available for analysis.

On the other hand, the $\langle \mathrm{d}E/\mathrm{d}x \rangle$ bias can be corrected on an event-by-event basis. Events affected by pileup interactions were used to parametrize the deviations in the $\langle \mathrm{d}E/\mathrm{d}x \rangle$ of tracks from the triggered events in four dimensions: pseudorapidity, $\langle \mathrm{d}E/\mathrm{d}x \rangle$, the multiplicity of the pileup event, and the relative distance of the pileup collision vertex from the main interaction vertex along the beam axis [116]. The performance of the multidimensional correction map is shown in the right panel of Figure 5.18, fully correcting the observed biases in $\langle \mathrm{d}E/\mathrm{d}x \rangle$. In the following, we refer to this map simply as "pileup correction map".

The $\langle \mathrm{d}E/\mathrm{d}x \rangle$ parametrization described in the previous sections was performed by excluding pileup events. The entire parametrization workflow can be repeated by simply correcting the $\langle \mathrm{d}E/\mathrm{d}x \rangle$ biases using the pileup correction map in the skimming phase of the workflow (step 1), allowing the use of the complete data set for the parametrization. The $\langle \mathrm{d}E/\mathrm{d}x \rangle$ used for the parametrization scheme is obtained by:

$$\langle \mathrm{d}E/\mathrm{d}x \rangle_{\mathrm{cor}} = \langle \mathrm{d}E/\mathrm{d}x \rangle - \delta_{\mathrm{pileup}} \tag{5.17}$$

where δ_{pileup} is the value from the pileup correction map.

Two modifications to the workflow are made when using the pileup correction map.

1. The parametrization as a function of occupancy, described in Section 5.4.4, is not applied. This is because the pileup correction map already corrects for event-by-event variations, taking into account the multiplicity of a given event.

2. For the resolution parametrization, a multidimensional fit on the width of the

$\langle \mathrm{d}E/\mathrm{d}x \rangle$ distribution is performed. The new parametrization is given by:

$$\sigma_{rel} = \sqrt{p_0 x_0 + p_1 x_2 p_5 \left(\frac{x_0}{\sqrt{\frac{1}{x_1^2}}} \right)^{p_2} + x_2 x_3 + (p_4 x_4)^2 + (p_6 x_5)^2 + (x_5 \frac{x_0}{\sqrt{1+x_1^2}} p_7)^2} \tag{5.18}$$

where track variables x_i i=0..5 stand for $1/\langle \mathrm{d}E/\mathrm{d}x \rangle$, tan(Θ), momentum p, the mass of the particle m, $1/p_{\mathrm{T}}$ and the normalized multiplicity, defined as the charged particle multiplicity in the TPC divided by 11000. This replaces the resolution parametrization shown in Section 5.4.5.

The parametrization obtained from the dataset by discarding the pileup events is referred to as the parametrization without pileup events, whereas the parametrization obtained from the dataset where the $\langle \mathrm{d}E/\mathrm{d}x \rangle$ was corrected using the pileup correction map is referred to as the parametrization with pileup events.

5.5 Performance of the $\langle \mathrm{d}E/\mathrm{d}x \rangle$ parametrization

In this section, we will evaluate the performance of the $\langle \mathrm{d}E/\mathrm{d}x \rangle$ parametrization and compare the results between two approaches: one obtained by discarding pileup events and another obtained by correcting pileup events using the pileup correction map.

First of all, the parametrization of the $\beta\gamma$ dependence,as were obtained in Section 5.4.2, are compared. This comparison is presented in Figure 5.19, where the left panel displays the Bethe-Bloch parametrization, and the right panel shows the ratios between the two. The $\langle \mathrm{d}E/\mathrm{d}x \rangle$ parametrization reveals a relatively constant offset of 6% across the entire momentum range, with fluctuations observed for protons, kaons, and deuterons below 1 GeV/c. These fluctuations can be attributed to the variations in the functional forms of the low-momentum correction. It is important to note that the pileup correction map already functions as a "precorrection" before the full parametrization is extracted. In the case of the dataset where pileup events were discarded, this precorrection was not applied. The pileup correction map can also describe the overall offset seen for both parametrization.
To judge the performance of the $\langle \mathrm{d}E/\mathrm{d}x \rangle$ parametrization, the nσ variable, commonly used for particle identification in ALICE, is employed. The expected $\langle \mathrm{d}E/\mathrm{d}x \rangle$ for a given particle track is obtained by folding the different parametrizations described in theSection 5.4.1 - Section 5.4.4. For the parametrization without pileup events, the expected $\langle \mathrm{d}E/\mathrm{d}x \rangle$ is given as:

$$\langle \mathrm{d}E/\mathrm{d}x \rangle_{\mathrm{exp}} = \langle \mathrm{d}E/\mathrm{d}x \rangle_{\mathrm{BB\ Fit}} \cdot C_\eta \cdot C_{mult} \tag{5.19}$$

where C_η is the η-dependent parametrization, C_η the multiplicity dependent parametrization, and $\langle \mathrm{d}E/\mathrm{d}x \rangle_{\mathrm{BB\ Fit}}$ the Bethe-Bloch parametrization as function of momentum p.
For the parametrization with pileup events its given as:

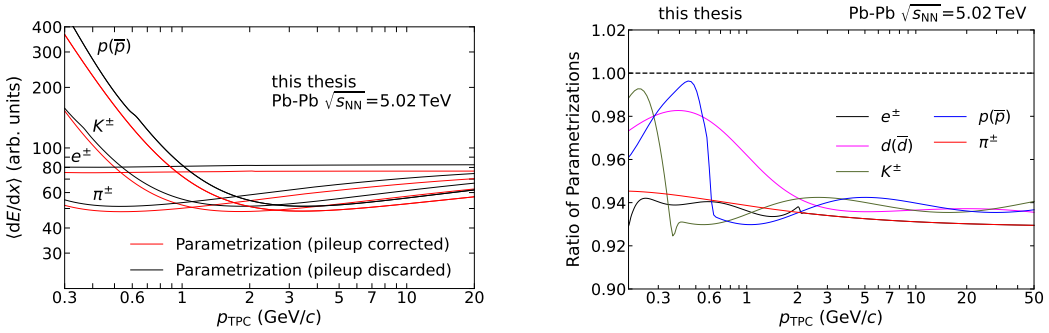

Figure 5.19: $\langle \mathrm{d}E/\mathrm{d}x \rangle$ parametrization as a function of momentum for electrons, pions, kaons and protons extracted by the two pileup treatment strategies together with their ratio.

$$\langle \mathrm{d}E/\mathrm{d}x \rangle_{\mathrm{exp}} = \left(\langle \mathrm{d}E/\mathrm{d}x \rangle_{\mathrm{BB\ Fit}} + \delta_{\mathrm{pileup}} \right) \cdot C_{\eta} \tag{5.20}$$

with δ_{pileup} the correction provided by the pileup correction map and C_{η} the η-dependent parametrization.

The mean and width of the nσ variable are shown in Figure 5.20 as functions of particle momentum for electrons, pions, and protons selected from their corresponding V^0 decays to increase the purity of the samples. Full markers represent the $\langle \mathrm{d}E/\mathrm{d}x \rangle$ parametrization with pileup events, while open markers represent the $\langle \mathrm{d}E/\mathrm{d}x \rangle$ parametrization without pileup events.

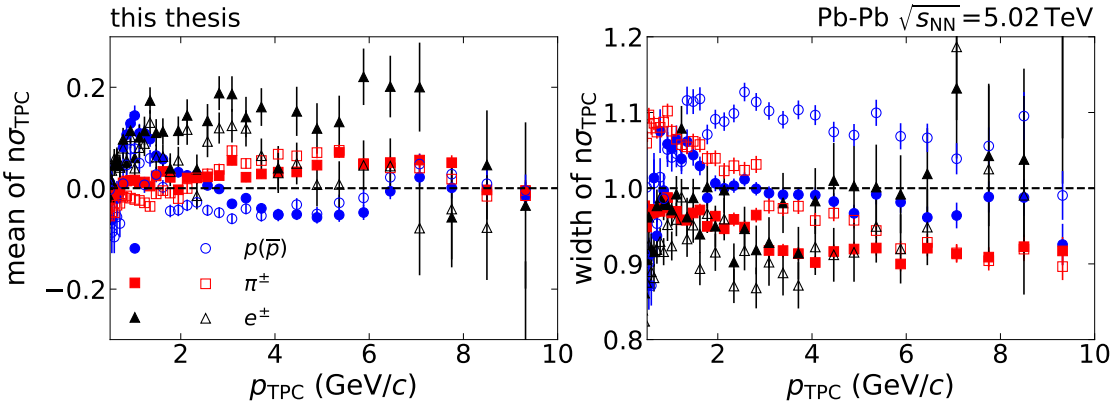

Figure 5.20: Mean [left panel] and width [right panel] of the nσ variable as a function of particle momentum for electrons, pions and protons obtained from the $\langle \mathrm{d}E/\mathrm{d}x \rangle$ parametrization with pileup events (full markers) and without pileup events (open markers).

The mean of nσ as a function of momentum shows a comparable performance for both

parametrizations. For protons and pions, the mean of nσ remains within a 0.05 range for momenta ranging from 2 GeV/c to 10 GeV/c. However, larger fluctuations are observed for protons with momenta below 1 GeV/c. In this low-momentum region, the separation between other particles is already quite large. Therefore the shift was considered not critical. In the case of electrons, a constant shift of 0.1 with respect to momentum is consistently observed. This finding aligns with the results of parametrization extractions conducted for other collision systems.

The width of nσ, however, displays more significant variations as a function of momentum. With the parametrization with pileup events, the width remains consistent with unity, accounting for statistical uncertainties for protons and electrons. In contrast, for pions, a constant offset of approximately 0.93 is observed. The width of nσ derived from the parametrization obtained from the pileup-discarded dataset exhibits larger deviations from unity, with pion widths most consistent with unity.
As described in Section 5.4.6, the resolution parametrization for $\langle \mathrm{d}E/\mathrm{d}x \rangle$ was altered depending on the treatment strategy of pileup events. In the case of the parametrization without pileup events, the proton sample was initially divided into momentum and tan(Θ) bins. Then, it was further subdivided into bins of N_{cls} to extract the resolution parametrization. This process is quite demanding in terms of statistics and could be one of the reasons for the larger variations observed in the width in comparison to the parametrization with pileup events, where the parametrization was obtained through a multidimensional fit.

The mean of the nσ variable as a function of pseudorapidity (as shown in Figure 5.21) is reasonably well described by both parametrizations, but the parametrization with pileup events outperforms in pseudorapidity ranges with $|\eta| > 0.5$. In the case of electrons, a consistent offset of 0.1 is observed for both parametrizations.

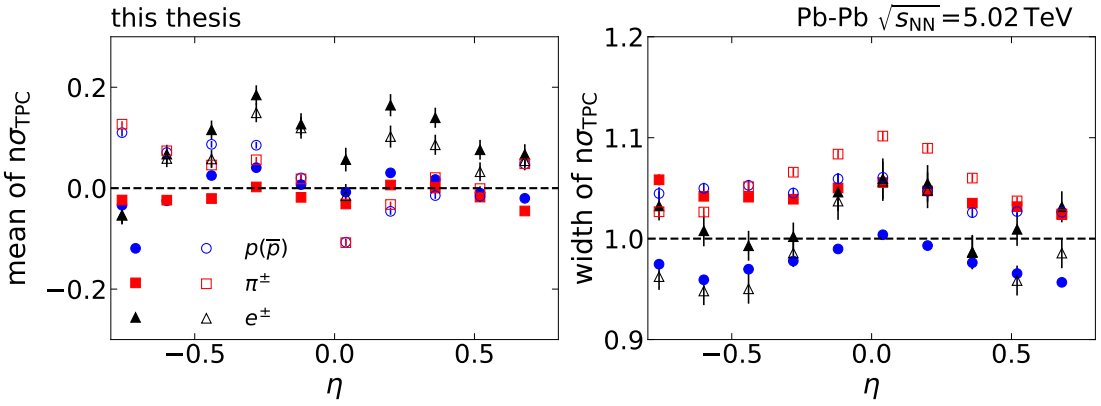

Figure 5.21: Mean [left panel] and width [right panel] of the nσ variable as a function of η for electrons, pions and protons obtained from the $\langle \mathrm{d}E/\mathrm{d}x \rangle$ parametrization with pileup events (full markers) and without pileup events (open markers).

Similar observations can be made regarding the width of nσ as a function of pseudorapidity.

With the parametrization without pileup events, pions and protons exhibit a constant offset of approximately 1.05, while electrons display significant variations. Overall, the performance of the parametrization with pileup events is better than the other parametrization, underlining the improvements achieved through the multi-dimensional fit procedure used to extract the resolution parametrization.

The variations in the mean and width as a function of multiplicity are the most pronounced ones and are shown in Figure 5.22. The mean as a function of multiplicity exhibits quantitatively similar trends for both parametrizations, with a slightly better performance observed for the parametrization with pileup events, particularly at higher multiplicities. The significant deviation at low multiplicities could be attributed to the fact that the Bethe-Bloch parametrization as a function of $\beta\gamma$ is extracted using all available events, including those with high and low multiplicities. This might introduce a bias towards high multiplicity events due to the greater number of tracks available for the parametrization. This bias should in principle, be corrected by the multiplicity correction as discussed in the Section 5.4.4 in the case of the parametrization without pileup events and by the pileup correction map used in case of the parametrization with pileup events. In the latter case, the discrepancies observed could hint at a worse description of low multiplicity events compared to high multiplicity events. In general, low-multiplicity events experience a stronger bias of pileup events than the ones from high-multiplicity events.

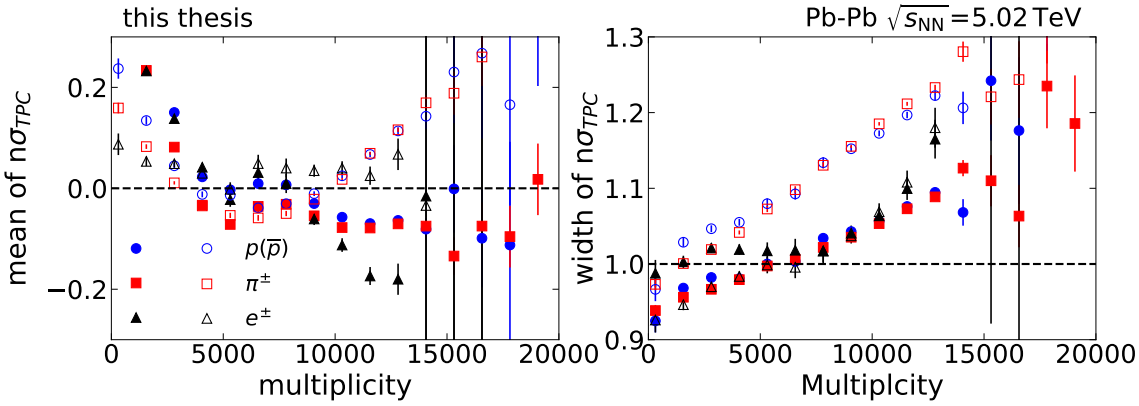

Figure 5.22: Mean [left panel] and width [right panel] of the nσ variable as a function of track multiplicity for electrons, pions and protons obtained from the $\langle dE/dx \rangle$ parametrization with pileup events (full markers) and without pileup events (open markers).

Regarding the width of nσ as a function of multiplicity, both parametrizations display an increasing trend as a function of multiplicity. This trend is more pronounced in the parametrization derived from the pileup-discarded dataset when compared to the pileup-corrected dataset.

In summary, the parametrization generally exhibits similar quantitative performance, with a slight advantage for the parametrization derived from the pileup-corrected dataset, partic-

ularly regarding the width of the nσ variable. Based on these checks, it was concluded that the Bethe-Bloch parametrization, along with the pileup correction map, should be the preferred choice for use within the ALICE collaboration. Nevertheless, both parametrization were released to the ALICE collaboration, to allow for an analysis-by-analysis to decide which parametrization should be used.

5.6 Final remarks about the $\langle \mathrm{d}E/\mathrm{d}x \rangle$ parametrization

The $\langle \mathrm{d}E/\mathrm{d}x \rangle$ parametrization for the Pb–Pb dataset recorded in 2018 presented in this thesis was released to the ALICE collaboration for daily work, with the caveat that the Bethe-Bloch parametrization together with the pileup correction map show better performance. The framework outlined in this thesis operates under the assumption that dependencies on different variables factorize and can be separately extracted, ignoring potential correlations between variables. In the context of high-multiplicity environments such as Pb–Pb collisions, the framework reasonably parametrizes the expected $\langle \mathrm{d}E/\mathrm{d}x \rangle$, resulting in the mean position of the nσ variable for various particle species to be contained within 0.2. Despite this success, it is apparent that there is room for improvement, leading to the development of a new $\langle \mathrm{d}E/\mathrm{d}x \rangle$ parametrization framework.

For Run 3 of the ALICE operation, a completely new $\langle \mathrm{d}E/\mathrm{d}x \rangle$ parametrization has been developed, discarding the factorization assumption and parametrization of the mean and width of the $\langle \mathrm{d}E/\mathrm{d}x \rangle$ distributions using a multidimensional approach. A neural network has been chosen for this task, which learns the relative deviation of the $\langle \mathrm{d}E/\mathrm{d}x \rangle$ signal from a basic Bethe-Bloch parametrization as a function of $\beta\gamma$. The parameters of the neural network are then released to the collaboration to correct the observed $\langle \mathrm{d}E/\mathrm{d}x \rangle$ biases. This approach was already tested in pp collisions recorded during the Run 2 operation of ALICE, showing promising results [122].

6 Data analysis

6.1 Data samples and Monte-Carlo simulations

The analysis conducted in this thesis uses a sample of data for Pb–Pb collisions at a center-of-mass energy of $\sqrt{s_{\mathrm{NN}}} = 2.76\,\mathrm{TeV}$ recorded by the ALICE experiment at the LHC in the year 2010. This dataset contains about 14 million collisions, which were selected using a minimum bias trigger.

The Pb–Pb data samples recorded in the years 2011, 2015, and 2018 are not considered for this analysis due to performance issues related to the extraction of the neutron spectator plane using the ZDC. These issues are likely a result of the strong beam focusing employed to enhance collision rates in these data samples. This focusing introduces correlations between the beam, the ZDC, and the TPC signals, which cannot be removed by the standard non-uniform acceptance correction used in this analysis (see Section 6.5). The question of resolving these issues is still a subject of ongoing discussions and investigations within the ALICE collaboration. For further information, readers are referred to [123].

The heavy-ion collisions are simulated using the HIJING event generator [124], which models particle production in heavy-ion collisions. It is important to note that the HIJING event generator lacks interactions beyond energy loss in jets and, consequently, does not model collective particle behavior like elliptic flow. The particle interactions within the detector material are simulated with the GEANT3 simulation package [125]. A Monte Carlo simulation is utilized to determine the track reconstruction efficiency for particle tracks and to extract the purity and efficiency of the Bayesian particle identification (PID). Additionally, it is used to calculate weights for each particle track correcting for the non-uniform efficiency of the ITS and TPC.

A summary of the data samples and Monte Carlo simulations used in this analysis can be found in Table 6.1.

System	LHC Run	Number of Events	$\sqrt{s_{\mathrm{NN}}}$	Type
Pb–Pb	2010	$14.2{\cdot}10^6$	2.76 TeV	data
Pb–Pb	2010	$6{\cdot}10^5$	2.76 TeV	HIJING+GEANT3

Table 6.1: Summary of data and Monte Carlo samples used this thesis.

6.2 Event selection

The heavy-ion collisions analyzed in this thesis, now referred to as an ”event”, must satisfy a minimum bias (MB) trigger requirement. This trigger is met if there are either signals detected in either the V0 or SPD detector, or if signals are detected in both V0 detectors.

Given that a perfect vacuum does not exist within the beam pipe, interactions between the beam and residual gas are possible. To mitigate such beam-gas interactions, the V0 detectors are employed. By comparing the sum and difference of the signal times measured in both detectors, beam-gas interactions can be distinguished from beam-beam interactions.

Another important source of background events arises from parasitic collisions, which occur when main and satellite bunches of the beams collide. The background resulting from main-satellite collisions cannot be ignored in Pb–Pb collisions and need to be removed. As described in Section 4.2.5, this removal can be achieved using the two ZDC detectors. Due to the separation between the main and satellite bunches, neutron spectators from main-satellite collisions arrive at different times at the ZNA and ZNC detectors, respectively. Consequently, these parasitic collisions can be effectively removed by utilizing the correlation between the sum and difference of signal times measured in both ZDC detectors.

The analysis presented in this thesis may be biased by residual pileup events, which have discussed in Section 5.4.6 in the context of extracting a $\langle \mathrm{d}E/\mathrm{d}x \rangle$-parametrization for the Pb–Pb data recorded in 2018. In-bunch pileup events, which occur within the same colliding bunches as the event triggering the data acquisition, can be removed through the reconstruction of multiple primary vertices. Due to the low interaction rate during the Pb–Pb data taking in 2010, such in-bunch pileup events occur rarely.

Out-of-bunch pileup events, happening if bunch crossings is different from the one triggering the data acquisition. These events are removed by using correlations between different detectors with varying readout times. In the Pb–Pb dataset recorded in 2010, the correlation between particle multiplicities measured in the TPC and the V0 detectors is used to remove residual pileup events. Additionally, out-of-bunch pile-up events are suppressed using the correlation between the number of tracks within the TPC and the total number of clusters in both SPD layers. Events that deviate more than three standard deviations from the mean of this distribution are excluded, as shown in Figure 6.1.

Selections described above remove approximately 26,000 events. This is necessary because these events would introduce a bias into the extraction of anisotropic flow from the four-particle cumulant in peripheral collisions. For these events, the four-particle cumulant Equation (3.3) will be incorrectly calculated due to the tracks from the pileup collision, mimicking non-flow contributions. Furthermore, when calculating the all-event-averaged cumulant (Equation (3.5)), each single event is weighted by the total number of four particle combinations that can be constructed with a given number of particles. This means that events affected by out-of-bunch pileup will receive a higher weight, and their ”incorrectly”

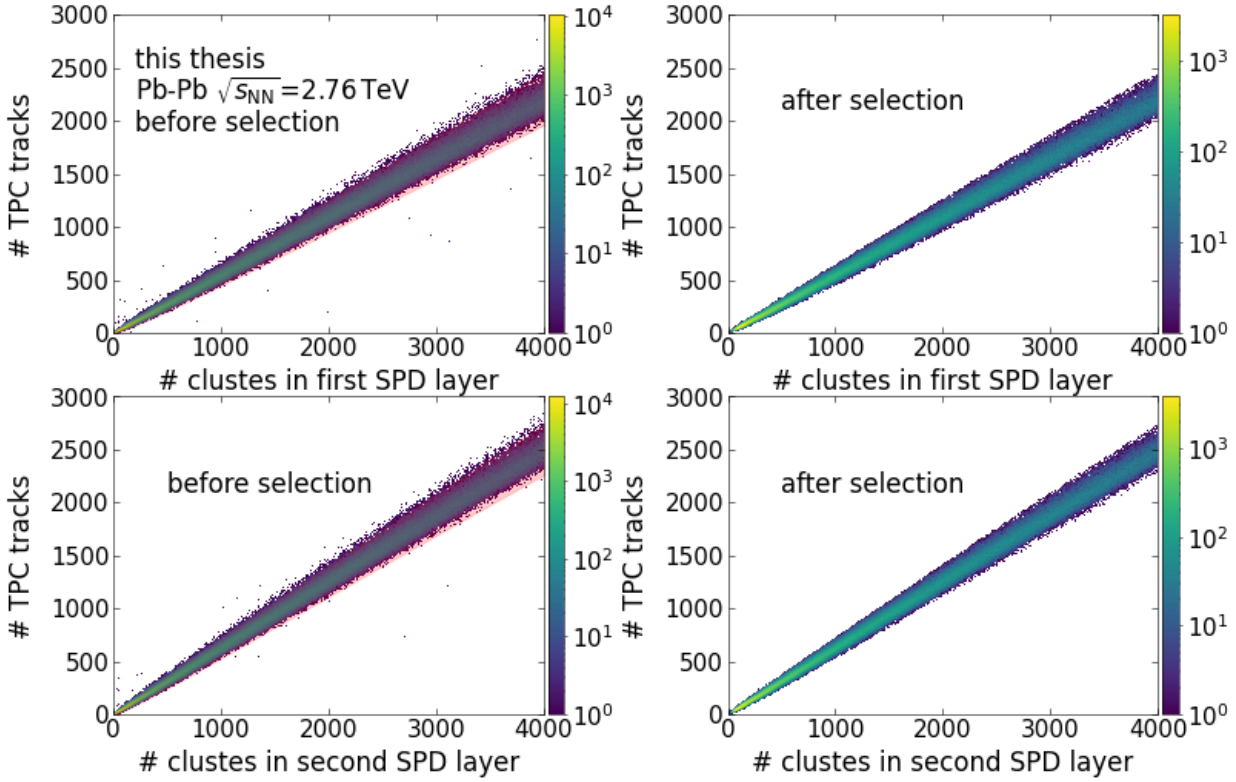

Figure 6.1: Correlation between TPC only tracks and the total number of clusters measured in the two layers of the SPD detector before and after the selection denoted as red band on the left side of the figure.

calculated four-particle cumulant will bias the measurement of the anisotropic flow.

In this analysis, only events within the centrality range of 5% to 60% were considered. The centrality of an event was determined using signals measured in the V0 detectors (V0M), while the estimation of centrality using the number of tracklets in the SPD detector (CL1) was used to estimate the systematic uncertainty from this centrality estimation. The choice to focus on this centrality range is driven by several factors. In central events, the limitation arises from the limited number of neutron spectators, making the extraction of the neutron spectator symmetry plane unreliable. In peripheral collisions, the number of neutron spectators is also limited, primarily because an increasing number of neutrons are bound to nuclear fragments, which are not detected by the ALICE detector. Second, the reduced number of particles produced in peripheral collisions reduces the total number of particles available for extracting the differential four-particle cumulant $d_2\{4\}$. This reduction in statistics affects the stability of its measurement, thereby restricting the analysis to centrality below 60%.

To ensure a uniform acceptance as a function of pseudorapidity, it is required that the primary vertex of the collision falls within $\pm$ 10 cm of the interaction point along the beam axis. This ensures a pseudorapidity coverage of $|\eta| < 0.8$ in both the ITS and TPC, maintaining a relatively symmetrical acceptance.

A summary of the event selection criteria can be found in Table 6.2.

Selection criteria	Value	# Events [10^6]
$\lvert v_z \rvert$	10 cm	14.2
Centrality	5% - 60%	8.9
Signal in neutron ZDCs	true	8.9
Pile-up rejection		8.9
Min. number of tracks for primary vertex	< 1	8.9

Table 6.2: Summary of the event selection criteria applied in the analysis.

6.3 Track selection

This section provide a description of the general track selection criteria used in the analysis. The selection criteria for the identification of pions, kaons and (anit)protons is described in the next Section 6.4.

Charged particle tracks are selected in the transverse momentum range from 0.2 to 6 GeV/c. The lower threshold for track selection is imposed by the detector setup. At a momentum of about 200 MeV/c, a sharp drop in track reconstruction efficiency is observed for all particle types due to their substantial bending in the magnetic field and the large energy

loss through ionization within the TPC gas. The analysis considers only tracks with pseudorapidity $|\eta| < 0.8$. This selection guarantees that all tracks are fully contained within the active volume of the TPC, ensuring a consistent efficiency across the pseudorapidity.

The tracks utilized in this analysis can be categorized into two sets linked to features of the Pb–Pb data recorded in 2010. The first category of tracks consists of those reconstructed using the TPC and ITS, with an additional requirement of at least one hit in one of the SPD layers. These tracks are commonly employed in various analyses due to their good transverse momentum resolution. It is important to state that in the Pb–Pb data a large fraction of SPD modules were inactive. As a result, particle tracks with the requirement of at least one hit in the SPD layers suffer from non-uniform azimuthal acceptance. This non-uniformity introduce a bias in the measurements of elliptic flow. To address this issue and recover a uniform azimuthal acceptance, a second category of tracks is introduced. This category does not require a hit in the SPD layers. In order to minimize the impact on the transverse momentum resolution, the ITS-TPC parametrization of these tracks is constrained to the primary vertex. By combining both sets of tracks, which will be referred to as "hybrid tracks", a uniform azimuthal acceptance of tracks is restored.

For hybrid tracks with an SPD hit, a refit to the ITS during the third iteration of the track reconstruction is required, which is not the case for tracks without an SPD hit. Tracks with incorrectly assigned clusters in the ITS detector are rejected by requiring the χ^2 per ITS cluster to be less than 36.

To ensure an overall good quality of the tracks, several criteria connected to the TPC are imposed. Firstly, the χ^2 per TPC cluster must be less than four. Additionally, the track must be refitted during the third iteration of the Kalman filter approach within the TPC. To filter out short tracks, tracks with poor acceptance, and maintain an overall high track quality, each track is required to have a minimum of 70 out of a total of 159 clusters. To minimize the fraction of fake tracks and multiple reconstructions of the same track, the maximum ratio of shared clusters, defined as the clusters shared with other tracks relative to the total number of clusters used for the track reconstruction, is set at 0.4.

Secondary tracks, primarily originating from interactions with the detector material, are discarded by considering the distance of closest approach to the reconstructed primary vertex. The distance of closest approach in the transverse plane (rϕ-plane) is required to be less than 2.4 cm, and in the longitudinal plane (z-plane), it must be smaller than 3.2 cm. Furthermore, all tracks must satisfy the elliptic relation, expressed as

$$(\frac{d_0^{xy}}{2.4cm})^2 + (\frac{d_0^z}{3.2cm})^2 < 1 \tag{6.1}$$

Tracks originating from weak decays are filtered out using a flag applied to the track in the final step of the track reconstruction process.

Track selection criteria	Hybrid (default)	Tight DCA (variation)
Required hits in ITS layers	SPD: any / -	SPD:any / SDD: 1
Max. χ^2_{ITS} per cluster	36	36
Refit in ITS	yes / no	yes
Max. χ^2_{TPC} per cluster	4	4
Min. number of TPC clusters	70	70
Max. Fraction of shared TPC cluster	0.4	-
Refit in TPC	yes	yes
Max. distance to primary vertex (xy) [cm]	2.4	7 $sigma_{d_0^{xy}}$
Max. distance to primary vertex (z) [cm]	3.2	2
2D ellipse constraint	yes	yes
Kink tracks	no	no
Max. squared distance $\chi^2_{ITS-TPC}$	36	36
Pseudorapdity	(-0.8,0.8)	(-0.8,0.8)
Transverse momentum range [GeV/c]	(0.2,6)	(0.2,6)

Table 6.3: Summary of the track selection criteria. The different column correspond to different track types, used for the default value of the analysis and as in estimate of the systematic uncertainty related to the track selection. Multiple values in the column "Hybrid (default)" separated by a slash correspond to different track selections depending on if a hit was found in the SPD detector or not.

To investigate the influence of different track selection criteria on the measurements, we introduce a second category of tracks known as "Tight DCA tracks". The main difference between those tracks and the hybrid tracks lies in the stronger requirement on the distance of the closest approach (DCA) to the primary vertex. This stronger requirement serves to reduce the number of secondary particles, such as those generated in interactions with the detector material. This reduction in secondary particles enables us to quantify their impact on the elliptic flow analysis.

A summary of all the applied track selection criteria can be found in Table 6.3.

6.4 Pion, kaon, and (anti)proton identification

The identification of pions, kaons, and (anti)protons is achieved by utilizing both the $\langle \mathrm{d}E/\mathrm{d}x \rangle$ information from the TPC and the time-of-flight information from the TOF detector. The information is combined using a Bayesian approach, to exploit the particle identification capabilities of both detectors.

Figure 6.2, displays the deviation of signals measured in TPC and TOF from the expected response of pions for a subset of selected tracks without particle identification (left panel), a proton selection employing the nσ approach (middle panel), and a proton selection using

the Bayesian approach (right panel). It is clear that the separation between the two particle peaks is more pronounced in the two-dimensional plane compared to the separation in one dimension alone. The Bayesian approach offers better control over the purity of the particle sample in contrast to the traditional nσ approach (refer to Equation (5.9)).

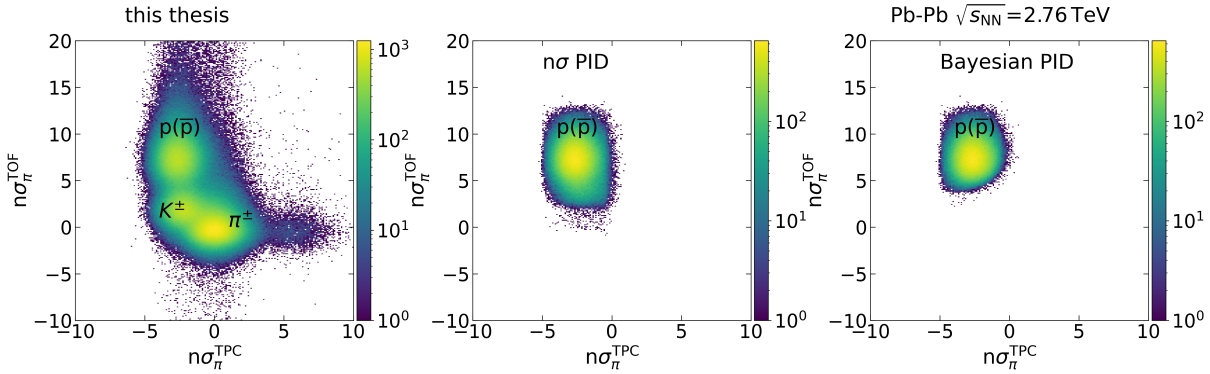

Figure 6.2: Combined particle identification in the TPC and TOF shown as a two-dimensional plot. The PID signals are expressed in nσ relative to the expected response for pions in each detector. The left panel shows a subsample of the data in the momentum range between 3.0 and 3.5 GeV/c without any PID. The middle (right) panel shows the particle identification of protons using the nσ (Bayesian) approach.

To combine the PID information from different detectors, the PID signals are first transformed into conditional probabilities that a particle of type H_i will yield a signal S. For detectors with Gaussian response, like the TPC, the conditional probability is defined as:

$$P(S|H_i) = \frac{1}{\sqrt{2\pi\sigma}} e^{-\frac{1}{2}n_\sigma^2} \tag{6.2}$$

Here, n_σ is defined as in Equation (5.9). The response of the TOF detector is slightly skewed to larger values of the time-of-flight and can be parametrized by a combination of a Gaussian and exponential function.

The conditional probabilities obtained from the TPC and TOF detectors can be combined by taking their product:

$$P(\vec{S}|H_i) = P_{TPC}(S_{TPC}|H_i) \cdot P_{TOF}(S_{TOF}|H_i) \tag{6.3}$$

The probability $P(\vec{S}|H_i)$ represents the likelihood that the set of detector signals $\vec{S}$ will be observed for a specific particle type H_i [126].

To determine the probability that a particle is of type H_i given the measured signals in both the TPC and TOF detectors, Bayes theorem is used [127]:

$$B(H_i) = P(H_i|\vec{S}) = \frac{P(\vec{S}|H_i)C(H_i)}{\sum_{k=e,\mu,\pi,\ldots} P(\vec{S}|H_k)C(H_k)} \tag{6.4}$$

Here, C_{H_i} is the prior probability of measuring the particle type H_i, serving as an informed estimate of the expected particle yields for a given event. By using Equation (6.4), one can assign a set of probabilities to each track, describing how likely the track corresponds to particle type H_i. For further insights into particle identification using the Bayesian approach in ALICE, along with a detailed explanation of how the prior probabilities are determined, refer to [126].

A track is attributed to a given particle type if the associated Bayesian probability $B(H_i)$ passes a certain threshold. For (anti)protons and kaons, this threshold is set at 85%, while for pions it is set at 95%. These thresholds are set above 50% to ensure that each track is only assigned one particle type, preventing the assignment of multiple particle types to a single track.

In addition to the PID selection based on the Bayesian probability, tracks assigned to a particular particle type required to be within three standard deviations from the expected value ofor this particle type ($|n\sigma^{H_i}_{TPC,TOF}| < 3$). This selection criterion remove potential outlier tracks, which may introduce a bias in the measurement of elliptic flow.

In cases when both TPC and TOF information are available, they are used for the calculation of the Bayesian probability. If tracks are outside of TOF detector acceptance only the TPC information is employed for calculations of the Bayesian probability.

Figure 6.3, shows the $\langle \mathrm{d}E/\mathrm{d}x \rangle$ as function of momentum for charged hadrons, pions, kaons and (anti)protons.

6.5 Corrections for non-uniform azimuthal acceptance

The corrections for the non-uniform azimuthal acceptance plays an important role in the anisotropic flow analysis, since biases from a non-uniform acceptance can mimic the physical signals. In the following sections, the corrections for non-uniformity of the flow vectors constructed using information from the ITS and TPC, and the ZDC detectors are described.

6.5.1 Correction of TPC flow vector

The non-uniform acceptance of a flow vector can be corrected by assigning a weight to each particle track during the calculation of the flow vector withEquation (3.1). A natural choice for these weights is the inverse of the detector efficiency ε:

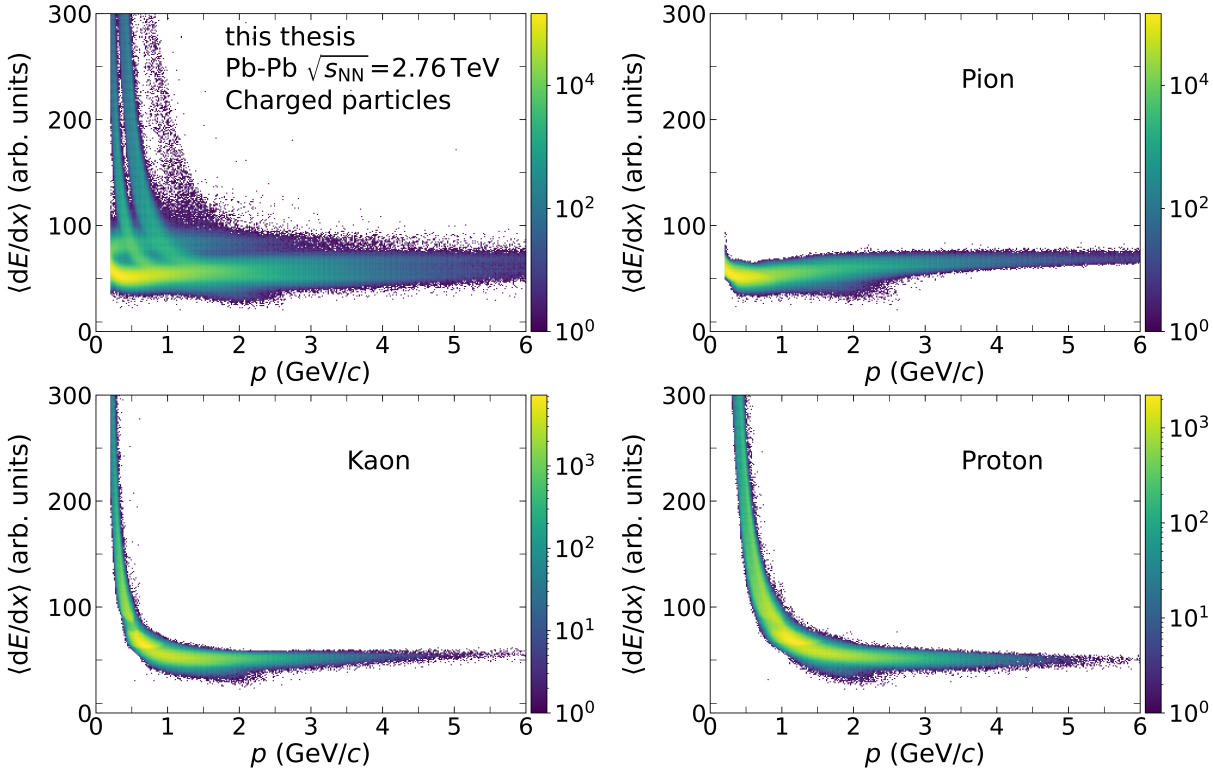

Figure 6.3: $\langle \mathrm{d}E/\mathrm{d}x \rangle$ as a function of momentum Different panels show distributions for charged hadrons, pions, kaons and (anti)protons.

$$w(\phi,\eta,\mathrm{PID},...) = \frac{1}{\varepsilon(\phi,\eta,\mathrm{PID},...)} \tag{6.5}$$

It is assumed that transverse momentum dependence of the efficiency factorizes:

$$\varepsilon(\phi,\eta,\mathrm{PID},...) = \alpha(\phi,\eta)\cdot\varepsilon(p_\mathrm{T})\cdot\varepsilon(\mathrm{PID}), \tag{6.6}$$

where α is the acceptance of particles in the detector, $\varepsilon(p_\mathrm{T})$ the track reconstruction efficiency and $\varepsilon(\mathrm{PID})$ the particle identification efficiency.

The acceptance correction α can be extracted directly from data. It can be calculated by comparing the number of tracks N in a given window $\Delta\phi$ to the maximum number of tracks N measured in a fixed $\Delta\phi$. Since the detector performance does not only depend on ϕ, but also on other variables, the acceptance correction is calculated as function of multiple variables:

$$\alpha(\phi,...) = N(\phi,...)/max(N(\phi,...)) \tag{6.7}$$

The acceptance is extracted as function of the azimuthal angle ϕ, the pseudorapidty η and the vertex position along the beam direction v_z.

The track reconstruction and PID efficiency are extracted using the Monte Carlo sample. Both efficiency corrections are calculated by taking the ratio of the reconstructed to generated number of particles in the Monte Carlo sample:

$$\varepsilon = N_{reconstructed}/N_{generated} \tag{6.8}$$

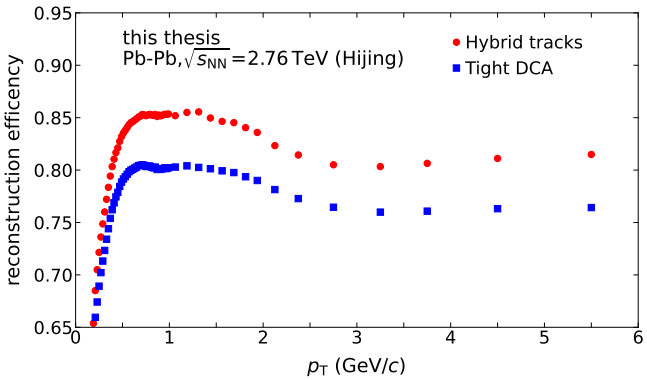

Figure 6.4: Track reconstruction efficiency as a function of the transverse momentum p_T for the two track categories (see text for details).

The track reconstruction efficiency is shown in Figure 6.4 for both hybrid and tight DCA tracks as a function of transverse momentum. One can observe a sharp reduction below 200 MeV/c above which it increases to a value about 83% (75%).

The efficiency of the identification of pions, kaons and (anti)protons is defined from Monte Carlo as the ratio of number of reconstructed particles to the number of generated particles of a given type. The purity is defined as the ratio of reconstructed particles matched to generated particles with respect to all reconstructed particles of a given type.

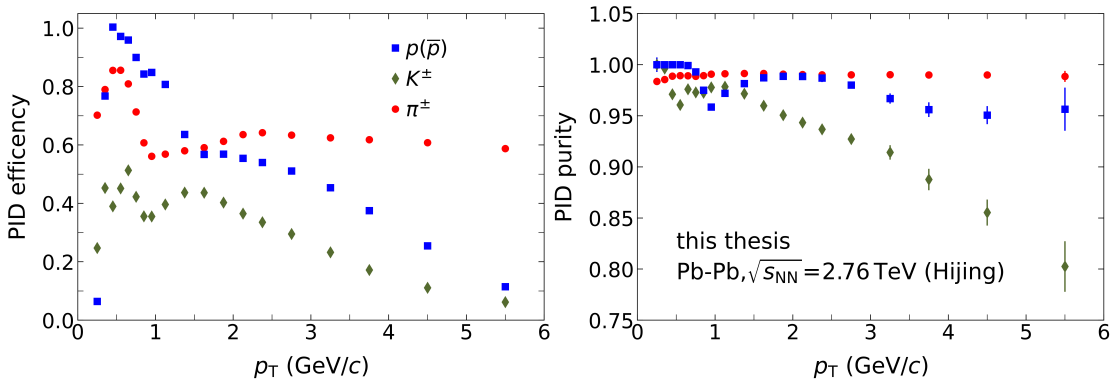

Figure 6.5: Purity and efficiency of the Bayesian particle identification of pions, kaons and (anti)protons.

The purity and efficiency of the Bayesian selection for pions, kaon and (anti)protons are shown in Figure 6.5. The purity is greater than 97% for $\pi^{\pm}$, 80% for $K^{\pm}$ and >95% for p($\overline{p}$). The Bayesian selection efficiency is the highest at low momenta, where TPC and TOF provide good particle discrimination, as outlined in Sections 4.2.2 and 4.2.3.

The correction for the efficiency as function of transverse momentum is important when extracting the p_{T}-integrated flow. In this analysis, the elliptic flow calculations are first performed as function of the transverse momentum and then they are used to extract the centrality-dependent results. In regions, where a strong dependence of both elliptic flow and detector efficiency on p_{T} is expected, a finer binning is needed. This is the case at low p_{T}, where the track reconstruction efficiency shows strong p_{T} dependence.

The comparison of results with and without efficiency correction will be discussed in Section 6.8.4. The main analysis is performed without applying corrections for p_{T}-dependent efficiency to the flow vectors of pions, kaons and (anti)protons.

6.5.2 Correction of ZDC flow vector

The ZNA and ZNC detectors non-uniformities in the aziumtuhal acceptance arise due to imperfect calibration and distortions in the distribution of incoming neutron spectators. The distributions of the first harmonic flow vector q_1 for both the ZNA and ZNC are plotted Figures 6.6 and 6.7 as a function of centrality and the three-dimensional position of the primary vertex. The latter is presented as normalized deviation in units of nσ:

$$n\sigma = \frac{V_i - \langle V_i \rangle}{\sigma_{V_i}} \tag{6.9}$$

Here, V_i is the vertex position in on of the three dimensions denoted as i, $\langle V_i \rangle$ the mean of the vertex position over all collisions in an analysis run and σ_{V_i} is its width. The red line in Figures 6.6 and 6.7 shows the event averaged flow vector position.

For a perfectly uniform detector acceptance, the flow vector averaged over many events, should be zero. However, this is not the case for the ZNA and ZNC flow vectors, for which a strong dependence on the different variables is observed, with the smallest deviation for the primary vertex position along the beam line (V_z). These biases are corrected via a data-driven method utilizing the flow vector from the ZDC itself. The data-driven correction is independent of imperfections of the Monte Carlo simulation. In addition, the correction method can be used in case of holes in the azimuthal acceptance.

The procedure for the non-uniform acceptance correction is described in detail in[128]. The main step is the recentering of flow vectors, which involves subtraction the average flow vector from the flow vector of each event:

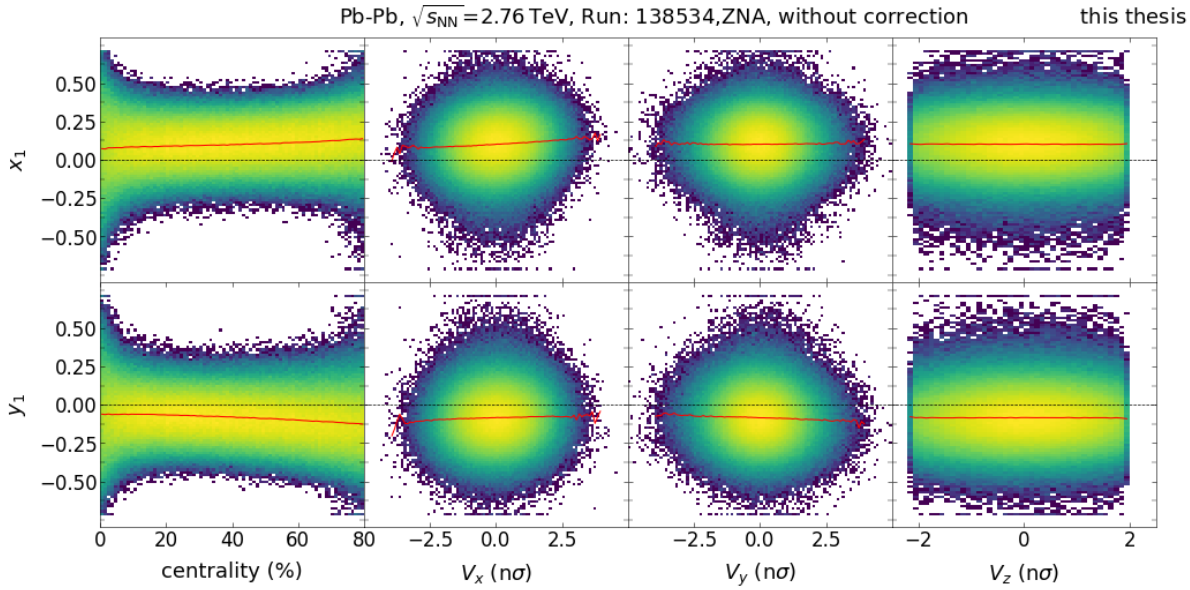

Figure 6.6: Distribution of the flow vector components x_1 and y_1 from the ZNA detector as a function of centrality and three-dimensional vertex position. The data is shown for a single data run. The red line corresponds to the average of the distribution.

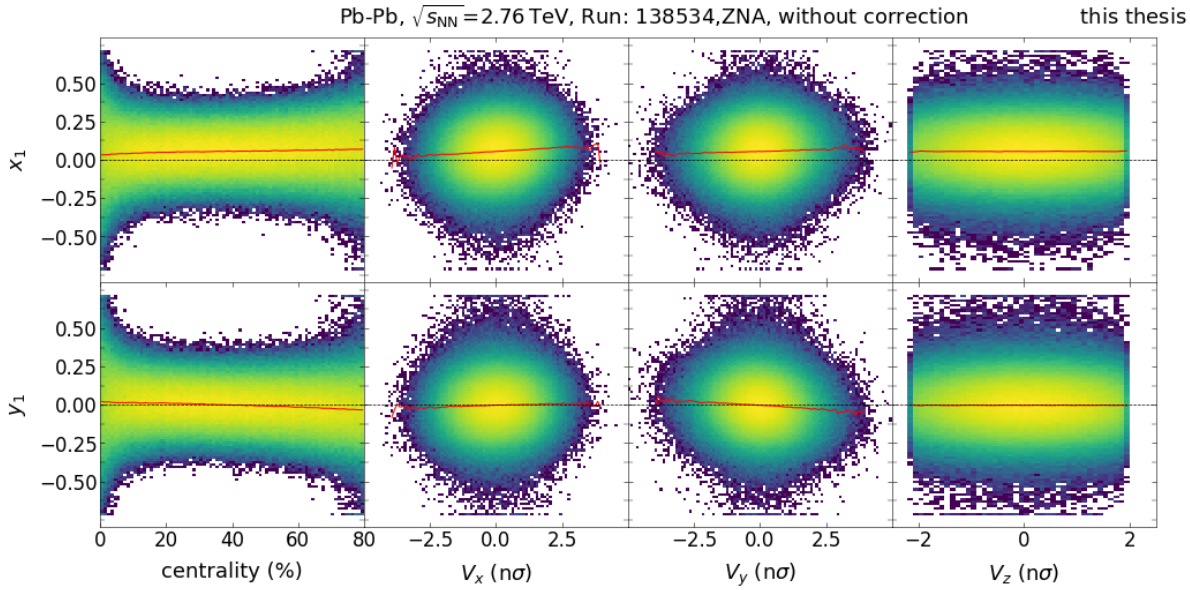

Figure 6.7: Distribution of the flow vector components x_1 and y_1 from the ZNC detector as a function of centrality and three-dimensional vertex position. The data is shown for a single data run. The red line corresponds to the average flow vector value.

$$x_n = x_n - \overline{x_n} \tag{6.10}$$

$$y_n = y_n - \overline{y_n} \tag{6.11}$$

The recentering procedure is simultaneously applied in four dimensions, including centrality and the three-dimensional positions of the primary vertex. This choice of a four-dimensional treatment allows the correction of correlations between the various variables. Given the potential variations in time and alterations to the experimental setup across different data-taking runs, the recentering procedure is individually applied to each of the analysis runs.

The binning for the recentering process is summarized in Table 6.4. The binning of the three-dimensional position of the primary vertex is performed using the $n\sigma$ variable. Each bin contains a similar number of events, what guarantees sufficient statistics at the edges of the distribution, to ensure a statistically stable determination of the correction.

Variable	Range	Number of bins	Binning
Time (data Runs)	(0,85)	85	equidistant
Centrality	(0,70)	70	equidistant
V_x [nσ]	(-4,4)	3	[-4,-0.42,0.42,4]
V_y [nσ]	(-4,4)	3	[-4,-0.42,0.42,4]
V_z [nσ]	(-4,4)	3	[-4,-0.42,0.42,4]

Table 6.4: Binning used to apply the four-dimensional recentering correction of the ZNA and ZNC flow vector.

The flow vectors in both the ZNA and ZNC detectors, before and after the recentering procedure, are shown in Figure 6.8. After the recentering procedure the average flow vector is found to be zero within statistical uncertainties.

The performance of the recentering procedure can be controlled by calculating before and after the recentering the correlators $\langle XX \rangle$, $\langle YY \rangle$, $\langle XY \rangle$ and $\langle YX \rangle$, where the first (second) flow vector is extracted from the ZNA (ZNC) detector. Figure 6.9 present these four correlators before and after the recentering procedure. These correlators, as discussed in Section 3.2.2, play a role of the resolution correction when extracting $v_2\{\Psi_{SP}\}$. The $\langle XY \rangle$ and $\langle YX \rangle$ should vanishand $\langle XX \rangle$ and $\langle YY \rangle$ are anticipated to exhibit negative values since spectators are deflected in the opposite direction, as reported in [42]. For numerical calculations, if $\langle XX \rangle$, $\langle YY \rangle$ is much larger than $\langle YX \rangle$, $\langle XY \rangle$ the resolution parameter is used for calculations of $v_2\{\Psi_{SP}\}$.

As shown in Figure 6.9, the four correlators exhibit different centrality dependencies before and after recentering. Before recentering, the $\langle XX \rangle$ and $\langle YY \rangle$ shows a spurious positive

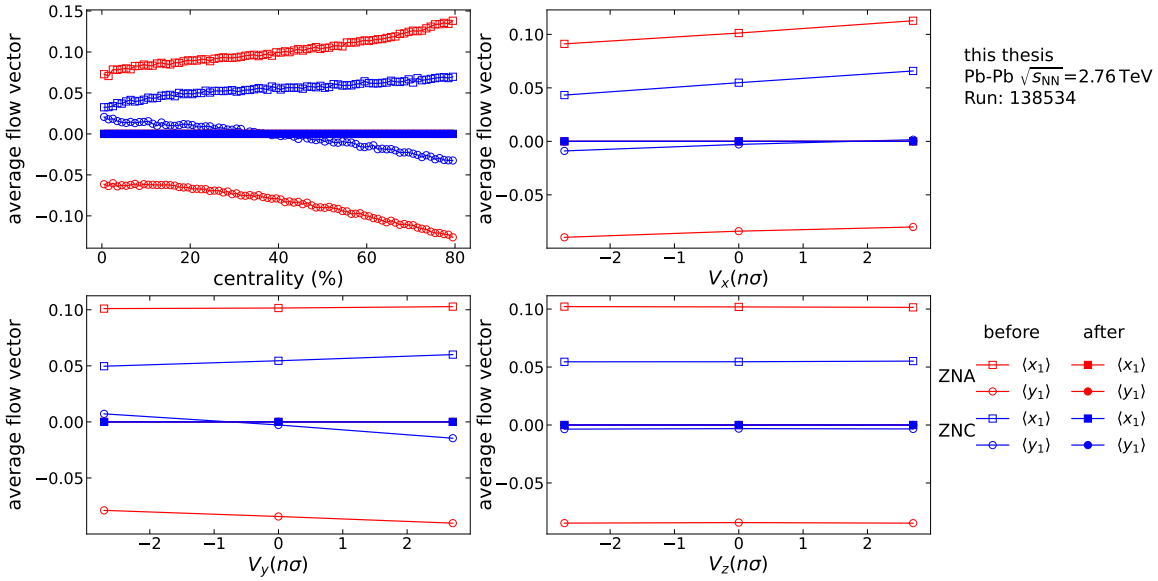

Figure 6.8: Average flow vector components x_1 and y_1 of ZNA and ZNC as a function of centrality and three-dimensional vertex position before (open markers) and after (full markers) the recentering is applied.

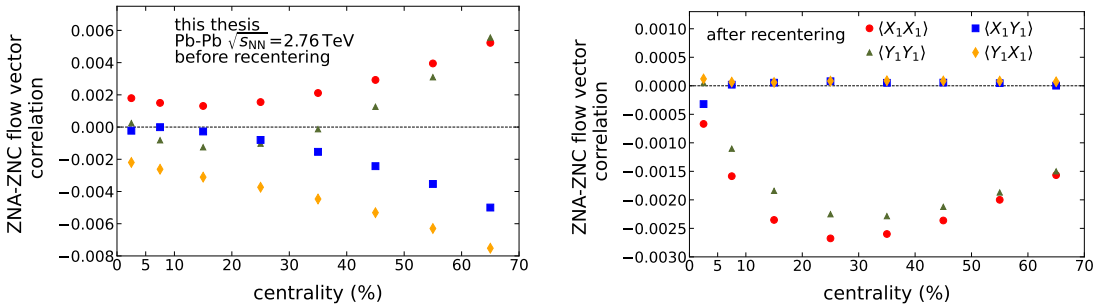

(a) (b)

Figure 6.9: Correlations between ZNA and ZNC flow vector components as a function of centrality. The left panel shows the correlation before the recentering on the flow vector components is applied, whereas the right panel showns the correlations after recentering.

correlation in some centrality regions, while $\langle$YX$\rangle$ and $\langle$XY$\rangle$ deviate significantly from zero across all centrality ranges, with the largest deviation in peripheral events. After recentering, $\langle$YX$\rangle$ and $\langle$XY$\rangle$ approach zero, with minor variations that is later used to assign systematic uncertainties. The $\langle$XX$\rangle$ and $\langle$YY$\rangle$ components are negative across the entire. These components reach a minimum at approximately 20-30%, corresponding to the maximum ZDC resolution to the spectator plane. This can be explained by the fact that in this centrality range, the number of neutrons reaching the ZDC detector is maximal.

6.6 Extracting the centrality-dependence of $v_2\{\Psi_{SP}\}/v_2\{4\}$

This section describes the procedure to calculate the ratio of the elliptic flow with respect to the spectator plane ($v_2\{\Psi_{SP}\}$, as defined in Equation 3.54), to that with respect to the participant plane, represented by the four-particle cumulant ($v_2\{4\}$, as defined in Equation 3.24). Both, $v_2\{\Psi_{SP}\}$ and $v_2\{4\}$ are extracted as a function of transverse momentum p_T in the centrality classes between 5% to 60% for pions, kaons, and (anti)protons. The extraction of the elliptic flow and the corresponding ratios for pions, kaons and (anti)protons as a function of centrality is complicated due to the differences of the p_T acceptance and efficiency of different particle types.
Rather than extrapolating for unmeasured low-p_T regions, the ratio $v_2\{\Psi_{SP}\}/v_2\{4\}$ is first calculated as a function of p_T and then fitted with two (constant and a linear) functions.

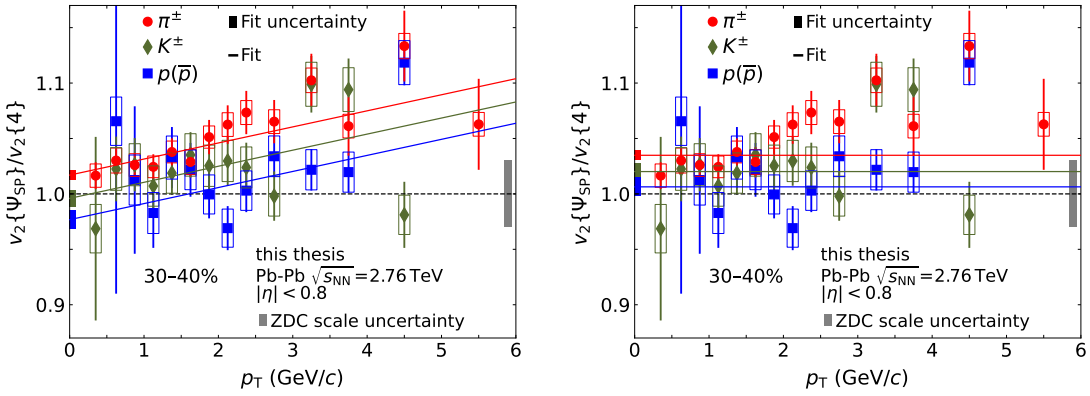

(a) (b)

Figure 6.10: $v_2\{\Psi_{SP}\}/v_2\{4\}$ ratio of pions, kaons and (anti)protons as a function of transverse momentum for the centrality interval between 30-40%. The colored lines show the linear (left panel) and constant (right panel) fit performed to each particle species in the transverse momentum range between 0.2 to 3.0 GeV/c. These fits are used to extract the slope and intercept at $p_T = 0$ GeV/c.

From the linear function, the slope of the ratio is determined, while the constant gives the $v_2\{\Psi_{SP}\}/v_2\{4\}$ ratio in a given centrality class. The intercept at $p_T = 0$ GeV/c, obtained from the linear fit, is smaller than the one derived from the constant fit. The assumption that the constant fit is a better proxy for the integrated $v_2\{\Psi_{SP}\}/v_2\{4\}$ was validated by comparing the different methods for extracting $v_2\{\Psi_{SP}\}/v_2\{4\}$ using charged hadrons. The results between the integrated $v_2\{\Psi_{SP}\}/v_2\{4\}$ and the $v_2\{\Psi_{SP}\}/v_2\{4\}$ from the constant fit were found to be in good agreement with each other.

Figure 6.10 presents the $v_2\{\Psi_{SP}\}/v_2\{4\}$ ratio for pions, kaons, and (anti)protons. It also shows the results of the linear fit (left panel) and constant fit (right panel) used

to extract the slope and $v_2\{\Psi_{\mathrm{SP}}\}/v_2\{4\}$ ratio for centrality of 30-40%. The results of the fits with a constant function to the ratios $v_2\{\Psi_{\mathrm{SP}}\}/v_2\{4\}$ can be found in appendix 1.1.

In addition to the ratio of $v_2\{\Psi_{\mathrm{SP}}\}/v_2\{4\}$ for pions, kaons, and (anti)protons as a function of centrality, a double ratio is extracted with respect to the charged hadron. This double ratio, can be obtained either by dividing the centrality integrated results or first dividing results in each p_{T} bin and then fitting the ratio with a constant. The latter is used for the main resuls, because systematic uncertanties related to the p_{T} dependence of the efficiency cancel out.

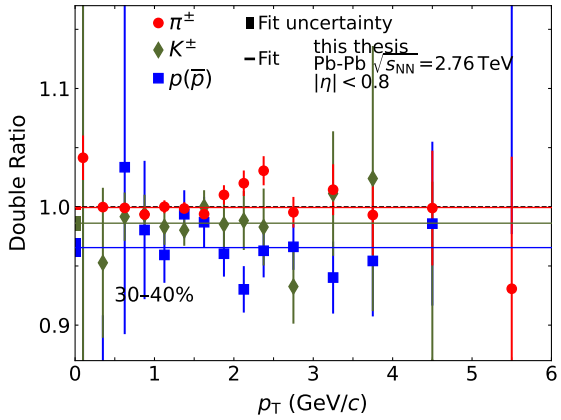

Figure 6.11: Double ratio for pions, kaons and (anti)protons as a function of transverse momentum for the centrality interval 30-40%. The colored line shows the fit each particle species in the transverse momentum range 0.2 to 3.0 GeV/c. These fits are used to extract the centrality dependent double ratio.

Figure 6.11 illustrates the double ratio as a function of p_{T} for the centrality range 30-40% for pions, kaons, and (anti)protons, along with the constant fit used to extract its centrality dependence result. The fits to the double ratios for the other centrality classes is found in Appendix 1.1. The centrality dependence is discussed in details in Chapter 7.

6.7 Systematic uncertainties

Systematic uncertainties can originate from different aspects, including a lack of understanding of the experimental setup, deficiencies in the applied corrections, or limitations of the analysis procedure. The procedure used to evaluate systematic uncertainty is summarized below. The first step involves identifying potential sources of systematic uncertainties. This often includes varying parameters or assumptions that are part of the main analysis strategy. After potential sources are identified, variations to the analysis strategy are used to understand how sensitive the results are to different aspects of the analysis. To determine the statistical significance of these variations, different tests are performed, such as the

Barlow criteria, which assesses the impact of variations in a purely statistical context. In the last step, all significant variations are added in quadrature and quoted as systematic uncertainties.

The systematic uncertainties can vary depending on the particle type, centrality, and transverse momentum p_{T}. The significance of these variations depend on the amount of available statistics for a given particle species, and as a result, they may be less pronounced for less abundant particles (e.g., (anti)protons compared to pions). In cases where no clear trend is observed for less abundant particles, the more abundant particles can be used as a reference for decision-making. The total systematic uncertainties are estimated by varying the analysis configuration, including event and track selection criteria, or by altering specific analysis steps. The details of each specific variation will be discussed in more depth in the next section.

6.7.1 Sources of systematic uncertainties

The sources of systematic uncertainties can be divided into the following groups:

- Track selection
- Event selection
- Particle identification
- Non-uniformity corrections
- Measurment extraction technique
- Scale uncertainty from non-zero ZNA-ZNC cross-correlations

The first three types of systematic uncertainties is straightforward to extract by varying the numerical values of the selection criteria. To estimate the bias due to the third and fourth types of systematic uncertainties, the analysis procedure needs to be changed.

Table 6.5 provides a summary of the various systematic uncertainties and variations performed with respect to the main analysis. A detailed overview of these uncertainties are provided in the following sections.

6.7.2 p_{T}-dependent uncertainties

In the case of p_{T}-differential analysis for each centrality range and particle species, the significance of a variation is assessed on a case-by-case basis using a combination of the following criteria, ordered by importance for decision-making:

Variation	Default setting	variation setting
Track Selection		
Track filterbit	hybrid tracks	tight DCA tracks
Number TPC cluster	< 70	< 90
χ^2_{TPC} per cluster	$0.1 < \chi^2_{TPC} < 4$	$0.1 < \chi^2_{TPC} < 4$
Track charge	all	positive, negative
Event Selection		
Primary vertex z-position	< 10	< 8
Centrality estimator	V0M	CL1
Solenoid magnet polarity	both	separate
Particle identification		
Threshold Bayesian PID	P(pi) > 0.95	P(pi) > 0.95
	P(K) > 0.85	P(K) > 0.9
	P(p) > 0.85	P(p) > 0.9
Non-uniformity corrections		
Recentering	4d	Iterative 1d
Non-uniform acceptance	no weights	ϕ weights
Observable extraction technique		
ZDC Q-vector component	averaged	XXX,XYY, sqrt(yxy,yyx)
ZDC resolution bias	not applied	applied

Table 6.5: Summary of variations of the selection criteria or analysis strategy used to extract of the systematic uncertainties.

- Barlow criteria [129], which helps to judge if a variation of the analysis setup is significant:

$$Barlow(B) = \frac{|x_{var} - x_{std}|}{|\sigma_\Delta|} \,. \tag{6.12}$$

  Here $|\sigma_\Delta| = \sqrt{|\sigma^2_{var} - \sigma^2_{std}|}$ is the difference between variances σ_{var} and σ_{std} of the result for cut variation and the standard analysis setting, respectively.

- Whether a majority of p_{T} bins in the ratio for a given analysis variation show a consistent trend in a given direction.

For each variation, the procedure involves checking whether the Barlow criteria is greater than two (B > 2) or whether a majority of points show a consistent trend in a particular direction.

Depending on whether the systematic variation is believed to be only dependent on the centrality of the collision (i.e., p_{T}-independent) or also on the p_{T} of the particles (i.e., p_{T}-dependent), the assignment of the systematic uncertainty for a given variation is as follows:

- For variations not expected to depend on p_{T}, the uncertainties are smoothed over the entire p_{T} range using a constant fit applied to all p_{T} bins.
- In the case of p_{T}-dependent variations, where certain p_{T} regions exhibit large deviations between the default and varied analysis strategy (e.g., due to Bayesian purity variation), the regions with strong deviations, typically below $p_{\mathrm{T}} < 2$ GeV/c, are retained as they are. For points at higher $p_{\mathrm{T}} > 2$ GeV/c, a constant fit is applied to provide a smoother representation of the uncertainties.

6.7.3 Centrality dependent uncertainties

The p_{T}-integrated results presented in this thesis are $v_2\{\Psi_{\mathrm{SP}}\}/v_2\{4\}$, the slope of the $v_2\{\Psi_{\mathrm{SP}}\}/v_2\{4\}$ ratio, and the double ratio of different particle type to that of charged particles. For each analysis variation, the p_{T}-differential ratio $v_2\{\Psi_{\mathrm{SP}}\}/v_2\{4\}$ is fitted with either linear or a constant function, as described in Section 6.6. The double ratios are fitted with a constant function. The fit results are then examined for significance of the deviation using criteria similar to those employed for p_{T}-differential analysis.

An analysis variation is considered significant if the Barlow criteria is greater than two (B > 2) for a majority of points or if a majority of points exhibit a consistent deviation in a particular direction. If an analysis variation is considered significant, the absolute systematic uncertainty is smoothed as a function of centrality using a polynomial function. Both linear and quadratic functions are tested, and the one with the better χ^2 fit is used.

6.8 Variations of the analysis strategy

In this section, the outcome of varying the analysis configurations is presented for $v_2\{\Psi_{\mathrm{SP}}\}$, $v_2\{2, |\Delta\eta| > 1\}$, $v_2\{4\}$, and $v_2\{\Psi_{\mathrm{SP}}\}/v_2\{4\}$ as function of p_{T} in all considered centrality classes for pions, kaons and (anti)protons. Also, analysis variations are presented for the ratio $v_2\{\Psi_{\mathrm{SP}}\}/v_2\{4\}$, slope of $v_2\{\Psi_{\mathrm{SP}}\}/v_2\{4\}$ and double ratio as a function of centrality. Each set of results is displayed in three different panels. The top panel shows the observables for both the default and varied cases, the middle panel displays the ratio of the main results to that for varied configuration, and the bottom panel provides the Barlow criteria values as defined in Equation (6.12).

6.8.1 Event selection variation

Vertex position along the beam direction (V_z)

Variation with the position of the primary vertex along the beam axis is shown in Figure 6.6, which shows that the vertex position have an effect on the signal observed in the ZDC. This may induce a correlated bias on both ZDCs, which if observed cannot be removed

by non-uniformity corrections. Tracks originating from events with large deviations of the vertex position from the center of the barrel can suffer from a worsening of the tracking performance due to the edge effects, potentially introducing a bias in the flow vector extracted from the produced particles. For all observable of interest no systematic deviation is observed.

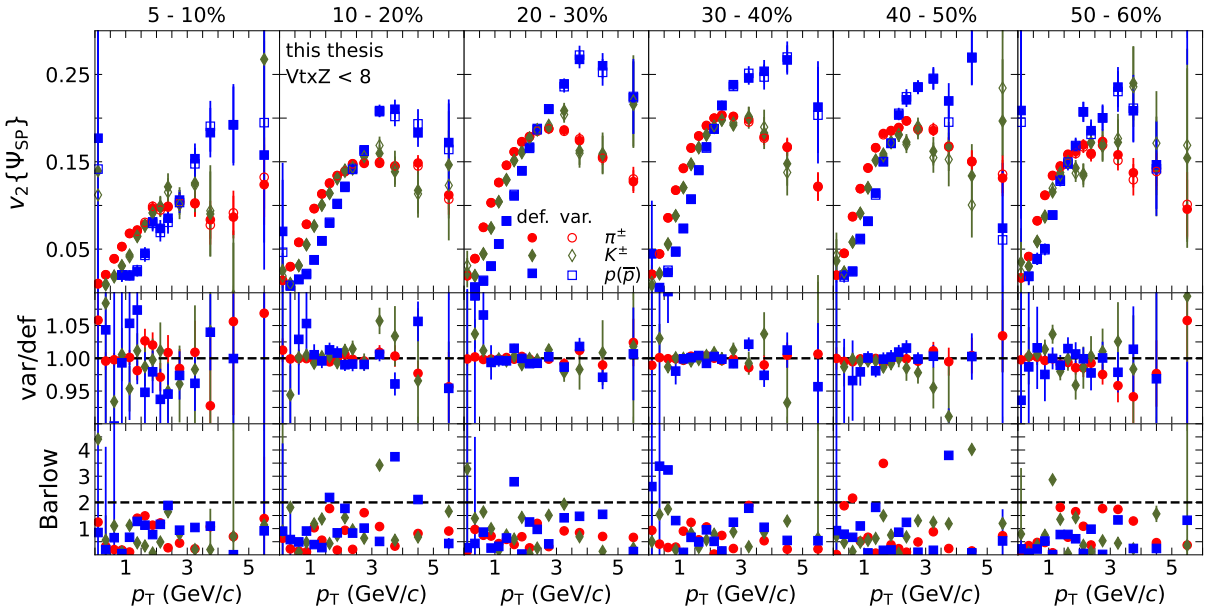

Figure 6.12: Comparison of the varied selection with the default selection for $v_2\{\Psi_{SP}\}$ for pions (red markers), kaons (green markers) and (anti)protons (blue markers) as a function of transverse momentum in all centrality intervals analyzed.

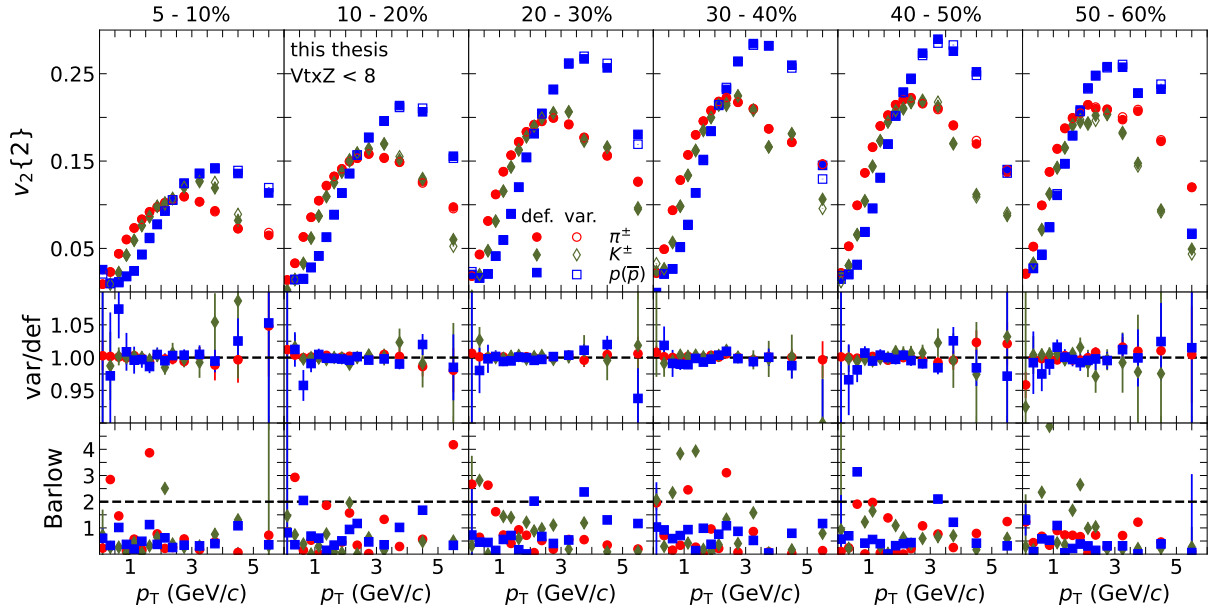

Figure 6.13: Comparison of the varied selection with the default selection for $v_2\{4\}$ for pions (red markers), kaons (green markers) and (anti)protons (blue markers) as a function of transverse momentum in all centrality intervals analyzed.

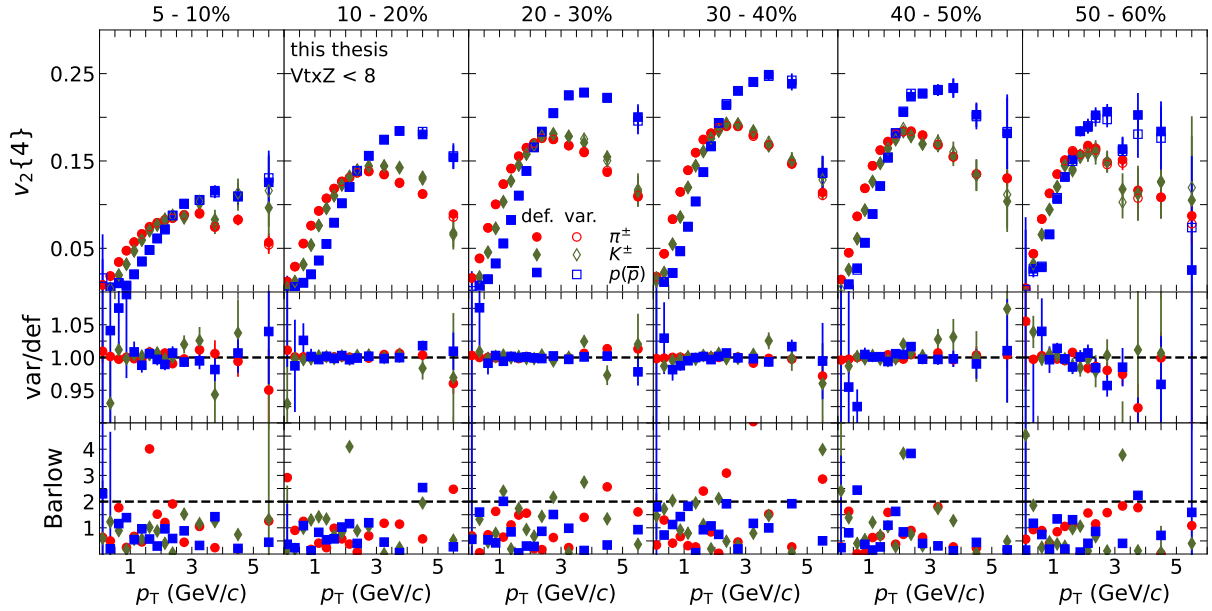

Figure 6.14: Comparison of the varied selection with the default selection for $v_2\{4\}$ for pions (red markers), kaons (green markers) and (anti)protons (blue markers) as a function of transverse momentum in all centrality intervals analyzed.

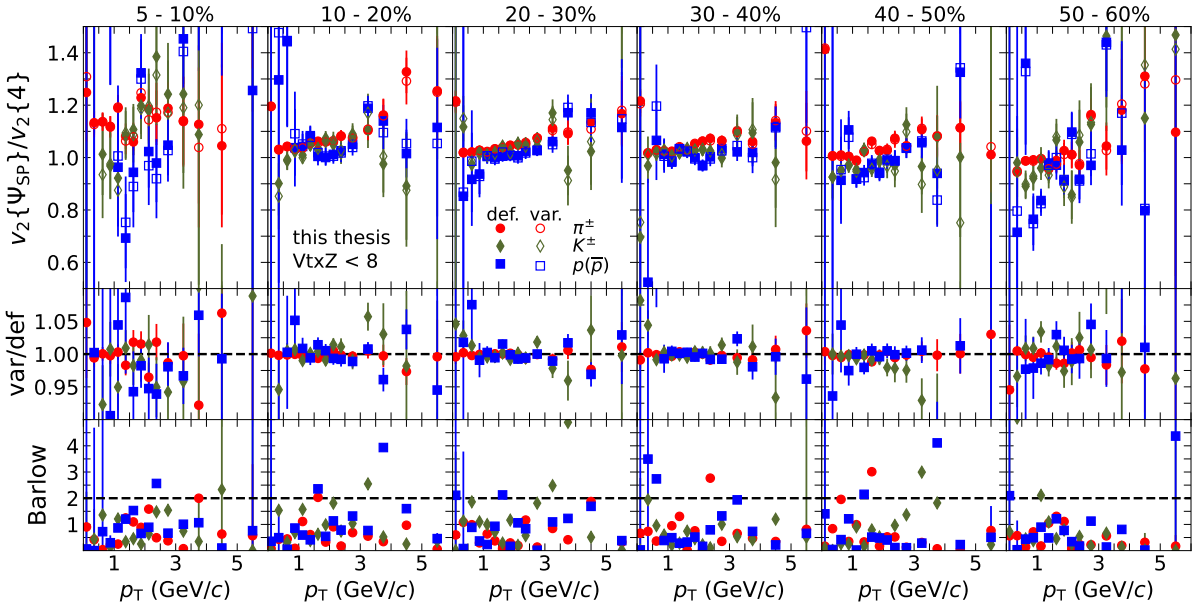

Figure 6.15: Comparison of the varied selection with the default selection for $v_2\{\Psi_{SP}\}/v_2\{4\}$ for pions (red markers), kaons (green markers) and (anti)protons (blue markers) as a function of transverse momentum in all centrality intervals analyzed.

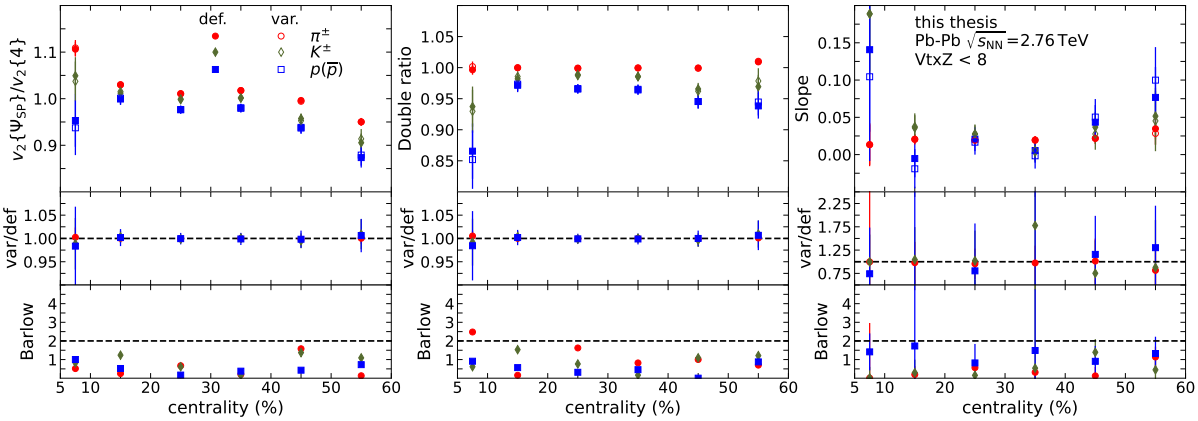

Figure 6.16: Comparison of the varied selection with the default selection for the ratio $v_2\{\Psi_{SP}\}/v_2\{4\}$, slope and double ratio for pions (red markers), kaons (green markers) and (anti)protons (blue markers) as a function of centrality.

Change of the centrality estimator

A potential source of systematic uncertainties is the choice of the centrality estimator. The default centrality estimator is the V0M, which relies on information from the forward detectors V0A and V0C. The CL1 estimator is based on the total number of SPD clusters and is used to check sensitivity to the acceptance for charged particles used for centrality

determination.
For all observables, the variation caused by the choice of centrality estimator is found to be statistically significant. The largest contribution to this variation is attributed to the most central and most peripheral collisions. It's important to note that the centrality estimator variation is assumed to be p_{T}-independent.

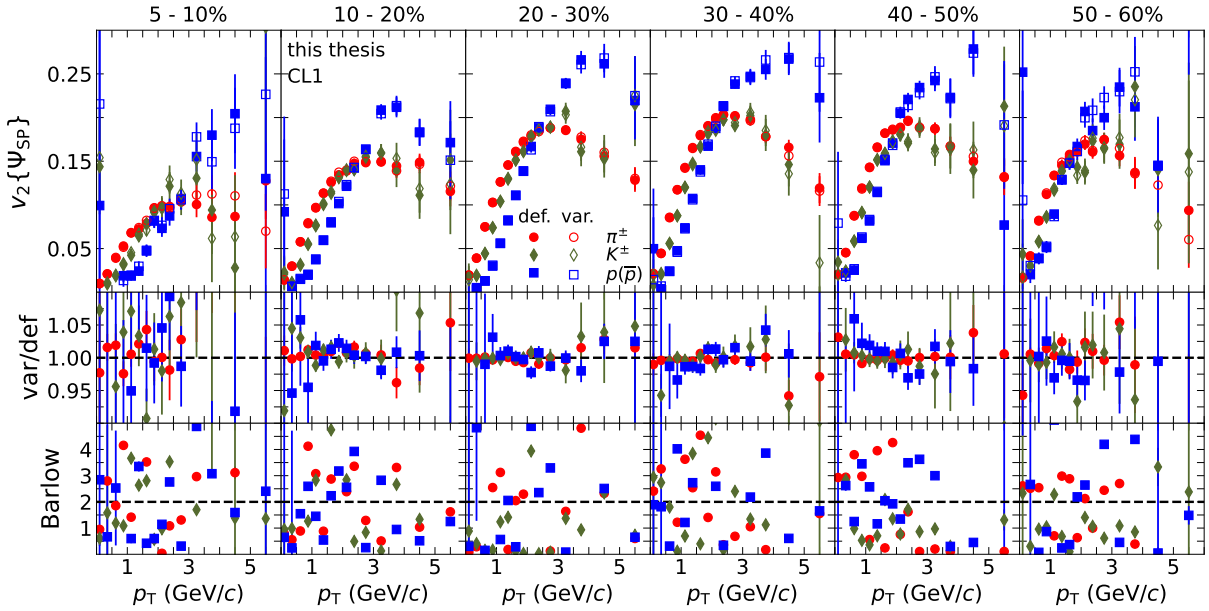

Figure 6.17: Comparison of the varied selection with the default selection for $v_2\{\Psi_{\mathrm{SP}}\}$ for pions (red markers), kaons (green markers) and (anti)protons (blue markers) as a function of transverse momentum in all centrality intervals analyzed.

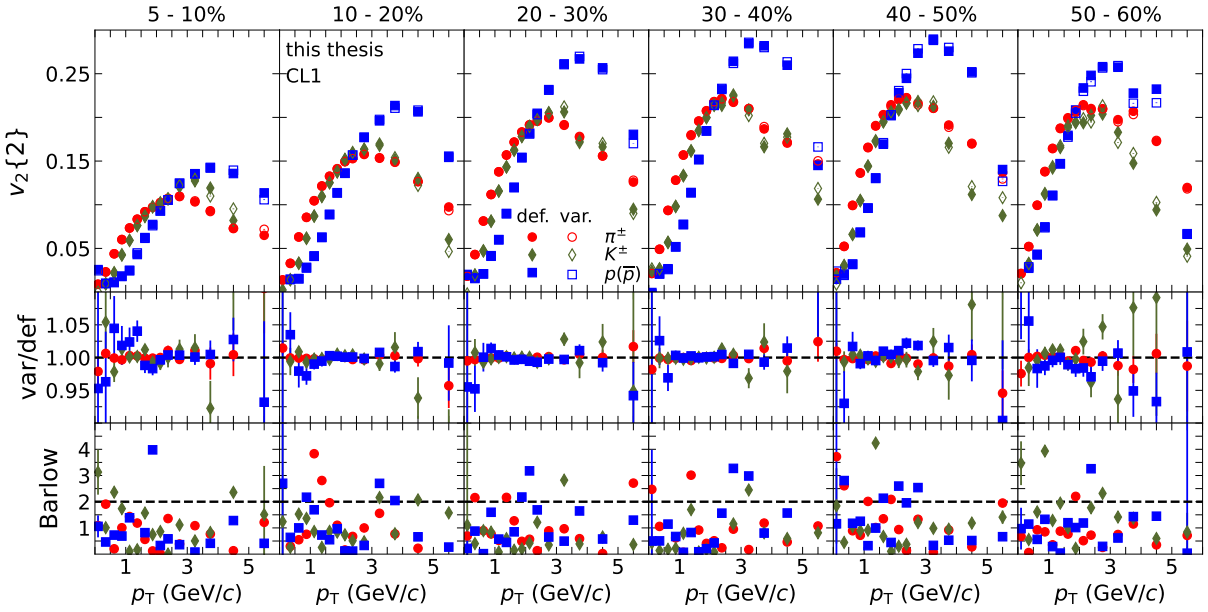

Figure 6.18: Comparison of the varied selection with the default selection for $v_2\{4\}$ for pions (red markers), kaons (green markers) and (anti)protons (blue markers) as a function of transverse momentum in all centrality intervals analyzed.

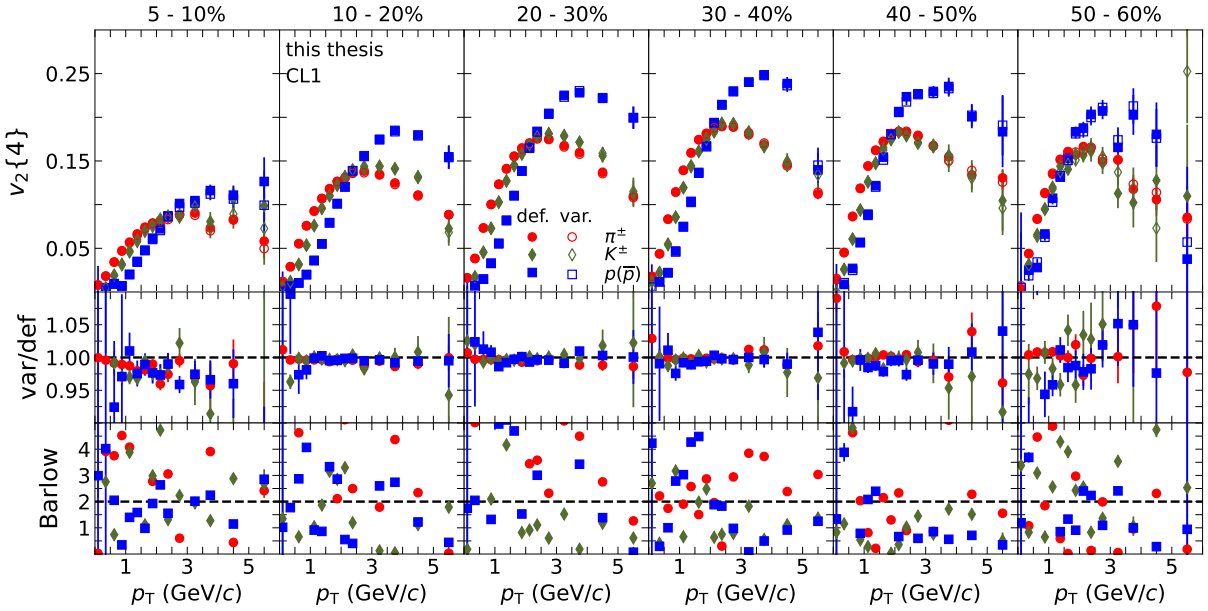

Figure 6.19: Comparison of the varied selection with the default selection for $v_2\{4\}$ for pions (red markers), kaons (green markers) and (anti)protons (blue markers) as a function of transverse momentum in all centrality intervals analyzed.

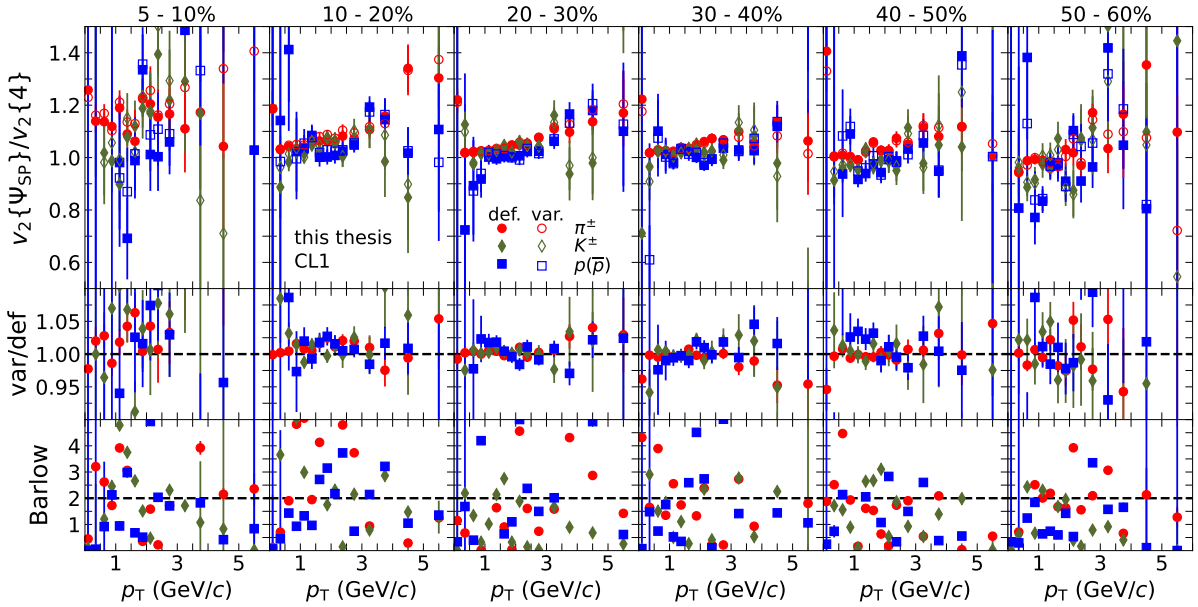

Figure 6.20: Comparison of the varied selection with the default selection for $v_2\{\Psi_{SP}\}/v_2\{4\}$ for pions (red markers), kaons (green markers) and (anti)protons (blue markers) as a function of transverse momentum in all centrality intervals analyzed.

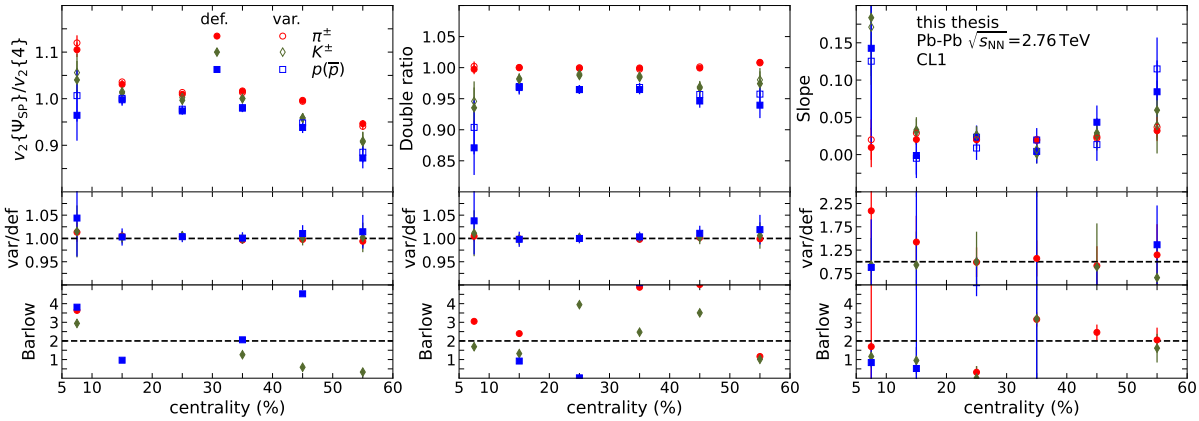

Figure 6.21: Comparison of the varied selection with the default selection for the ratio $v_2\{\Psi_{SP}\}/v_2\{4\}$, slope and double ratio for pions (red markers), kaons (green markers) and (anti)protons (blue markers) as a function of centrality.

Magnetic polarity

The Pb–Pb data analyzed in this thesis was recorded with two different polarities of the solenoid magnet: positive and negative. Both data samples with different magnetic polarities have similar sizes. This variation is considered to be sensitive to the correlations between the ZDC and TPC flow vectors, as well as the extraction of the TPC flow vector

itself.
When comparing the results from the individual polarity settings of the solenoid magnet with the default selection, the variations exhibit opposite behavior. As a result, the systematic uncertainties for the magnetic polarity were estimated by comparing the data sample of positive magnetic polarity with the data sample of negative magnetic polarity and taking half of the observed variations as the systematic uncertainty.

Despite the Barlow criteria not suggesting statistical significance of the variation, a systematic uncertainty was assigned to all observables due to the observed shift of a majority of data points in the same direction. It is important to note that the magnetic polarity variation is assumed to be p_{T}-independent.

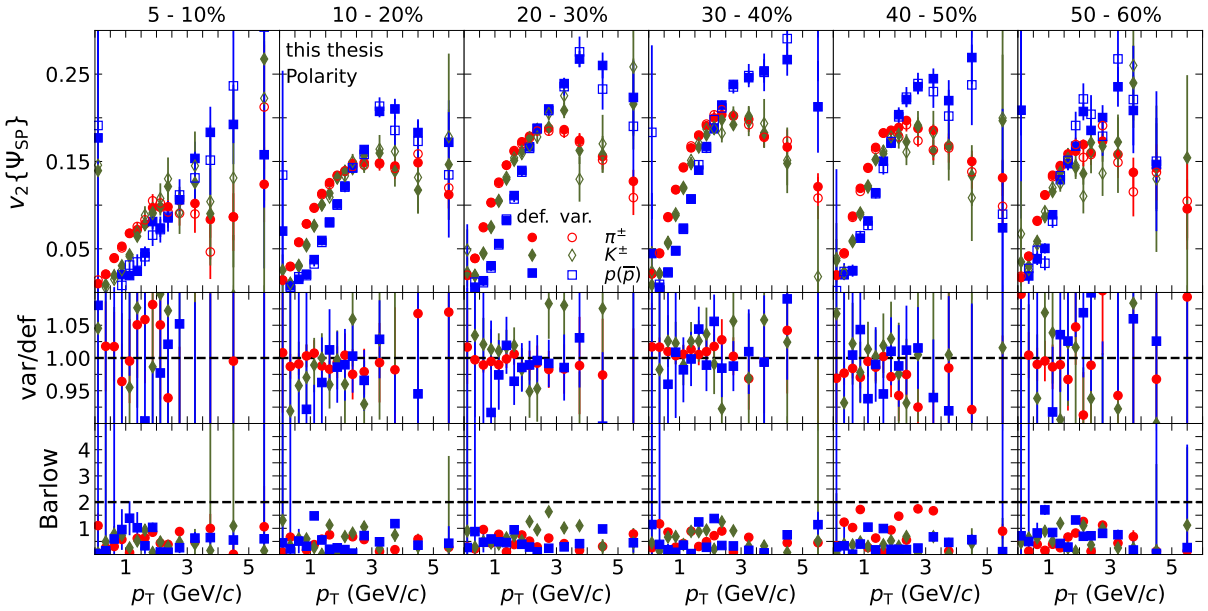

Figure 6.22: Comparison of the varied selection with the default selection for $v_2\{\Psi_{\mathrm{SP}}\}$ for pions (red markers), kaons (green markers) and (anti)protons (blue markers) as a function of transverse momentum in all centrality intervals analyzed.

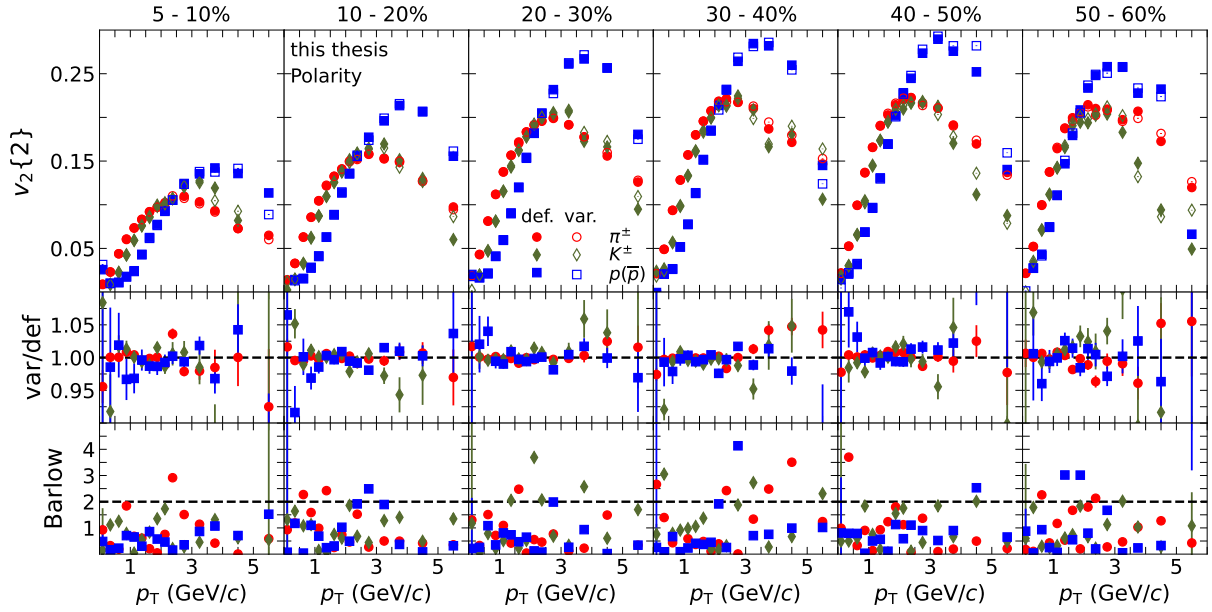

Figure 6.23: Comparison of the varied selection with the default selection for $v_2\{4\}$ for pions (red markers), kaons (green markers) and (anti)protons (blue markers) as a function of transverse momentum in all centrality intervals analyzed.

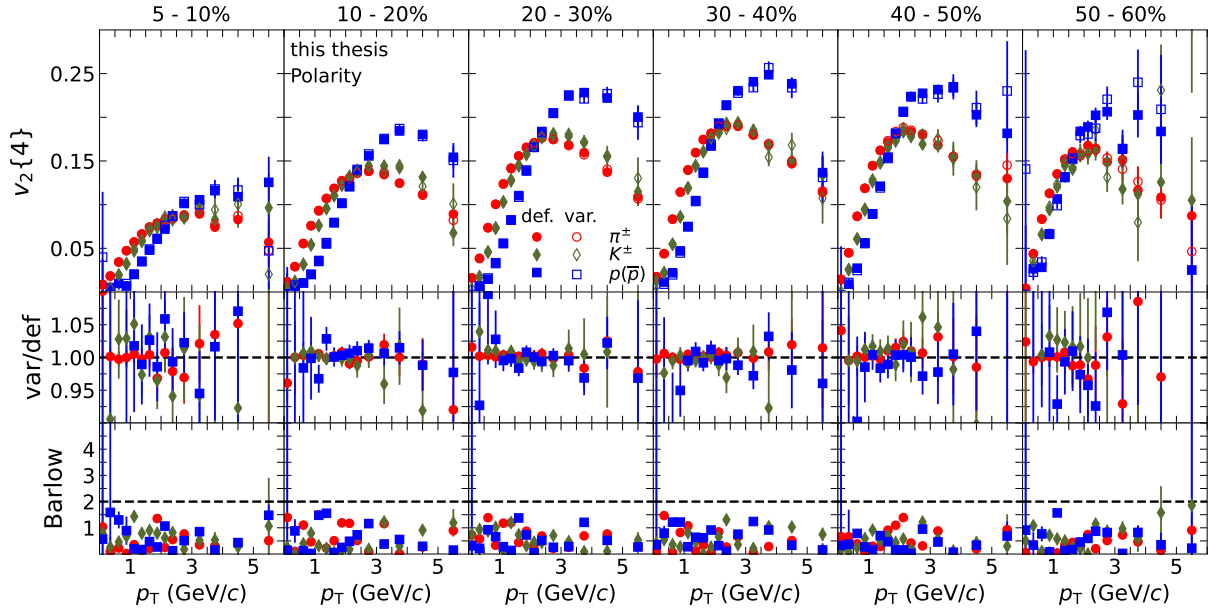

Figure 6.24: Comparison of the varied selection with the default selection for $v_2\{4\}$ for pions (red markers), kaons (green markers) and (anti)protons (blue markers) as a function of transverse momentum in all centrality intervals analyzed.

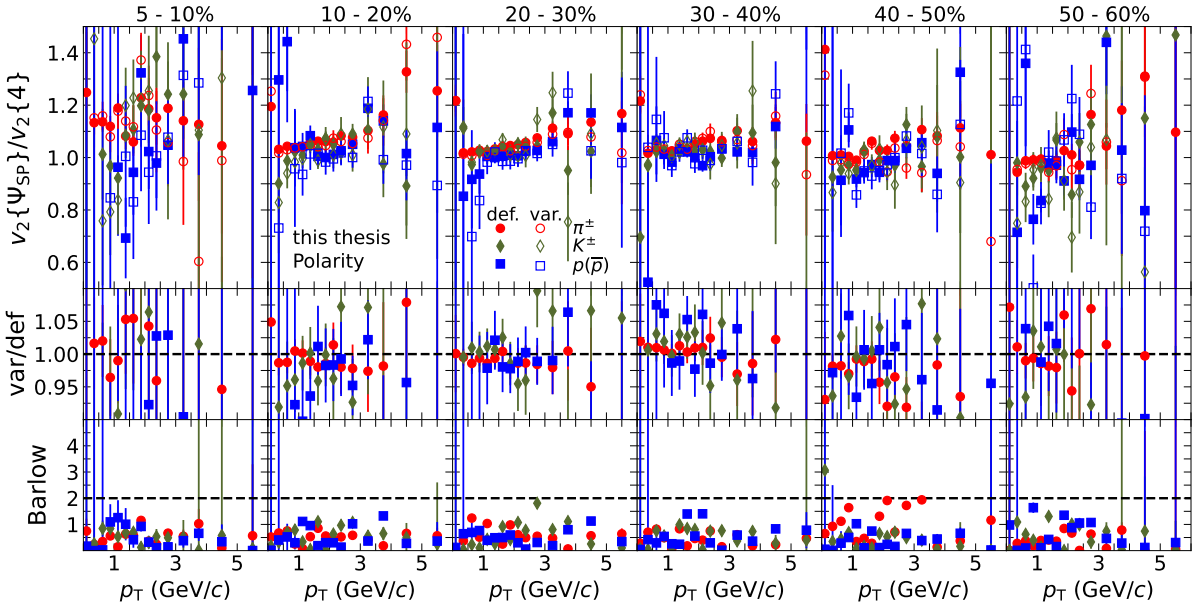

Figure 6.25: Comparison of the varied selection with the default selection for $v_2\{\Psi_{SP}\}/v_2\{4\}$ for pions (red markers), kaons (green markers) and (anti)protons (blue markers) as a function of transverse momentum in all centrality intervals analyzed.

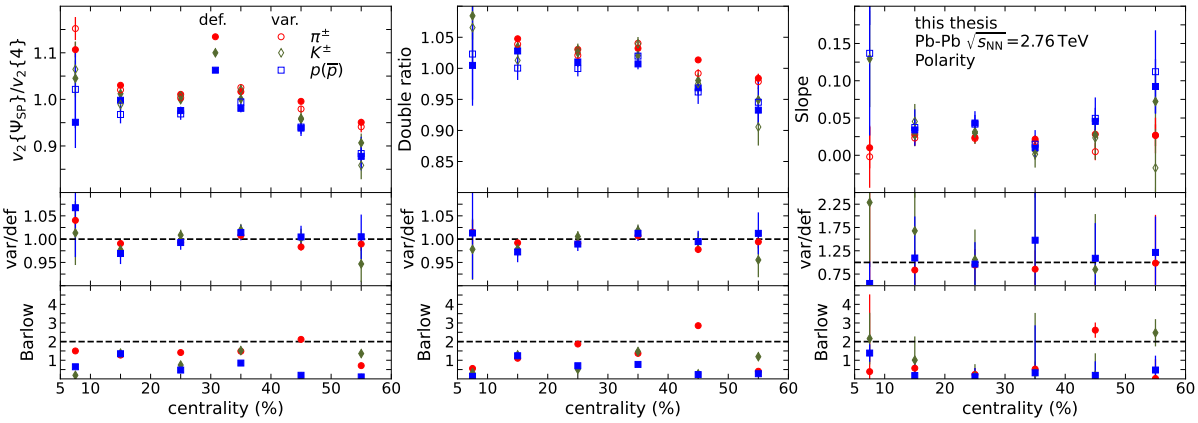

Figure 6.26: Comparison of the varied selection with the default selection for the ratio $v_2\{\Psi_{SP}\}/v_2\{4\}$, slope and double ratio for pions (red markers), kaons (green markers) and (anti)protons (blue markers) as a function of centrality.

6.8.2 Track selection variations

Charge variation

As a systematic variation, flow observables $v_2\{\Psi_{SP}\}$, $v_2\{2, |\Delta\eta| > 1\}$ and $v_2\{4\}$ were extracted using separately positive and negative charged tracks. A significant deviation was observed for protons and anti-protons at low p_T. The reason for this is that a fraction

of the proton sample is contaminated by protons from spallation processes in the silicon of the ITS. Since most of the points for protons below $p_{\mathrm{T}} = 1$ GeV/c show deviations of the order of 20% and larger, the protons were excluded from the calculation of the flow observables $v_2\{4\}$ and $v_2\{\Psi_{\mathrm{SP}}\}$ below $p_{\mathrm{T}} < 1.0$ GeV/c.

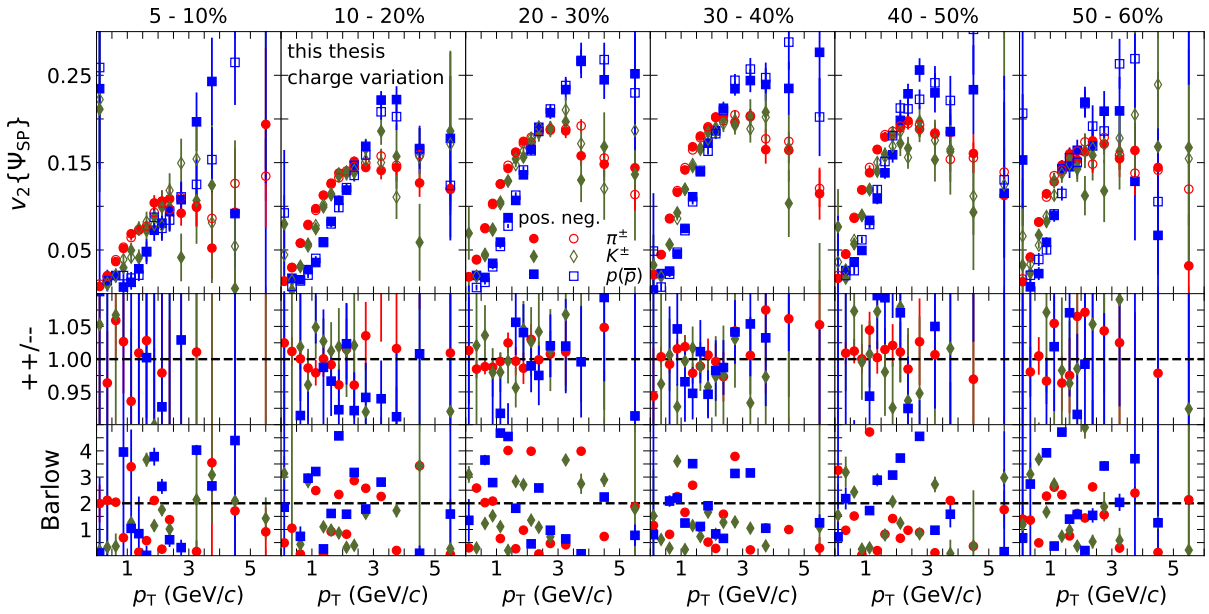

Figure 6.27: Comparison of the varied selection with the default selection for $v_2\{\Psi_{\mathrm{SP}}\}$ for pions (red markers), kaons (green markers) and (anti)protons (blue markers) as a function of transverse momentum in all centrality intervals analyzed.

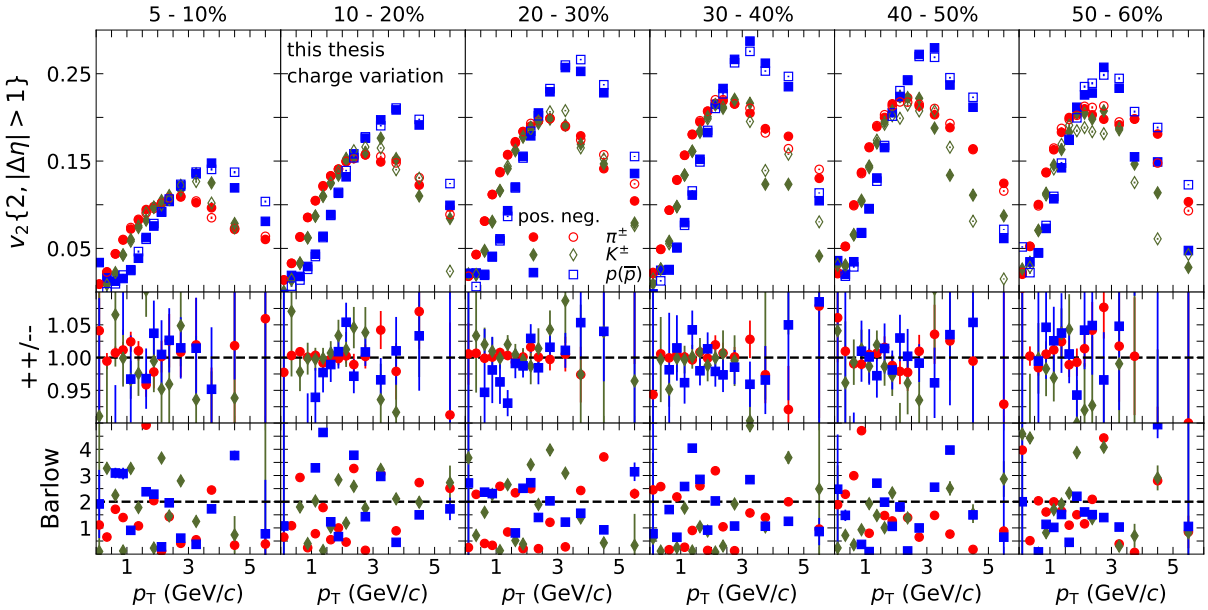

Figure 6.28: Comparison of the varied selection with the default selection for $v_2\{4\}$ for pions (red markers), kaons (green markers) and (anti)protons (blue markers) as a function of transverse momentum in all centrality intervals analyzed.

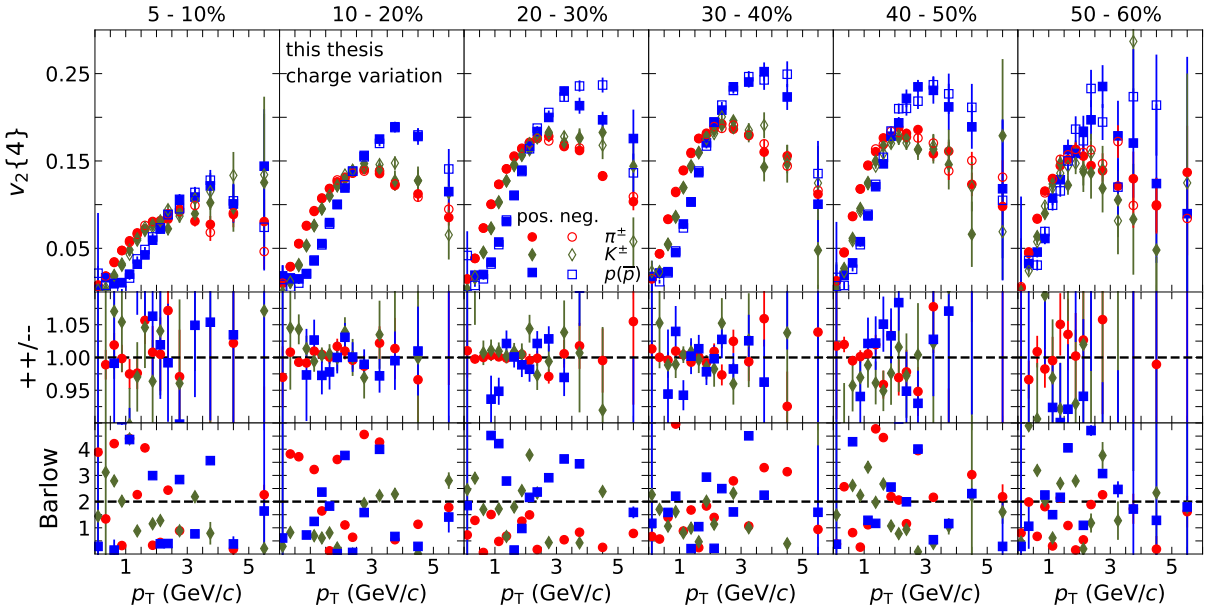

Figure 6.29: Comparison of the varied selection with the default selection for $v_2\{4\}$ for pions (red markers), kaons (green markers) and (anti)protons (blue markers) as a function of transverse momentum in all centrality intervals analyzed.

Variation of the track types

As described in Section 6.3, two categories of tracks are considered: hybrid tracks and tight DCA tracks. The default tracks used for this analysis are hybrid tracks, which were discussed in Section 6.3. The primary difference between both track categories is the tighter selection in the distance-of-closest approach to the primary vertex for the tight DCA tracks. This variation checks the influence on the measurement of particles that do not originate from the heavy-ion collision but are instead created in the detector material. These secondary particles introduce non-flow contributions to the flow observable, not originating from the initial geometry of the collision. During the analysis, no statistically significant variation was found due to this change in track category.

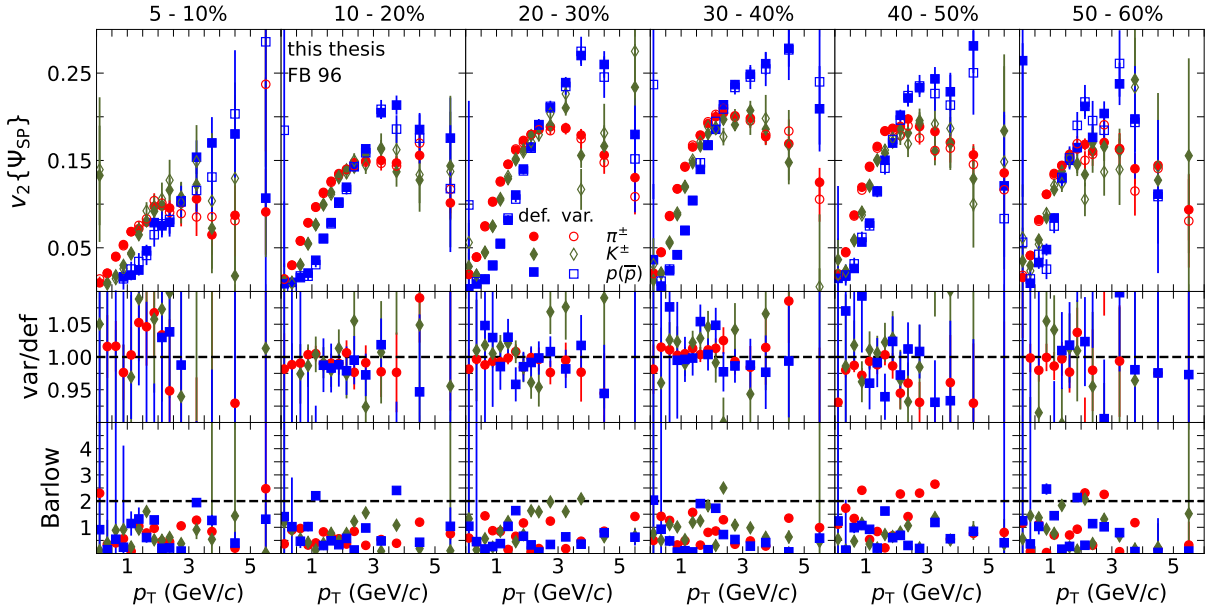

Figure 6.30: Comparison of the varied selection with the default selection for $v_2\{\Psi_{SP}\}$ for pions (red markers), kaons (green markers) and (anti)protons (blue markers) as a function of transverse momentum in all centrality intervals analyzed.

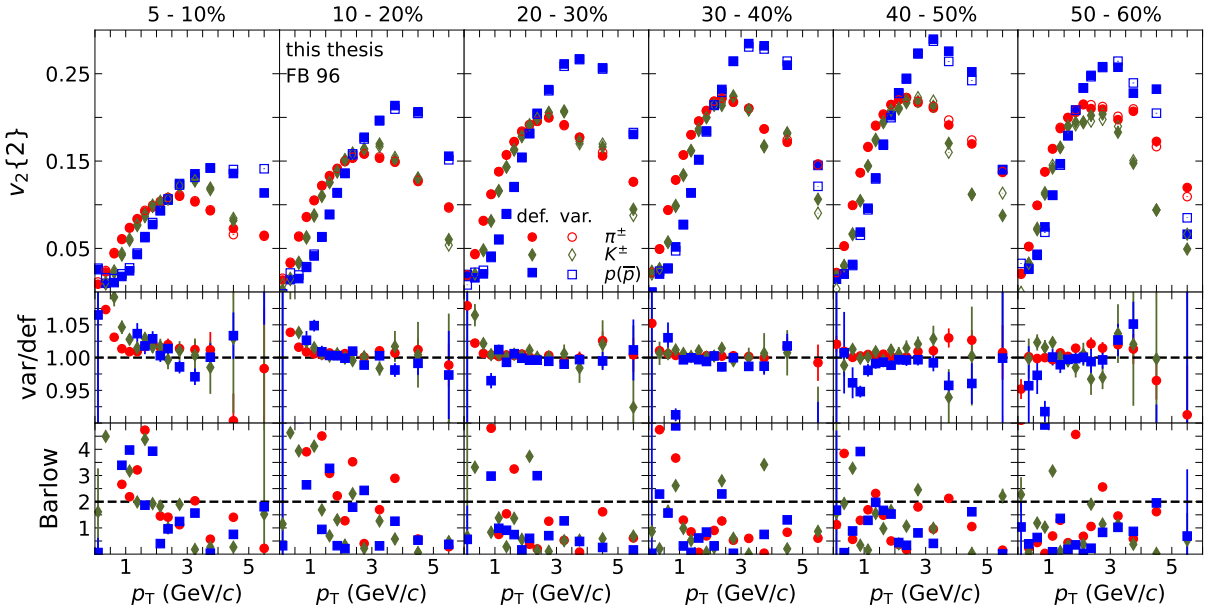

Figure 6.31: Comparison of the varied selection with the default selection for $v_2\{4\}$ for pions (red markers), kaons (green markers) and (anti)protons (blue markers) as a function of transverse momentum in all centrality intervals analyzed.

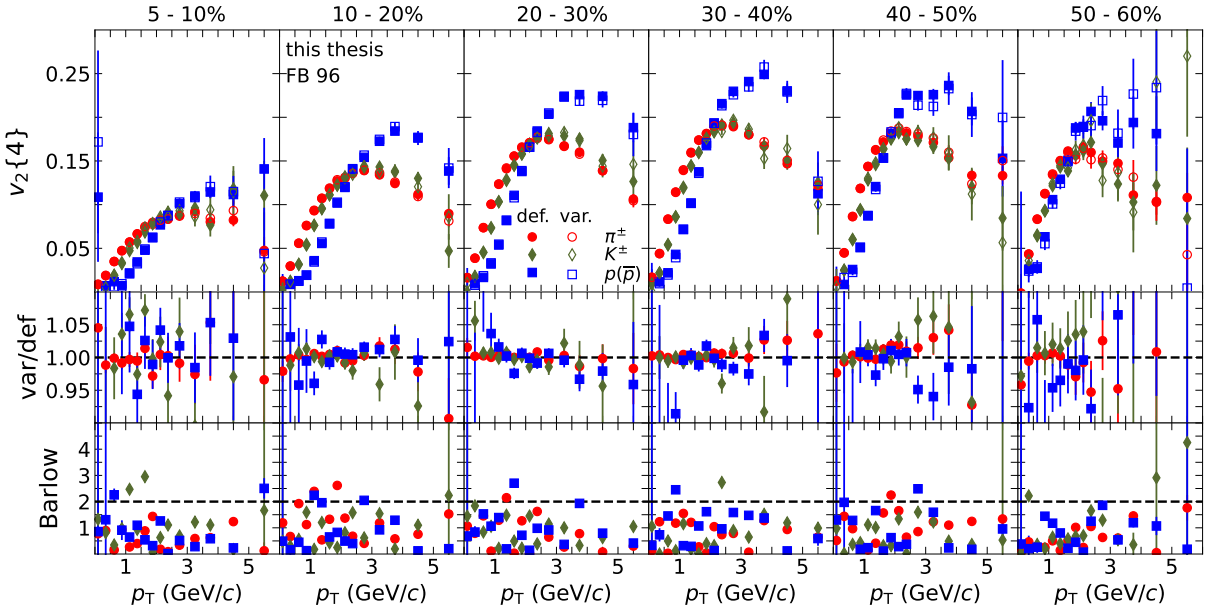

Figure 6.32: Comparison of the varied selection with the default selection for $v_2\{4\}$ for pions (red markers), kaons (green markers) and (anti)protons (blue markers) as a function of transverse momentum in all centrality intervals analyzed.

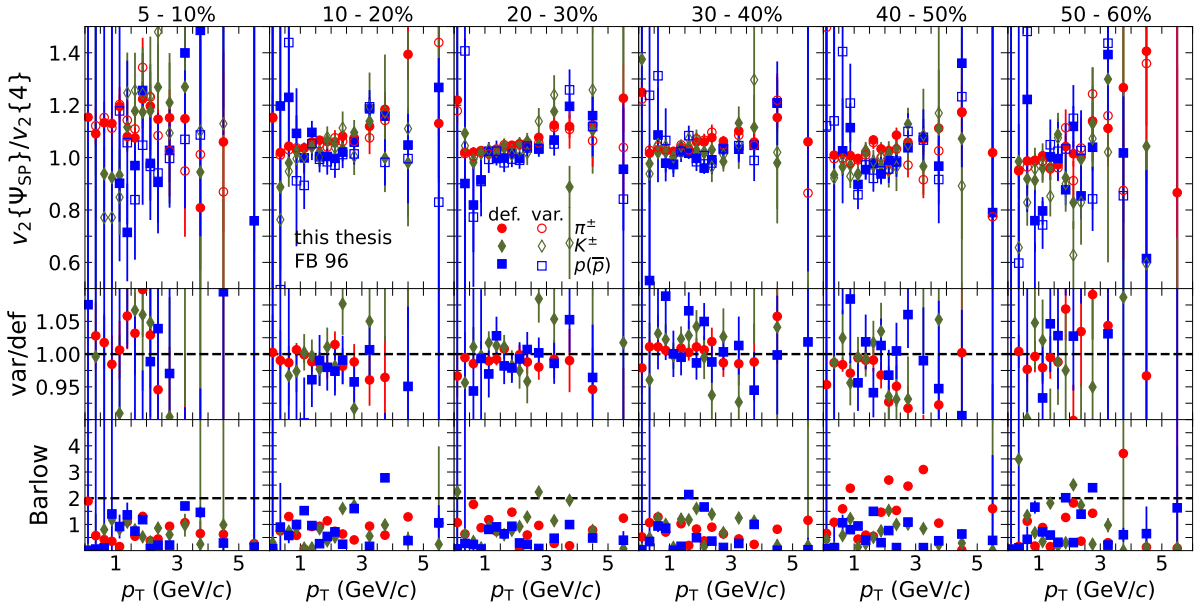

Figure 6.33: Comparison of the varied selection with the default selection for $v_2\{\Psi_{SP}\}/v_2\{4\}$ for pions (red markers), kaons (green markers) and (anti)protons (blue markers) as a function of transverse momentum in all centrality intervals analyzed.

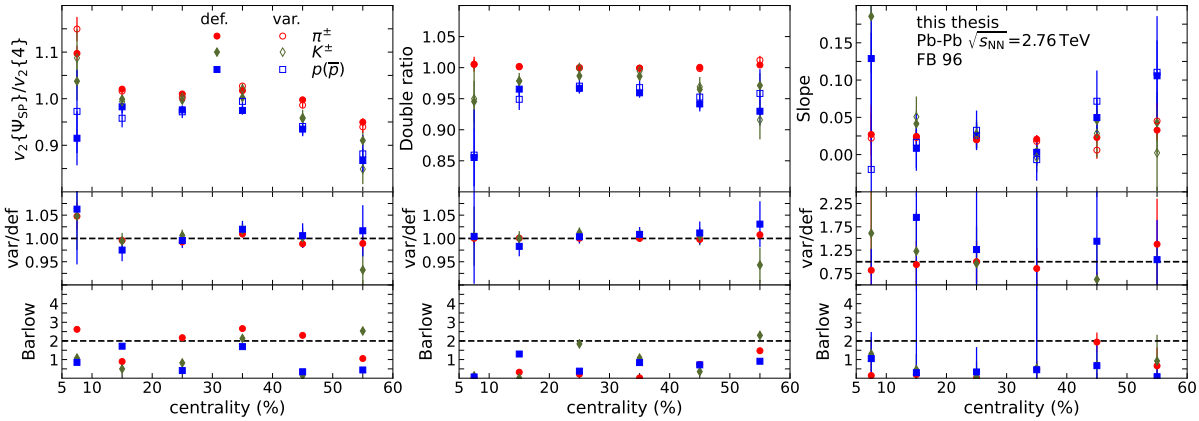

Figure 6.34: Comparison of the varied selection with the default selection for the ratio $v_2\{\Psi_{SP}\}/v_2\{4\}$, slope and double ratio for pions (red markers), kaons (green markers) and (anti)protons (blue markers) as a function of centrality.

Variation with the number of TPC clusters

Increasing the number of clusters assigned to a track improve tracking accuracy and serves as a test of the tracking performance in the flow analysis. This variation can also potentially bias the results towards larger transverse momenta, as low-momentum tracks tend to have a smaller number of clusters assigned. Based on the Barlow criteria, no systematic

uncertainty was assigned to the variation in the number of TPC clusters.

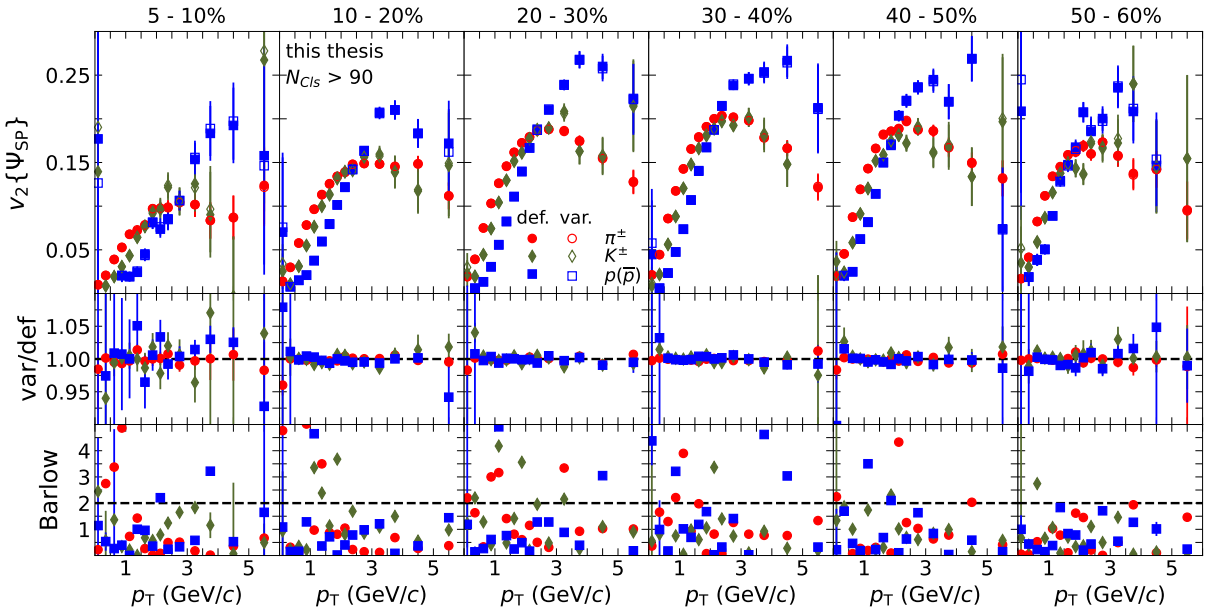

Figure 6.35: Comparison of the varied selection with the default selection for $v_2\{\Psi_{SP}\}$ for pions (red markers), kaons (green markers) and (anti)protons (blue markers) as a function of transverse momentum in all centrality intervals analyzed.

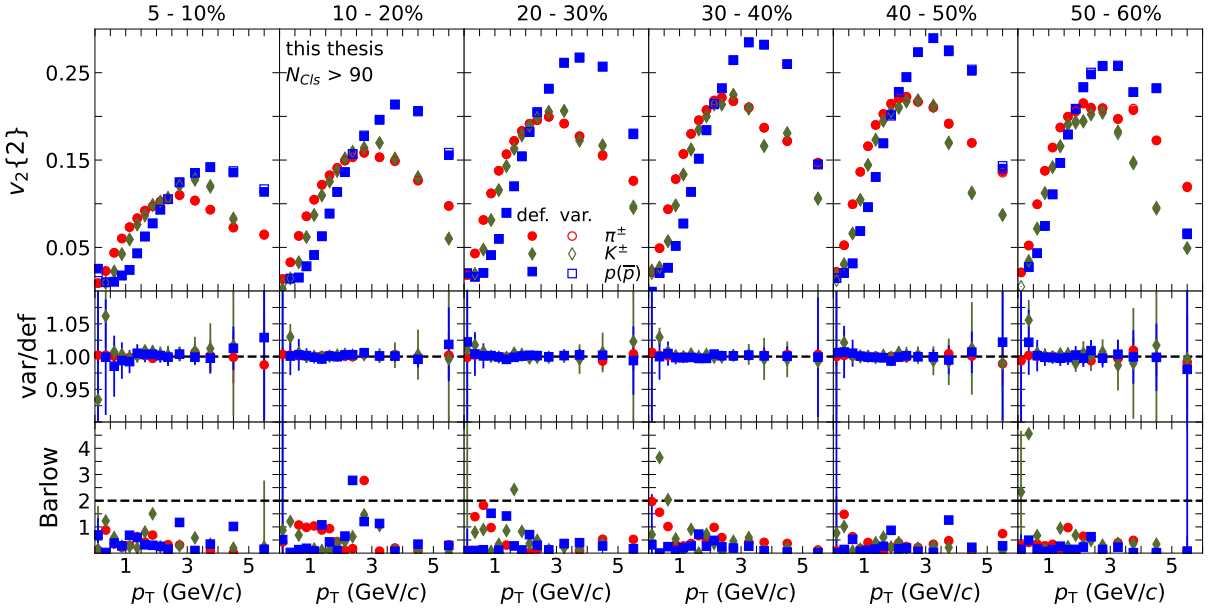

Figure 6.36: Comparison of the varied selection with the default selection for $v_2\{4\}$ for pions (red markers), kaons (green markers) and (anti)protons (blue markers) as a function of transverse momentum in all centrality intervals analyzed.

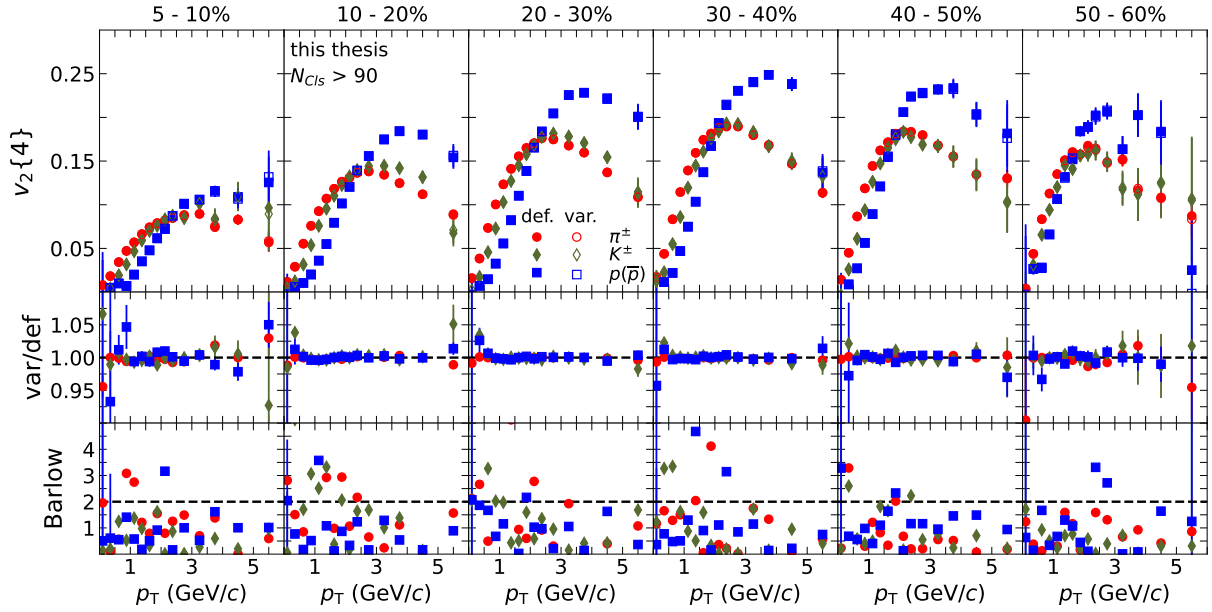

Figure 6.37: Comparison of the varied selection with the default selection for $v_2\{4\}$ for pions (red markers), kaons (green markers) and (anti)protons (blue markers) as a function of transverse momentum in all centrality intervals analyzed.

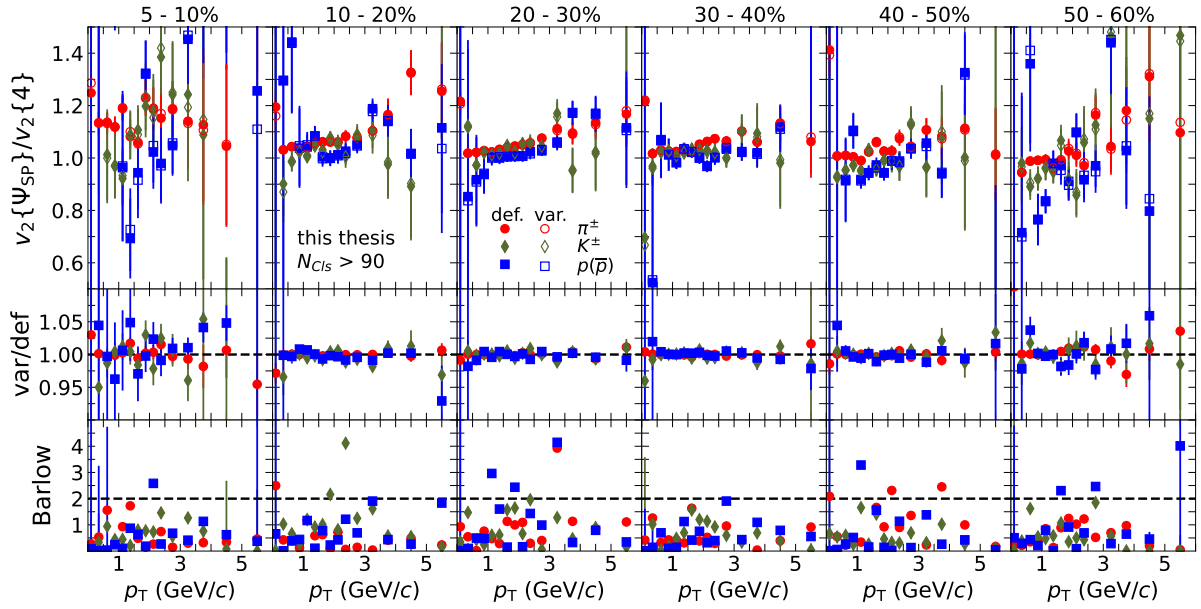

Figure 6.38: Comparison of the varied selection with the default selection for $v_2\{\Psi_{SP}\}/v_2\{4\}$ for pions (red markers), kaons (green markers) and (anti)protons (blue markers) as a function of transverse momentum in all centrality intervals analyzed.

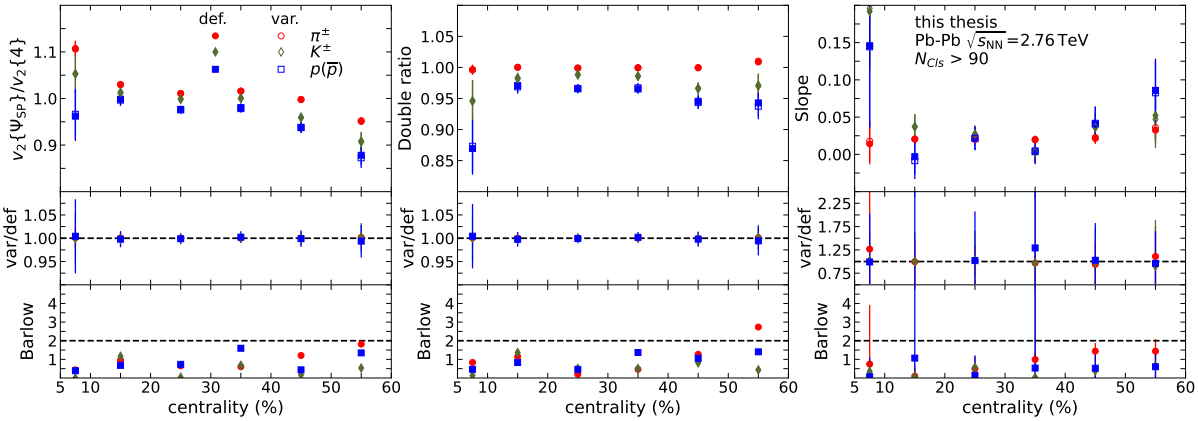

Figure 6.39: Comparison of the varied selection with the default selection for the ratio $v_2\{\Psi_{SP}\}/v_2\{4\}$, slope and double ratio for pions (red markers), kaons (green markers) and (anti)protons (blue markers) as a function of centrality.

Variation with the χ^2 per number of TPC clusters

The χ^2 per TPC cluster, similar to the number of TPC clusters, serves as a test of the stability of track reconstruction. For $v_2\{\Psi_{SP}\}$ and $v_2\{4\}$ as functions of p_T, a statistically signficant variation is observed at momenta below 2 GeV/c. This variation is more pronounced for $v_2\{4\}$ than for $v_2\{\Psi_{SP}\}$, most likely due to the fact that $v_2\{4\}$ is a four-particle correlator, while $v_2\{\Psi_{SP}\}$ is constructed by correlating the flow vector of the TPC with the flow vector of both ZDCs. For $v_2\{\Psi_{SP}\}/v_2\{4\}$ as a function of p_T, no systematic shift is observed, as the uncertainties cancel in the ratio. For the p_T-integrated results, no statistically signficant shift was observed, and, therefore, no systematic uncertainty is assigned.

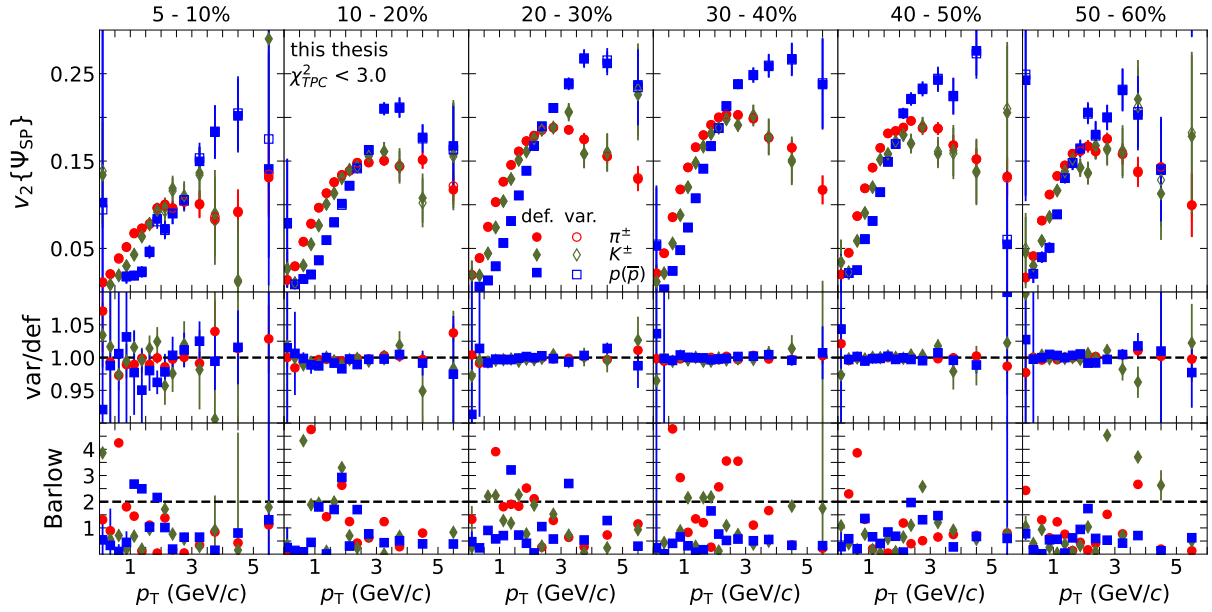

Figure 6.40: Comparison of the varied selection with the default selection for $v_2\{\Psi_{SP}\}$ for pions (red markers), kaons (green markers) and (anti)protons (blue markers) as a function of transverse momentum in all centrality intervals analyzed.

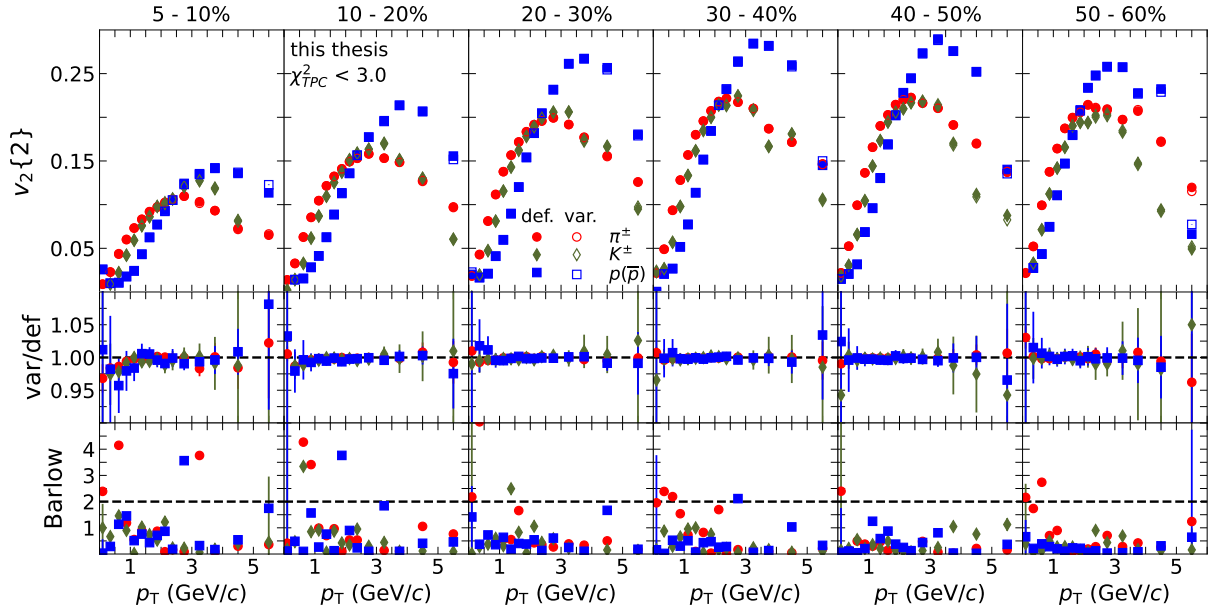

Figure 6.41: Comparison of the varied selection with the default selection for $v_2\{4\}$ for pions (red markers), kaons (green markers) and (anti)protons (blue markers) as a function of transverse momentum in all centrality intervals analyzed.

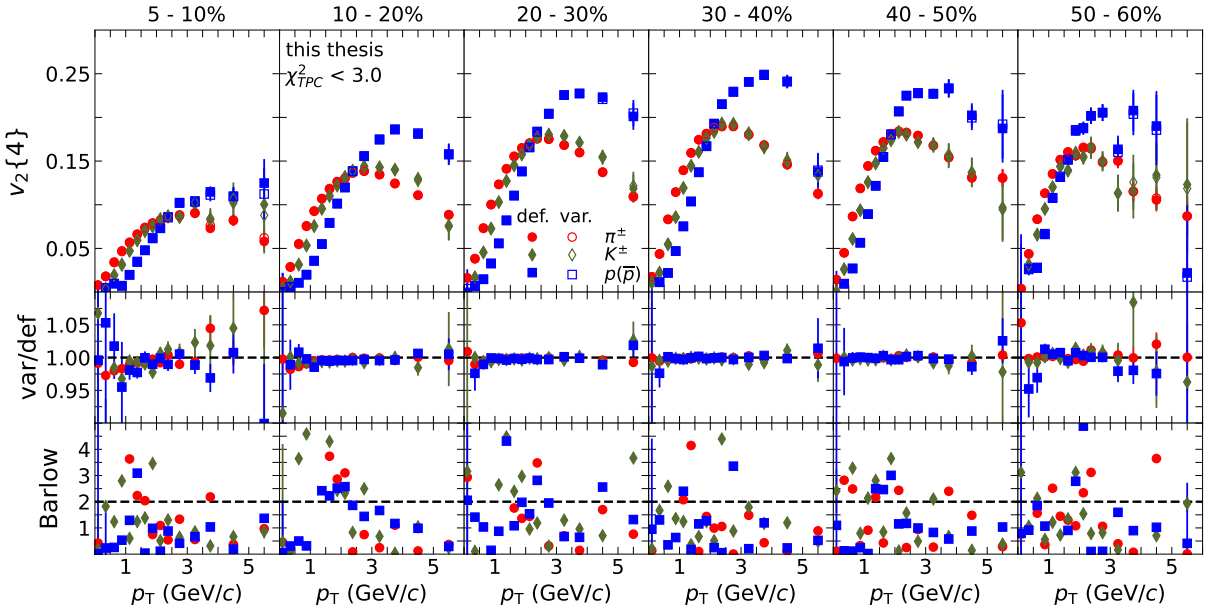

Figure 6.42: Comparison of the varied selection with the default selection for $v_2\{4\}$ for pions (red markers), kaons (green markers) and (anti)protons (blue markers) as a function of transverse momentum in all centrality intervals analyzed.

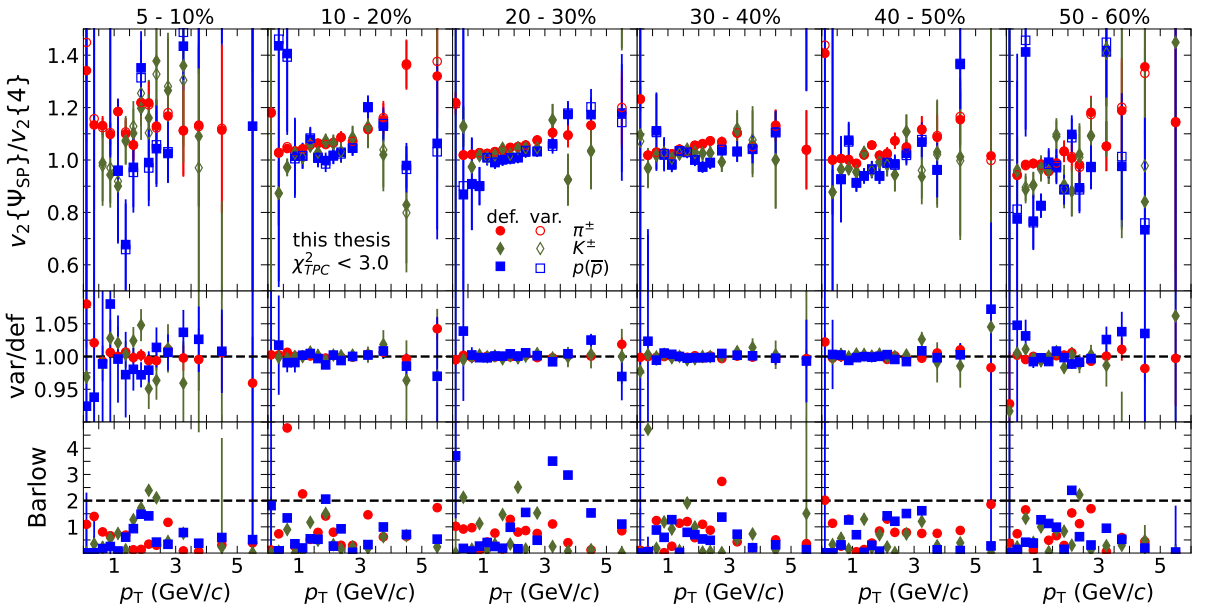

Figure 6.43: Comparison of the varied selection with the default selection for $v_2\{\Psi_{SP}\}/v_2\{4\}$ for pions (red markers), kaons (green markers) and (anti)protons (blue markers) as a function of transverse momentum in all centrality intervals analyzed.

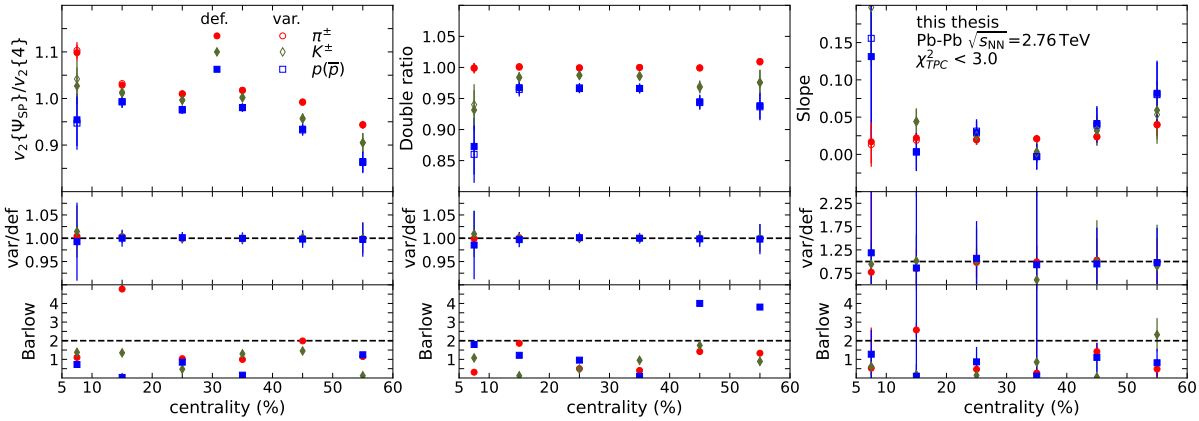

Figure 6.44: Comparison of the varied selection with the default selection for the ratio $v_2\{\Psi_{SP}\}/v_2\{4\}$, slope and double ratio for pions (red markers), kaons (green markers) and (anti)protons (blue markers) as a function of centrality.

6.8.3 Variation of the procedure for particle identification

The performance of the particle identification was tested by increasing the threshold of the Bayesian probability, which in turn increased the purity of the selected sample. This check is sensitive to potential impurities from other particle species in the extraction of the elliptic flow. For all particle species, a statistically signficant deviation was observed, and it represents the largest contribution to both the $v_2\{\Psi_{SP}\}$ and $v_2\{4\}$ observables as functions of p_T .

For the ratio $v_2\{\Psi_{SP}\}/v_2\{4\}$, the contribution from the particle identification variation is reduced significantly, largely due to the partial cancellation of the systematic bias. For the centrality-dependent results, no systematic uncertainty is applied

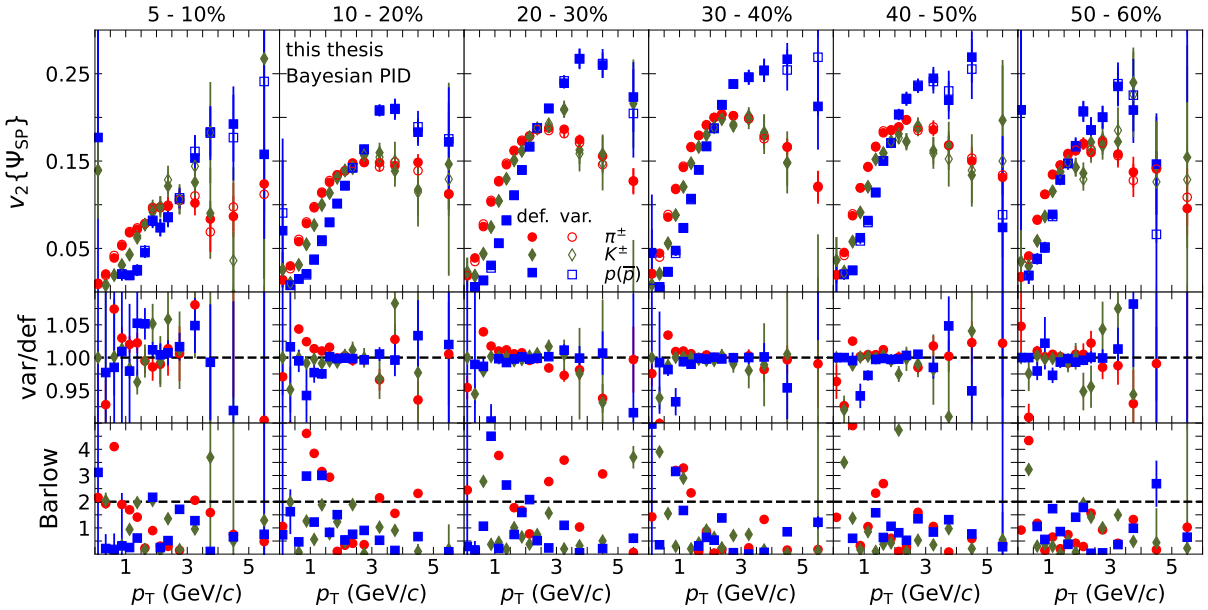

Figure 6.45: Comparison of the varied selection with the default selection for $v_2\{\Psi_{SP}\}$ for pions (red markers), kaons (green markers) and (anti)protons (blue markers) as a function of transverse momentum in all centrality intervals analyzed.

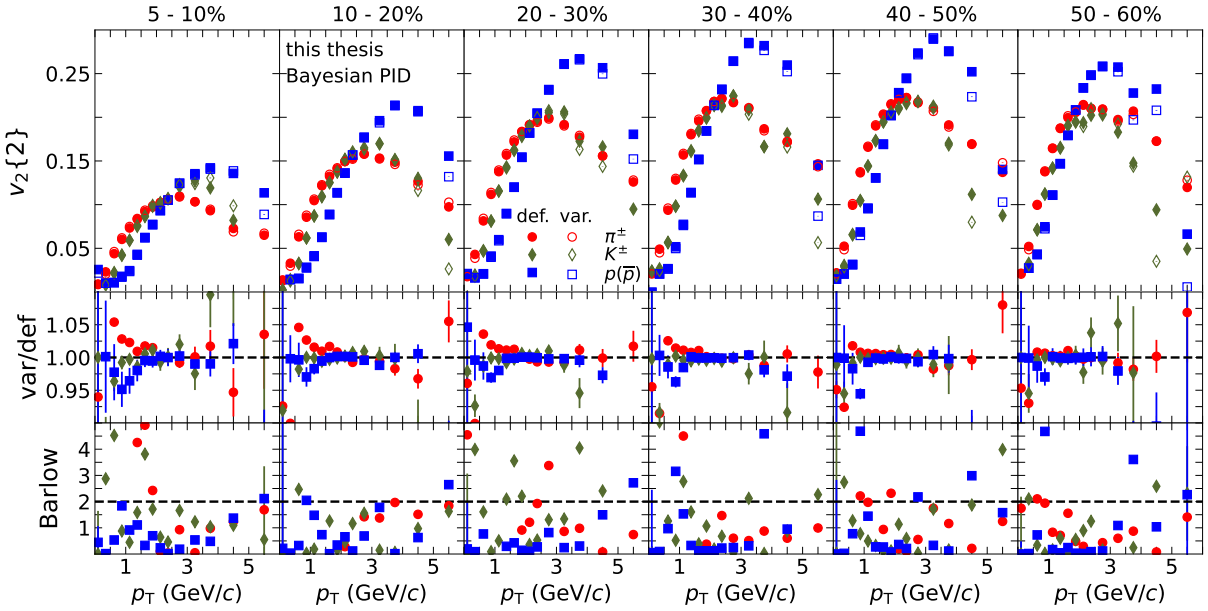

Figure 6.46: Comparison of the varied selection with the default selection for $v_2\{4\}$ for pions (red markers), kaons (green markers) and (anti)protons (blue markers) as a function of transverse momentum in all centrality intervals analyzed.

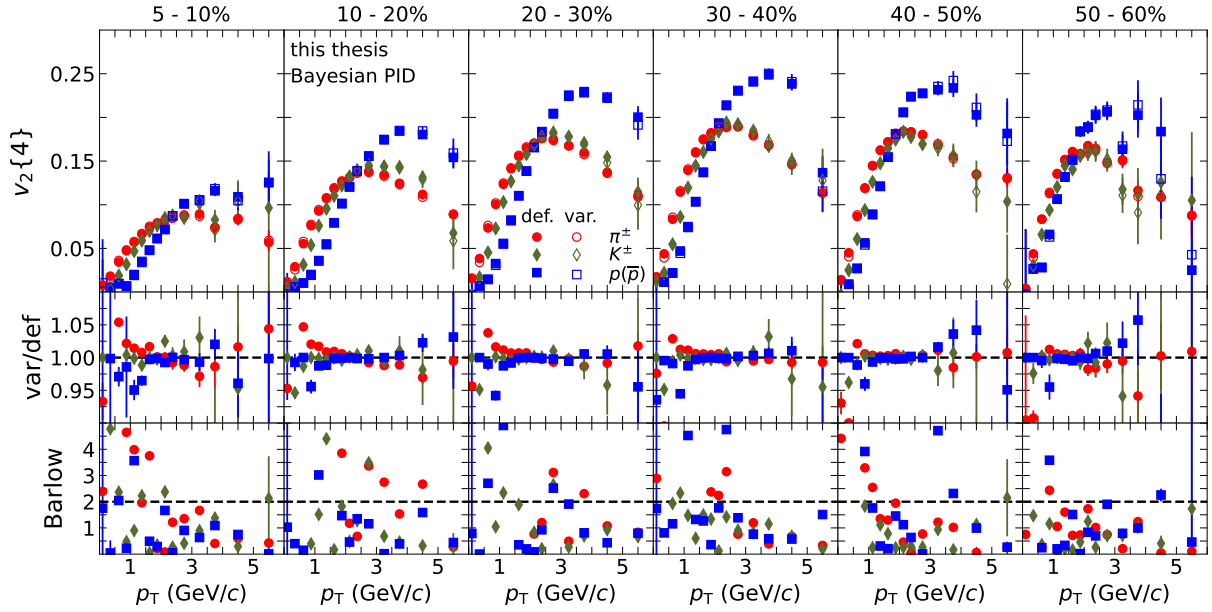

Figure 6.47: Comparison of the varied selection with the default selection for $v_2\{4\}$ for pions (red markers), kaons (green markers) and (anti)protons (blue markers) as a function of transverse momentum in all centrality intervals analyzed.

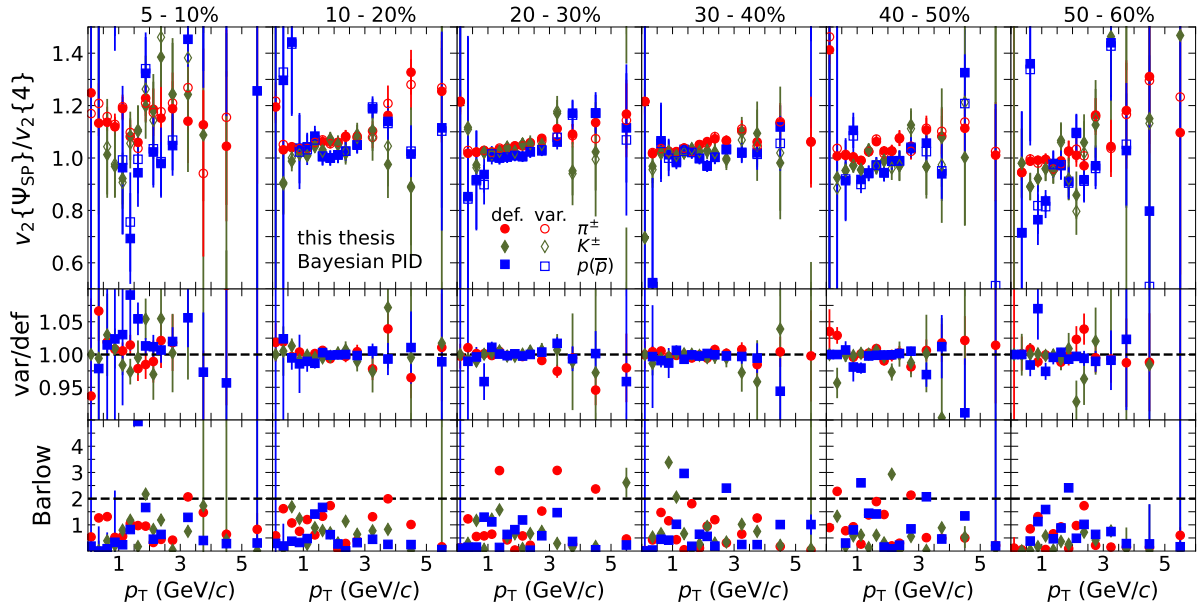

Figure 6.48: Comparison of the varied selection with the default selection for $v_2\{\Psi_{SP}\}/v_2\{4\}$ for pions (red markers), kaons (green markers) and (anti)protons (blue markers) as a function of transverse momentum in all centrality intervals analyzed.

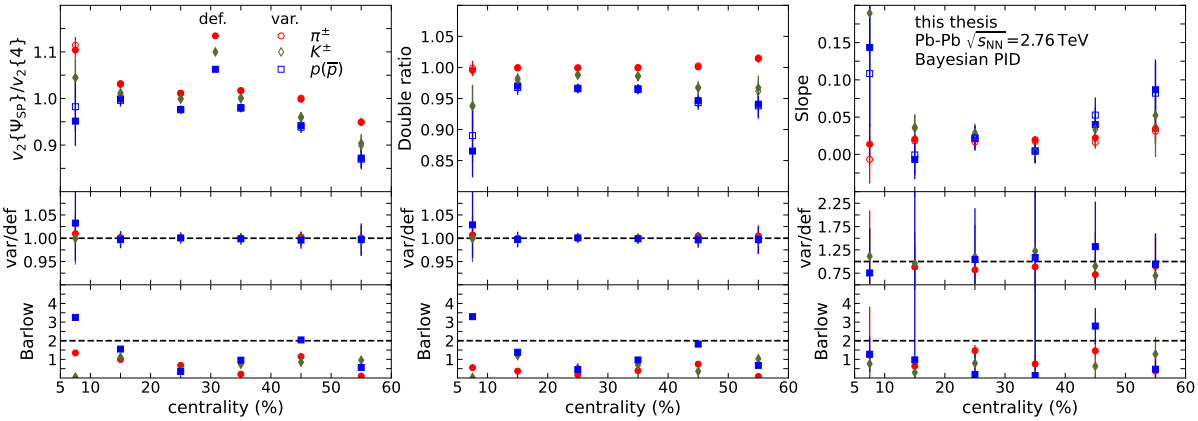

Figure 6.49: Comparison of the varied selection with the default selection for the ratio $v_2\{\Psi_{SP}\}/v_2\{4\}$, slope and double ratio for pions (red markers), kaons (green markers) and (anti)protons (blue markers) as a function of centrality.

6.8.4 Non-uniformity corrections

Non-uniform acceptance in the TPC

As described in Section 6.5.1, the TPC non-uniformities are corrected using ϕ-weights. Additionally, each particle species is corrected for tracking and particle identification efficiency to account for the different tracking and PID performance in different p_T intervals. For the p_T-dependent analysis, these efficiency corrections are assumed to be negligible, as the weights should cancel out depending on the with of the binning in a p_T-dependent analysis. They become more important for p_T-integrated results, since the weights as a function of p_T can vary significantly (Figure 6.4).

To test the impact of the non-uniformity corrections the flow vector of produced particles was constructed assigning ϕ-weights to each no weights should be applied particle reconstructed in the ITS and TOF and compare them to calculations with weights set to unity. No significant variation in the p_T-differential flow observables were found except for the first p_T bin between 0.2 and 0.5 GeV/c.

The impact on the p_T-integrated results was checked by varying the fit range of the linear and constant functions to the p_T-differential ratio $v_2\{\Psi_{SP}\}/v_2\{4\}$, as well as including or not the lowest p_T bin. No significant change in the p_T-integrated result was found for all variables. It was concluded that for the default analysis configuration no weights should be applied to the flow vectors. This mitigates potential biases from using efficiency correction estimated from Monte Carlo simulations.

Change in the Non-uniformity correction of the ZDC

The sensitivity of the elliptic flow measurement with respect to the spectator plane due to the non-uniformity corrections on the ZDC was tested by changing the recentering scheme.

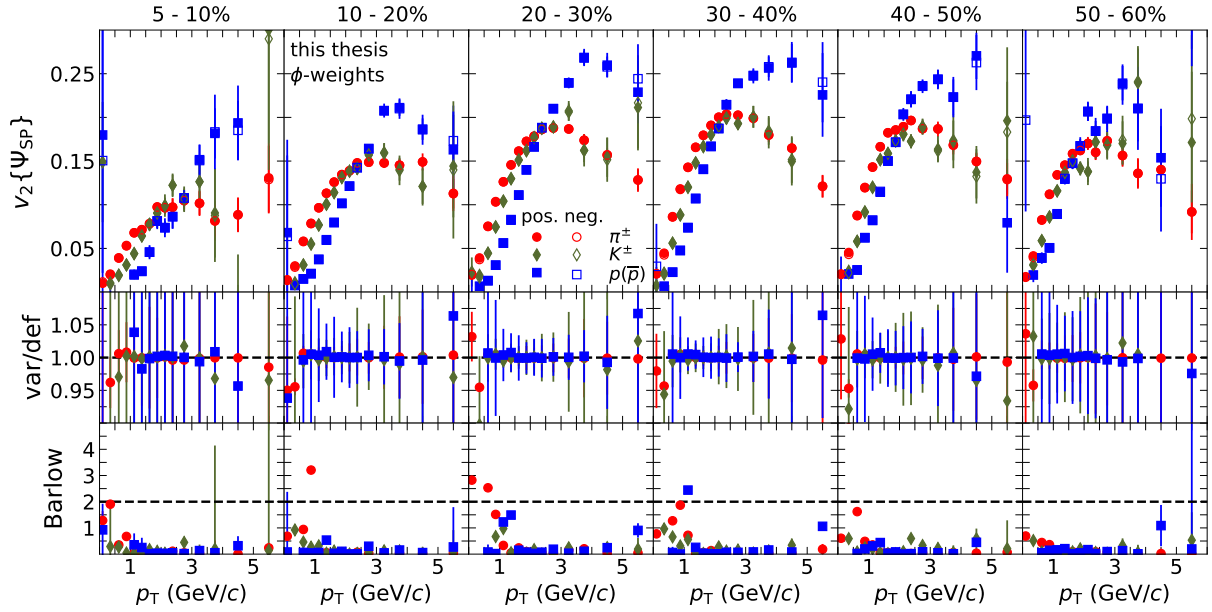

Figure 6.50: Comparison of the varied selection with the default selection for $v_2\{\Psi_{SP}\}$ for pions (red markers), kaons (green markers) and (anti)protons (blue markers) as a function of transverse momentum in all centrality intervals analyzed.

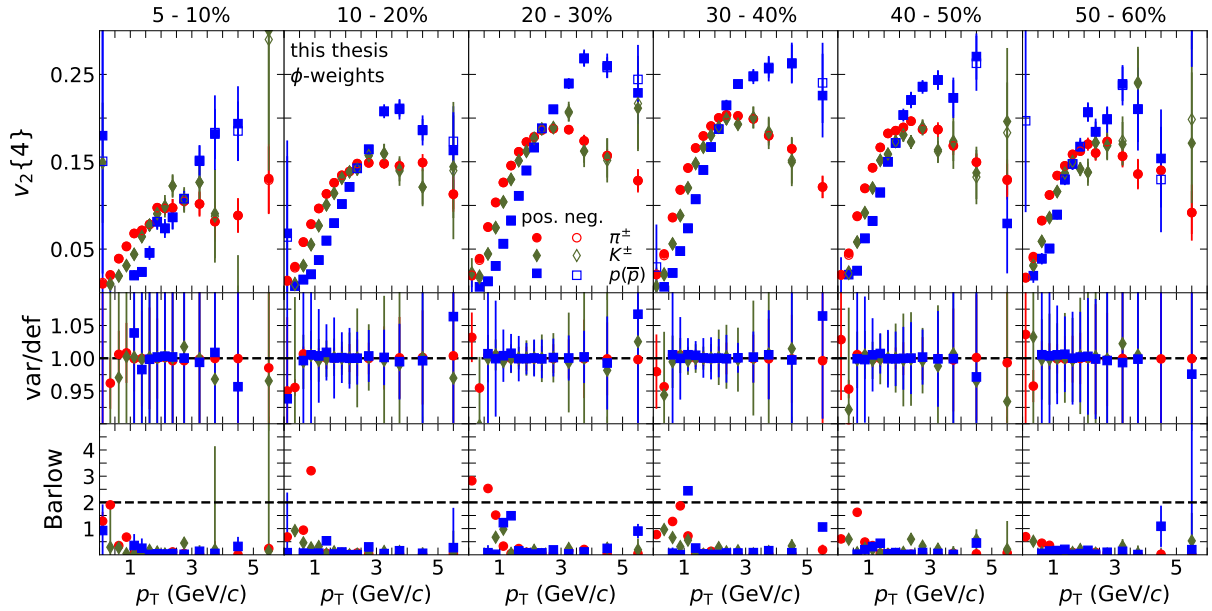

Figure 6.51: Comparison of the varied selection with the default selection for $v_2\{4\}$ for pions (red markers), kaons (green markers) and (anti)protons (blue markers) as a function of transverse momentum in all centrality intervals analyzed.

Instead of recentering the ZDC flow vectors only once in all four dimensions, an iterative recentering scheme was used, which alternates between a 4D recentering with coarse

Variable	Range	Coarse	Fine	finer
Centrality	(0,70)	5	25	50
V_x [nσ]	(-4,4)	5	25	50
V_y [nσ]	(-4,4)	5	25	50
V_z [nσ]	(-4,4)	5	25	50

Table 6.6: Binning of the iterative recentering procedure described in more detail in the text.

binning and four 1D corrections in each dimension with finer binning. The binning for the different steps is illustrated in Table 6.6. The procedure consist of three steps, where in each step the binning of the 1D corrections is changed according to Table 6.6. Each step of this iterative recentering can be summarized as follows:

- 4D recentering with coarse binning
- 1D recentering in centrality
- 1D recentering in the x-vertex position
- 1D recentering in the y-vertex position
- 1D recentering in the z-vertex position

This iterative recentering scheme was used to investigate the impact of non-uniformity corrections and to ensure that the results are robust with respect to the recentering procedure. A statistically significant shift is observed for the $v_2\{\Psi_{\mathrm{SP}}\}$ and $v_2\{\Psi_{\mathrm{SP}}\}/v_2\{4\}$ as function of p_{T}, as well as the $v_2\{\Psi_{\mathrm{SP}}\}/v_2\{4\}$ ratio as a function of centrality. This shift is approximately of the order of 1%.

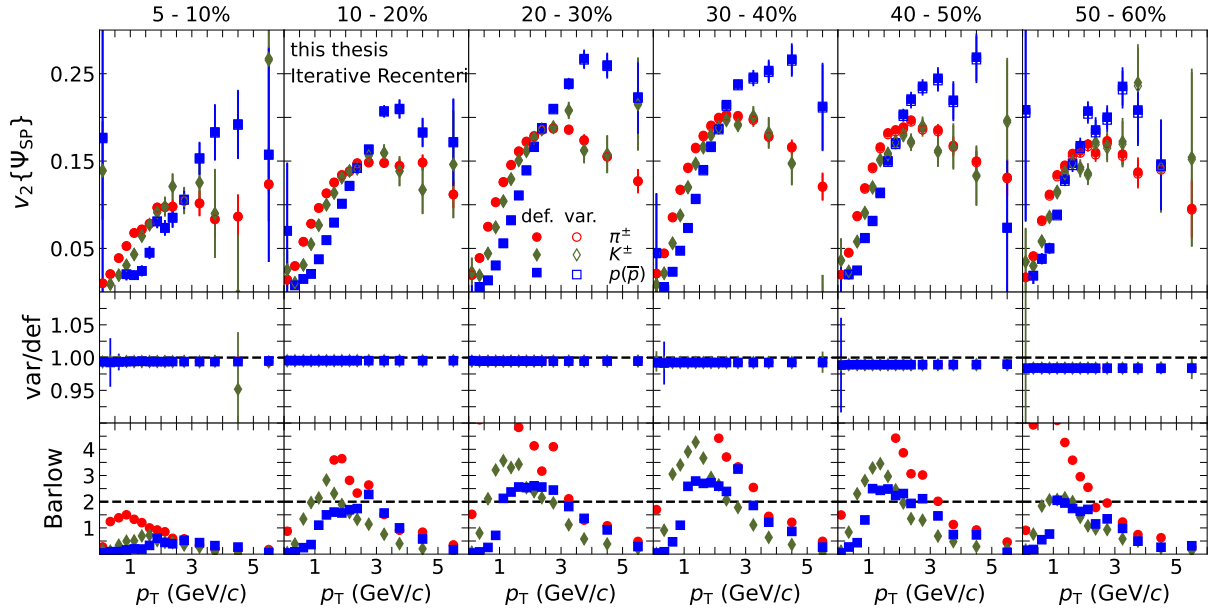

Figure 6.52: Comparison of the varied selection with the default selection for $v_2\{\Psi_{SP}\}$ for pions (red markers), kaons (green markers) and (anti)protons (blue markers) as a function of transverse momentum in all centrality intervals analyzed.

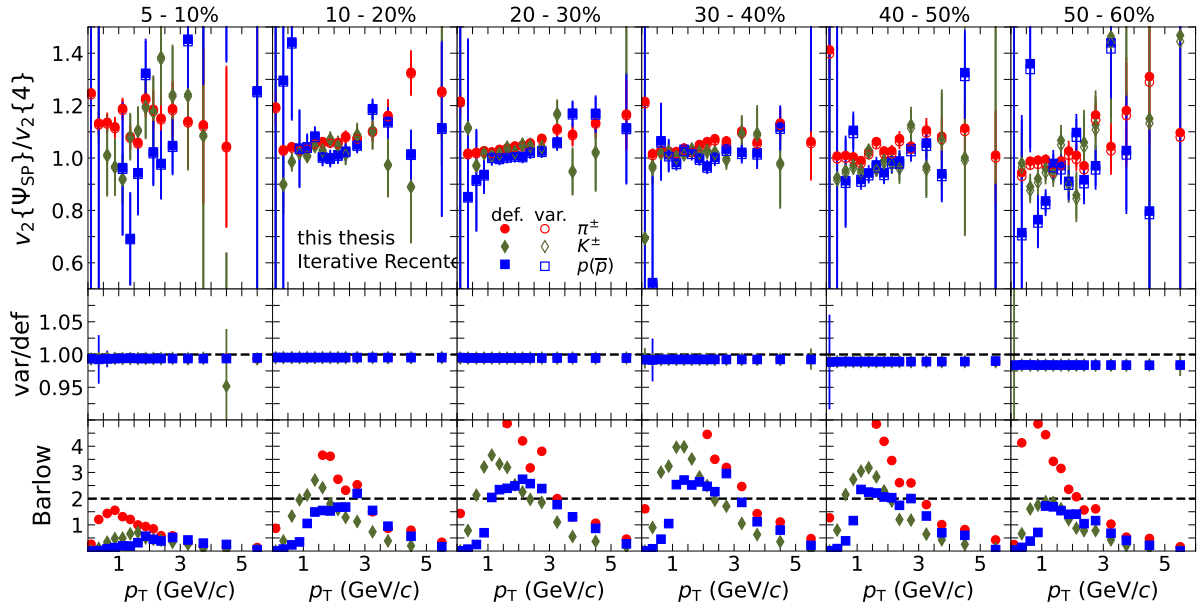

Figure 6.53: Comparison of the varied selection with the default selection for $v_2\{\Psi_{SP}\}/v_2\{4\}$ for pions (red markers), kaons (green markers) and (anti)protons (blue markers) as a function of transverse momentum in all centrality intervals analyzed.

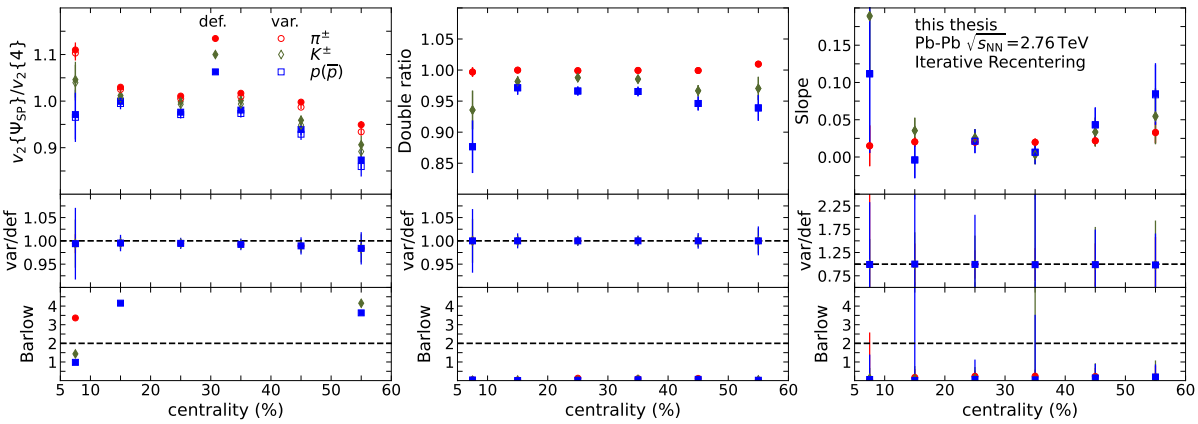

Figure 6.54: Comparison of the varied selection with the default selection for the ratio $v_2\{\Psi_{SP}\}/v_2\{4\}$, slope and double ratio for pions (red markers), kaons (green markers) and (anti)protons (blue markers) as a function of centrality.

6.8.5 ZDC Q-vector components

The three observables in Equation (3.54) provide independent estimates of $v_2\{\Psi_{SP}\}$. Each of these observables were compared with the average over all three combinations. Possible reasons for differences could be remaining ZDC-LHC beam-related biases or unphysical correlations between the TPC and ZDC flow vectors that are not corrected by the recentering procedure of the ZDC flow vectors. The bias can be connected to the observed non-zero correlation $\langle XY \rangle$ and $\langle YX \rangle$ as shown in Figure 6.9. In all cases, no significant difference was observed between three different observable, which are used to the elliptic flow with respect to the spectator plane.

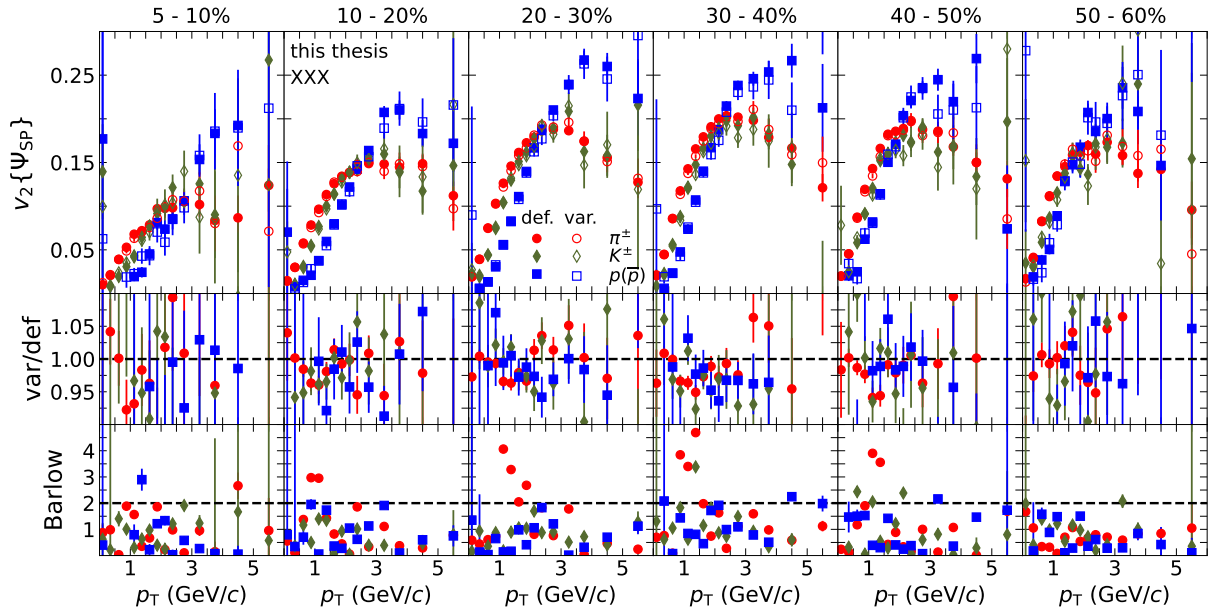

Figure 6.55: Comparison of the varied selection with the default selection for $v_2\{\Psi_{SP}\}$ for pions (red markers), kaons (green markers) and (anti)protons (blue markers) as a function of transverse momentum in all centrality intervals analyzed.

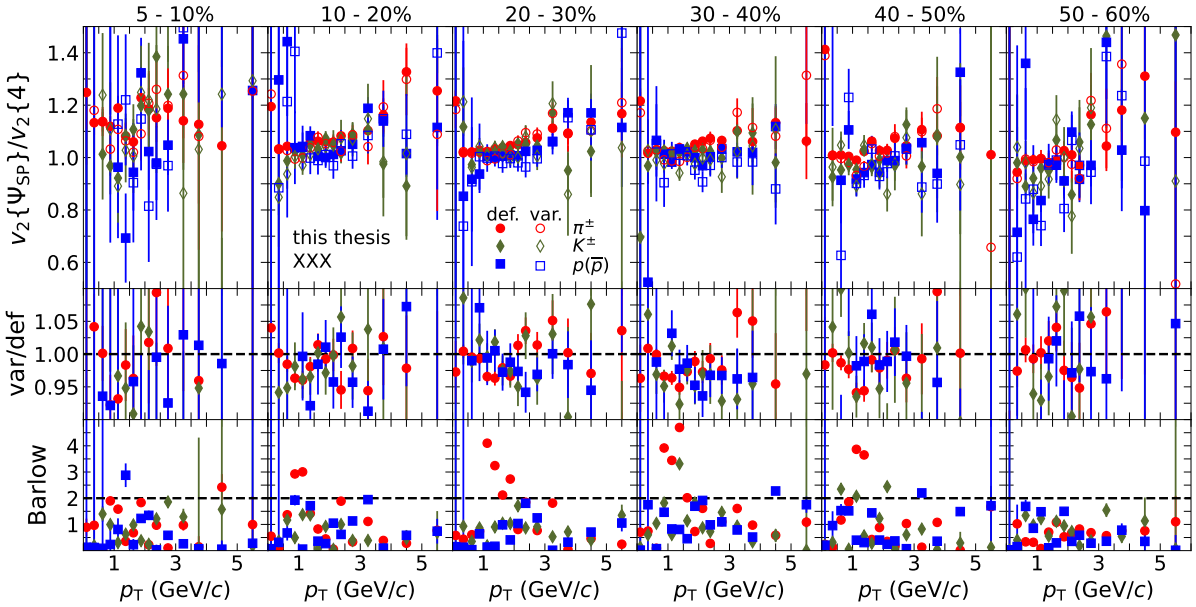

Figure 6.56: Comparison of the varied selection with the default selection for $v_2\{\Psi_{SP}\}/v_2\{4\}$ for pions (red markers), kaons (green markers) and (anti)protons (blue markers) as a function of transverse momentum in all centrality intervals analyzed.

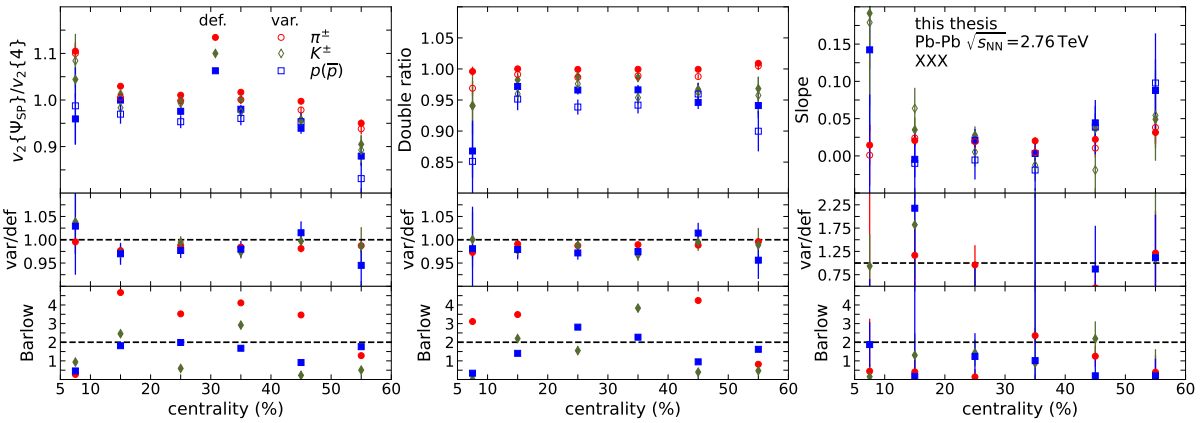

Figure 6.57: Comparison of the varied selection with the default selection for the ratio $v_2\{\Psi_{SP}\}/v_2\{4\}$, slope and double ratio for pions (red markers), kaons (green markers) and (anti)protons (blue markers) as a function of centrality.

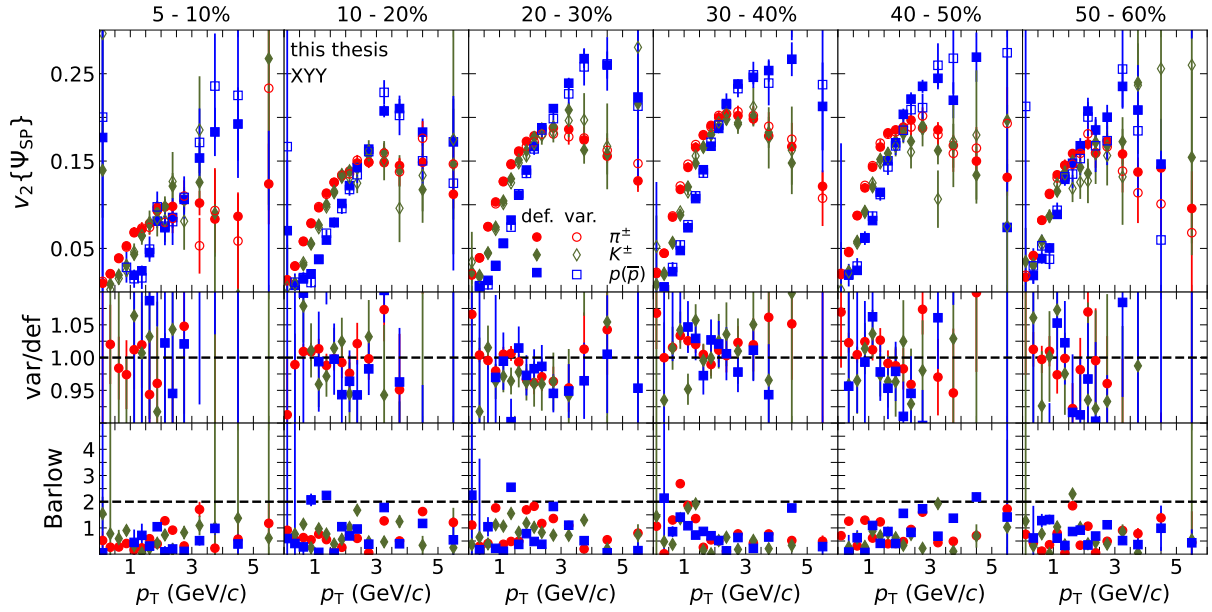

Figure 6.58: Comparison of the varied selection with the default selection for $v_2\{\Psi_{SP}\}$ for pions (red markers), kaons (green markers) and (anti)protons (blue markers) as a function of transverse momentum in all centrality intervals analyzed.

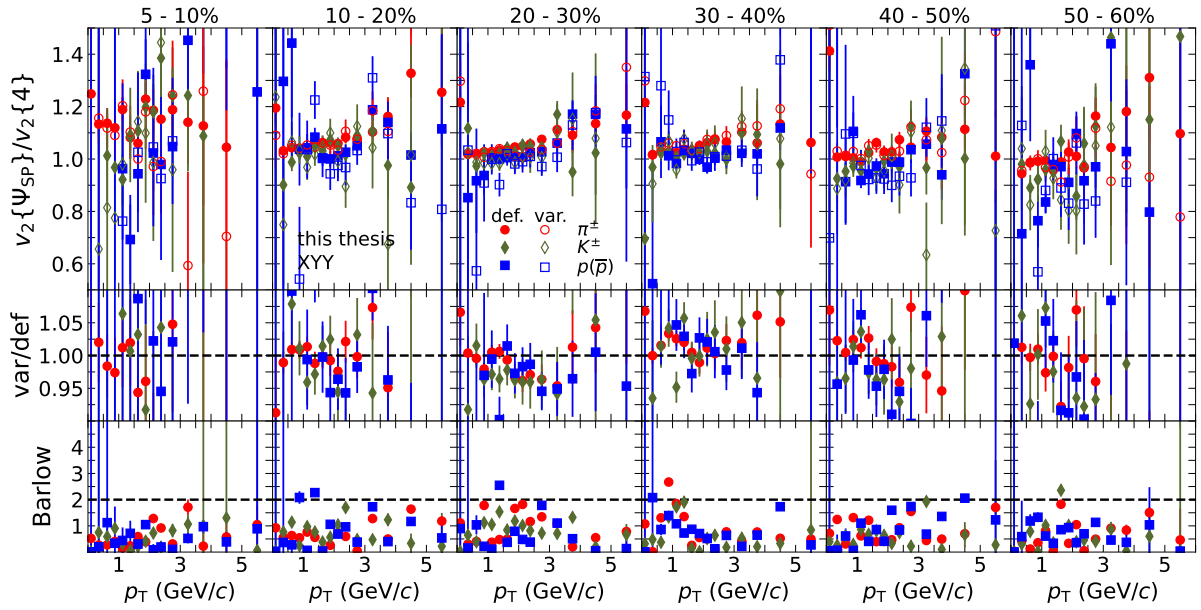

Figure 6.59: Comparison of the varied selection with the default selection for $v_2\{\Psi_{SP}\}/v_2\{4\}$ for pions (red markers), kaons (green markers) and (anti)protons (blue markers) as a function of transverse momentum in all centrality intervals analyzed.

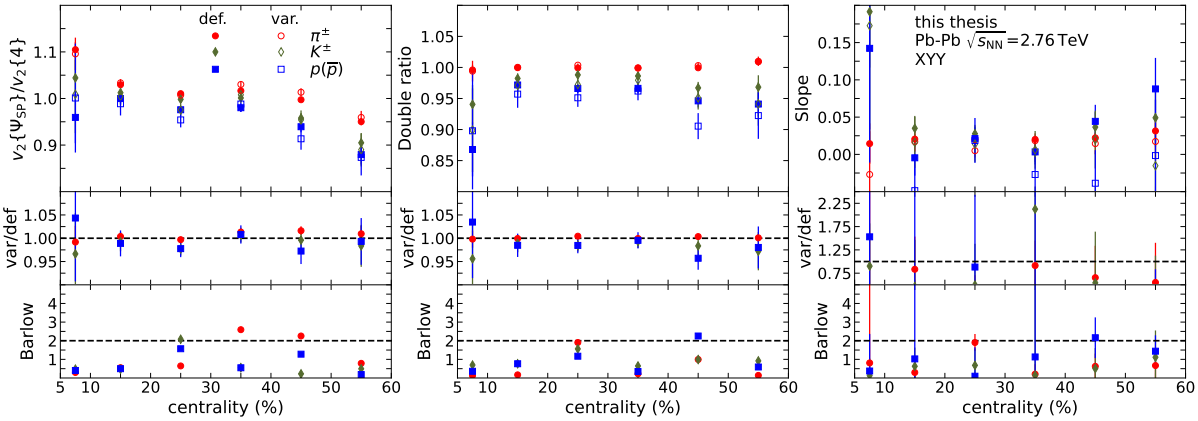

Figure 6.60: Comparison of the varied selection with the default selection for the ratio $v_2\{\Psi_{SP}\}/v_2\{4\}$, slope and double ratio for pions (red markers), kaons (green markers) and (anti)protons (blue markers) as a function of centrality.

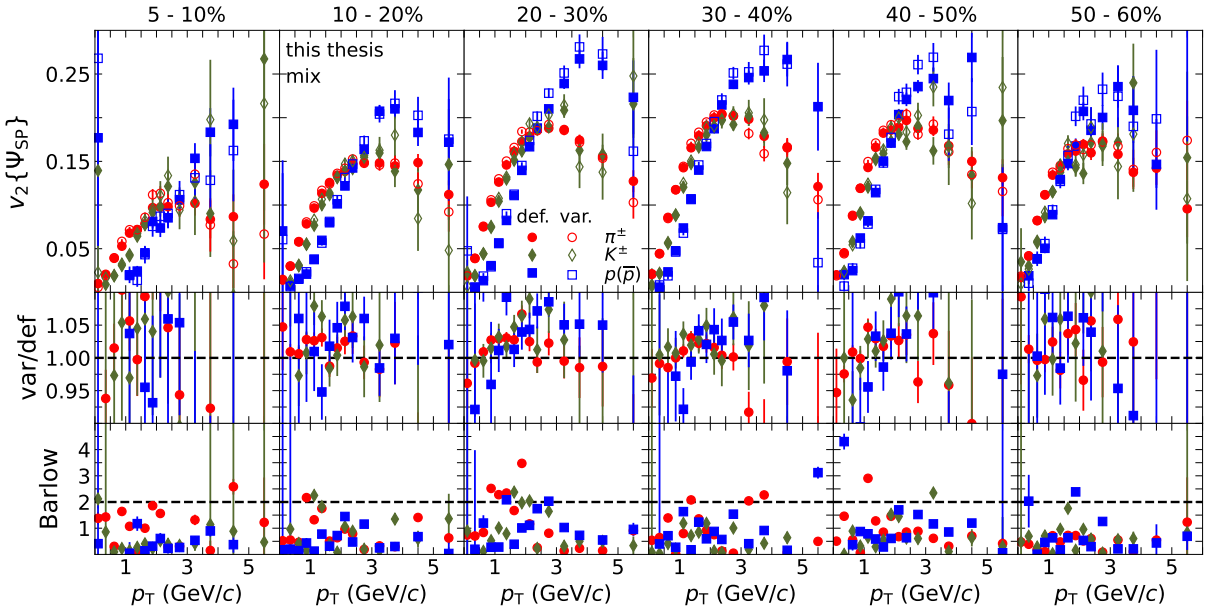

Figure 6.61: Comparison of the varied selection with the default selection for $v_2\{\Psi_{SP}\}$ for pions (red markers), kaons (green markers) and (anti)protons (blue markers) as a function of transverse momentum in all centrality intervals analyzed.

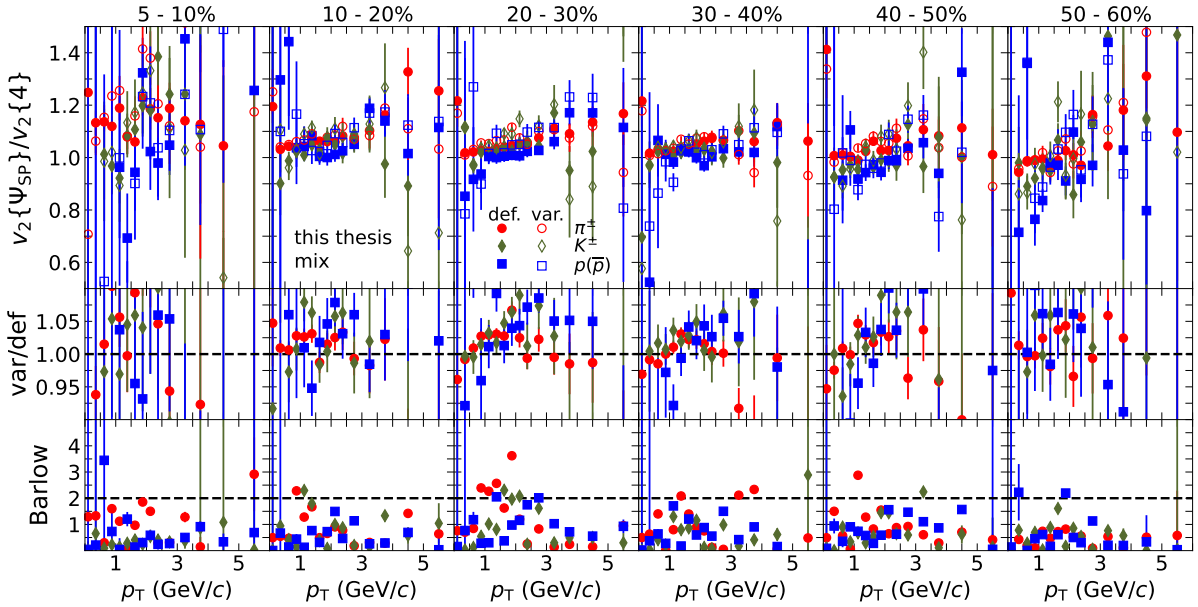

Figure 6.62: Comparison of the varied selection with the default selection for $v_2\{\Psi_{SP}\}/v_2\{4\}$ for pions (red markers), kaons (green markers) and (anti)protons (blue markers) as a function of transverse momentum in all centrality intervals analyzed.

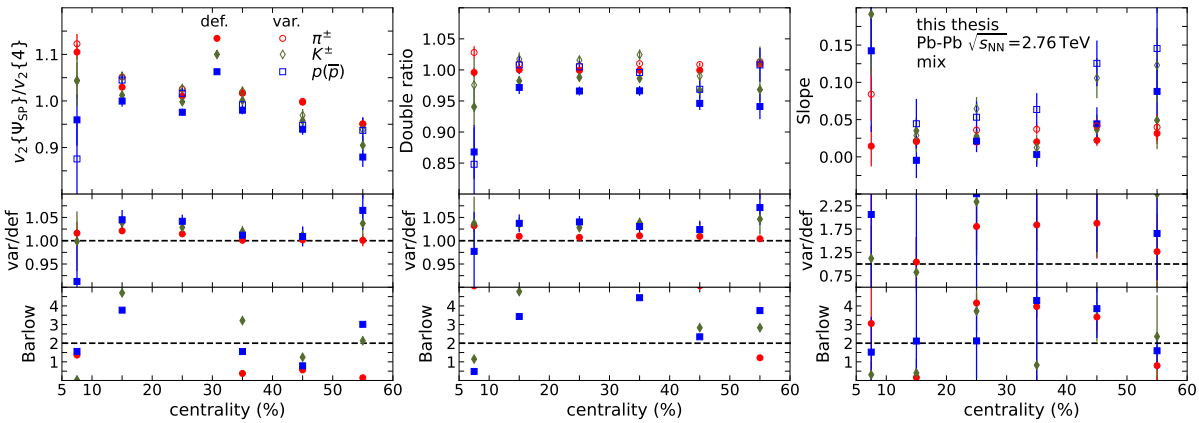

Figure 6.63: Comparison of the varied selection with the default selection for the ratio $v_2\{\Psi_{SP}\}/v_2\{4\}$, slope and double ratio for pions (red markers), kaons (green markers) and (anti)protons (blue markers) as a function of centrality.

Scale uncertainty from ZDC cross-correlations

Non-zero values of the $\langle XY \rangle$ and $\langle YX \rangle$ correlations are observed after recentering. This provides an estimate of the possible residual detector effects in $v_2\{\Psi_{SP}\}$ calculation. To assign the uncertainty, their values are scaled using the following formula:

$$\Delta v_2\{\Psi_{SP}\} = v_2\{\Psi_{SP}\} \times \sqrt{\frac{\langle XY \rangle \langle YX \rangle}{\langle YY \rangle \langle XX \rangle}} \tag{6.13}$$

Since the non-vanishing correlations of $\langle XY \rangle$ and $\langle YX \rangle$ only affect the ZDC Q-Vector, a relative systematic uncertainty is applied independent of p_T as a function of centrality. Table 6.7 shows the relative uncertainty contributed to the scaling uncertainty for different centrality classes.

Table 6.7: Scale uncertainties for different centrality classes assigned from $\langle XY \rangle$ and $\langle YX \rangle$ correlations between ZDC flow vectors.

Centrality [%]	rel. Uncertainties [%]
5 - 10	3.0
10 - 20	2.7
20 - 30	3.2
30 - 40	2.8
40 - 50	2.9
50 - 60	3.0

6.8.6 Total systematic uncertainties

As outlined in Section 6.7, a smoothing process is applied to the uncertainties derived from various sources before they are combined into total uncertainty. This smoothing helps to reduce the impact of statistical fluctuations in the extraction of the total systematic uncertainties. Particularly for results obtained as functions of transverse momentum, significant bin-to-bin variations in systematic uncertainties if observed, needs to be smoothened.
The sources of analysis variations considered significant for the observables extracted as a function of transverse momentum are indicated by crosses in Table 6.8. The significant sources are the same for pions, kaons and (anti)protons.
For the $v_2\{\Psi_{SP}\}/v_2\{4\}$ ratio, most of these uncertainties are considerably reduced due to their partial cancellation in both $v_2\{\Psi_{SP}\}$ and $v_2\{4\}$. Sources of systematic uncertainties of the observable extracted as a function of centrality are summarized in Table 6.9.

The total systematic uncertainties assigned to the measurment are calculated by summing the individual significant contributions in quadrature. Figures 6.64 to 6.68 show the total systematic uncertainties for all observable as function of transverse momentum and centrality. The systematic uncertainty due to the non-vanishing cross correlations between ZNA and ZNC are not shown in the figures, but are quoted separately in Table 6.7. The

Systematic source	$v_2\{\Psi_{\mathrm{SP}}\}$	$v_2\{2, \lvert\Delta\eta\rvert > 1\}$	$v_2\{4\}$	$v_2\{\Psi_{\mathrm{SP}}\}/v_2\{4\}$
Track Selection				
Track filterbit Number TPC cluster χ^2_{TPC} per cluster	X	X	X	X
Event Selection				
Primary vertex z-position Centrality estimator	X	X	X	X
Solenoid magnet polarity	X	X	X	X
Particle identification				
Threshold Bayesian PID	X	X	X	X
Non-uniformity corrections				
Recentering	X			X
Observable extraction technique				
ZDC Q-vector component ZDC resolution bias	X			X

Table 6.8: Sources of systematic uncertainties, which were considered significant (marked with a "X") for the observables extracted as a function of transverse momentum.

Systematic source	$v_2\{\Psi_{\mathrm{SP}}\}/v_2\{4\}$	Slope	Double ratio
Track Selection			
Track filterbit Number TPC cluster χ^2_{TPC} per cluster			
Event Selection			
Primary vertex z-position Centrality estimator	X	X	X
Solenoid magnet polarity	X	X	X
Particle identification			
Threshold Bayesian PID			
Non-uniformity corrections			
Recentering	X	X	X
Observable extraction technique			
ZDC Q-vector component ZDC resolution bias	X	X	X

Table 6.9: Sources of systematic uncertainties, which were considered significant (marked with a "X") for the observables extracted as a function of centrality.

total systematic uncertainties assigned to the measurement vary between 0-10% depending on the observable, centrality range and p_{T}-range.

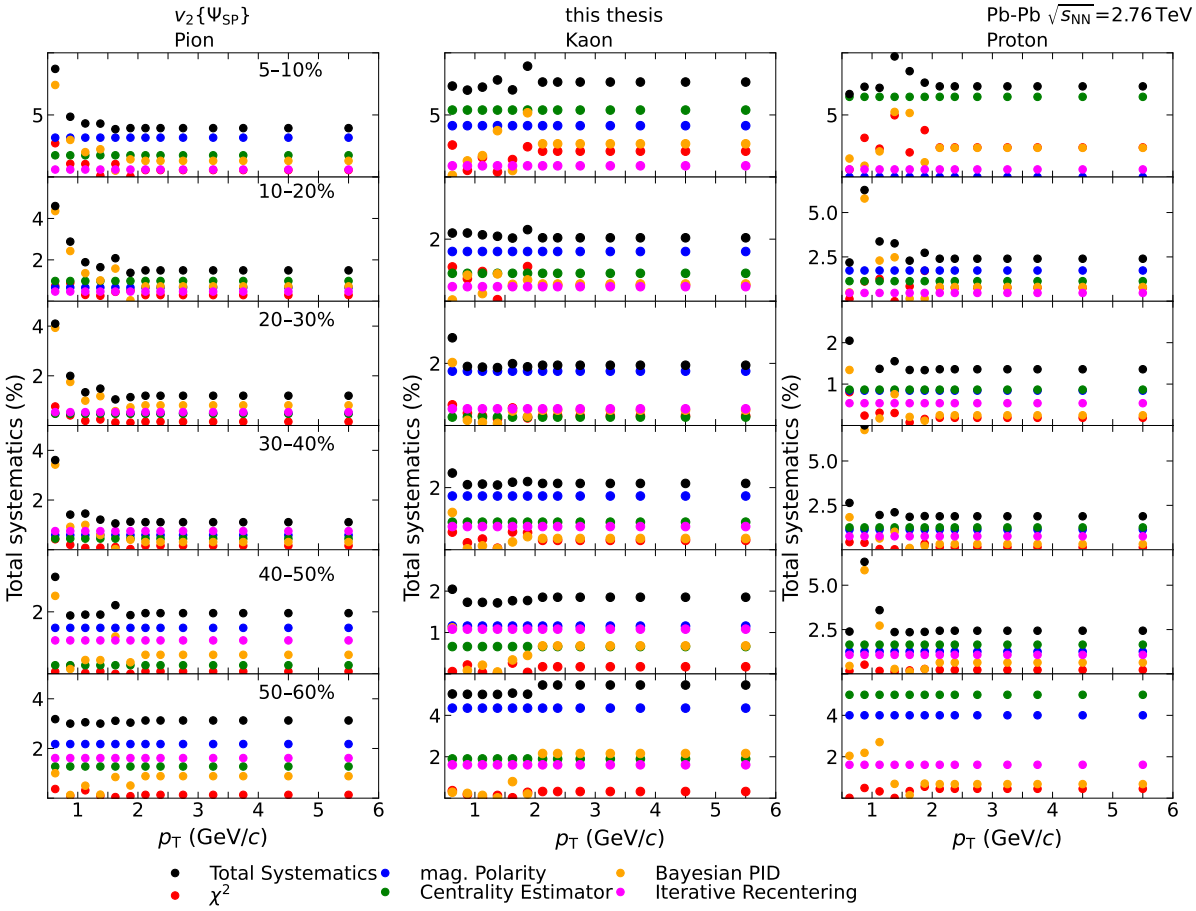

Figure 6.64: Total systematic uncertainties applied to the $v_2\{\Psi_{SP}\}$ of pions (left panels), kaons (middle panels) and (anti)protons (right panels) as a function of transverse momentum in all analyzed centrality intervals. The ZDC scale uncertainty of ≈ 3 % is not shown in the figure.

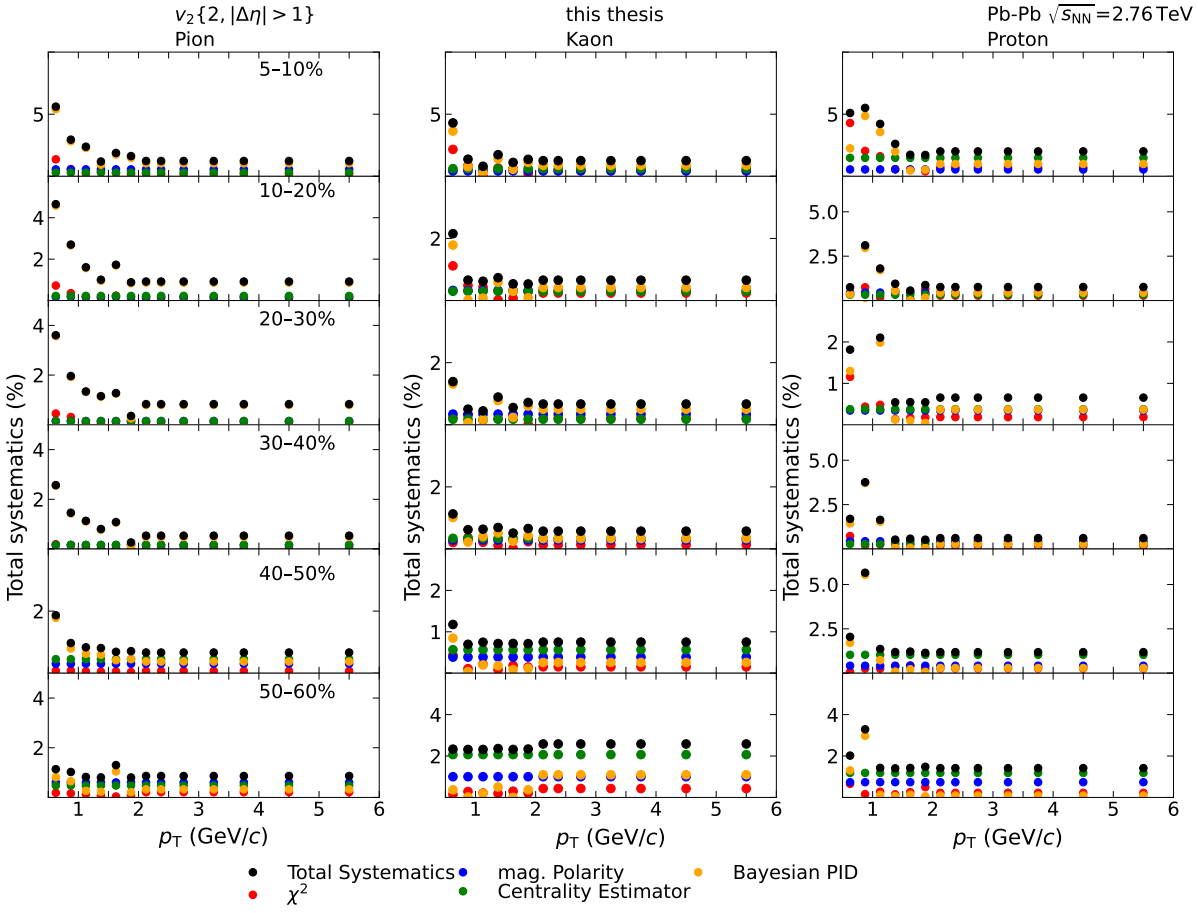

Figure 6.65: Total systematic uncertainties applied to the $v_2\{2, |\Delta\eta| > 1\}$ of pions (left panels), kaons (middle panels) and (anti)protons (right panels) as a function of transverse momentum in all analyzed centrality intervals.

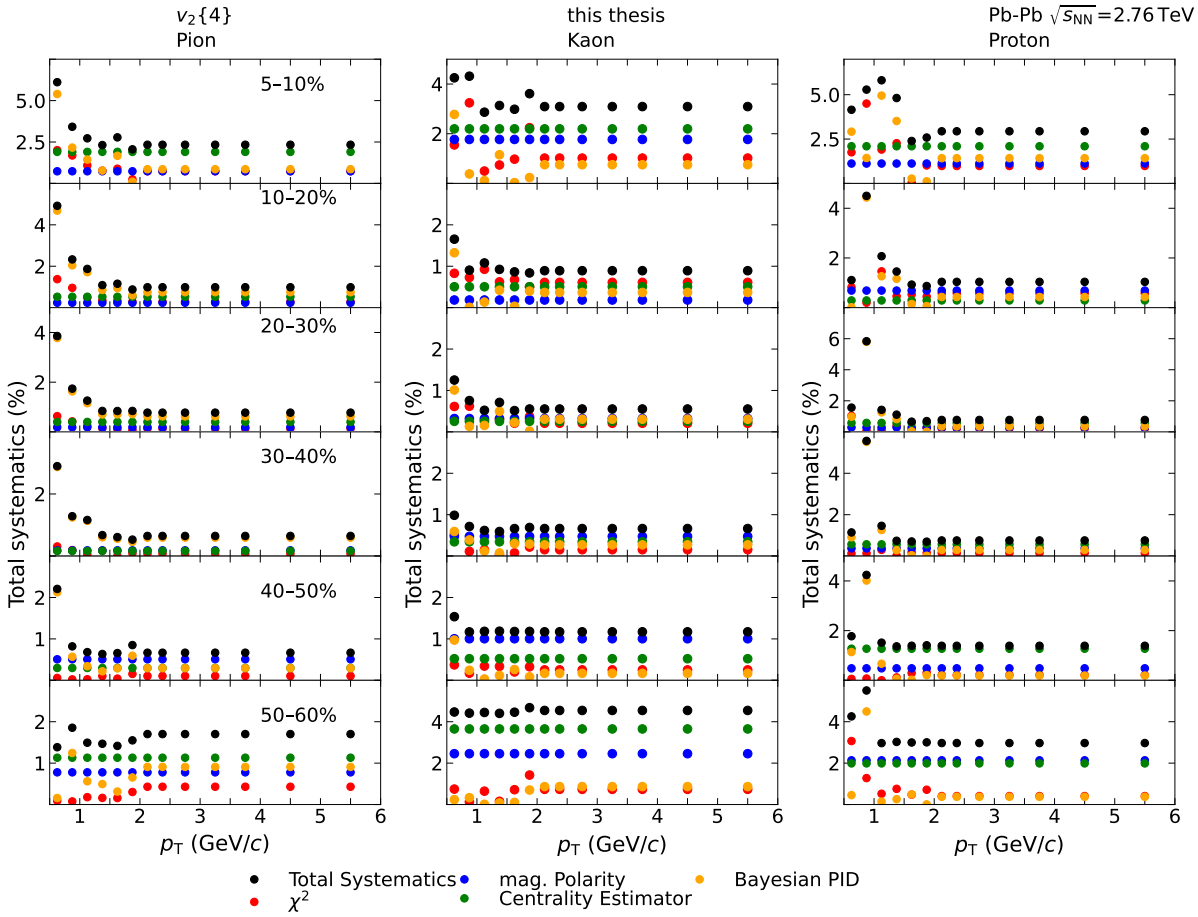

Figure 6.66: Total systematic uncertainties applied to the $v_2\{4\}$ of pions (left panels), kaons (middle panels) and (anti)protons (right panels) as a function of transverse momentum in all analyzed centrality intervals.

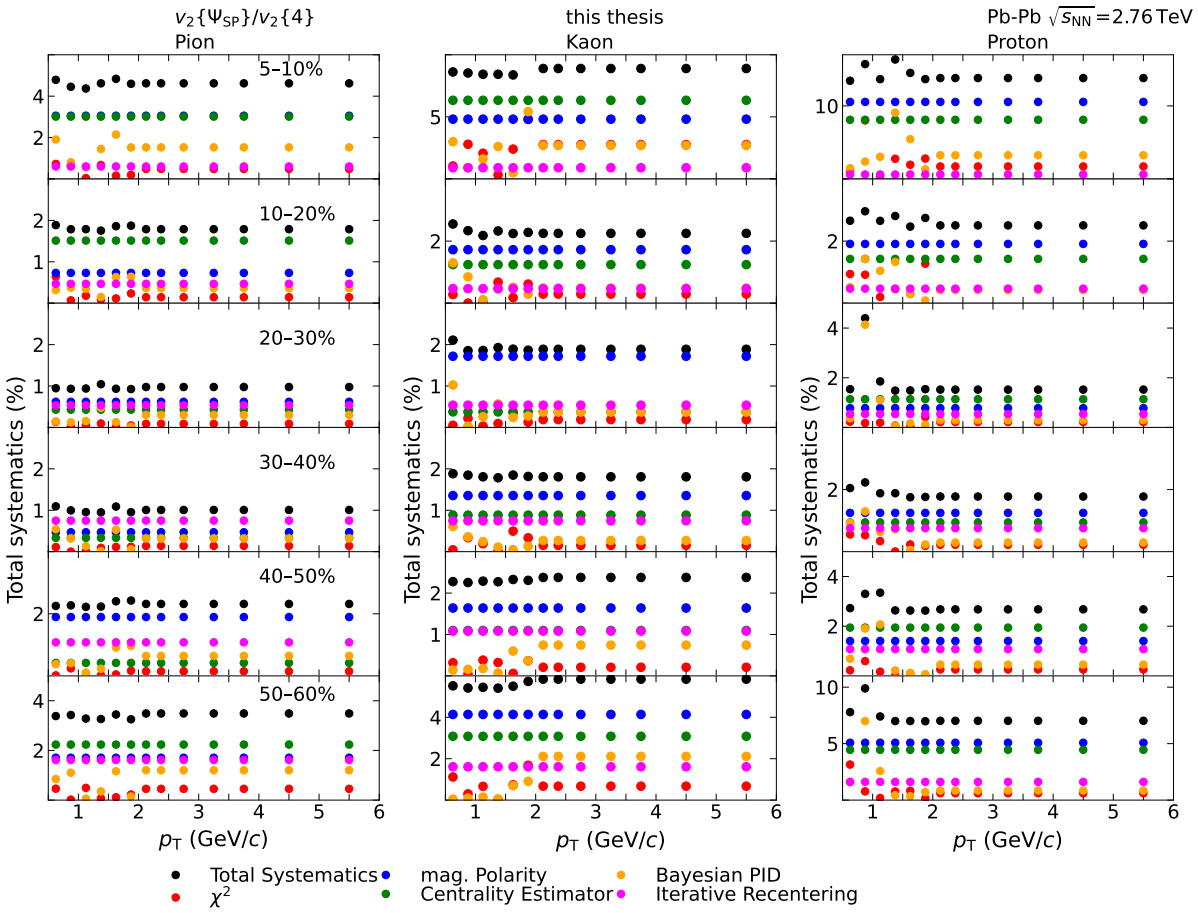

Figure 6.67: Total systematic uncertainties applied to the $v_2\{\Psi_{SP}\}/v_2\{4\}$ of pions (left panels), kaons (middle panels) and (anti)protons (right panels) as a function of transverse momentum in all analyzed centrality intervals. The ZDC scale uncertainty of ≈ 3 % is not shown in the figure.

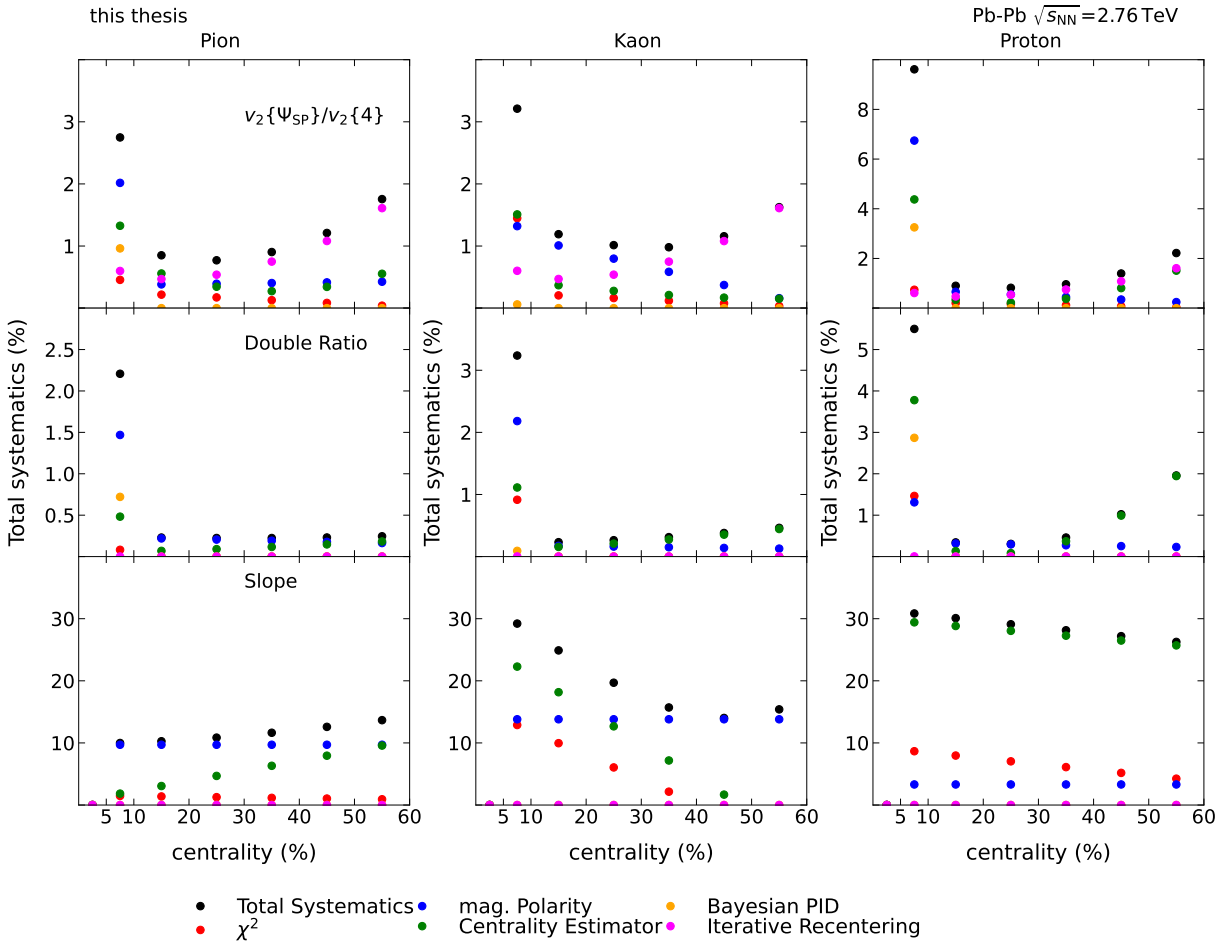

Figure 6.68: Total systematic uncertainties applied to the $v_2\{\Psi_{SP}\}/v_2\{4\}$, slope and double ratio of pions (left panels), kaons (middle panels) and (anti)protons (right panels) as a function of centrality. The ZDC scale uncertainty of ≈ 3 % is not shown in the figure for $v_2\{\Psi_{SP}\}/v_2\{4\}$.

7 Results

This section of the thesis presents the results for the particle-type dependence of elliptic flow in Pb–Pb collisions at a center-of-mass energy of $\sqrt{s_{\mathrm{NN}}} = 2.76\,\mathrm{TeV}$. The measurement of elliptic flow was carried out using three distinct methods: one based on the neutron spectator plane ($v_2\{\Psi_{\mathrm{SP}}\}$) and the other two using the two- and four-particle cumulants ($v_2\{2,|\Delta\eta|>1\}$ and $v_2\{4\}$), serving as a proxy of the elliptic flow with respect to the participant plane. Results are presented for charged hadrons, pions, kaons, and (anti)protons in the centrality intervals between 5% to 60% as a function of the transverse momentum. Results as a function of centrality are extracted from the p_{T}-differential results. The ratios $v_2\{\Psi_{\mathrm{SP}}\}/v_2\{4\}$ were compared with the corresponding eccentricity ratios obtained from initial state models. The double ratio of $v_2\{\Psi_{\mathrm{SP}}\}/v_2\{4\}$ to that of charged hadrons was used to quantify the particle-type dependence of the $v_2\{\Psi_{\mathrm{SP}}\}/v_2\{4\}$. The results presented in this chapter have been internally reviewed by the ALICE collaboration and approved to be published. The publication is currently under preparation.

7.1 p_{T} dependence of $v_2\{\Psi_{\mathrm{SP}}\}$, $v_2\{2,|\Delta\eta|>1\}$ and $v_2\{4\}$

The p_{T}-differential elliptic flow using the three different flow estimates $v_2\{2,|\Delta\eta|>1\}$, $v_2\{4\}$, and $v_2\{\Psi_{\mathrm{SP}}\}$ for charged hadrons, pions, kaons, and (anti)protons for the 20-30% centrality class are shown in Figure 7.1. The flow extracted via the spectator plane and the four-particle cumulant, are expected to be free from non-flow contributions. For $v_2\{\Psi_{\mathrm{SP}}\}$, this is the case due to the large pseudorapidity separation between the produced particles at mid-rapidity and the neutron spectators, whereas for $v_2\{4\}$ the non-flow contribution is suppressed because genuine four-particle correlations are used to extract the observable.

The measured p_{T}-dependence of the elliptic flow is similar for different flow estimates and particle species. As discussed in section 2.3, the differences are sensitive to the shape of flow fluctuations. Across all particle species, the $v_2\{2,|\Delta\eta|>1\}$ is larger than $v_2\{4\}$ in the measured transverse momentum range, which is expected from both the Bessel-Gaussian and EPM models of initial state fluctuations. The elliptic flow relative to the neutron spectator plane is similar to $v_2\{4\}$, which is also suggested by the two models. In the Bessel-Gaussian (EPM) model, the spectator plane Ψ_{SP} is assumed to be the same as the reaction plane Ψ_{RP}, so, the four-particle cumulant flow $v_2\{4\}$ is expected to be equal (greater) than the $v_2\{\Psi_{\mathrm{SP}}\}$. The deviation from these expectations would be a sign of the

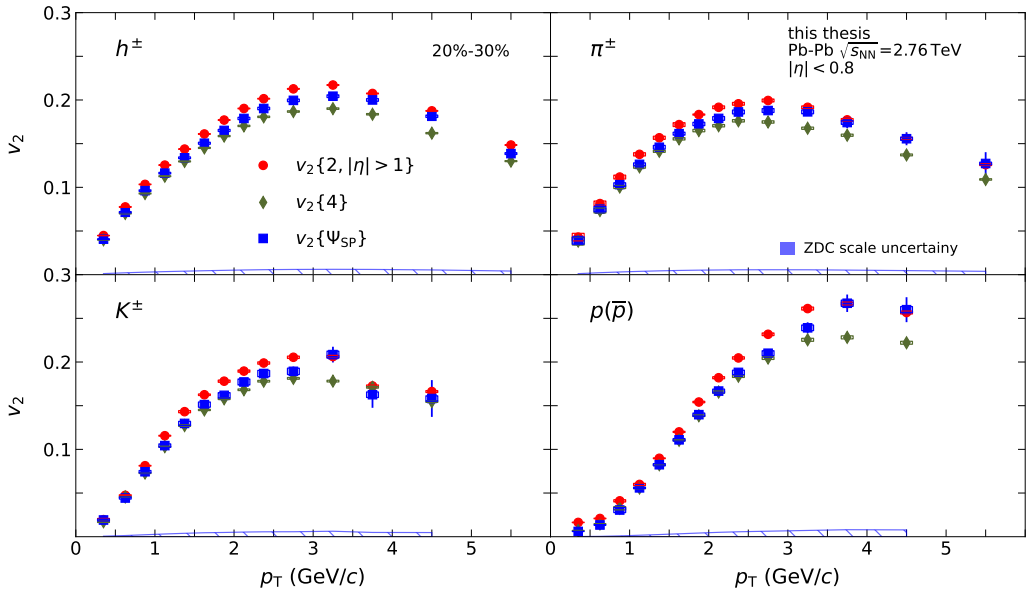

Figure 7.1: p_T-dependence of the elliptic flow with respect to the participant and spectator planes for charged hadrons, pions, kaons and (anti)protons for the 20-30% centrality class. The ZDC scale uncertainties are shown separately as hashed areas.

decorrelation between the spectator and reaction planes.

The ordering $v_2\{2\} > v_2\{4\} \approx v_2\{\Psi_{SP}\}$ for $p_T < 2$ GeV/c is observed for all particle species. This suggests that differences between flow estimates predominantly originate from the fluctuations in the initial energy density. Similar ordering of the flow estimates is found for all centrality classes, as shown in Figure 7.2 of the elliptic flow ($v_2\{2, |\Delta\eta| > 1\}$, $v_2\{4\}$ and $v_2\{\Psi_{SP}\}$) of charged pions, kaons, and (anti)protons in all centrality classes between 5-60%.

7.2 Particle type dependence of v_2 as function of p_T

Figure 7.3 shows the elliptic flow measured for charged pions, kaons, and (anti)protons as a function of p_T in the 20-30% centrality class. The particle-type dependence of the elliptic flow relative to the spectator plane $v_2\{\Psi_{SP}\}$ exhibits similar features as the flow relative to the participant plane. At low momentum, $p_T < 3$ GeV/c, the mass ordering is observed. It is a specific signature of the hydrodynamic expansion of the QGP, as can be seen in Figure 7.3 (right), which shows good agreement between previously published elliptic flow results [130] and hydrodynamic model calculations, iEBE-VISHNU [131]. The novel measurement of the flow relative to the spectator plane of charged pions, kaons, and (anti)protons provides new data that can be used in the extraction of the QGP transport coefficients by comparing it with hydrodynamic model calculations. This would require to

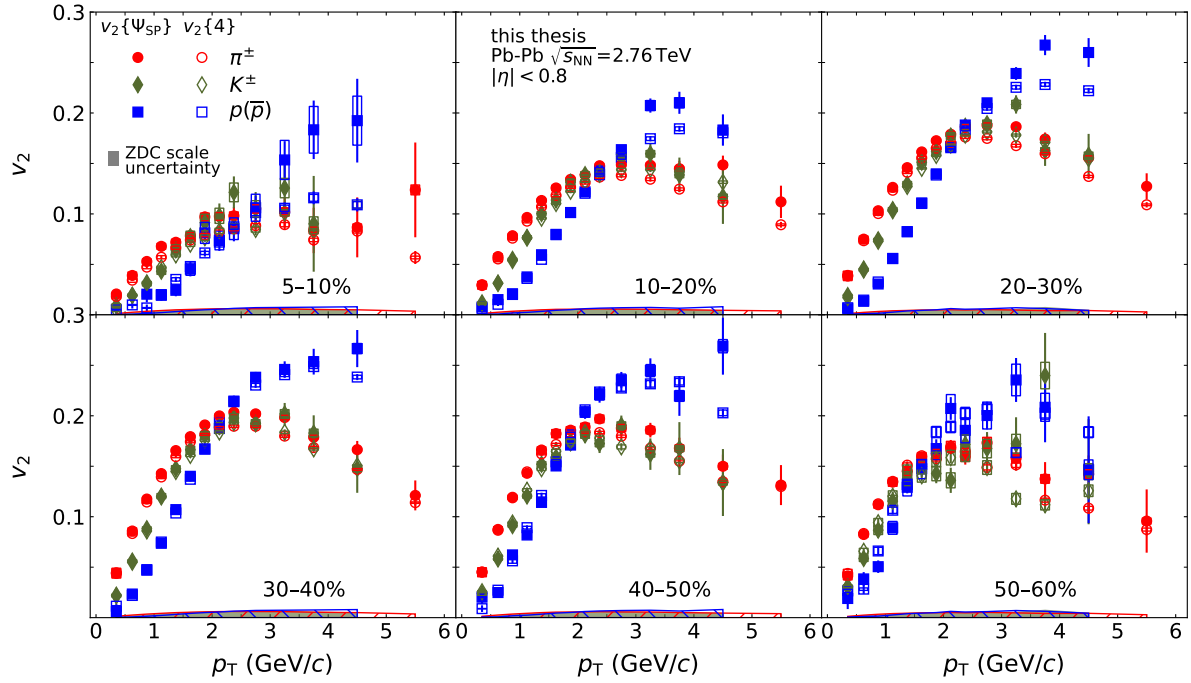

Figure 7.2: p_T-dependence of the elliptic flow with respect to the participant and spectator planes for pions, kaons and (anti)protons in different centrality classes. The ZDC scale uncertainties are shown as hashed areas.

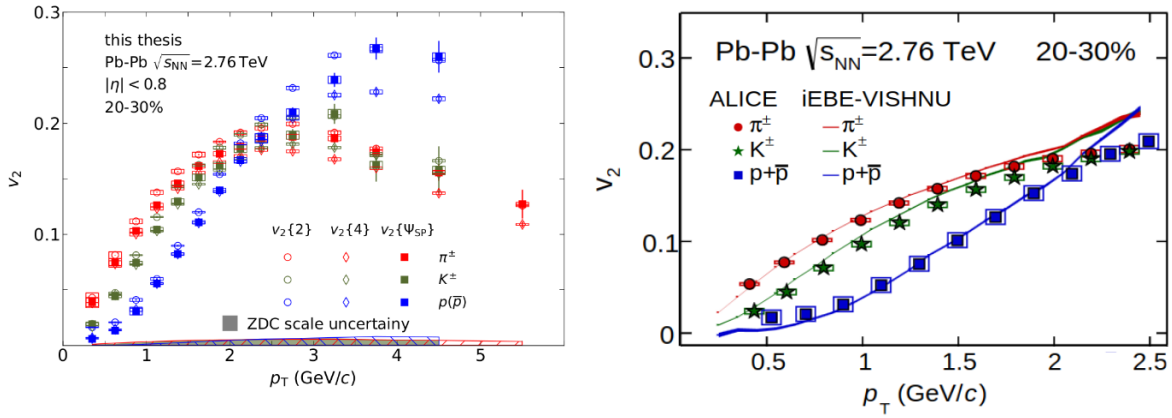

Figure 7.3: [Left Panel] p_T-dependence of the elliptic flow with respect to the participant and spectator planes for charged hadrons, pions, kaons and (anti)protons for the 20-30% centrality class. The ZDC scale uncertainties are shown separately as hashed areas. [Right panel] p_T-dependence of the elliptic flow for pions, kaons and (anit)protons from previous measurements [130] compared with hydrodynamic model calculations iEBE-VISHNU [131].

incorporate the spectator dynamics into the state-of-the-art initial state models.

7.3 Constituent quark number scaling

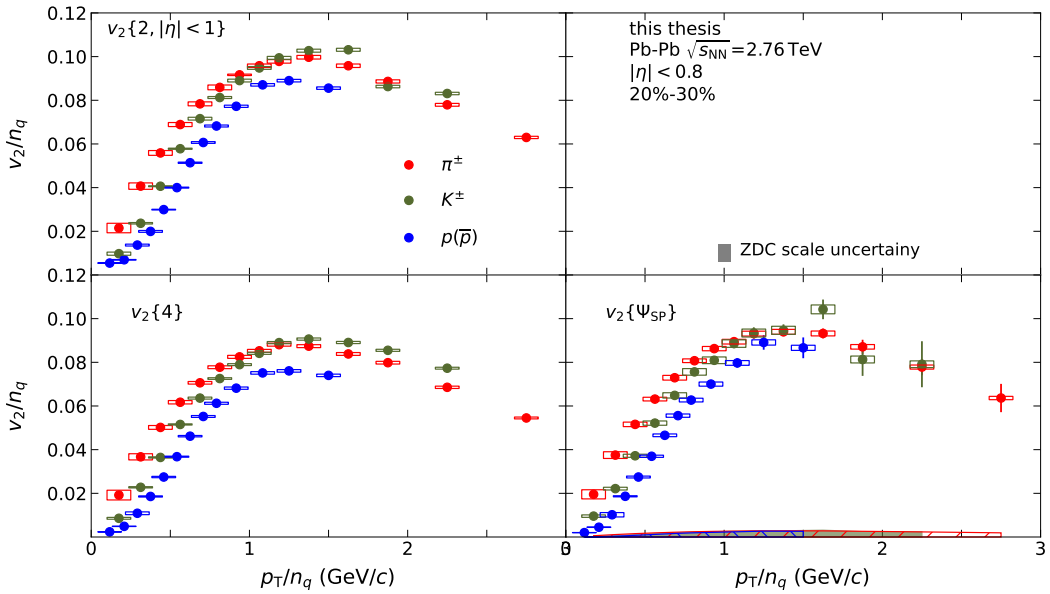

Figure 7.4: v_2/n_q as a function of p_T/n_q for charged pions, kaons and (anti)protons in the centrality class 20-30%. The different panels show the elliptic flow using different flow estimates. The ZDC scale uncertainties are shown separately as hashed areas.

At intermediate transverse momentum (3 GeV/c $< p_T <$ 6 GeV/c), the elliptic flow of baryons and mesons exhibits scaling with the number of constituent quarks (NCQ). This scaling is interpreted in the context of hadron production via quark coalescence and its presence suggests that flow develops at the partonic stage. According to the NCQ scaling, the anisotropic flow of mesons (baryons) should be twice (three times) the flow of their constituent quarks. The NCQ scaling can be tested by dividing both the p_T and the elliptic flow with the number of valence quarks (n_q) in the hadron.

Figure 7.4 shows the scaled elliptic flow relative to the spectator ($v_2\{\Psi_{SP}\}$) and participant ($v_2\{2, |\Delta\eta| > 1\}$ and $v_2\{4\}$) planes for charged pions, kaons and (anti)protons for the 20-30% centrality class. The new measurement of the elliptic flow of pions, kaons, and (anti)protons relative to the spectator plane reveals similar NCQ scaling behavior as those relative to the participant plane. The scaling is only approximate which is consistent with the findings of previous measurements of flow relative to the participant plane. For all centrality classes, similar scaling behavior is as can been seen from Figure 7.5, which shows the results for $v_2\{\Psi_{SP}\}/n_q$ as a function of p_T/n_q relative to the spectator plane for pions, kaons, and (anti)protons for the centrality classes between 5-60%.

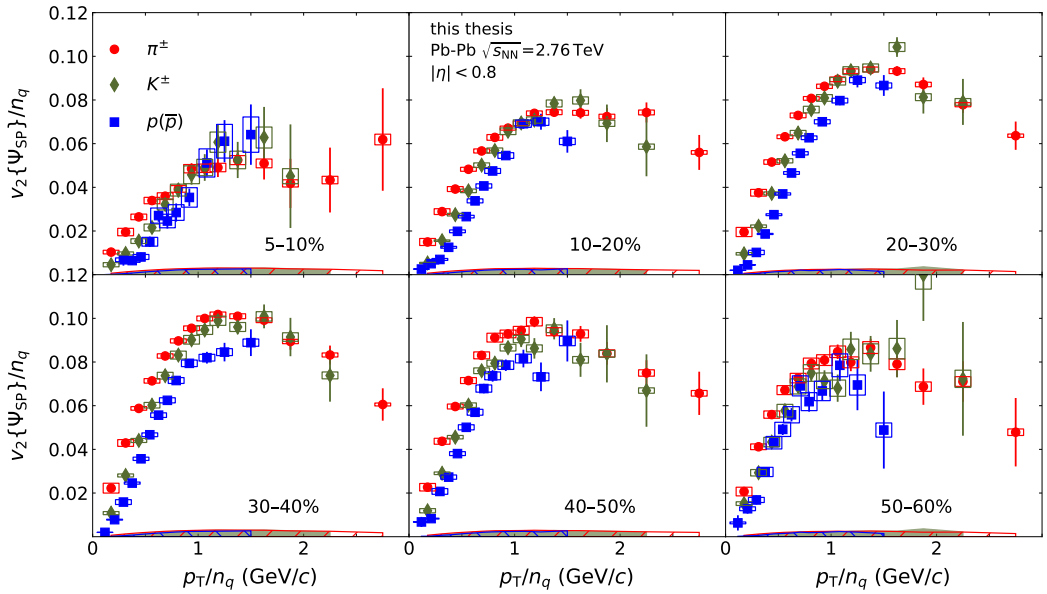

Figure 7.5: v_2/n_q as a function of p_T/n_q for charged pions, kaons and (anti)protons for centrality classes between 5-60%. The ZDC scale uncertainties are shown as hashed areas.

7.4 p_T-dependence of $v_2\{\Psi_{SP}\}/v_2\{4\}$

To separate the effect of flow fluctuations from those developed during the QGP expansion and hadronization, the ratio $v_2\{\Psi_{SP}\}/v_2\{4\}$ is studied as a function of p_T and centrality, and for different particle species. This ratio is unity in the case of no fluctuations or for Bessel-Gaussian shape of eccentricity fluctuations. Deviation from unity as a function of p_T and its particle-type dependence will signal effects of the QGP expansion and hadronization.

Figure 7.6 shows the measured $v_2\{\Psi_{SP}\}/v_2\{4\}$ for pions, kaons, and (anti)protons in the 20-30% centrality class together with a linear fit in the p_T region between 0.2 and 3 GeV/c. A weak p_T-dependence of the ratio was found. This means that the difference between v_2 relative to the spectator and participant planes is not only governed by a common source associated with eccentricity fluctuations but is sensitive to the effects from hydrodynamic evolution or hadronization. These observations are in line with measurements of the particle-type dependence of $v_2\{4\}/v_2\{2\}$ for Pb–Pb collisions at $\sqrt{s_{NN}} = 5.02$ TeV [54]. Together, they strongly suggest that the weak dependencies are not coming from the participant or spectator plane fluctuations but from the later stages of the heavy-ion collision evolution. This interpretation is supported by a comparison of the $v_2\{4\}/v_2\{2\}$ ratio with hydrodynamic model calculations incorporating quark coalescence and fragmentation, as shown in the bottom right panel of Figure 7.6. A collection of the ratio $v_2\{\Psi_{SP}\}/v_2\{4\}$ for charged pions, kaons, and (anti)protons for centrality classes between 5-60% together with a linear fit are shown in Figure 7.7.

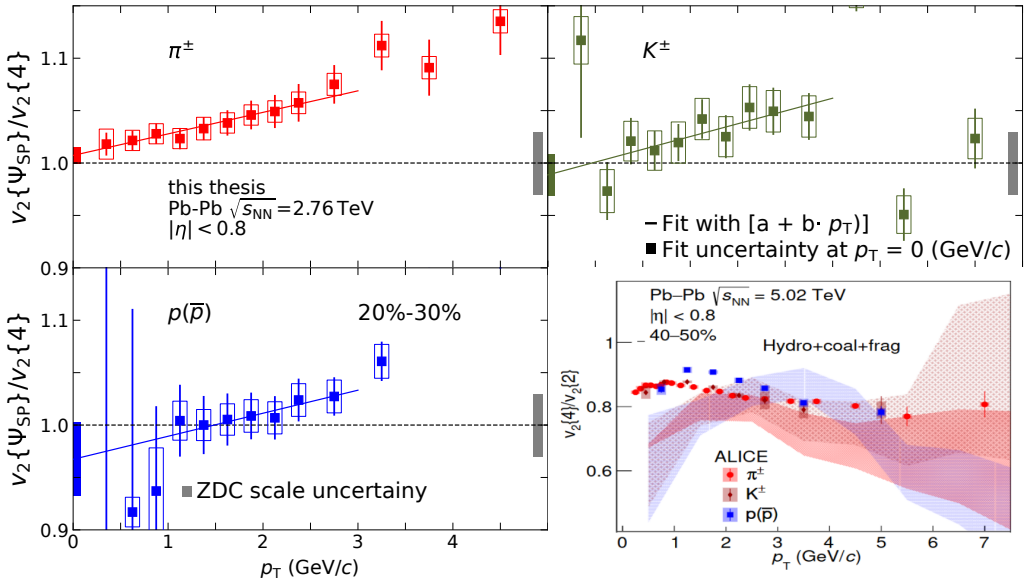

Figure 7.6: [upper and lower-left panels] The ratio $v_2\{\Psi_{SP}\}/v_2\{4\}$ as a function of p_T for pions, kaons and (anti)protons for the centrality class 20-30%. The ZDC scale uncertainty is shown as shaded gray area on the right side of each panel. The colored lines correspond to the linear fits performed in the transverse momentum region of 0.2 to 3.0 GeV/c. [Bottom right panel] $v_2\{4\}/v_2\{2\}$ as a function of p_T for pions, kaons and (anti)protons in Pb–Pb collisions at $\sqrt{s_{NN}} = 5.02$ TeV for the centrality class 40-50% [54]. Shaded bands show CoLBT [50] hydrodynamic model calculations.

7.5 Centrality dependence of $v_2\{\Psi_{SP}\}/v_2\{4\}$ for charged hadrons

The centrality dependence of the ratio $v_2\{\Psi_{SP}\}/v_2\{4\}$ and its slope as a function of p_T were extracted using a constant and a linear fit, respectively. All fits were performed in the transverse momentum range of 0.2 to 3.0 GeV/c. For details see Section 6.6.

Figure 7.8 shows the ratios $v_2\{\Psi_{SP}\}/v_2\{4\}$ and $v_2\{2,|\Delta\eta| > 1\}/v_2\{4\}$ [44], together with the corresponding eccentricity ratios from initial state models T$_R$ENTo (cyan and orange bands) and the EPM (dashed lines). The parameters of the T$_R$ENTo model were chosen according to [29]. The $v_2\{\Psi_{SP}\}/v_2\{4\}$ ratio agrees with the published results for the p_T-integrated $v_2\{\Psi_{SP}\}$ and $v_2\{4\}$ [44]. The ratio $v_2\{\Psi_{SP}\}/v_2\{4\}$ shows a maximum in most central collisions, with a plateau in 10-50%. In very peripheral collisions it approaches values below unity. The maximum in central collisions of $v_2\{\Psi_{SP}\}/v_2\{4\}$ is associated with the large fluctuation of a small number of neutron spectators used to estimate the spectator symmetry plane. This, consequently, leads to an increase of $v_2\{\Psi_{SP}\}$. The decrease in peripheral events is connected to the small number of particles produced in the participant zone and a decrease in the number of unbound neutron spectators, due to

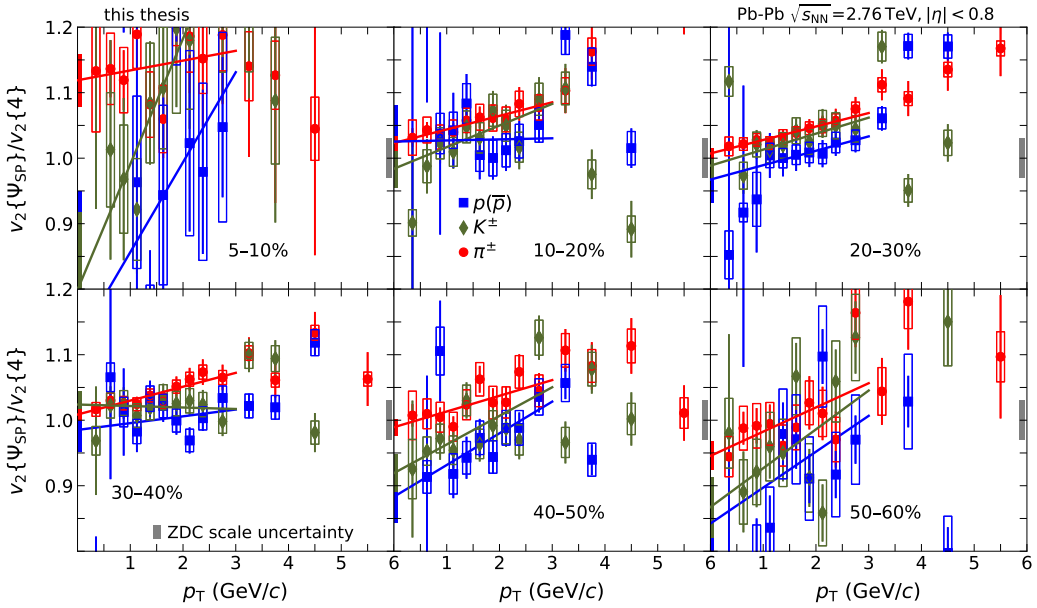

Figure 7.7: $v_2\{\Psi_{SP}\}/v_2\{4\}$ as a function of p_T for pions, kaons and (anti)protons for different centrality classes. The ZDC scale uncertainties are shown separately as shaded black areas on the right side of each panel. The colored lines correspond to the linear fit performed in the transverse momentum range of 0.2 to 3.0 GeV/c.

charged fragment formation. The charged fragments are deflected by the LHC magnets outside the acceptance of the ALICE ZDCs. These effects induce a decorrelation between participant and spectator planes.

The ratios $v_2\{\Psi_{SP}\}/v_2\{4\}$ are compared with corresponding eccentricities from three models of flow fluctuations (Bessel-Gaussian, Elliptic-power and T$_R$ENTo). The comparison is used to study deviations from linear ($v_n \approx \kappa\varepsilon_n$) scaling expected for flow observables. In both central and mid-central ($< 50\%$) collisions, the ratio $v_2\{\Psi_{SP}\}/v_2\{4\}$ is significantly larger than the expectation from the Bessel-Gaussian model (unity) and the predictions for $\varepsilon_2\{\Psi_{RP}\}/\varepsilon_2\{4\}$ from the EPM and T$_R$ENTo models. The small deviation of $\varepsilon_2\{\Psi_{RP}\}/\varepsilon_2\{4\}$ from unity of both the EPM and T$_R$ENTo model calculations can be explained by a non-zero skewness in the underlying eccentricity distribution (see Section 2.3). The difference observed between $\varepsilon_2\{\Psi_{RP}\}/\varepsilon_2\{4\}$ and $v_2\{\Psi_{SP}\}/v_2\{4\}$ can be due to a number of reasons. Firstly, it can be due to a decorrelation of the spectator plane Ψ_{SP} and the reaction plane Ψ_{RP}, which consequently leads to a difference of $\varepsilon_2\{\Psi_{RP}\}$ and $\varepsilon_2\{\Psi_{SP}\}$. This contribution is estimated by the eccentricity ratio $\varepsilon_2\{\Psi_{SP}\}/\varepsilon_2\{4\}$, which is shown in Figure 7.8 with the cyan line. Secondly, the $\varepsilon_2\{\Psi_{SP}\}$ is calculated from the position of non-interacting neutron spectators simulated by the T$_R$ENTo model. The T$_R$ENTo model does not include fragment formation from the spectator nucleons. This means that depending on the centrality, the number of neutron spectators can be

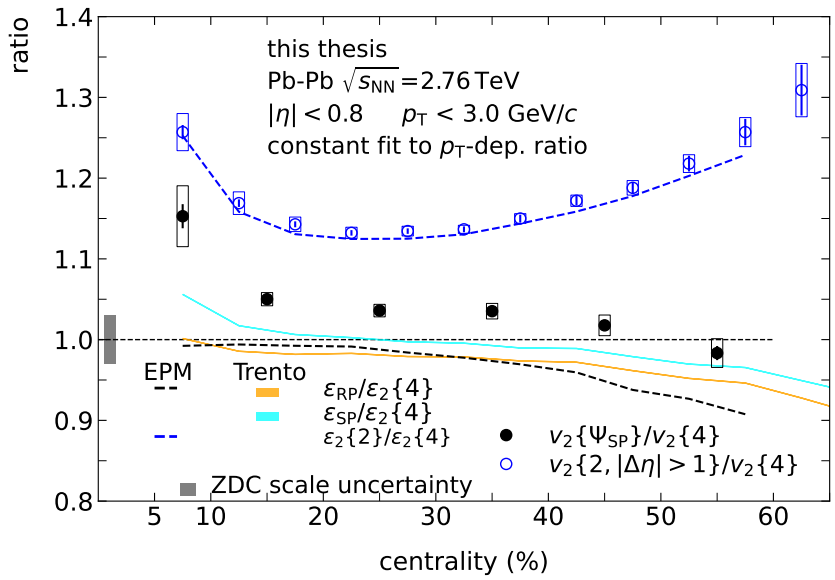

Figure 7.8: Centrality dependence of $v_2\{\Psi_{SP}\}/v_2\{4\}$, extracted from the constant fit to its p_T-dependenence, and $v_2\{2, |\Delta\eta| > 1\}/v_2\{4\}$ [44] for charged hadrons. The ZDC scale uncertainty is shown on the left-hand side as a shaded gray box. The cyan and orange (dashed) lines correspond to the eccentricity ratios extracted from the TRENTo (EPM) initial state model.

significantly overestimated compared to the experiment, where charged fragments are deflected by the LHC magnets outside the ZDC acceptance.

The TRENTo calculations for $\varepsilon_2\{\Psi_{SP}\}$ are larger than $\varepsilon_2\{\Psi_{RP}\}$, which brings the eccentricity ratios closer to the measured ratio $v_2\{\Psi_{SP}\}/v_2\{4\}$. However, there is a difference between $v_2\{\Psi_{SP}\}/v_2\{4\}$ and $\varepsilon_2\{\Psi_{SP}\}/\varepsilon_2\{4\}$, especially in non-central collisions. This remaining difference could be because the TRENTo model does not take into account the momentum exchange between the participant and the spectator regions at the early times of the heavy-ion collision. Another explanation could be a non-linear response to the initial eccentricities developed during the QGP evolution and its hadronization, which is not reflected in the TRENTo calculations.

7.6 Centrality dependence of the $v_2\{\Psi_{SP}\}/v_2\{4\}$ for identified hadrons

To further disentangle initial and final state contributions to the $v_2\{\Psi_{SP}\}/v_2\{4\}$ ratio it was measured for different types of hadrons. Figure 7.9 shows the $v_2\{\Psi_{SP}\}/v_2\{4\}$ ratio for charged hadrons, pions, kaons, and (anti)protons. The ratios $v_2\{\Psi_{SP}\}/v_2\{4\}$ calculated for different particle species exhibit a similar centrality dependence, yet a particle-type-dependent splitting is observed. This splitting can only be associated with

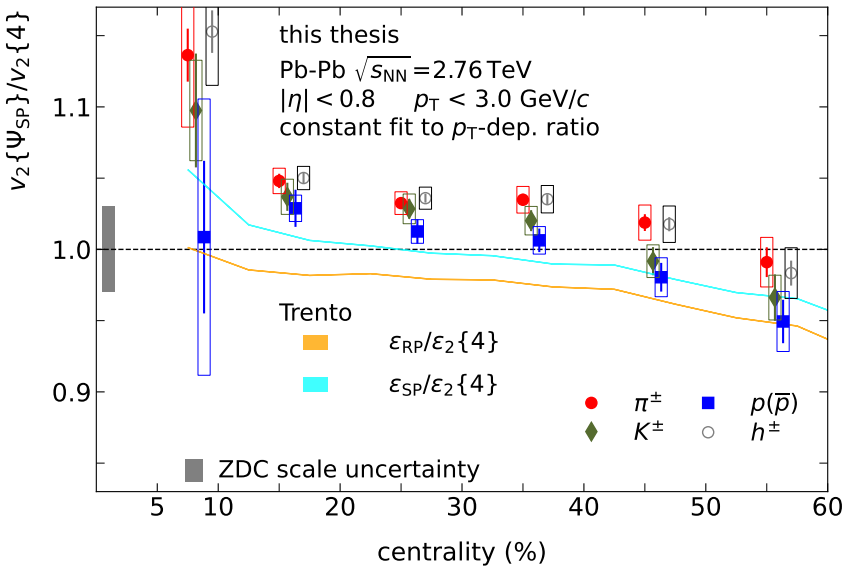

Figure 7.9: Centrality dependence of the ratio $v_2\{\Psi_{SP}\}/v_2\{4\}$ for charged hadrons, pions, kaons, and (anti)protons extracted from the constant fit to its p_T-dependence. The ZDC scale uncertainty is shown on the left-hand side as a shaded black box. The cyan and orange lines correspond to eccentricity ratios $\varepsilon_{RP}/\varepsilon_2\{4\}$ and $\varepsilon_{SP}/\varepsilon_2\{4\}$ extracted from TRENTo.

the hydrodynamic evolution of the QGP and the subsequent hadronization.

The difference between $v_2\{\Psi_{SP}\}/v_2\{4\}$ of pions, kaons, and (anti)protons can be quantified by double ratios relative to that of charged hadrons. In the case of a linear hydrodynamic response to eccentricity fluctuations, this cancels out the common contribution from initial state fluctuations. The double ratios also offer the advantage of partially canceling systematic uncertainties, thus enhancing the measurement precision. The double ratios, as a function of centrality for charged pions, kaons, and (anti)protons are shown in Figure 7.10. Considering both statistical and systematic uncertainties, a constant function was fitted to the double ratio. The result is shown by solid lines, with the bands representing the 1σ confidence interval. The particle-type-dependent splitting between pions and (anti)protons (kaons) was found to be 3.6% (1.6%) with a significance of 5.8σ (3.0σ). This splitting can be attributed to the viscous effects in the QGP evolution and the hadronization of the QGP.

In the assumption of a linear scaling between the anisotropic flow and the corresponding eccentricities, the slope of $v_2\{\Psi_{SP}\}/v_2\{4\}$ as a function of p_T should be zero. Deviation from a non-linear scaling would introduce a p_T-dependence of $v_2\{\Psi_{SP}\}/v_2\{4\}$. Figure 7.11 shows the slope of the linear fit to the p_T-differential ratio $v_2\{\Psi_{SP}\}/v_2\{4\}$ for charged hadrons, pions, kaons, and (anti)protons. The slopes of all particle types were found to be consistent within statistical and systematic uncertainties. A non-zero slope, which is observed for charged hadrons and pions (kaons and (anti)protons) starting from

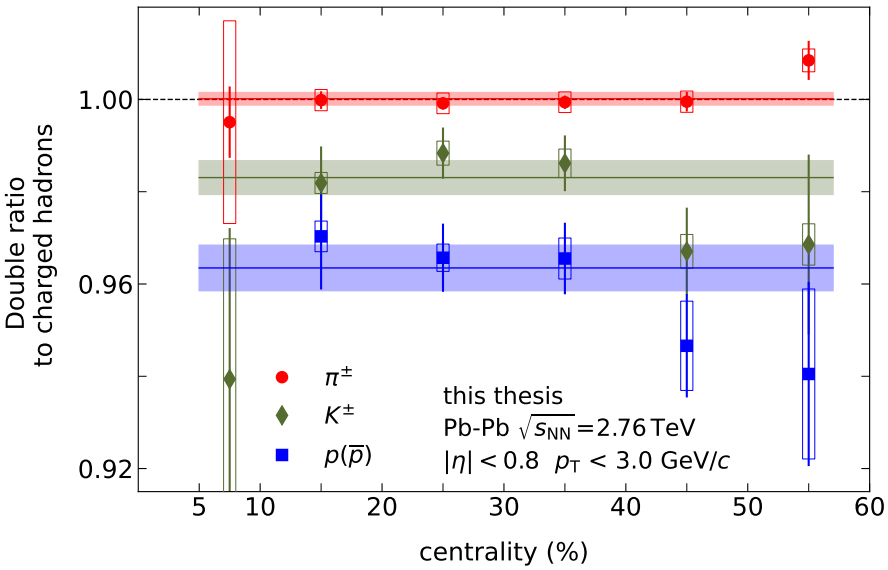

Figure 7.10: Centrality dependence of the double ratio for pions, kaons, and (anti)protons extracted with the constant fit to its p_T-dependence. The lines correspond to a constant fit to the centrality dependence of the double ratios. The shaded area around the fit lines corresponds to its 1σ confidence interval.

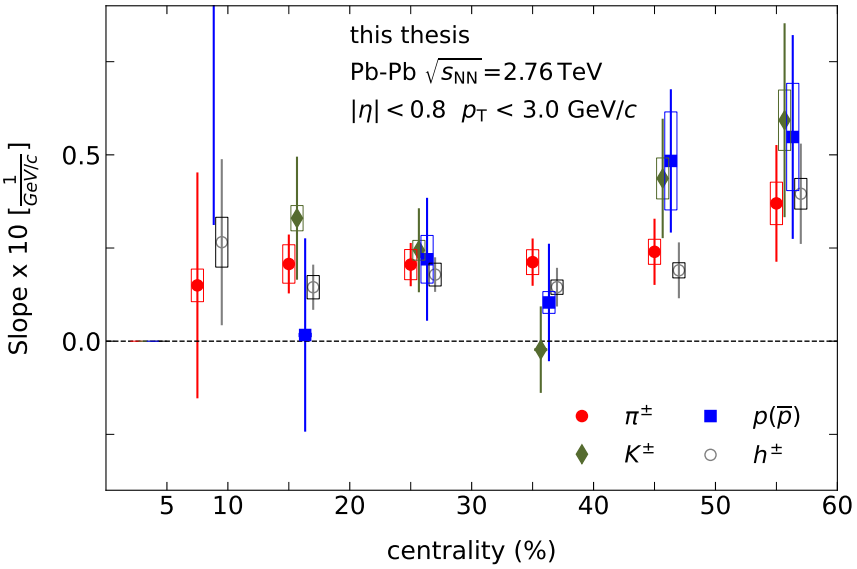

Figure 7.11: Centrality dependence of the slope of $v_2\{\Psi_{SP}\}/v_2\{4\}$ for charged hadrons, pions, kaons, and (anti)protons extracted from the linear fit to the p_T-dependent ratio $v_2\{\Psi_{SP}\}/v_2\{4\}$.

the centrality region of 20-30% (40-50%), indicates non-linear coupling of the hydrodynamic expansion to the initial state fluctuations. Drawing further conclusions about the particle type dependence is challenging due to the relatively large statistical uncertainties

associated with the current measurements. In the future, this will be improved by the LHC operations in Run 3 and beyond.

8 Summary and Outlook

At a temperature of about 156 MeV, the QCD matter undergoes a crossover phase transition from nuclear matter, where quarks and gluons are bound to hadrons, to a phase where they are deconfined, known as quark-gluon plasma (QGP). This state of matter is believed to exist shortly after the Big Bang. The ALICE experiment at the LHC recreates these extreme conditions via relativistic heavy-ion collisions, allowing the investigation of the QGP properties. Since a direct observation of the QGP is not possible, one depends on the measurement of final-state particles produced in the collision.

During the relativistic heavy-ion collision, in the overlap region of two strongly Lorentz-contracted nuclei, an extreme entropy and energy density is produced. The shape of the initial energy density fluctuates on a collision-by-collision basis due to the varying nucleon positions within the nuclei. Once thermalized, the quarks and gluons created in the overlap region of the nuclei form the QGP. The expansion of the QGP is described within the framework of relativistic fluid dynamics. Upon cooling below the critical temperature of the crossover transition, the QGP hadronizes into a gas of color-neutral hadrons. During the different stages of the collision, the large pressure and temperature gradients result in the transformation of the spatial anisotropy in the initial energy density into momentum anisotropy of the produced particles. This phenomena is known as anisotropic flow.

Anisotropic flow and its fluctuations are a unique tool for studying different stages of a heavy-ion collision and to extract the QGP transport properties, such as shear and bulk viscosities. The hydrodynamic QGP expansion and its hadronization lead to a specific particle-type dependence of the anisotropic flow. The transport coefficients of the QGP can be extracted by comparing the measured anisotropic flow with model calculations, which incorporate initial state fluctuations with a subsequent hydrodynamic evolution and hadronization. Such studies were done using Bayesian inference methods, see e.g. [29], integrating initial state models with hydrodynamic evolution. Currently, the extracted temperature dependence of the QGP shear and bulk viscosities are subject to large uncertainties. This is, in particular, due to a limited understanding of the initial energy density fluctuations, which propagates to the uncertainty in the extraction of the QGP transport coefficients.

One way to improve the understanding of the initial state fluctuations is to study collective flow with respect to the collision plane determined by the deflection of the spectator nucleons, which are the remnants of the colliding nuclei. Due to strong Lorentz contraction of the colliding nuclei at LHC energies, spectators decouple very early in the collision evolution and, therefore, only interact with the matter created in the nuclei over-

lap zone at the initial stage of the collision. This makes collective flow measurements with respect to the spectators especially sensitive to the early time dynamics of the collision.

This thesis presents new results on the particle-type dependence of elliptic flow relative to the neutron spectator plane, $v_2\{\Psi_{\rm SP}\}$, in Pb–Pb collisions at $\sqrt{s_{\rm NN}} = 2.76\,$TeV recorded with the ALICE experiment at the LHC. The results were compared with the elliptic flow relative to the participant plane, estimated with the two- and four-particle cumulants, $v_2\{2\}$ and $v_2\{4\}$.

The difference between the elliptic flow relative to the spectator plane ($v_2\{\Psi_{\rm SP}\}$) and participant plane ($v_2\{2\}$ and $v_2\{4\}$) is sensitive to the shape of flow fluctuations. Without flow fluctuations all observables reduce to the same value of the elliptic flow relative to the reaction plane of the collision, spanned by the impact parameter and the colliding nuclei direction. For a Bessel-Gaussian shape of fluctuations, which reflects a limit of the large number of nucleon participants, the $v_2\{2\}$ should be larger than $v_2\{4\}$, while $v_2\{4\}$ and $v_2\{\Psi_{\rm SP}\}$ stay the same. The observation of $v_2\{2\} > v_2\{4\}$ and a small difference between $v_2\{\Psi_{\rm SP}\}$ and $v_2\{4\}$ demonstrates a deviation from a Bessel-Gaussian model of fluctuations and underline the importance of flow measurements with spectators for understanding the pattern of initial state fluctuations.

The ordering of the different elliptic flow estimates was tested for charged pions, kaons, and (anti)protons. An ordering of $v_2\{2\}>v_2\{4\} \approx v_2\{\Psi_{\rm SP}\}$ at $p_{\rm T} < 2$ GeV/c is observed for all particle species. This suggests that the ordering of the elliptic flow estimates predominantly originates from the fluctuations in the initial state, since the particle type dependence only develops at the later stages of the collision. The particle-type dependence of the elliptic flow relative to the spectator plane $v_2\{\Psi_{\rm SP}\}$ exhibits similar features as the flow relative to the participant plane. At low momentum, $p_{\rm T} < 3$ GeV/c, the typical mass ordering, due to the hydrodynamic expansion of the QGP, is observed. At intermediate transverse momentum (3 GeV/$c < p_{\rm T} < 6$ GeV/c), the elliptic flow of baryons and mesons exhibits scaling with the number of constituent quarks, which is interpreted in the context of hadron production via quark coalescence. The new measurement of the elliptic flow of pions, kaons, and (anti)protons relative to the spectator plane reveals similar NCQ scaling behaviors as the flow measurements relative to the participant plane, confirming the findings from previous measurements relative to the participant plane.

In order to separate the effects of flow fluctuations from those developed during the QGP expansion and hadronization, the ratio $v_2\{\Psi_{\rm SP}\}/v_2\{4\}$ is studied differentially as a function of $p_{\rm T}$, centrality and for different particle species. This ratio should be unity in the case of no fluctuations or for Bessel-Gaussian shape of eccentricity fluctuations. Deviations from unity as a function of $p_{\rm T}$ and particle-type will signal effects of the QGP expansion and hadronization. A weak $p_{\rm T}$-dependence of the ratio was found, which means that the difference between v_2 relative to the spectator and participant planes is not only governed by a common source associated with eccentricity fluctuations but is sensitive to the effects from hydrodynamic evolution or hadronization of the QGP. These

observations are in line with the particle-type dependence of participant plane fluctuations, probed with the measurement of $v_2\{4\}/v_2\{2\}$, in Pb–Pb collisions at $\sqrt{s_{\rm NN}} = 5.02\,\text{TeV}$ [54], which also revealed a weak $p_{\rm T}$-dependent difference. This strongly suggests that the weak $p_{\rm T}$-dependencies are not coming from the participant and spectator fluctuations but from the later stages of the heavy-ion evolution. Such an interpretation is also supported by comparison of the $v_2\{4\}/v_2\{2\}$ with hydrodynamic model calculations incorporating quark coalescence and fragmentation. The new measurements of the flow relative to the spectator plane for charged pions, kaons, and (anti)protons can be used as a new input to the extraction of the QGP transport coefficients from comparison with hydrodynamic model calculations.

The ratio $v_2\{\Psi_{\rm SP}\}/v_2\{4\}$ as a function of the collision centrality was also compared with corresponding eccentricities from three models of flow fluctuations:Bessel-Gaussian, Elliptic-power, and T$_{\rm R}$ENTo. This is used to study deviations from linear ($v_n \approx \kappa\varepsilon_n$) scaling of flow estimates. The comparisons of $v_2\{\Psi_{\rm SP}\}/v_2\{4\}$ with $\varepsilon_2\{\Psi_{\rm RP}\}/\varepsilon_2\{4\}$ show significant tension between the data and predictions of initial state models. One reason for the observed discrepancy is a decorrelation between the spectator and reaction planes, due to the fluctuations in the initial state. This was already suggested by previous measurements relative to the spectator plane [42, 44]. Such decorrelation results in a difference of $\varepsilon_2\{\Psi_{\rm RP}\}$ and $\varepsilon_2\{\Psi_{\rm SP}\}$. In this thesis, the measurements of $v_2\{\Psi_{\rm SP}\}/v_2\{4\}$ of charged hadrons were compared with new calculations of $\varepsilon_2\{\Psi_{\rm SP}\}/\varepsilon_2\{4\}$, in which $\varepsilon_2\{\Psi_{\rm SP}\}$ was extracted from the position of non-interacting neutron spectators simulated by the initial state (T$_{\rm R}$ENTo) model. The initial state model calculations for $\varepsilon_2\{\Psi_{\rm SP}\}$ is found to be larger than $\varepsilon_2\{\Psi_{\rm RP}\}$, which brings the eccentricity ratios closer to the measured ratio $v_2\{\Psi_{\rm SP}\}/v_2\{4\}$. However, there is still a significant difference between $v_2\{\Psi_{\rm SP}\}/v_2\{4\}$ and $\varepsilon_2\{\Psi_{\rm SP}\}/\varepsilon_2\{4\}$, especially in non-central collisions. This remaining difference could be because the initial state model does not take into account the dynamics between the participant and the spectator regions at the early times of the heavy-ion collision. Another explanation could be a non-linear hydrodynamic response to the initial eccentricities, which develop during the hydrodynamic evolution of the QGP and its hadronization. The non-linear effects are not reflected in the initial state calculations. To extract the relative contribution of both these effects, model calculations, which incorporate the initial state dynamics between spectators and participants together with later stages of the QGP expansion and hadronization, are needed.

The effects of the hydrodynamic expansion of the QGP can be identified by comparing the ratio $v_2\{\Psi_{\rm SP}\}/v_2\{4\}$ for charged hadrons, pions, kaons, and (anti)protons. The ratios $v_2\{\Psi_{\rm SP}\}/v_2\{4\}$ for different particle species show a particle-type dependent splitting, which can only be associated with the stages of the hydrodynamic evolution of the QGP and the subsequent hadronization. The difference between $v_2\{\Psi_{\rm SP}\}/v_2\{4\}$ of pions, kaons, and (anti)protons is quantified by double ratios relative to that of charged hadrons. In the case of a linear hydrodynamic response to eccentricity fluctuations, this cancels out the common contribution from initial state fluctuations. The particle-type-dependent splitting between pions and (anti)protons (kaons) was found to be 3.6% (1.6%) with a

significance of 5.8σ (3.0σ). This splitting is attributed to the viscous effects in the QGP evolution and the hadronization of the QGP.

In the assumption of a linear scaling between the anisotropic flow and the corresponding eccentricities, the slope of $v_2\{\Psi_{\mathrm{SP}}\}/v_2\{4\}$ as a function of p_{T} should be zero. Non-linear scaling would introduce a p_{T}-dependence of $v_2\{\Psi_{\mathrm{SP}}\}/v_2\{4\}$. The slopes of all particle types were found to be non-zero and consistent within statistical and systematic uncertainties. A non-zero slope, which is observed for charged hadrons and pions (kaons and (anti)protons) starting from the centrality region of 20-30% (40-50%), indicates non-linear coupling of the hydrodynamic expansion to the initial state fluctuations. However, with the current data it is hard to draw strong conclusions due to their relatively large statistical uncertainties.

Results presented in this thesis for the anisotropic flow relative to the spectator plane demonstrated the unique potential of using spectators to improve the understanding of the initial state fluctuations in heavy-ion collisions. In future, the measurements can be expanded by more differential analyses, including additional particle species or performing the measurements at higher transverse momentum or in finer centrality classes. The extension to intermediate and very high p_{T} would allow to study how initial state fluctuations are coupled to different physics mechanisms, such as the quark coalescence at medium p_{T} and the hard processes and jet fragmentation at high p_{T}.

Extending the measurement of the anisotropic flow relative to the spectator plane would require larger statistics, which are expected in the future operation of the ALICE experiment. There is a growing interest in measuring spectator nucleons in heavy-ion collisions also by other LHC collaborations, evident in the joint effort of ATLAS and CMS Collaborations to develop new zero-degree calorimeters for the High-Luminosity LHC [132]. This will allow not only cross-experiment comparisons but also will help to exploit different experiment capabilities to measure complementary observables involving spectator plane.

From a theoretical perspective, the measurements presented in this thesis already stimulated theoretical developments to incorporate spectators into the modeling of the collision dynamics at the early stages for the LHC energies. An initial step was taken by using the spectator eccentricities from the T$_{\mathrm{R}}$ENTo initial state model. Results presented in this thesis for the particle-type dependence of $v_2\{\Psi_{\mathrm{SP}}\}$ and $v_2\{\Psi_{\mathrm{SP}}\}/v_2\{4\}$ into the future Bayesian analysis using hydrodynamic model calculations would allow reducing uncertainties in the extraction of the QGP transport properties and to quantify the relative contributions of different stages of the heavy-ion collision evolution to the observed flow fluctuations relative to the spectator plane.

Apendix

1 Supplemenatry figures

1.1 Variation of the fitting procedure to extract $v_2\{\Psi_{SP}\}/v_2\{4\}$ and double ratio

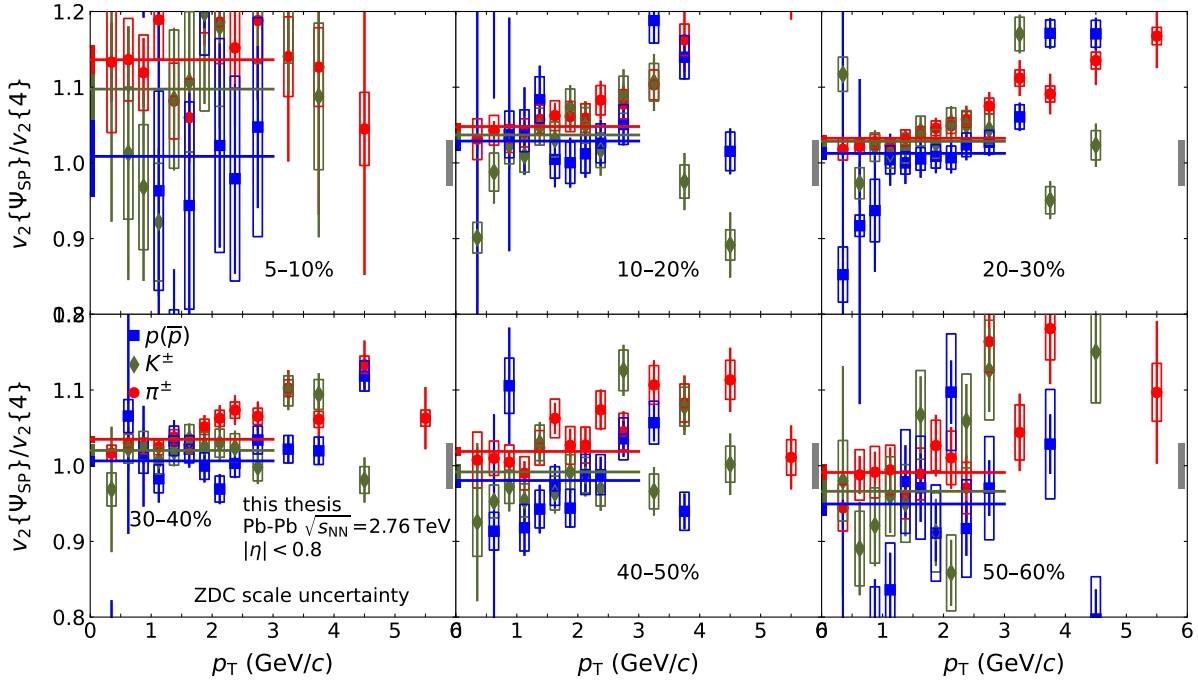

Figure 1: p_T-dependence of the ratio $v_2\{\Psi_{SP}\}/v_2\{4\}$ for pions, kaons and (anti)protons for different centrality classes. The different colors correspond to the different particle species. The vertical lines correspond to the statistical uncertainties, whereas the boxes show the systematic uncertainty. The ZDC scale uncertainties are showed separately as shaded black areas for all centrality classes on the right side of each panel. The colored lines correspond to the constant fit performed in the transverse momentum region of 0.2 to 3.0 GeV/c.

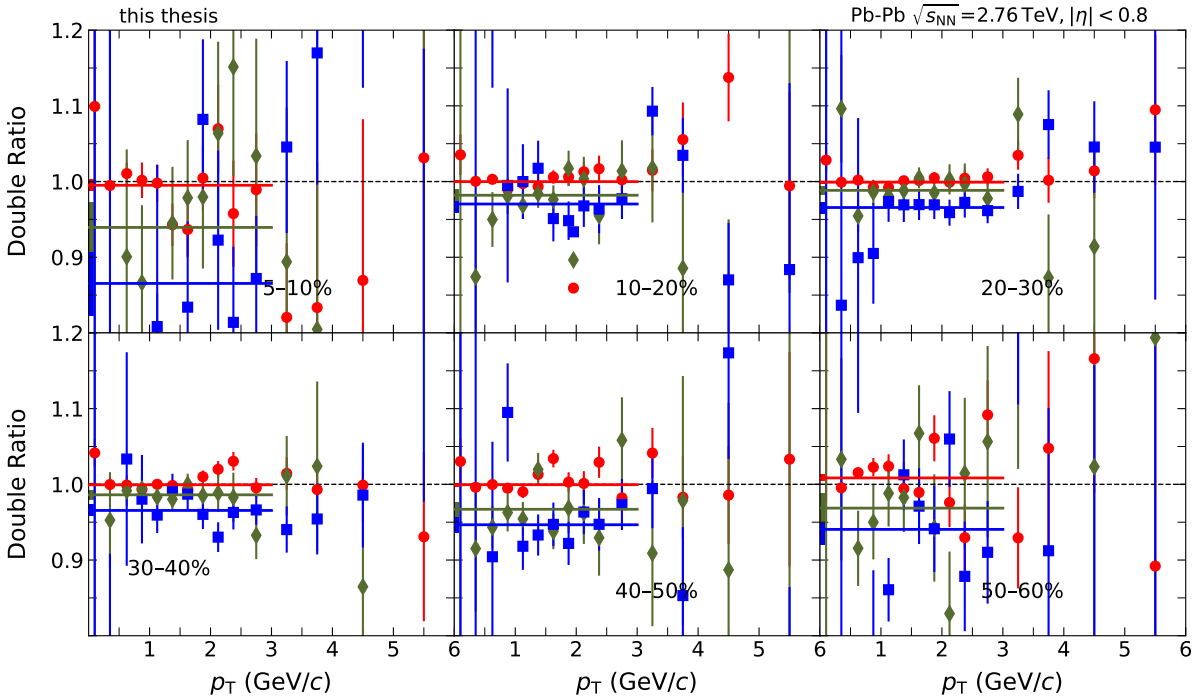

Figure 2: p_T-dependence of the double ratio for pions, kaons and (anti)protons to the one of charged hadrons for different centrality classes. The different colors correspond to the different particle species. The vertical lines correspond to the statistical uncertainties, whereas the boxes show the systematic uncertainty. The ZDC scale uncertainties are showed separately as shaded black areas for all centrality classes on the right side of each panel. The colored lines correspond to the constant fit performed in the transverse momentum region of 0.2 to 3.0 GeV/c.

1.2 NCQ scaling of $v_2\{2, |\Delta\eta| > 1\}$ and $v_2\{4\}$

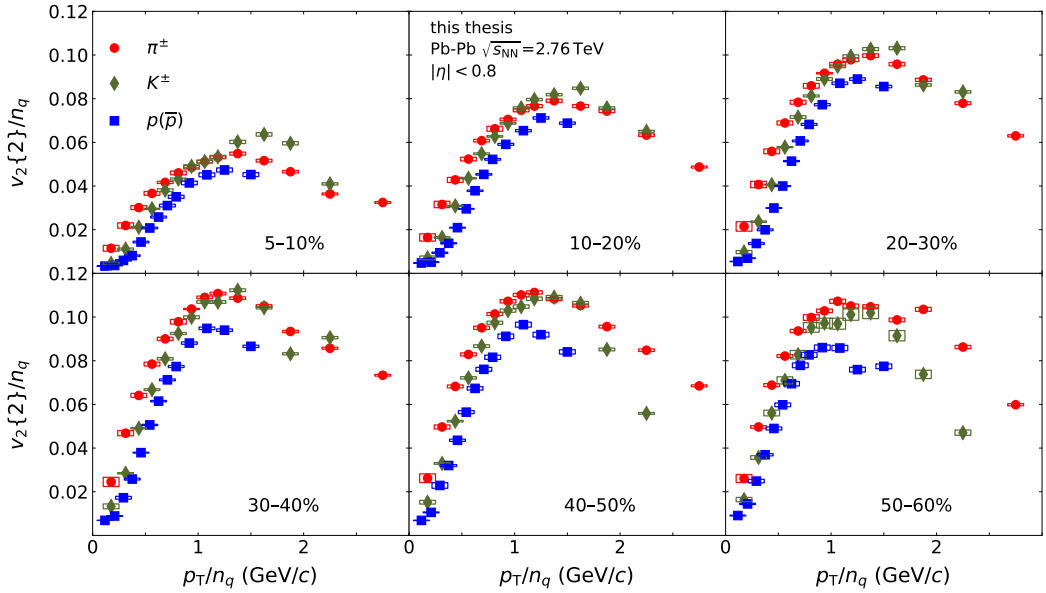

Figure 3: $v_2\{2, |\Delta\eta| > 1\}/n_q$ as a function of p_T/n_q for charged pions, kaons and (anti)protons for centrality classes between 5-60%.

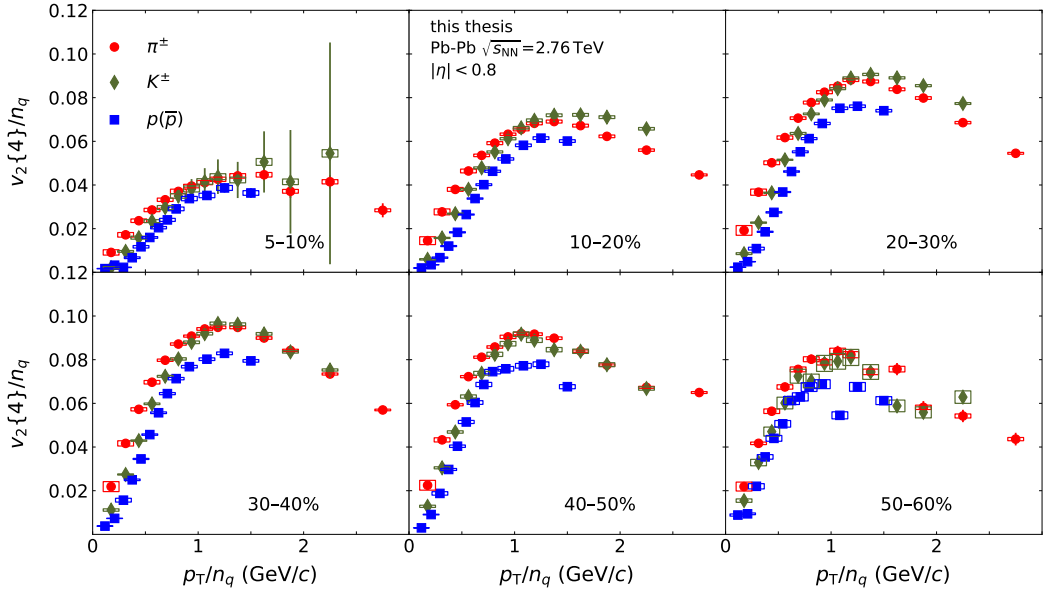

Figure 4: $v_2\{4\}/n_q$ as a function of p_T/n_q for charged pions, kaons and (anti)protons for centrality classes between 5-60%.

List of Publications

This thesis is based on a publication currently under preparation. The physics analysis, on which the publication is based, has be reviewed internally in the ALICE collaboration and has been approved for publication. The target format of the publication is a letter.

1. ALICE Collaboration, "Elliptic flow fluctuations of charged pions, kaons, and (anti)protons relative to the spectator plane in Pb–Pb collisions at $\sqrt{s_{\mathrm{NN}}} = 2.76\,\mathrm{TeV}$ "

Bibliography

[1] D. Boyanovsky, H. J. de Vega, and D. J. Schwarz, "Phase transitions in the early and the present universe," *Ann. Rev. Nucl. Part. Sci.*, vol. 56, pp. 441–500, 2006.

[2] M. Valente, *The Standard Model of Particle Physics*, pp. 5–25. Cham: Springer International Publishing, 2022.

[3] M. E. Peskin and D. V. Schroeder, *An Introduction to Quantum Field Theory*. Westview Press, 1995. Reading, USA: Addison-Wesley (1995) 842 p.

[4] R. B. Mann, *An introduction to particle physics and the standard model*. Boca Raton, FL: CRC Press, 2010.

[5] D. d'Enterria and P. Z. Skands, eds., *Proceedings, High-Precision α_s Measurements from LHC to FCC-ee: Geneva, Switzerland, October 2-13, 2015*, (Geneva), CERN, 12 2015.

[6] K. G. Wilson, "Confinement of Quarks," *Phys. Rev. D*, vol. 10, pp. 2445–2459, 1974.

[7] H. Satz, "The Quark-Gluon Plasma: A Short Introduction," *Nucl. Phys. A*, vol. 862-863, pp. 4–12, 2011.

[8] A. Bazavov *et al.*, "Equation of state in (2+1)-flavor QCD," *Phys. Rev. D*, vol. 90, p. 094503, 2014.

[9] P. Achenbach *et al.*, "The Present and Future of QCD," 3 2023.

[10] M. G. Alford, A. Schmitt, K. Rajagopal, and T. Schäfer, "Color superconductivity in dense quark matter," *Rev. Mod. Phys.*, vol. 80, pp. 1455–1515, 2008.

[11] E. Laermann and O. Philipsen, "The Status of lattice QCD at finite temperature," *Ann. Rev. Nucl. Part. Sci.*, vol. 53, pp. 163–198, 2003.

[12] Y. Aoki, G. Endrodi, Z. Fodor, S. D. Katz, and K. K. Szabo, "The Order of the quantum chromodynamics transition predicted by the standard model of particle physics," *Nature*, vol. 443, pp. 675–678, 2006.

[13] A. Bazavov *et al.*, "Chiral crossover in QCD at zero and non-zero chemical potentials," *Phys. Lett. B*, vol. 795, pp. 15–21, 2019.

[14] P. de Forcrand, "Simulating QCD at finite density," *PoS*, vol. LAT2009, p. 010, 2009.

[15] "The ALICE experiment – A journey through QCD," 11 2022.

[16] K. Agarwal, "The compressed baryonic matter (CBM) experiment at FAIR—physics, status and prospects," *Phys. Scripta*, vol. 98, no. 3, p. 034006, 2023.

[17] W. Busza, K. Rajagopal, and W. van der Schee, "Heavy Ion Collisions: The Big Picture, and the Big Questions," *Ann. Rev. Nucl. Part. Sci.*, vol. 68, pp. 339–376, 2018.

[18] J. Adam *et al.*, "Direct photon production in Pb-Pb collisions at $\sqrt{s_{NN}} = 2.76$ TeV," *Phys. Lett. B*, vol. 754, pp. 235–248, 2016.

[19] A. Monnai, *Relativistic Dissipative Hydrodynamic Description of the Quark-Gluon Plasma Relativistic Dissipative Hydrodynamic Description of the Quark-Gluon Plasma*. PhD thesis, Tokyo U., New-York, 2014.

[20] R. D. Woods and D. S. Saxon, "Diffuse Surface Optical Model for Nucleon-Nuclei Scattering," *Phys. Rev.*, vol. 95, pp. 577–578, 1954.

[21] B. Schenke, P. Tribedy, and R. Venugopalan, "Fluctuating Glasma initial conditions and flow in heavy ion collisions," *Phys. Rev. Lett.*, vol. 108, p. 252301, 2012.

[22] M. L. Miller, K. Reygers, S. J. Sanders, and P. Steinberg, "Glauber modeling in high energy nuclear collisions," *Ann. Rev. Nucl. Part. Sci.*, vol. 57, pp. 205–243, 2007.

[23] J. S. Moreland, J. E. Bernhard, and S. A. Bass, "Alternative ansatz to wounded nucleon and binary collision scaling in high-energy nuclear collisions," *Phys. Rev. C*, vol. 92, no. 1, p. 011901, 2015.

[24] A. Andronic, P. Braun-Munzinger, K. Redlich, and J. Stachel, "Decoding the phase structure of QCD via particle production at high energy," *Nature*, vol. 561, no. 7723, pp. 321–330, 2018.

[25] F. Becattini, "An Introduction to the Statistical Hadronization Model," in *International School on Quark-Gluon Plasma and Heavy Ion Collisions: past, present, future*, 1 2009.

[26] E. Fermi, "High Energy Nuclear Events," *Progress of Theoretical Physics*, vol. 5, pp. 570–583, 07 1950.

[27] F. Becattini and L. Ferroni, "Statistical hadronization and hadronic microcanonical ensemble. 2.," *Eur. Phys. J. C*, vol. 38, pp. 225–246, 2004. [Erratum: Eur.Phys.J. 66, 341 (2010)].

[28] P. Braun-Munzinger, J. Stachel, and C. Wetterich, "Chemical freezeout and the QCD phase transition temperature," *Phys. Lett. B*, vol. 596, pp. 61–69, 2004.

[29] J. E. Bernhard, J. S. Moreland, and S. A. Bass, "Bayesian estimation of the specific shear and bulk viscosity of quark–gluon plasma," *Nature Phys.*, vol. 15, no. 11, pp. 1113–1117, 2019.

[30] D. Devetak, A. Dubla, S. Floerchinger, E. Grossi, S. Masciocchi, A. Mazeliauskas, and I. Selyuzhenkov, "Global fluid fits to identified particle transverse momentum spectra from heavy-ion collisions at the Large Hadron Collider," *JHEP*, vol. 06, p. 044, 2020.

[31] B. Abelev *et al.*, "Pion, Kaon, and Proton Production in Central Pb–Pb Collisions at $\sqrt{s_{NN}} = 2.76$ TeV," *Phys. Rev. Lett.*, vol. 109, p. 252301, 2012.

[32] E. Schnedermann, J. Sollfrank, and U. W. Heinz, "Thermal phenomenology of hadrons from 200-A/GeV S+S collisions," *Phys. Rev. C*, vol. 48, pp. 2462–2475, 1993.

[33] G. Che, J. Gu, W. Zhang, and H. Zheng, "Identified particle spectra in Pb–Pb, Xe–Xe and p–Pb collisions with the Tsallis blast-wave model," *J. Phys. G*, vol. 48, no. 9, p. 095103, 2021.

[34] S. Voloshin and Y. Zhang, "Flow study in relativistic nuclear collisions by Fourier expansion of Azimuthal particle distributions," *Z. Phys. C*, vol. 70, pp. 665–672, 1996.

[35] B. Schenke, S. Jeon, and C. Gale, "Anisotropic flow in $\sqrt{s} = 2.76$ TeV Pb+Pb collisions at the LHC," *Phys. Lett. B*, vol. 702, pp. 59–63, 2011.

[36] J. e. a. Adam, "Anisotropic Flow of Charged Particles in Pb-Pb Collisions at $\sqrt{s_{NN}} = 5.02$ TeV," *Phys. Rev. Lett.*, vol. 116, p. 132302, Apr 2016.

[37] J. Noronha-Hostler, L. Yan, F. G. Gardim, and J.-Y. Ollitrault, "Linear and cubic response to the initial eccentricity in heavy-ion collisions," *Phys. Rev. C*, vol. 93, no. 1, p. 014909, 2016.

[38] S. A. Voloshin, A. M. Poskanzer, A. Tang, and G. Wang, "Elliptic flow in the Gaussian model of eccentricity fluctuations," *Phys. Lett. B*, vol. 659, pp. 537–541, 2008.

[39] L. Yan, J.-Y. Ollitrault, and A. M. Poskanzer, "Eccentricity distributions in nucleus-nucleus collisions," *Phys. Rev. C*, vol. 90, no. 2, p. 024903, 2014.

[40] S. Acharya *et al.*, "Energy dependence and fluctuations of anisotropic flow in Pb-Pb collisions at $\sqrt{s_{\mathrm{NN}}} = 5.02$ and 2.76 TeV," *JHEP*, vol. 07, p. 103, 2018.

[41] G. Giacalone, L. Yan, J. Noronha-Hostler, and J.-Y. Ollitrault, "Skewness of elliptic flow fluctuations," *Phys. Rev. C*, vol. 95, no. 1, p. 014913, 2017.

[42] B. Abelev *et al.*, "Directed Flow of Charged Particles at Midrapidity Relative to the Spectator Plane in Pb-Pb Collisions at $\sqrt{s_{NN}}$=2.76 TeV," *Phys. Rev. Lett.*, vol. 111, no. 23, p. 232302, 2013.

[43] K. Aamodt *et al.*, "Harmonic decomposition of two-particle angular correlations in Pb-Pb collisions at $\sqrt{s_{NN}} = 2.76$ TeV," *Phys. Lett. B*, vol. 708, pp. 249–264, 2012.

[44] S. Acharya *et al.*, "Elliptic flow of charged particles at midrapidity relative to the spectator plane in Pb–Pb and Xe–Xe collisions," *Phys. Lett. B*, vol. 846, p. 137453, 2023.

[45] S. Ryu, J.-F. Paquet, C. Shen, G. Denicol, B. Schenke, S. Jeon, and C. Gale, "Effects of bulk viscosity and hadronic rescattering in heavy ion collisions at energies available at the BNL Relativistic Heavy Ion Collider and at the CERN Large Hadron Collider," *Phys. Rev. C*, vol. 97, no. 3, p. 034910, 2018.

[46] P. Huovinen, P. F. Kolb, U. W. Heinz, P. V. Ruuskanen, and S. A. Voloshin, "Radial and elliptic flow at RHIC: Further predictions," *Phys. Lett. B*, vol. 503, pp. 58–64, 2001.

[47] S. Acharya *et al.*, "Anisotropic flow of identified particles in Pb-Pb collisions at $\sqrt{s}_{\mathrm{NN}} = 5.02$ TeV," *JHEP*, vol. 09, p. 006, 2018.

[48] V. Minissale, F. Scardina, and V. Greco, "Hadrons from coalescence plus fragmentation in AA collisions at energies available at the BNL Relativistic Heavy Ion Collider to the CERN Large Hadron Collider," *Phys. Rev. C*, vol. 92, no. 5, p. 054904, 2015.

[49] K. Werner, B. Guiot, I. Karpenko, and T. Pierog, "Analysing radial flow features in p-Pb and p-p collisions at several TeV by studying identified particle production in EPOS3," *Phys. Rev. C*, vol. 89, no. 6, p. 064903, 2014.

[50] W. Zhao, W. Ke, W. Chen, T. Luo, and X.-N. Wang, "From Hydrodynamics to Jet Quenching, Coalescence, and Hadron Cascade: A Coupled Approach to Solving the RAA⊗v2 Puzzle," *Phys. Rev. Lett.*, vol. 128, no. 2, p. 022302, 2022.

[51] S. A. Voloshin, "Anisotropic flow," *Nucl. Phys. A*, vol. 715, pp. 379–388, 2003.

[52] D. Molnar and S. A. Voloshin, "Elliptic flow at large transverse momenta from quark coalescence," *Phys. Rev. Lett.*, vol. 91, p. 092301, 2003.

[53] B. Abelev *et al.*, "Anisotropic flow of charged hadrons, pions and (anti-)protons measured at high transverse momentum in Pb-Pb collisions at $\sqrt{s_{NN}}$=2.76 TeV," *Phys. Lett. B*, vol. 719, pp. 18–28, 2013.

[54] S. Acharya *et al.*, "Anisotropic flow and flow fluctuations of identified hadrons in Pb–Pb collisions at $\sqrt{s_{\mathrm{NN}}}$ = 5.02 TeV," *JHEP*, vol. 05, p. 243, 2023.

[55] A. Bilandzic, C. H. Christensen, K. Gulbrandsen, A. Hansen, and Y. Zhou, "Generic framework for anisotropic flow analyses with multiparticle azimuthal correlations," *Phys. Rev. C*, vol. 89, no. 6, p. 064904, 2014.

[56] A. Bilandzic, R. Snellings, and S. Voloshin, "Flow analysis with cumulants: Direct calculations," *Phys. Rev. C*, vol. 83, p. 044913, 2011.

[57] R. Kubo, "Generalized Cumulant Expansion Method," *Journal of the Physical Society of Japan*, vol. 17, no. 7, pp. 1100–1120, 1962.

[58] N. Borghini, P. M. Dinh, and J.-Y. Ollitrault, "Flow analysis from multiparticle azimuthal correlations," *Phys. Rev. C*, vol. 64, p. 054901, 2001.

[59] N. Borghini, P. M. Dinh, and J.-Y. Ollitrault, "A New method for measuring azimuthal distributions in nucleus-nucleus collisions," *Phys. Rev. C*, vol. 63, p. 054906, 2001.

[60] A. Bilandzic, R. Snellings, and S. Voloshin, "Flow analysis with cumulants: Direct calculations," *Phys. Rev. C*, vol. 83, p. 044913, 2011.

[61] C. Adler *et al.*, "Elliptic flow from two and four particle correlations in Au+Au collisions at s(NN)**(1/2) = 130-GeV," *Phys. Rev. C*, vol. 66, p. 034904, 2002.

[62] B. B. Abelev *et al.*, "Multiparticle azimuthal correlations in p -Pb and Pb-Pb collisions at the CERN Large Hadron Collider," *Phys. Rev. C*, vol. 90, no. 5, p. 054901, 2014.

[63] A. M. Poskanzer and S. A. Voloshin, "Methods for analyzing anisotropic flow in relativistic nuclear collisions," *Phys. Rev. C*, vol. 58, pp. 1671–1678, Sep 1998.

[64] S. A. Voloshin, A. M. Poskanzer, and R. Snellings, "Collective phenomena in non-central nuclear collisions," *Landolt-Bornstein*, vol. 23, pp. 293–333, 2010.

[65] "LHC Machine," *JINST*, vol. 3, p. S08001, 2008.

[66] M. Benedikt, P. Collier, V. Mertens, J. Poole, and K. Schindl, *LHC Design Report*. CERN Yellow Reports: Monographs, Geneva: CERN, 2004.

[67] E. Lopienska, "The CERN accelerator complex, layout in 2022. Complexe des accélérateurs du CERN en janvier 2022," 2022. General Photo.

[68] G. Aad *et al.*, "The ATLAS Experiment at the CERN Large Hadron Collider," *JINST*, vol. 3, p. S08003, 2008.

[69] S. Chatrchyan *et al.*, "The CMS Experiment at the CERN LHC," *JINST*, vol. 3, p. S08004, 2008.

[70] A. A. Alves, Jr. *et al.*, "The LHCb Detector at the LHC," *JINST*, vol. 3, p. S08005, 2008.

[71] K. Aamodt *et al.*, "The ALICE experiment at the CERN LHC," *JINST*, vol. 3, p. S08002, 2008.

[72] G. Antchev *et al.*, "The TOTEM detector at LHC," *Nucl. Instrum. Meth. A*, vol. 617, pp. 62–66, 2010.

[73] J. Pinfold *et al.*, "Technical Design Report of the MoEDAL Experiment," 6 2009.

[74] O. Adriani *et al.*, "The LHCf detector at the CERN Large Hadron Collider," *JINST*, vol. 3, p. S08006, 2008.

[75] H. Abreu *et al.*, "The FASER Detector," 7 2022.

[76] A. Tauro, "ALICE Schematics." General Photo, 2017.

[77] "ALICE upgrades during the LHC Long Shutdown 2," 2 2023.

[78] P. Cortese *et al.*, "ALICE: Physics performance report, volume I," *J. Phys. G*, vol. 30, pp. 1517–1763, 2004.

[79] C. W. Fabjan *et al.*, "ALICE: Physics Performance Report," *J. Phys. G*, vol. 32, pp. 1295–2040, 2006.

[80] B. B. Abelev *et al.*, "Performance of the ALICE Experiment at the CERN LHC," *Int. J. Mod. Phys. A*, vol. 29, p. 1430044, 2014.

[81] G. Dellacasa *et al.*, "ALICE technical design report of the inner tracking system (ITS)," 6 1999.

[82] K. Aamodt *et al.*, "Alignment of the ALICE Inner Tracking System with cosmic-ray tracks," *JINST*, vol. 5, p. P03003, 2010.

[83] M. Šuljić, "ALPIDE: the Monolithic Active Pixel Sensor for the ALICE ITS upgrade," *Nuovo Cim. C*, vol. 41, no. 1-2, p. 91, 2018.

[84] F. Reidt, "Upgrade of the ALICE ITS detector," *Nucl. Instrum. Meth. A*, vol. 1032, p. 166632, 2022.

[85] B. Abelev *et al.*, "Technical Design Report for the Upgrade of the ALICE Inner Tracking System," *J. Phys. G*, vol. 41, p. 087002, 2014.

[86] I. Ravasenga, "Commissioning and Performance of the New ALICE Inner Tracking System in the First Phase of LHC Run 3," tech. rep., 2023. 12 pages, 13 figures. Proceeding at Vertex 2022 held in Tateyama Resort Hotel, Japan.

[87] G. Dellacasa *et al.*, "ALICE: Technical design report of the time projection chamber," 1 2000.

[88] J. Alme *et al.*, "The ALICE TPC, a large 3-dimensional tracking device with fast readout for ultra-high multiplicity events," *Nucl. Instrum. Meth. A*, vol. 622, pp. 316–367, 2010.

[89] J. Adolfsson *et al.*, "The upgrade of the ALICE TPC with GEMs and continuous readout," *JINST*, vol. 16, no. 03, p. P03022, 2021.

[90] R. Münzer, "Upgrade of the ALICE Time Projection Chamber," *Nucl. Instrum. Meth. A*, vol. 958, p. 162058, 2020.

[91] R. Schicker, "Overview of ALICE results in pp, pA and AA collisions," *EPJ Web Conf.*, vol. 138, p. 01021, 2017.

[92] *ALICE Time-Of-Flight system (TOF): Technical Design Report*. Technical design report. ALICE, Geneva: CERN, 2000.

[93] P. Cortese *et al.*, "ALICE technical design report on forward detectors: FMD, T0 and V0," 9 2004.

[94] E. Abbas *et al.*, "Performance of the ALICE VZERO system," *JINST*, vol. 8, p. P10016, 2013.

[95] M. Gallio, W. Klempt, L. Leistam, J. De Groot, and J. Schükraft, *ALICE Zero-Degree Calorimeter (ZDC): Technical Design Report*. Technical design report. ALICE, Geneva: CERN, 1999.

[96] G. Dellacasa *et al.*, "The neutron zero degree calorimeter for the ALICE experiment," *Nucl. Instrum. Meth. A*, vol. 564, pp. 235–242, 2006.

[97] P. Cortese, "Performance of the ALICE Zero Degree Calorimeters and upgrade strategy," *J. Phys. Conf. Ser.*, vol. 1162, no. 1, p. 012006, 2019.

[98] C. W. Fabjan, L. Jirdén, V. Lindestruth, L. Riccati, D. Rorich, P. Van de Vyvre, O. Villalobos Baillie, and H. de Groot, *ALICE trigger data-acquisition high-level trigger and control system: Technical Design Report*. Technical design report. ALICE, Geneva: CERN, 2004.

[99] M. Arslandok, E. Hellbär, M. Ivanov, R. H. Münzer, and J. Wiechula, "Track Reconstruction in a High-Density Environment with ALICE," *Particles*, vol. 5, no. 1, pp. 84–95, 2022.

[100] R. Fruhwirth, "Application of Kalman filtering to track and vertex fitting," *Nucl. Instrum. Meth. A*, vol. 262, pp. 444–450, 1987.

[101] "Centrality determination in heavy ion collisions," 2018.

[102] B. Abelev *et al.*, "Centrality determination of Pb-Pb collisions at $\sqrt{s_{NN}} = 2.76$ TeV with ALICE," *Phys. Rev. C*, vol. 88, no. 4, p. 044909, 2013.

[103] D. Kharzeev, E. Levin, and M. Nardi, "Color glass condensate at the LHC: Hadron multiplicities in pp, pA and AA collisions," *Nucl. Phys. A*, vol. 747, pp. 609–629, 2005.

[104] H. Bethe, "Theory of the Passage of Fast Corpuscular Rays Through Matter," *Annalen Phys.*, vol. 5, pp. 325–400, 1930.

[105] N. Bohr, "II. On the theory of the decrease of velocity of moving electrified particles on passing through matter," *The London, Edinburgh, and Dublin Philosophical Magazine and Journal of Science*, vol. 25, no. 145, pp. 10–31, 1913.

[106] H. Bethe, "Bremsformel für Elektronen relativistischer Geschwindigkeit," *Zeitschrift für Physik*, vol. 76, pp. 293–299, May 1932.

[107] F. Bloch, "Zur Bremsung Rasch Bewegter Teilchen beim Durchgang durch Materie," *Annalen Phys.*, vol. 408, pp. 285–320, 1933.

[108] F. Bloch, "Zur Bremsung Rasch Bewegter Teilchen beim Durchgang durch Materie," *Annalen Phys.*, vol. 408, pp. 285–320, 1933.

[109] R. L. Workman and Others, "Review of Particle Physics," *PTEP*, vol. 2022, p. 083C01, 2022.

[110] E. Fermi, "The Ionization Loss of Energy in Gases and in Condensed Materials," *Phys. Rev.*, vol. 57, pp. 485–493, 1940.

[111] R. M. Sternheimer, M. J. Berger, and S. M. Seltzer, "Density Effect for the Ionization Loss of Charged Particles in Various Substances," *Atom. Data Nucl. Data Tabl.*, vol. 30, pp. 261–271, 1984.

[112] H. Kolanoski and N. Wermes, *Particle Detectors: Fundamentals and Applications*. Oxford University Press, 2020.

[113] W. Blum, L. Rolandi, and W. Riegler, *Particle detection with drift chambers*. Particle Acceleration and Detection, 2008.

[114] P. V. Vavilov, "Ionization losses of high-energy heavy particles," *Sov. Phys. JETP*, vol. 5, pp. 749–751, 1957.

[115] L. Landau, "On the energy loss of fast particles by ionization," *J. Phys. (USSR)*, vol. 8, pp. 201–205, 1944.

[116] M. Arslandok, E. Hellbär, M. Ivanov, R. H. Münzer, and J. Wiechula, "Track Reconstruction in a High-Density Environment with ALICE," *Particles*, vol. 5, no. 1, pp. 84–95, 2022.

[117] B. A. Hess, *Particle Identification in Jets and High-Multiplicity pp Events with the ALICE TPC*. PhD thesis, Tubingen U., 6 2015.

[118] P. Christiansen, "High p_t identified particle production in ALICE," *Nucl. Phys. A*, vol. 910-911, pp. 20–26, 2013.

[119] J. Podolanski and R. Armenteros, "Iii. analysis of v-events," *The London, Edinburgh, and Dublin Philosophical Magazine and Journal of Science*, vol. 45, no. 360, pp. 13–30, 1954.

[120] I. Antcheva *et al.*, "ROOT: A C++ framework for petabyte data storage, statistical analysis and visualization," *Comput. Phys. Commun.*, vol. 180, pp. 2499–2512, 2009.

[121] S. Rossegger and W. Riegler, "Signal shapes in a TPC wire chamber," *Nuclear Instruments and Methods in Physics Research Section A: Accelerators, Spectrometers, Detectors and Associated Equipment*, vol. 623, no. 3, pp. 927–930, 2010.

[122] C. Sonnabend, "Neural network regression for particle identification with the ALICE TPC detector in Run 3," 2022. Presented 28 Nov 2022.

[123] L. Kreis, "Investigating the Initial State of Heavy-Ion Collisions through Measurements of Anisotropic Flow using Spectator Neutrons with ALICE at the LHC," 2021.

[124] M. Gyulassy and X.-N. Wang, "HIJING 1.0: A Monte Carlo program for parton and particle production in high-energy hadronic and nuclear collisions," *Comput. Phys. Commun.*, vol. 83, p. 307, 1994.

[125] R. Brun, F. Bruyant, F. Carminati, S. Giani, M. Maire, A. McPherson, G. Patrick, and L. Urban, *GEANT: Detector Description and Simulation Tool; Oct 1994*. CERN Program Library, Geneva: CERN, 1993. Long Writeup W5013.

[126] J. Adam *et al.*, "Particle identification in ALICE: a Bayesian approach," *Eur. Phys. J. Plus*, vol. 131, no. 5, p. 168, 2016.

[127] P. Gregory, *Bayesian Logical Data Analysis for the Physical Sciences: A Comparative Approach with Mathematica® Support*. Cambridge University Press, 2005.

[128] I. Selyuzhenkov and S. Voloshin, "Effects of non-uniform acceptance in anisotropic flow measurement," *Phys. Rev. C*, vol. 77, p. 034904, 2008.

[129] R. Barlow, "Systematic errors: Facts and fictions," in *Conference on Advanced Statistical Techniques in Particle Physics*, pp. 134–144, 7 2002.

[130] J. Adam *et al.*, "Higher harmonic flow coefficients of identified hadrons in Pb-Pb collisions at $\sqrt{s_{\mathrm{NN}}} = 2.76$ TeV," *JHEP*, vol. 09, p. 164, 2016.

[131] C. Shen, Z. Qiu, H. Song, J. Bernhard, S. Bass, and U. Heinz, "The iEBE-VISHNU code package for relativistic heavy-ion collisions," *Comput. Phys. Commun.*, vol. 199, pp. 61–85, 2016.

[132] G. Apollinari, O. Brüning, T. Nakamoto, and L. Rossi, "High Luminosity Large Hadron Collider HL-LHC," *CERN Yellow Rep.*, no. 5, pp. 1–19, 2015.